

# **CoCrTa thin films for magnetic recording media**

*structures, magnetic properties and time-dependence effect*



# **Màng mỏng ghi từ CoCrTa**

*cấu trúc, các tính chất từ và hiệu ứng phụ thuộc thời gian*

Phan Le Kim

Composition of the Ph.D. dissertation committee:

**Promotors:**

Prof. Dr. Th. J. A. Popma	University of Twente, the Netherlands
Prof. Dr. Than Duc Hien	International Training Institute for Materials Science, Vietnam

**Assistant promotor:**

Ass. Prof. Dr. J. C. Lodder	University of Twente, the Netherlands
-----------------------------	---------------------------------------

**Members:**

Dr. J. Beyer	University of Twente, the Netherlands
Prof. Dr. S. B. Luitjens	University of Twente, the Netherlands
Prof. Dr. R. W. Chantrell	University of Wales, UK
Ass. Prof. Dr. Nguyen Hoang Luong	National University of Hanoi, Vietnam
Dr. D. Givord	CNRS, France

This thesis was carried out at

- the Information Storage Technology Group (ISTG), MESA research institute, University of Twente, P.O. Box 217, 7500AE Enschede, the Netherlands,
- the International Training Institute for Materials Science (ITIMS), 1 Dai Co Viet street, Hanoi, Vietnam.

Title: CoCrTa thin films for magnetic recording media: structures, magnetic properties and time-dependence effect.

Author: Phan Le Kim

ISBN: 90-3651276X

Subject: Materials science, magnetic recording media

Copyright © 1999 by Phan Le Kim

All rights reserved.

Printed by Print Partners Ipskamp, 7500AH, Enschede.

Cover: Schematic diagram of the epitaxial relationship between  $\text{Co}(10\bar{1}1)$  and  $\text{Cr}(110)$  textures (see Fig. 6.1.1 for further detail).

# **CoCrTa THIN FILMS FOR MAGNETIC RECORDING MEDIA**

## ***STRUCTURES, MAGNETIC PROPERTIES AND TIME-DEPENDENCE EFFECT***

PROEFSCHRIFT

ter verkrijging van  
de graad van doctor aan de Universiteit Twente,  
op gezag van de rector magnificus,  
prof. dr. F. A. van Vught,  
volgens besluit van het College voor Promoties  
in het openbaar te verdedigen  
op donderdag 15 april 1999 te 15.00 uur.

door

Phan Le Kim

geboren op 2 maart 1971

te Hanoi, Vietnam

This thesis has been approved by

the promoters:

Prof. Dr. Th. J. A. Popma  
Prof. Dr. Than Duc Hien

the assistant promotor:

Ass. Prof. Dr. J. C. Lodder

*To my parents*

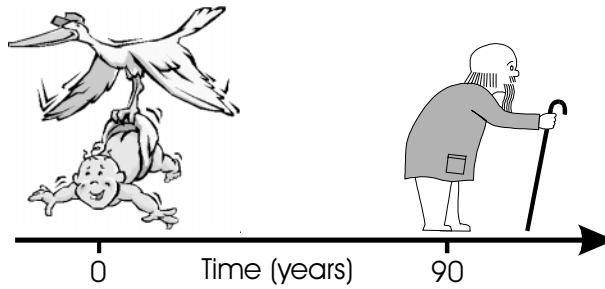
## The contents of the thesis at a glance



*Structural properties*



*Magnetic properties*



*Time-dependence effect*

# Contents

<b>CHAPTER 1</b>	
<b>INTRODUCTION .....</b>	<b>13</b>
1.1. FROM A GLOBAL PERSPECTIVE... ..	13
1.2. ... TO THE SCOPE AND CONTENTS OF THE THESIS .....	16
1.3. REFERENCES .....	19
<b>CHAPTER 2</b>	
<b>SOME BASICS OF CoCrTa RECORDING MEDIA.....</b>	<b>21</b>
2.1. CRITERIA FOR A GOOD RECORDING MEDIUM .....	21
2.2. THE ROLE OF Cr AND Ta AND SEGREGATION IN CoCrTa MEDIA .....	24
2.3. UNDERLAYERS IN Co-ALLOY RECORDING MEDIA .....	29
2.3.1. PERPENDICULAR MEDIA.....	29
2.3.2. LONGITUDINAL MEDIA.....	30
2.4. MAIN ISSUES OF Co-ALLOY MAGNETIC RECORDING MEDIA RESEARCH .....	31
2.5. CONCLUSION .....	30
2.6. REFERENCES .....	30
<b>CHAPTER 3</b>	
<b>TIME-DEPENDENCE EFFECT IN MAGNETIC RECORDING MEDIA .....</b>	<b>33</b>
3.1. SOME BASICS ABOUT THE TIME-DEPENDENCE EFFECT .....	34
3.1.1. MAGNETIC RELAXATION AND MAGNETIC VISCOSITY.....	34
3.1.2. ENERGY BARRIER OF A MAGNETIC PARTICLE .....	35
3.1.3. SUPERPARAMAGNETIC LIMIT .....	38
3.1.4. FROM NON-INTERACTING STONER-WOLFHARTH PARTICLES TO PRACTICAL RECORDING MEDIA .....	39
3.2. ANALYTICAL MODEL FOR THE TIME-DEPENDENCE EFFECT .....	41
3.3. FLUCTUATION FIELD AND ACTIVATION VOLUME .....	43
3.4. DEMAGNETIZATION CORRECTIONS FOR PERPENDICULAR MEASUREMENTS.....	43
3.5. EXPERIMENTAL METHODS.....	44

## Contents

---

3.5.1. MAGNETIC VISCOSITY MEASUREMENTS .....	44
3.5.2. FLUCTUATION FIELD MEASUREMENTS .....	45
3.5.2.1. <i>The DCD method</i> .....	45
3.5.2.2. <i>The waiting time method</i> .....	47
<b>3.6. FITTING PROCEDURES.....</b>	<b>48</b>
<b>3.7. DEFINITIONS OF THE CONFUSING VOLUMES .....</b>	<b>50</b>
<b>3.8. CONCLUSION .....</b>	<b>52</b>
<b>3.9. REFERENCES .....</b>	<b>52</b>

## **CHAPTER 4**

### **SAMPLE PREPARATION AND EXPERIMENTAL METHODS ..... 55**

<b>4.1. PREPARATION OF SPUTTERED SAMPLES: SPUTTER DEPOSITION.....</b>	<b>55</b>
4.1.1. RF SPUTTERING SYSTEM.....	55
4.1.2. OPERATION OF THE SYSTEM .....	57
4.1.3. SUBSTRATE HEATING.....	57
<b>4.2. MAGNETIC CHARACTERIZATION.....</b>	<b>58</b>
4.2.1. VSM MEASUREMENTS .....	58
4.2.2. TORQUE MEASUREMENTS.....	59
<b>4.3. STRUCTURAL CHARACTERIZATION.....</b>	<b>62</b>
4.3.1. X-RAY DIFFRACTION.....	62
4.3.1.1. <i>High-angle measurements</i> .....	62
4.3.1.2. <i>Rocking curve measurements</i> .....	63
4.3.1.3. <i>Low-angle measurements</i> .....	64
4.3.2. MICROSCOPY.....	65
4.3.2.1. <i>SEM</i> .....	65
4.3.2.2. <i>TEM</i> .....	65
4.3.2.3. <i>AFM</i> .....	67
4.3.2.4. <i>Comparison between AFM and TEM plane-view images</i> .....	68
4.3.3. XRF .....	69
4.3.4. AES AND DEPTH PROFILING MEASUREMENTS .....	70
<b>4.4. CONCLUSION .....</b>	<b>70</b>
<b>4.5. REFERENCES .....</b>	<b>71</b>

## **CHAPTER 5**

### **EXPERIMENTAL RESULTS OF SPUTTERED CoCrTa THIN FILMS ..... 73**

<b>5.1. INFLUENCES OF SPUTTERING CONDITIONS .....</b>	<b>73</b>
5.1.1. INFLUENCE OF AR PRESSURE AT ROOM TEMPERATURE.....	73

5.1.1.1. <i>Deposition rate</i> .....	75
5.1.1.2. <i>Texture</i> .....	75
5.1.1.3. <i>Composition</i> .....	78
5.1.1.4. <i>Lattice spacings</i> .....	81
5.1.1.5. <i>Magnetic properties</i> .....	82
5.1.2. INFLUENCE OF AR PRESSURE AT HIGH TEMPERATURE .....	83
5.1.2.1. <i>Texture</i> .....	83
5.1.2.2. <i>Coercivities</i> .....	85
5.1.3. INFLUENCE OF SUBSTRATE TEMPERATURE .....	86
5.1.3.1. <i>Textures</i> .....	86
5.1.3.2. <i>Roughness</i> .....	87
5.1.3.3. <i>Depth profile of composition</i> .....	88
5.1.3.4. <i>Magnetic properties</i> .....	91
<b>5.2. CoCrTa THIN FILMS VERSUS FILM THICKNESS .....</b>	<b>93</b>
5.2.1. INITIAL LAYER .....	93
5.2.2. DEPENDENCE OF GRAIN SIZE ON FILM THICKNESS .....	96
<b>5.3. INFLUENCES OF ALLOY COMPOSITION .....</b>	<b>97</b>
5.3.1. THE ROLES OF CR AND TA IN THE CoCrTa FILMS.....	97
5.3.2. EXPERIMENTS.....	98
5.3.3. RESULTS AND DISCUSSION .....	99
<b>5.4. CONCLUSION .....</b>	<b>104</b>
<b>5.5. REFERENCES .....</b>	<b>105</b>
<b>CHAPTER 6</b>	
<b>CoCrTa/Cr THIN FILMS FOR LONGITUDINAL RECORDING .....</b>	<b>109</b>
<b>6.1. ABOUT THE CR UNDERLAYER AND ITS CRYSTALLOGRAPHIC TEXTURES .....</b>	<b>109</b>
6.1.1. THE ROLE OF THE CR UNDERLAYER AND CRYSTALLOGRAPHY OF CO-ALLOY LAYER GROWN ON CR UNDERLAYER.....	109
6.1.1.1. <i>Crystal structures of Cr and Co-alloys</i> .....	110
6.1.1.2. <i>Epitaxial relationships between Co-alloy layer and Cr underlayer</i> .....	110
6.1.1.3. <i>Optimum texture for longitudinal recording media</i> .....	112
6.1.2. MODEL FOR THE FORMATION OF CRYSTALLOGRAPHIC TEXTURE OF CR THIN FILMS .....	112
<b>6.2. EXPERIMENTAL RESULTS ON CR THIN FILMS .....</b>	<b>114</b>
6.2.1. CR FILMS ON DIFFERENT TYPES OF SUBSTRATES .....	114
6.2.2. CR FILMS PRODUCED AT VARIOUS SUBSTRATE TEMPERATURES .....	116
6.2.3. CR FILMS OF VARIOUS THICKNESSES .....	118
6.2.3.1. <i>Development of film textures</i> .....	118
6.2.3.2. <i>Development of morphology</i> .....	120
6.2.4. CR FILMS PRODUCED AT VARIOUS AR PRESSURES .....	122

6.2.5. DISCUSSION AND SUMMARY .....	123
<b>6.3. EXPERIMENTS ON CoCrTa ON Cr UNDERLAYER: VARYING CoCrTa THICKNESS</b> .....	<b>125</b>
6.3.1. SPUTTERING PROCESS.....	125
6.3.2. TEXTURE.....	127
6.3.3. GENERAL MAGNETIC PROPERTIES .....	129
6.3.3.1. <i>Hysteresis loops</i> .....	129
6.3.3.2. <i>Coercivities</i> .....	130
6.3.3.3. <i>Squareness</i> .....	134
6.3.3.4. <i>Effective anisotropy constants</i> .....	134
6.3.4. VISCOSITY .....	135
6.3.5. ANGULAR DEPENDENT MEASUREMENTS.....	136
6.3.5.1. <i>Angular dependence of coercivity</i> .....	137
6.3.5.2. <i>Angular dependence of hysteresis loss</i> .....	140
<b>6.4. EXPERIMENTS ON CoCrTa ON Cr UNDERLAYER: VARYING Cr THICKNESS .....</b>	<b>141</b>
6.4.1. SPUTTERING PROCESS.....	141
6.4.2. MORPHOLOGY .....	142
6.4.2.1. <i>Plane-view images</i> .....	142
6.4.2.2. <i>Cross-sectional images</i> .....	144
6.4.3. GENERAL MAGNETIC PROPERTIES .....	147
6.4.3.1. <i>Coercivity</i> .....	147
6.4.3.2. <i>Squareness</i> .....	148
6.4.3.3. <i>Effective anisotropy constant</i> .....	149
6.4.3.4. <i>Discussion</i> .....	150
6.4.4. INITIAL SUSCEPTIBILITY .....	151
6.4.4.1. <i>Principle</i> .....	151
6.4.4.2. <i>Results</i> .....	152
6.4.5. ANGULAR DEPENDENT MEASUREMENTS.....	153
<b>6.5. CONCLUSION .....</b>	<b>155</b>
<b>6.6. REFERENCES .....</b>	<b>156</b>

## CHAPTER 7

### EXPERIMENTAL AND FITTING RESULTS OF THE TIME-DEPENDENCE

#### EFFECT IN RECORDING MEDIA ..... 161

<b>7.1. TIME-DEPENDENCE EFFECT IN IN-PLANE MEDIA .....</b>	<b>161</b>
7.1.1. EXPERIMENTAL RESULTS AND DISCUSSION .....	161
7.1.2. FITTING RESULTS AND DISCUSSION .....	167
7.1.2.1. <i>Discussion on the parameters of the fit</i> .....	167
7.1.2.2. <i>Discussion on <math>V_{switching}</math></i> .....	168
7.1.2.3. <i>What is the nature of the viscosity curve ?</i> .....	168
7.1.2.4. <i>Energy barrier and relaxation time as a function of applied field</i> .....	170

7.1.3. INFLUENCE OF THE DELAY TIME ON THE DCD AND $\chi_{\text{IRR}}$ MEASUREMENTS OF IN-PLANE MEDIA.....	172
<b>7.2. TIME-DEPENDENCE EFFECT IN PERPENDICULAR MEDIA .....</b>	<b>175</b>
7.2.1. ALUMITE MEDIA .....	175
7.2.1.1. <i>About the samples and their important parameters .....</i>	<i>175</i>
7.2.1.2. <i>Viscosity and remanence measurements .....</i>	<i>177</i>
7.2.1.3. <i>Fluctuation fields and activation volumes .....</i>	<i>179</i>
7.2.1.4. <i>Fitting results and discussion.....</i>	<i>182</i>
7.2.2. CoCrTa SINGLE LAYERS.....	186
7.2.2.1. <i>Viscosity curves.....</i>	<i>186</i>
7.2.2.2. <i>Activation volumes .....</i>	<i>190</i>
7.2.2.3 <i>Fitting results and discussion.....</i>	<i>192</i>
<b>7.3. CONCLUSION .....</b>	<b>192</b>
<b>7.4. REFERENCES .....</b>	<b>193</b>
<b>CHAPTER 8</b>	
<b>SUMMARY, GENERAL CONCLUSIONS AND FUTURE TRENDS .....</b>	<b>197</b>
8.1. SUMMARY .....	197
8.2. GENERAL CONCLUSIONS.....	200
8.3. FUTURE TRENDS OF DATA STORAGE TECHNOLOGIES.....	201
8.4. REFERENCES .....	203
<b>APPENDIX .....</b>	<b>205</b>
<b>LIST OF SYMBOLS AND ABBREVIATIONS .....</b>	<b>207</b>
<b>ACKNOWLEDGEMENTS.....</b>	<b>211</b>
<b>BIOGRAPHY.....</b>	<b>217</b>
<b>PUBLICATIONS AND PRESENTATIONS .....</b>	<b>217</b>

## Contents

---

# Chapter 1

---

## Introduction

### 1.1. From a global perspective...

Magnetic recording technology celebrated its 100-year-old birthday last year, in 1998. It is indeed an old technology, compared to the newly developing storage technologies such as semiconductor memory and (magneto)optical recording. However, the computer hard disk drive (HDD) technology has been and is still based on the magnetic recording principle. Thanks to the development of recording media and recording system of HDD, especially the recent invention of the *magnetoresistive (MR)* and *giant magnetoresistive (GMR)* heads, the compound annual growth rate in areal density has changed from about 30% to 60% since the beginning of the 1990s [Speliotis-97]. A hot topic in the recent forums for magnetic recording technology is the goal of 10 Gbits/in<sup>2</sup> (equivalent to 1.55 Gbits/cm<sup>2</sup>). In the fall of 1998, IBM released the highest density HDD for notebook computer, that is the Travelstar 14GN, having a maximum areal density of 5.7 Gbits/in<sup>2</sup> [Uimonen-98]. With a dimension of merely 9.5×70×100 mm<sup>3</sup> and a weight of 95g, it can hold 6.4 Gbytes of information. This event affirms the prospect of magnetic recording technology beyond the turn of the 21st century. Recently, IBM has announced their new areal density of even 11.6 Gbits/in<sup>2</sup> achieved in the laboratory [IBM-99], which sets the goal for magnetic recording research further to 40 Gbits/in<sup>2</sup>.

The magnetic recording technology consists of two main disciplines: *recording media* and *recording system*. The evolution of magnetic recording, i.e. the growth of recording density, is based on two conditions:

- The necessary condition is to achieve a better magnetic recording medium. The recording media should be improved to carry more bits on a unit of medium area with low noise. This includes development of new medium materials, new configuration of the layers and optimization of parameters of the media by changing fabrication conditions.

## 1.1. From a global perspective...

---

- The sufficient condition is to design a better recording system. This includes the improvement of the head. The head can be improved by scaling down its dimensions and the head-to-medium spacing while increasing its sensitivity. Besides, the development of the servo system, encode and decode techniques and electronics also contributes considerable roles in the evolution of the magnetic recording technology.

Research of recording media should always progress one step forward the development of recording system. Since the first bulky RAMAC hard disk, holding not more than 5 Mbytes, which was released by IBM in 1956, the areal recording density has increased by six orders of magnitude [Lodder-98 and Speliotis-97]. A large part of this improvement is attributed to the development of the recording media.

Another way to improve drastically the recording density is to change the recording mode. To date, the longitudinal recording mode is still used in all commercial hard disk drives. In this mode, the recorded bits are stored in form of domains with magnetization lying in the plane of the medium (see Fig. 1.1.1). Two well-known problems of this mode which hinder the evolution of recording density are i) the relatively large bit transition which restricts the increase in linear density and ii) the existence of the zigzag shape of the transitions which results in read-back noise. A solution to these problems, which has been under development for more than 20 years, is the perpendicular recording mode. In this mode, magnetization of the recorded bits is directed perpendicular to the plane of the medium, thus reducing remarkably the bit size, bit transition and eliminating the zigzag shape of the bit transitions (see Fig. 1.1.1). Therefore, if successful, perpendicular recording is expected to reach a density of 100 Gbits/in<sup>2</sup> [Thompson-97], which is very close to the superparamagnetic limit, a limit at which the recorded information can be erased by the thermal energy  $kT$  at normal temperature. However, there are numbers of difficulties which obstruct the dream of bringing perpendicular recording into application, at least, in the near future [Thompson-97].

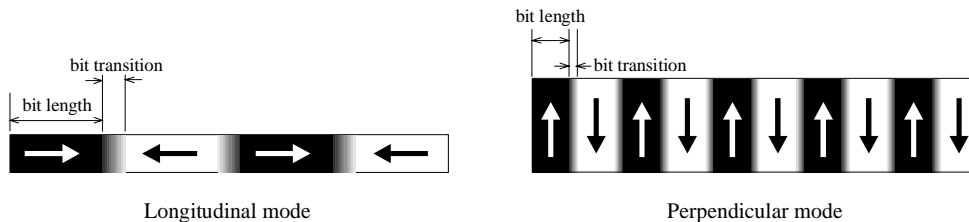


*Fig. 1.1.1. Schematic diagram of longitudinal and perpendicular recording modes.*

As mentioned above, there are two disciplines in magnetic recording technology: recording media and recording system. Figure 1.1.2 explains how these two disciplines share their job in a HDD. The left part of the figure shows a picture of the inside of a HDD. The most important part is the disk stack, which consists of several (typically 3, 5 or more) hard disks. These are the storage media. The surrounding components are used to write and read information from the media, including the heads (each head is responsible for one side of a disk), the servo system and the electronics. Let's focus attention on the media, i.e. the disks. A magnified cross-section of one side of a disk is shown in the right part of Fig. 1.1.2. The disk, which serves as the substrate of the medium, is made of Mg-Al alloy. In the up-to-date hard disks like the Travelstar family, glass could displace the conventional Mg-Al alloy [Brown-99]. Each side of the disk is coated with several layers. Let's start from the bottom layer [Mallinson-93]:

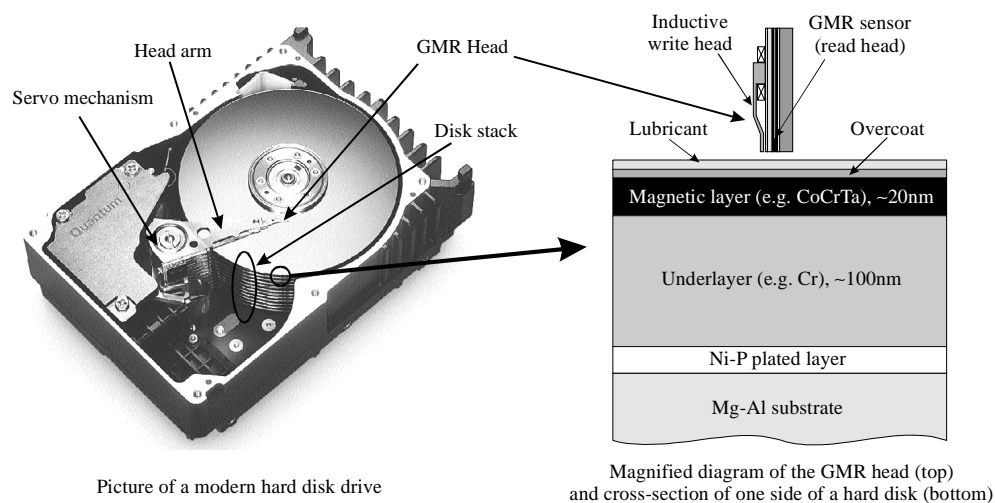


*Fig. 1.1.2. Left: Picture of a modern hard disk drive [Quantum-99], in which the disk stack belongs to the recording media technology and the rest, including the heads, servo system, electronics (at the bottom, not visible), etc. belongs to the recording system technology. Right: Magnified diagrams of the GMR head [IBM-99] and cross-section of one side of a hard disk [Mallinson-93, p. 35 and Lodder-98].*

- The *chemically plated Ni-P layer*. This layer is used as an interface between the thin film layer and the substrate. It can be polished to an excellently

## 1.1. From a global perspective...

---

smooth surface and can also be circumferentially textured\* afterwards to induce a circumferential anisotropy of the medium [Johnson-95].

- The *sputtered Cr underlayer*, which is used to control the easy-axis orientation of the magnetic layer (the medium). Besides, the Cr underlayer helps to improve the performance of the medium by means of uncoupling mechanism. This layer has a typical thickness of about 100nm.
- The *sputtered magnetic layer*. This is the recording medium, which is made of a Co-alloy thin film such as CoCrTa or CoPtCr alloy or these alloy with a small amount of other additive elements, such as B in the Travelstar family [Brown-99]. The thickness of this layer is about 20nm.
- The *overcoat layer*, which is normally a sputtered amorphous C or zirconia, etc. layer, to protect the inner layers from wear.
- The *lubricant layer* is finally applied on top of the disk to reduce friction between the head and the disk and to create air bearing for the head to fly over.

Among the above layers, the most important parts of the hard disk are the magnetic layer and the underlayer. For more than 30 years, numbers of works have been devoted to improve these two layers, in order to reach a higher density.

## 1.2. ... to the scope and contents of the thesis

Studying the CoCrTa magnetic layer and the Cr underlayer is the main subject of this thesis. Although the study keeps a distance from the real application, it tries to navigate to meet the demands of application. This means that thin films produced in this study are in form of media samples, deposited on Si or glass substrates. Different properties of the samples are then investigated. However we do not perform any recording characterization. During the investigations, we seek a way to optimize the deposition conditions that result in media with good quality, able to meet criteria of recording application. Another aspect of the thesis is to study the time-dependence effect of different types of recording media, chiefly of CoCrTa media. The time-dependence effect is related to thermal stability of media. As the

---

\* Circumferential texturing can be done by scratching the surface along the circumference of the disk.

recording density increases, this issue becomes more and more important and attracts much attention of the recent works.

At first, the CoCrTa and the Cr thin films are treated separately. Then they are studied as double layers, which means the CoCrTa layer is grown on top of the Cr layer.

Three chapters following this introduction chapter give some foundations for the studies carried out in the thesis. *Chapter 2* gives some broad knowledge of the CoCrTa media. *Chapter 3* presents a foundation for the study of the time-dependence effect, including some theoretical basics and experimental methods that have been developed to investigate this effect. *Chapter 4* outlines other experimental methods and techniques, which are used in the thesis, including sputtering technique, magnetic and structural characterization methods.

In *Chapter 5*, studies of properties of the CoCrTa single layer under different sputtering conditions and with different compositions are presented. From the results of these studies, optimized conditions and composition are deduced.

Next, in the first part of *Chapter 6*, we investigate texture and morphology of the Cr single layers, trying to find a way to control properties of this layer. Based on the results of this study and of Chapter 5, the CoCrTa/Cr double layers are investigated in the rest of the chapter. The investigation is divided into two steps. In the first step, the CoCrTa layer thickness is varied while the thickness of Cr is constant. In the second step, a fixed CoCrTa layer is grown on a Cr underlayer of various thicknesses.

*Chapter 7* deals with another aspect of recording media research, that is the time-dependence effect. The general aim of the study is to investigate and explain the field-dependence of magnetic viscosity in different samples, from in-plane CoCrTa/Cr media to perpendicular media. There is a section in this chapter, Section 7.2.1, which studies the time-dependence effect of perpendicular alumite media because this type of media is often considered as a good model to study the switching mechanisms. With the benefit of this study, the next section investigates the time-dependence effect in CoCrTa single layers having perpendicular c-axis orientation.

Finally, *Chapter 8* gives a conclusion of the whole thesis and a future perspective of data storage technologies.



## 1.3. References

- [Brown-99] N. G. Brown (IBM corp.). Private communication.
- [IBM-99] Web site of IBM corp: [www.storage.ibm.com/oem/mrheads/](http://www.storage.ibm.com/oem/mrheads/)
- [Johnson-95] K. E. Johnson. "In-plane anisotropy in thin film media: Physical origins of orientation ratio (invited)". *IEEE Trans. Magn.* 31 (1995), 2721.
- [Lodder-98] J. C. Lodder. "Magnetic recording hard disk thin film media". *Handbook of magnetic materials*. Vol. 11 (1998), edited by K. H. J. Buschow.
- [Mallinson-93] J. C. Mallinson. "The foundations of magnetic recording". Academic press, inc. 1993.
- [Quantum-99] Web site of Quantum corp: [www.quantum.com/products/](http://www.quantum.com/products/)
- [Speliotis-97] D. Speliotis. "Magnetic recording: 100 years old and still growing". *J. Magn. Soc. of Japan* 21 (Supp. No. S2) (1997), 119.
- [Thompson-97] D. Thompson. "The role of perpendicular recording in the future of hard disk storage". *J. Magn. Soc. of Japan* 21 (Supp. No. S2) (1997), 9.
- [Uimonen -98] T. Uimonen. "IBM unveils record 14.1GB drive for notebooks". *PC World Today*, October 22, 1998.

### 1.3. References

---

# Chapter 2

---

## Some basics of CoCrTa recording media

### 2.1. Criteria for a good recording medium

Researchers of recording media have been following a guideline which keeps themselves progressing. For the hard disk drive technology, the final goal is to raise the areal recording density. However, the nature is not always kind to us; we gain the density but we may lose the stability and the signal-to-noise ratio (SNR). Therefore, the primary criteria for a good recording medium should be a compromise between these parameters:

- High areal recording density.
- Sufficiently high thermal stability.
- Sufficiently high SNR.

To achieve one of the above criteria, we have to act on the causes of them, i.e. we have to improve numbers of other magnetic and structural parameters. For instance, to increase the density, the transition length must be reduced. A famous formula, expressing the relationship between the transition length,  $a$ , and other parameters of a medium, can be considered [e.g. Speliotis-97]:

$$a = \left[ \frac{8}{\sqrt{3}} \frac{M_r \delta}{H_c} \left( d + \frac{\delta}{2} \right) \right]^{1/2} \quad (2.1.1)$$

where  $M_r$  is the remanent magnetization (remanence),  $H_c$  is the coercivity,  $\delta$  is the medium thickness and  $d$  is the head-to-medium spacing.

From this formula, we can deduce that to reduce  $a$ ,  $H_c$  must be increased while  $M_r$  and  $\delta$  must be decreased. It should be noted that all of the magnetic and structural

## 2.1. Criteria for a good recording medium

parameters are not independent; they have complicated relationships with one another. Figure 2.1.1 shows a diagram describing the relationships between the most important parameters of magnetic recording media. This diagram also serves as a strategy to achieve high recording density media with high stability and high SNR.

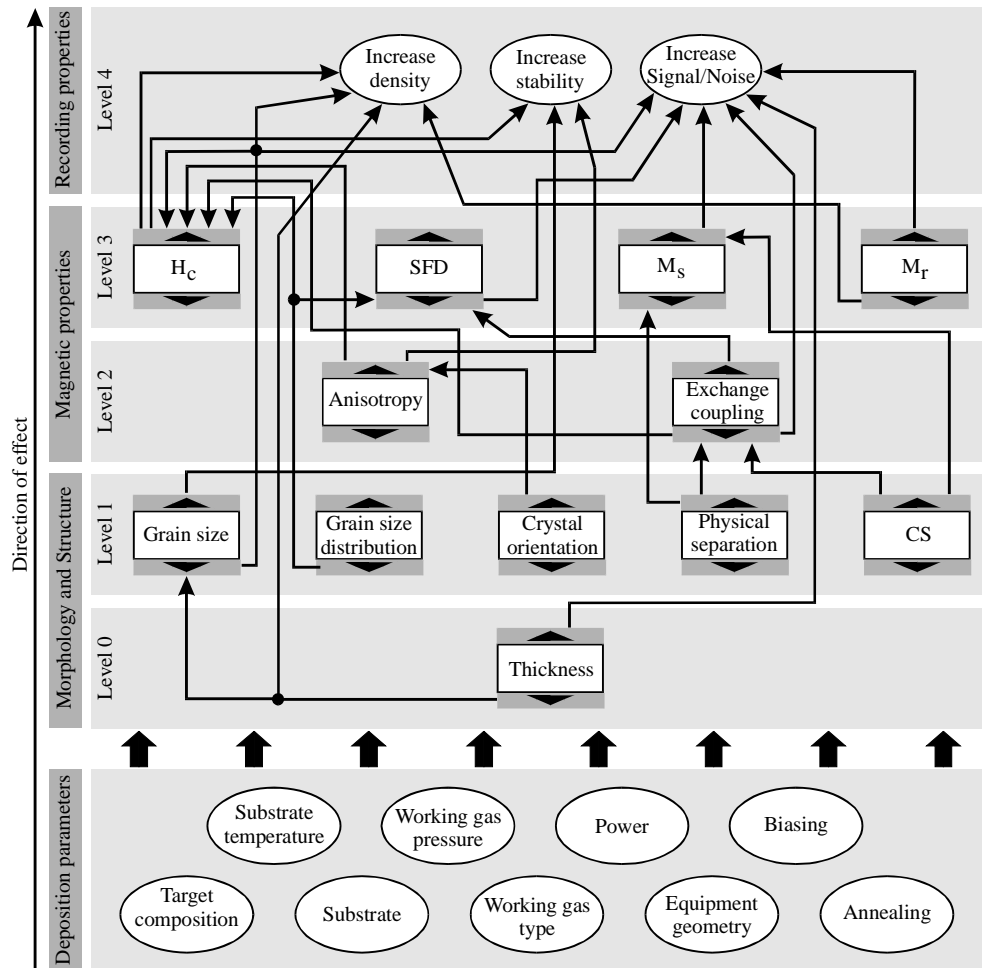


Fig. 2.1.1. Strategic diagram to achieve high-density media with high stability and high SNR. This diagram also shows the relationships between parameters of recording media. See text below for explanations of the diagram. Abbreviations:  $H_c$ : coercivity; SFD: Switching Field Distribution;  $M_s$ : Saturation magnetization;  $M_r$ : Remanence; CS: Compositional Separation.

The diagram classifies all parameters into 4 groups:

**The upper three groups** describe the main parameters of recording media: The group of recording properties containing the three primary criteria, the group of magnetic properties and the group of morphology and structural properties. These groups are further divided into several levels, from level 0 to 4. The bearing of the levels is that the lower level is the cause of the higher level, or in other words, the higher level is the effect of the lower one. Therefore, the direction of effect is from the bottom to the top, as indicated by the arrow on the left side of the diagram. On top of the diagram, level 4 contains the three primary criteria and at the bottom, level 0 contains film thickness, which is a parameter we can freely control, without influence of anything else.

Each parameter has two indicators: the increase indicator (up) and the decrease indicator (down). The arrows from one parameter to another show the cause-and-effect relationship. For instance, an arrow coming from the decrease indicator of the thickness parameter (level 0) to the decrease indicator of the grain size parameter (level 1) means that a decrease in medium thickness causes a decrease in grain size. Note that the cause-and-effect relationships described in the diagram are generally correct but not absolutely correct in all cases. Care must be taken when one considers the relationships of a particular medium.

From the diagram, one can know which parameter(s) to improve to achieve a certain criterion. For example, one of the ways to increase the recording density (level 4) is to increase  $H_c$  (level 3). Subsequently, to increase  $H_c$ , the diagram suggests four ways: to decrease grain size (level 1) (to a certain extent only), to increase anisotropy (level 2), to decrease exchange coupling (level 2) and to decrease grain size distribution (level 1), i.e. to create a medium containing homogeneous grains. It should be noted here that the diagram shows only simple and direct relations. The above-suggested ways are in fact interacting mutually. They should be optimized to increase  $H_c$ .

In addition, one has to be aware that a change in a parameter may sometimes cause opposite effects. For instance, to increase the recording density,  $M_r$  should be reduced. However, doing so causes a loss in the read-back signal, and thus making the SNR decrease. For that reason, all parameters should be optimized to obtain a good overall performance.

**The lower group**, at the bottom of the diagram, contains main parameters of the deposition process. Only the sputter deposition method is mentioned here. This group rules all media parameters in the upper three groups. Because the relationships between the deposition parameters and the media parameters are very complicated, they can not be shown here. Investigating the influences of deposition parameters on media parameters and optimizing the deposition

## 2.1. Criteria for a good recording medium

---

parameters to achieve high density, low noise and stable recording media are the task of researchers in the field as well of this thesis.

From the above diagram, we can set up the detailed criteria for a good medium as follows:

- Small grain size.
- High coercivity.
- Sufficiently small medium thickness.
- High magnetization of the medium to compensate for the loss of the read-back signal caused by the decrease in thickness.
- High anisotropy in the direction of recording.
- The product  $KV$  should be kept well beyond  $kT$ . The ratio  $kV/KT$  is preferably larger than 40, which ensures enough stability of the media ( $K$  is the anisotropy constant,  $V$  is the volume of the switching unit,  $kT$  is the thermal energy). Nowadays, with increasing recording density, maintaining the thermal stability has become a key issue in recording media research. The problem of thermal stability belongs to the subject of the time-dependence effect, which will be introduced in Chapter 3 and thoroughly studied in Chapter 7.
- Good crystalline orientation.
- Narrow grain size distribution, i.e. a medium of homogeneous grains, which is also termed a monodisperse medium.
- Weak magnetic interactions between grains by physical voids or compositional separation (CS).
- High remanence squareness  $S$ , coercivity squareness  $S^*$  and switching field distribution (SFD).

## 2.2. The role of Cr and Ta and segregation in CoCrTa media

When non-magnetic elements such as Cr and Ta dissolve in Co, the saturation magnetization  $M_s$  and the Curie temperature of the alloy are substantially reduced. Figure 2.2.1 shows  $M_s$  versus temperature for CoCr alloy of different Cr contents, from 0 to 25 at.% [Gavoille-82]. This figure can also be used to estimate  $M_s$  of CoCrTa alloys. In CoCrTa alloys for recording media, the content of the non-magnetic elements (Cr and Ta) is kept at less than about 25 at.%, typically around

14-20at.% (the shaded area) to preserve stable ferromagnetic state of the media at room temperature. Values of  $M_s$  of the recording media thus drops to around 350-650kA/m, which is about 1/4 to 1/3 of the pure Co material.

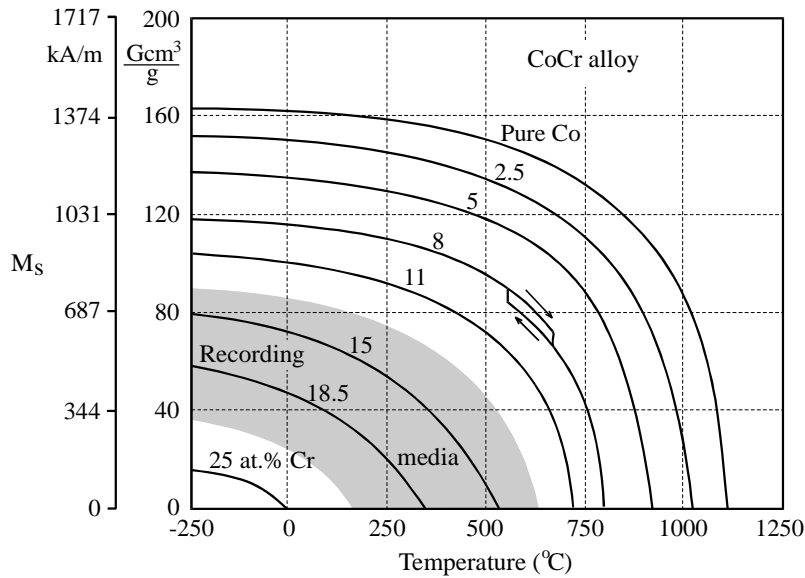


Fig. 2.2.1. Saturation magnetization as a function of temperature for different Cr contents [Gavoille-82]. The shaded area is the typical region of recording media.

From the signal point of view, adding non-magnetic elements into Co poses a disadvantage, that is the substantial reduction of signal-to-noise ratio due to the drop in  $M_s$ . However, to compensate for this, the coercivity of Co-alloy recording media is drastically increased. High coercivity in Co-alloy media is mainly attributed to the so-called *segregation*, or *compositional separation* (CS). Compositional separation is a phenomenon in which, by diffusion, Cr is segregated to the grain boundaries or inside the grains, forming Cr-enriched regions. The Co-enriched regions remained in between the Cr-enriched regions are partly isolated to each other. Due to this isolation, the magnetic interactions between Co-rich regions are broken or become weak, thus resulting in a high coercivity. CS does not occur in bulk materials due to sluggish diffusion. In thin films, the deposited atoms are mobile when they impinge on the surface and therefore may create CS via short-range diffusion [Maeda-94].

When Ta is added, it is not segregated but enhances the CS of Cr. By using Electron Energy Loss Spectroscopy (EELS) and Energy Dispersion x-ray Spectrometer (EDS), it was proven that Ta stays homogeneously in the entire film while Co and Cr are segregated (Fig. 2.2.2) [Nakai-94, Inaba-97, Futamoto-99].

## 2.2. The role of Cr and Ta and segregation in CoCrTa media

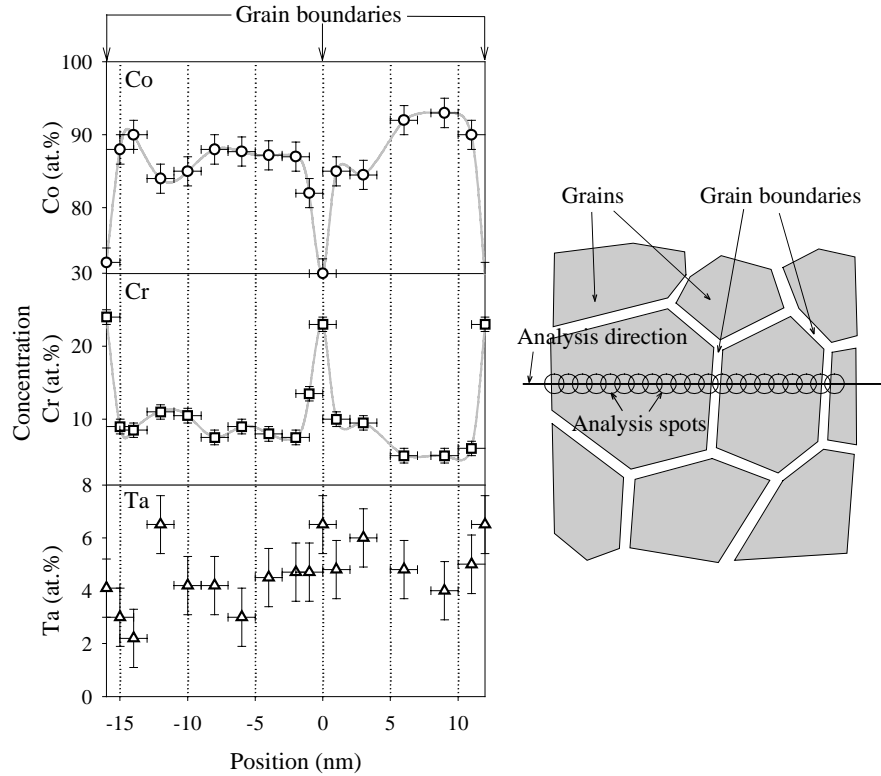


Fig. 2.2.2. Left: Line scan compositional profiles measured for two crystalline grains of plane-view  $\text{CoCr}_{15}\text{Ta}_4$  longitudinal thin film sample [Inaba-97]. Right: Schematic diagram of the scan. A focused  $e$ -beam having a diameter of 1.5nm was scanned along the analysis direction to get the EDS spectra.

It is shown in Fig. 2.2.2 that Cr is segregated to the grain boundaries, consequently Co is enriched inside the grains. There have been many works studying the microstructure of CS in Co-alloy recording media. The followings are descriptions of several examples of CS structures reported in literature. There are two main types of CS which have been observed:

**Type 1:** By local elemental analysis methods such as EDS or EELS, contents of Co, Cr (and Ta) are measured across several grains [Nakai-94, Inaba-97, Futamoto-99] (see the diagram on the right of Fig. 2.2.2). It was concluded from these studies that Cr is segregated to the grain boundaries, Co is concentrated inside the grains and Ta stays homogeneously (see the graphs of Fig. 2.2.2). The structure of CS based on these measurements is sketched in Fig. 2.2.3.a.

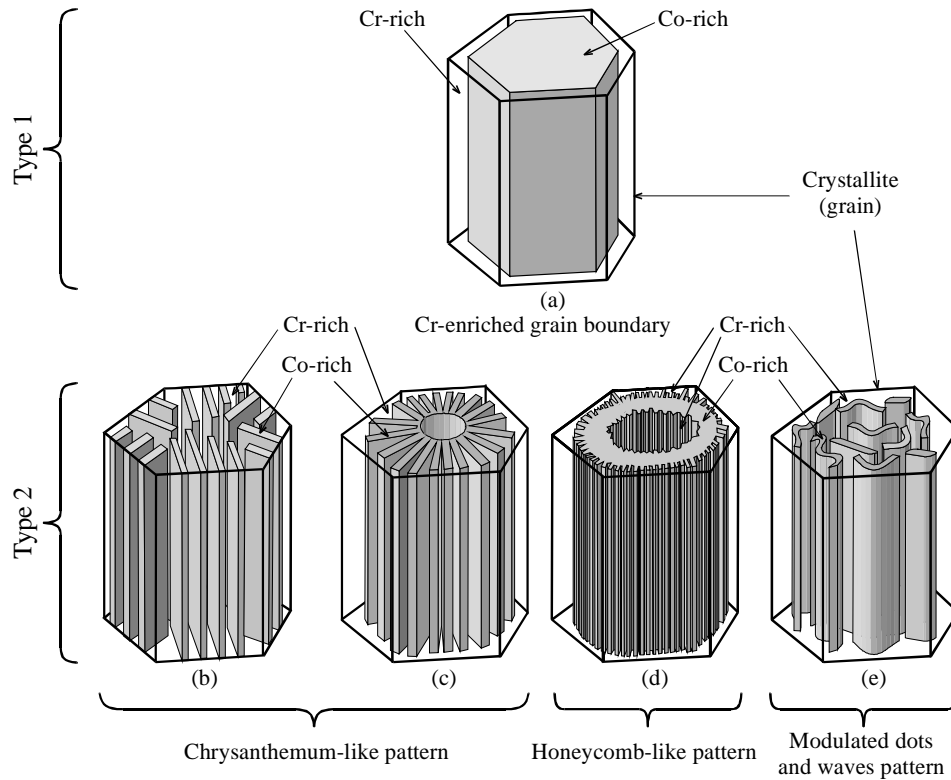


Fig. 2.2.3. Several observed examples of compositional separation structures. Type 1: (a), Cr is enriched at the grain boundaries and the inner part of the grain is Co-enriched. Type 2: (b), (c), (d), (e), Co-enriched regions are at the grain boundaries as well as inside the grains. (a) and (b) are after [Maeda-87].

**Type 2:** The CS structures of type 2 are suggested to contain Co-enriched regions inside the grains and as well as at the grain boundaries. In 1985, Maeda et al. [Maeda-85] investigated segregated microstructure in CoCr films for the first time. By using preferential chemical etching of Co on the samples, Co-enriched regions are partly etched away. Observing these samples on TEM, they discovered the so-called Chrysanthemum-like Pattern (CP) structure (Fig. 2.2.4). Figures 2.2.3.b and c show diagrams of two common shapes of CP structure visible in Fig. 2.2.4. The chrysanthemum-like pattern consists of bright stripes, representing Co-enriched regions, inside the crystallite. These stripes lie perpendicular to the grain boundaries and do not extend beyond the grain boundaries (Fig. 2.2.3.b) or they gather together to form a Cr-enriched core which is surrounded by Co-enriched rings with radial stripes (Fig. 2.2.3.c) [Rogers-94]. Later on, this technique has been developed and other media have been investigated, such as CoCrTa, CoCrPt longitudinal and perpendicular media, etc. of various ranges of thickness [Maeda-

## 2.2. The role of Cr and Ta and segregation in CoCrTa media

---

91, Suzuki-91, Rogers-94a, Hirayama-96, Maeda-97]. Several other variations of type 2 have been discovered. Figure 2.2.3.d shows the diagram of a structure found in CoCrTa longitudinal media [Maeda-94], which consists of honeycomb-like pattern of Co-enriched regions. In figure 2.2.3.e, another variation found in CoCr film [Maeda-94] is shown. This structure consists of Cr-enriched grain boundaries and finely, modulated dots and waves of Co-enriched regions inside the grains.

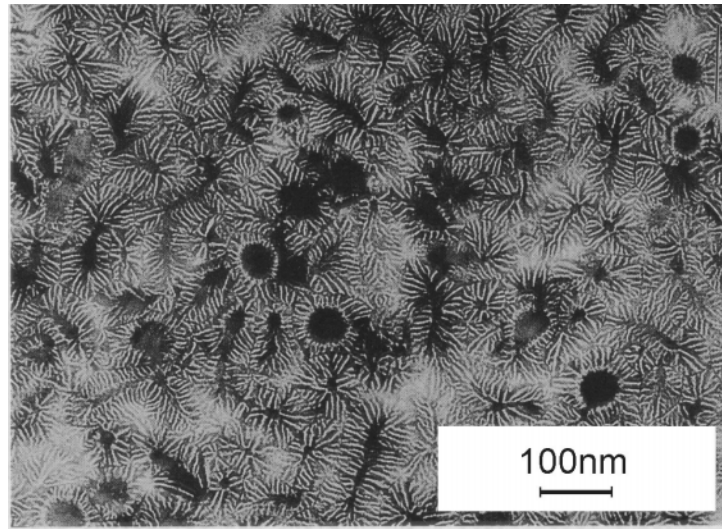


*Fig. 2.2.4. TEM image of chemically etched  $Co_{78}Cr_{22}$  film deposited at  $200^{\circ}C$  showing chrysanthemum-like pattern. The bright stripes are corresponding to Co-enriched regions and the dark areas are corresponding to Cr-enriched regions [Takei-91].*

Compositional separation was observed to depend strongly on substrate temperature  $T_s$  and composition. Films deposited at high  $T_s$  have drastic CS and strong Cr-enrichment at the grain boundaries [Rogers-94b]. Ta addition was also reported to enhance the Cr segregation at the grain boundaries [Rogers-94b] due to the chemical affinity difference among the atoms [Hwang-93]. Those are the causes of high  $H_c$  obtained when the films are deposited at high  $T_s$  or with Ta in the composition. The influences of the Ta content and  $T_s$  on structures and magnetic properties of CoCrTa thin films will be discussed in Section 5.3.

As said above, the diagrams of CS in Fig. 2.2.3 show only some examples reported in literature. To date, there has been no universal model for this structure. In which material, at which thickness, in which condition, etc., a certain pattern of CS occurs is still unknown.

## 2.3. Underlayers in Co-alloy recording media

### 2.3.1. Perpendicular media

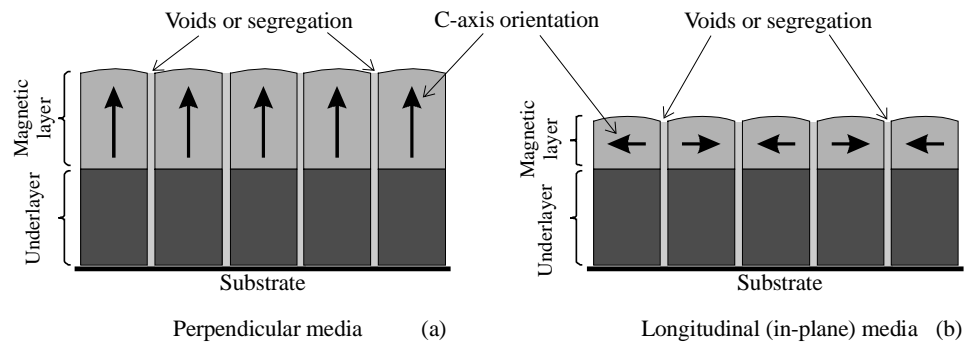


Fig. 2.3.1. Diagram of perpendicular (a) and longitudinal (b) recording media with underlayer.

When a Co-alloy thin film grown on a substrate such as glass or Si wafer, the preferable texture of the film will be (0002) (c-axes perpendicular to the film plane) because the (0002) planes have the lowest surface energy. However, this texture is only stabilized after a growth of an initial layer of thickness of about 20nm where the c-axes are randomly distributed in-plane. More details of the initial layer will be discussed in Section 5.2. If the film is thick enough, the portion of the film having (0002) texture will overwhelm the initial layer and thus resulting in a film having perpendicular anisotropy induced by crystalline orientation. In the early days of perpendicular recording research, a thick Co-alloy film was used as the medium. Later on, researchers were not satisfied with the initial layer since it degrades the perpendicular anisotropy of the media and they tried to get rid of this layer by introducing an *underlayer* which is deposited prior to the deposition of the magnetic Co-alloy layer (see Fig. 2.3.1.a). The underlayer should have the following properties:

- non-magnetic or very weak magnetic, because it should not affect the magnetic behaviors of the medium layer. In some cases, a soft layer of NiFe or CoZrNb can also be used, as discussed below.
- having a texture so that the Co-alloy magnetic layer deposited on this underlayer has a good perpendicular c-axis orientation by means of epitaxial growth. Besides eliminating the initial layer and promoting the perpendicular

### 2.3. Underlayers in Co-alloy recording media

---

c-axis orientation, the underlayer also helps to reduce the exchange coupling between grains of the magnetic layer by enhancing physical voids.

- having a smooth surface.

The most commonly used underlayer for perpendicular recording media is a Ti layer [Tanaka-87, Kitakami-89] because Ti has an hcp structure like Co, with close lattice parameters. CoCr layer can also be used as an underlayer. Co content in this composition should be small enough to have non- or weak magnetic behavior; on the other hand, it should be dominant to preserve the hcp structure. A composition of  $\text{Co}_{69}\text{Cr}_{31}$  is an example [Nagaoka-91]. Several other types of underlayer for perpendicular media can be found in literature, such as Pt [Mapps-93],  $\text{Co}_3\text{O}_4/\text{Pt}$  [Song-96]. Besides, a soft magnetic layer of NiFe [Lin-96] or CoZrNb [Ando-91] can also be used. This layer serves as the layer to induce (0002) texture, as well as a soft layer to close the magnetic flux from the single pole head to the medium and back to the single pole head. The soft layer is always required in perpendicular media.

#### 2.3.2. Longitudinal media

In longitudinal recording media (also called in-plane media), to force the c-axes growing in-plane, another type of underlayer is used (see Fig. 2.3.1.b). The necessary properties of the underlayer for longitudinal media are slightly different from those for perpendicular media:

- non-magnetic.
- having a texture so that the Co-alloy magnetic layer deposited on this underlayer has a good in-plane c-axis orientation by means of epitaxial growth. Besides inducing in-plane c-axis orientation, the underlayer also helps to reduce the exchange coupling between grains of the magnetic layer by enhancing physical voids.
- having a smooth surface.

Cr is commonly used to make the underlayer for longitudinal recording media [Laughlin-91]. Cr thin films naturally have the (200) and/or (110) textures which can make the Co-alloy layer have c-axes parallel to the film plane and/or make an angle of  $28^\circ$  out of plane. Both orientations result in compatibly good longitudinal recording behaviors. In Chapter 6, we will discuss in detail about the Cr underlayer.

Besides using pure Cr as the underlayer, researchers have tried to add a second element into Cr to alter the lattice parameters of Cr thus reducing the lattice mismatch between the underlayer and the magnetic layer. The second element

could be Ti [Matsuda-96, Choe-96], Si [Choe-96] or V [Parker-93, Nguyen-93]. Recently, NiAl alloy as a substitute for Cr and Cr-alloys has been being developed. It appears that NiAl can provide potential benefits over the Cr underlayer due to its small grain size, good thermal conductivity, high stiffness and good environmental corrosion resistance, etc. [Lee-94].

## **2.4. Main issues of Co-alloy magnetic recording media research**

With the aim of raising recording density of Co-alloy magnetic, or more particularly, of achieving the criteria as listed in Section 2.2, the researchers have to solve numbers of problems. These problems can be divided into several main issues which appear in all recent relevant journals and conferences. The issues are:

- 1- Studies of the influences of sputtering conditions on properties of the media. This includes studies of the influences of working gas pressure, substrate temperature, biasing, working gas type (Ar, Kr, etc.), substrate type, annealing, reactive gases, etc. and optimizing these parameters to obtain better media.
- 2- Studies of the influences of the underlayer and searching for proper materials for the underlayer.
- 3- The time-dependence effect, which is related to the stability problem of the media.
- 4- Fundamental studies of structure and microstructures, magnetic properties, reversal mechanisms, domain structures and magnetic interactions of the media, recording performances, etc.
- 5- Development of materials of the magnetic layer, for example, addition of a forth or fifth element into the classical Co alloys such as CoCrTa or CoPtCr to improve various properties of the media.
- 6- Development of new configurations of the constituent layers of the media, such as laminated media, sandwich media, multilayer media, etc.
- 7- Development and improvement of other components of the media, such as substrates, pre-coat layer, over-coat layer, lubricant layer, etc.

The subjects of this thesis fall into the first four issues (see Section 1.2).

## 2.5. Conclusion

In this chapter, the most important topics about Co-alloy (including CoCrTa) magnetic recording media have been given. In the first section, we discussed about the criteria for a good recording medium. There are three primary criteria, namely, a high recording density, sufficiently high thermal stability and high signal-to-noise ratio. To achieve these criteria, we have to improve numbers of parameters which interact to one another in complicated ways. A diagram showing these interactions has been given, based on which, detailed criteria to obtain a good medium has been proposed. Some knowledge about the roles of Cr and Ta in CoCrTa media was given in the second section. Additions of Cr and Ta result in a reduction in  $M_s$ . However, the benefit of these additions is that the additional elements create the so-called compositional separation (CS), due to which the magnetic interactions in the media are reduced, thus increasing the coercivity of the media. Several types of CS have been presented in this section. In Section 2.3, we discussed about the importance of using an underlayer. The underlayer is used to control the crystalline orientation, thus controlling the easy-axis direction of the media. There are two types of underlayer: underlayer for longitudinal recording and underlayer for perpendicular recording media. In the last section, we presented seven main issues in Co-alloy recording media research. The subjects of the thesis belong to the first four issues.

## 2.6. References

- [Ando-91] T. Ando and T. Nishihara. "CoCrTa/CoZrNb perpendicular magnetic hard disk". *J. Magn. Soc. of Japan* 15 (Supp. No. S2) (1991), 1019.
- [Choe-96] G. Choe. "Grain morphology and magnetic properties of CoCrPt/Cr(Si, Ti) films sputtered at room temperature". *J. Appl. Phys.* 79(8) (1996), 4923.
- [Futamoto-99] M. Futamoto, N. Inaba, Y. Hirayama, K. Ito and Y. Honda. "Microstructure and micromagnetics of future thin film media". *J. Magn. Mat.* (1999), in press.
- [Gavoille-82] G. Gavoille, S. Durupt, J.Hubsch. *J. Phys. (Les. Ulis, Fr.)* 43 (1982), 773.
- [Hwang-93] C. H. Hwang, Y. S. Park, P. W. Jang and T. D. Lee. "Magnetic properties and structures of CoCrTa films for wide range of Cr variation". *IEEE Trans. Magn.* 29 (1993), 3733.
- [Hirayama-96] Y. Hirayama, M. Futamoto, K. Kimoto and K. Usami. "Compositional

## 2. Some basics of CoCrTa recording media

---

- microstructure of CoCr-alloy perpendicular magnetic recording media". IEEE Trans. Magn. 32 (1996), 3807.
- [Inaba-97] N. Inaba, T. Yamamoto, Y. Hosoe, M. Futamoto. "Microstructural segregation in CoCrTa and CoCrPt longitudinal magnetic recording media". J. Magn. Magn. Mat. 168 (1997), 222.
- [Kitakami-89] O. Kitakami, Y. Ogawa, H. Fujiwara, F. Kugiyu and M. Suzuki. "Influence of initial growth layer and Ti underlayer on magnetic properties and recording characteristics of very thin films of evaporated Co-Cr media". IEEE Trans. Magn. 25 (1989), 2607.
- [Laughlin-91] D. E. Laughlin and B. Y. Wong. "Crystallography and texture of Co-based thin film deposited on Cr underlayers". IEEE Trans. Magn. 27 (1991), 4713.
- [Lee-94] L. L. Lee, D. E. Laughlin and D. N. Lamberth. "NiAl underlayers for CoCrTa magnetic thin films". IEEE Trans. Magn. 30 (1994), 3951.
- [Lin-96] C. L. Lin, T. Yeh, G. Wang, J. C. Lin, J. M. Sivertsen and J. H. Judy. "Structure and magnetic properties of CoCrTa films deposited on thin NiFe films". J. Magn. Magn. Mat. 155 (1996), 168.
- [Maeda-85] Y. Maeda, S. Hirono and M. Asahi. "TEM observation of microstructure in sputtered Co-Cr film". Jap. J. Appl. Phys. 24, No. 12 (1985), L951.
- [Maeda-87] Y. Maeda and M. Asahi. "Segregation in sputtered Co-Cr films". IEEE Trans. Magn. MAG-23 (1987), 2061.
- [Maeda-91] Y. Maeda and K. Takei. "Compositional inhomogeneities in Co-Cr-Ta/Cr films for longitudinal magnetic recording". IEEE Trans. Magn. 27 (1991), 4721.
- [Maeda-94] Y. Maeda, K. Takei and D. Rogers. "Compositional microstructures in Co-Cr films for magnetic recording". J. Magn. Magn. Mat. 134 (1994), 315.
- [Maeda-97] Y. Maeda, D. Rogers, O. Song, K. Takei, T. Ohkubo, S. Hirono, J. I. Suzuki and Y. Morii. "Magnetic microstructures produced by compositional separation in Co-Cr based alloy thin films". IEEE Trans. Magn. 33 (1997), 879.
- [Mapps-93] D. J. Mapps, G. Pan, M. A. Akhter, S. Onodera and A. Okabe. "In-contact magnetic recording performance of Pt/CoCrTa thin films on glass computer disks". J. Magn. Magn. Mat. 120 (1993), 305.
- [Matsuda-96] Y. Matsuda, Y. Yahisa, J. Inagaki, E. Fujita, Ishikawa and Y. Hosoe. "Reduction of Co-Cr-Pt media noise by addition of Ti to Cr underlayer". J. Appl. Phys. 79(8) (1996), 5351.
- [Nagaoka-91] T. Nagaoka, J. Takahashi, N. Iwato, B. Higgins and C. Baldwin. "Recording performance in CoCrTa media with CoCr seed layer for

## 2.6. References

---

- perpendicular recording". J. Magn. Soc. of Japan 15 (Supp. No. S2) (1991), 359.
- [Nakai-94] J. Nakai, E. Kusumoto, M. Kuwabara, T. Miyamoto, M. R. Visokay, K. Yoshikawa and K. Itayama. "Relation between microstructure of grain boundary and the intergranular exchange in CoCrTa thin film for longitudinal recording media". IEEE Trans. Magn. 30 (1994), 3969.
- [Nguyen-93] T. A. Nguyen and J. K. Howard. "Enhanced coercivity in CoPtCr thin films media using CrV underlayer (abstract)". J. Appl. Phys. 73(10) (1993), 5579.
- [Parker-93] M. A. Parker, J. K. Howard, R. Ahlert and K. R. Coffey. "Crystallographic structure of CoPtCr/CrV thin films as revealed by cross-section TEM and x-ray pole-figure analysis and its relevance to magnetic properties". J. Appl. Phys. 73(10) (1993), 5560.
- [Rogers-94a] D. Rogers, Y Maeda and K. Takei. "The dependence of compositional separation on film thickness for Co-Cr and Co-Cr-Ta magnetic recording media". IEEE Trans. Magn. 30 (1994), 3972.
- [Rogers-94b] D. Rogers, Y. Maeda, K. Takei, Y. Shen and D. E. Laughlin. "Investigations of compositional separation in Co-Cr-Ta/Cr thin films recording media". J. Magn. Magn. Mat. 135 (1994), 82.
- [Song-96] X. Song, J. Loven, J. Sivertsen and J. Judy. "Structural, magnetic and recording properties of CoCrTa/Co<sub>3</sub>O<sub>4</sub>/Pt perpendicular thin film media". IEEE Trans. Magn. 32 (1996), 3840.
- [Speliotis-97] D. Speliotis. "Magnetic recording: 100 years old and still growing". J. Magn. Soc. of Japan 21 (Supp. No. S2) (1997), 119.
- [Suzuki-91] H. Suzuki, N. Goda, S. Nagaike, Y. Shiroishi, N. Shige and N. Tsumita. "Compositional separation of (Co-Cr-Pt)/Cr films for longitudinal recording and (Co-Cr)/Ti films for perpendicular recording". IEEE Trans. Magn. 27 (1991), 4718.
- [Takei-91] K. Takei and Y. Maeda. "NMR study of compositional inhomogeneities in sputtered Co-Cr films". Jap. J. Appl. Phys. 30, No. 6B (1991), L1125.
- [Tanaka-87] T. Tanaka and H. Masuya. "Effect of Ti sublayer on the structural and magnetic properties of evaporated Co-Cr film". Jap. J. Appl. Phys. 26 (1987), 897.

# Chapter 3

---

## Time-dependence effect in magnetic recording media

After any change in magnetic field applied on a magnetic body, although the field is held constant, magnetization of the body will keep changing with time. This phenomenon is called the *time-dependence effect* or the *magnetic after-effect*. Particularly, in magnetic recording media, the remanence will degrade with time after writing due to thermal excitation, resulting in the loss of information after a certain time of storage. Therefore, one of the most important criteria for making good recording media is the long-term storage stability.

The nature of the time-dependence phenomenon in magnetic materials is a conflict between the energy barrier of the material caused by the anisotropy at one side and the thermal energy and the external field (if present) at the other side, trying to force the magnetization away from the easy axis.

By studying the time-dependence effect, we can evaluate:

- storage stability of the media,
- strength of the anisotropy energy compared to the thermal excitation,
- energy barrier,
- volumes of switching unit and reversal mechanisms of the media,
- coercivities at different writing frequencies.

The first part of this chapter gives some basics about the time-dependence effect in magnetic materials and especially in recording media. The second part will present the experimental methods and the fitting procedures used in this thesis. This chapter will be continued later by chapter 7, which investigates in detail about the time-dependence effect in several magnetic recording media, including in-plane and perpendicular media.

## 3.1. Some basics about the time-dependence effect

### 3.1.1. Magnetic relaxation and magnetic viscosity

Let's consider a system of identical Stoner-Wohlfarth (S-W) particles having no mutual interaction. After a sudden change in external field, magnetic moments of the particles switch to a new direction, causing the magnetization of the system to change. The standard kinetic theory predicts that the magnetization of the system should decay with an exponential function, approaching a new equilibrium value corresponding to the new external field [Street-49]:

$$M(t) = a + b.e^{-t/\tau} \quad (3.1.1)$$

where  $a$  and  $b$  are constant;  $\tau$  is called the *relaxation time*. The time-dependence of magnetization  $M$  described in Eq. (3.1.1) is often called the *relaxation curve of magnetization*. The theories of stochastic processes result in the Arrhenius-Néel law [Neel-51]:

$$\frac{1}{\tau} = f_0 \times \exp(-\Delta E / kT) \quad (3.1.2)$$

where  $f_0$  is the *frequency of gyromagnetic precession*. The frequency  $f_0$  was reported to change with the applied field, temperature, anisotropy, crystal structure, etc. However, it is commonly considered constant with a value of about  $10^9 \text{ s}^{-1}$  [Brown-63].  $\Delta E$  is the *energy barrier* between the old and the new direction of the magnetic moments in a particle. The product  $kT$  is *the thermal energy*. From Eq. (3.1.2), one can estimate qualitatively that when either the energy barrier  $\Delta E$  is reduced or the ambient temperature increases, the magnetization relaxes faster (smaller  $\tau$ ).

In practice, the exponential time-dependence [Eq. (3.1.1)] is not generally observed, due to the presence of a distribution function of the energy barrier  $f(\Delta E)$  of particles. Equation (3.1.1) then becomes [Chantrell-94]:

$$M(t) = a + b \int_0^{\infty} e^{-t/\tau} f(\Delta E) d\Delta E \quad (3.1.3)$$

This function can be approximated as:

$$M = M_0 + S \ln t \quad (3.1.4)$$

where,  $M_0$  is the magnetization of the sample at the beginning of the relaxation curve;

$S$  is the *magnetic viscosity*, representing the relaxation rate of the magnetization;

$t$  is the elapsed time since the measurement starts.

To avoid the undefined point of the logarithmic function at zero,  $t$  is counted from one second.

One should be aware that Eq. (3.1.4), with a constant  $S$ , is only valid for a limited range of time. The logarithmic dependence Eq. (3.1.4) has been observed to break down for very short and very long  $t$  [Lyberatos-94]. It was also found that  $S$  varies slowly over very long time ranges [Lyberatos-91]. So in practice, the relaxation curve ( $M$  vs.  $\ln t$ ) is often called *quasi-logarithmic dependence*, rather than logarithmic dependence.

#### 3.1.2. Energy barrier of a magnetic particle

In the previous section, it was shown that the relaxation time  $\tau$  is a function of the energy barrier  $\Delta E$  between two directions of magnetization.  $\Delta E$  is in turn a function of other parameters such as particle volume, anisotropy and applied field. For the sake of simplicity, let us consider a single domain particle having the shape of an ellipsoid of revolution and a volume  $V$ . This shape is assumed to assure that the magnetization of the particle switches coherently. This reversal mode is called the *coherent rotation* or *Stoner-Wohlfarth rotation*, proposed by Stoner and Wohlfarth [Stoner-48]. The particle is placed in a magnetic field  $H$  whose direction is parallel to the easy axis of the particle (Fig. 3.1.1). Now we can calculate the total free energy of the particle as a function of the angle  $\theta$  between the magnetic moment  $M_s V$  of the particle and the easy axis.

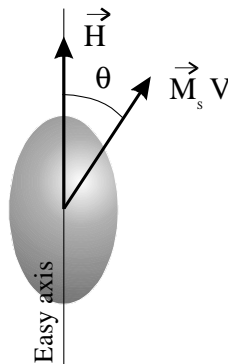


Fig. 3.1.1. A Stoner-Wohlfarth particle placed in a magnetic field.

### 3.1. Some basics about the time-dependence effect

The total free energy consists of the anisotropy energy and the Zeeman energy caused by the applied field:

$$E(\theta, H) = K.V.\sin^2\theta - \mu_0.H.M_s.V.\cos\theta \quad (3.1.5)$$

in which  $K$  is the anisotropy constant of the particle (in  $J/m^3$ ). The anisotropy constant is related to the anisotropy field  $H_K$  by the formula:

$$K = \frac{1}{2} \mu_0.H_K.M_s \quad (3.1.6)$$

We denote the reduced energy:

$$e(\theta, H) = \frac{E(\theta, H)}{\mu_0 H_K M_s} \quad (3.1.7)$$

and the reduced applied field  $h = H/H_K$ . Equation (3.1.5) becomes:

$$e(\theta, H) = \frac{1}{2} \sin^2\theta - h \cos\theta \quad (3.1.8)$$

A plot of several  $e(\theta, H)$  curves v.s  $\theta$  at different  $h$  values is given in Fig. 3.1.2.

Most curves in Fig. 3.1.2 (except the curve  $h=1.0$ ) have two minima where the magnetic moment can stably stay. If the magnetic moment wants to jump from  $\theta=180^\circ$  to  $\theta=0^\circ$ , it has to overcome an energy barrier  $\Delta e$  between these two minima. The field  $h$  tends to force the magnetic moment in its direction, i.e. at  $\theta = 0^\circ$ , whereas the thermal energy  $kT$  tends to disalign it.

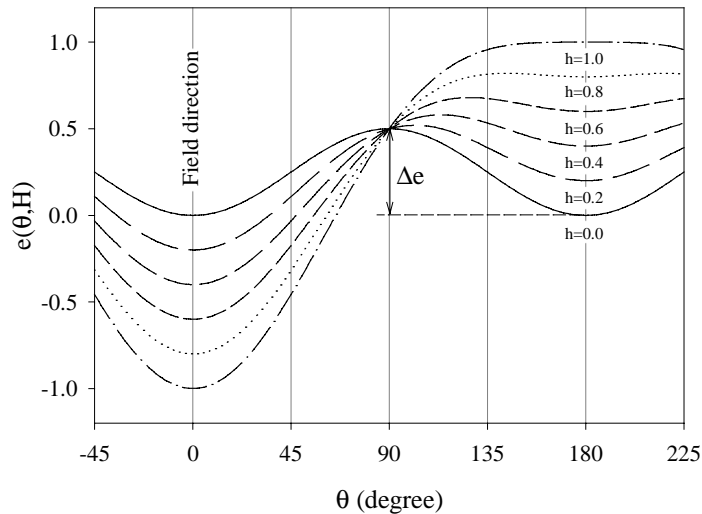


Fig. 3.1.2. Energy curves of a Stoner-Wolffarth particle in an applied reduced field  $h$ .

Let us calculate the height of  $\Delta e$  by taking the derivation of Eq. (3.1.8) and equaling it to zero:

$$\frac{\partial e(\theta, H)}{\partial \theta} = \sin \theta \times \cos \theta + h \times \sin \theta = 0$$

The solutions are  $\theta_{1,2} = 0^\circ$  and  $180^\circ$  and  $\theta_{3,4} = \pm \arccos(-h)$ . By taking the second derivative of Eq. (3.1.8), we can define that  $\theta_1 = 0^\circ$  and  $\theta_2 = 180^\circ$  are the two minima and  $\theta_3 = \arccos(-h)$  is the maximum between them. The energy barrier between  $\theta_2$  and  $\theta_1$  is:

$$\Delta e = \frac{1}{2} (1-h)^2 \quad (3.1.9)$$

Using the definitions (3.1.6) and (3.1.7) we come to the final formula for the energy barrier  $\Delta E$  (in Joule) of the particle:

$$\Delta E = K \times V \times \left(1 - \frac{H}{H_K}\right)^2 \quad (3.1.10)$$

This energy barrier is the energy needed to switch the magnetic moment of the S-W particle from the minimum at  $180^\circ$  to the minimum at  $0^\circ$  where the field  $H$  is acting.

At zero applied field,  $H=0$ , let us assume that the magnetic moment originally stays at  $\theta = 180^\circ$ , the energy barrier  $\Delta E$  is now  $KV$ , according to Eq. (3.1.10). This state is equivalent to the curve  $h=0.0$  of Fig. 3.1.2, and therefore  $\Delta e=1/2$  [see Eq. (3.1.9)]. The thermal energy  $kT$  constantly tries to demagnetize the particle and on the other hand, the particle resists the thermal energy and tries to keep the magnetic moment in the original direction with its energy barrier  $KV$ . Therefore, the ratio  $KV/kT$  can be used to evaluate the magnetic stability of the particle at zero field. The ratio can also be used to evaluate the storage stability of recording media which consist of many particles. In this case,  $K$  and  $V$  are the median anisotropy constant and the median volume of the switching units.

When the applied field  $H$  is increased, the energy barrier is reduced. This is equivalent to the curves  $h>0$  of Fig. 3.1.2. The reduction of energy barrier makes the magnetic moment switch more easily. The energy barrier therefore determines the probability for the magnetic moment of the particle to switch as characterized by the relaxation time  $\tau$  in Eq. (3.1.2). When the applied field is equal or greater than the anisotropy field of the particle,  $H>H_K$ , or  $h\geq 1$ , the energy barrier vanishes ( $\Delta E=0$ ). This means that the magnetic moment of the particle can no longer stay at  $180^\circ$  but switches instantaneously to the direction of the applied field (at  $\theta = 0^\circ$ ).

### 3.1.3. Superparamagnetic limit

As discussed in the previous section, the ratio  $KV/kT$  is used to evaluate the stability of recording media at zero field. First, we assume here that the media consist of non-interacting S-W particles and  $V$  is the median volume of the particles. The ratio should be large enough to prevent the information loss. If the ratio  $KV/kT$  is smaller than a certain value, the remanence state of the media is not stable, or in other words, the relaxation time  $\tau$  is negligibly small (let's call  $\tau$  in this case  $\tau_{\text{critical}}$ ). In this state, the particles of the media are said to be superparamagnetic.

How large should this ratio be to assure that a medium is magnetically stable ? Let's define  $\tau_{\text{critical}}$  equals 100s, a normal value of time required to measure the magnetization of a sample [Cullity-72, p.413]. Replace this value into Eq. (3.1.2), we obtain  $\Delta E/kT \approx 25$ . In the absence of applied field, it becomes  $KV_{\text{critical}}/kT \approx 25$ .  $V_{\text{critical}}$  is the *critical volume*, below which the material is not magnetically stable, or in other words, the material is superparamagnetic. The ratio  $KV/kT$  of about 25 is called the *superparamagnetic limit*.

For a good recording medium, this ratio should be greater than about 40, which is equivalent to a relaxation time of 10 years. Figure 3.1.3 gives some examples of the relation between the relaxation time  $\tau$  and the ratio  $KV/kT$ .

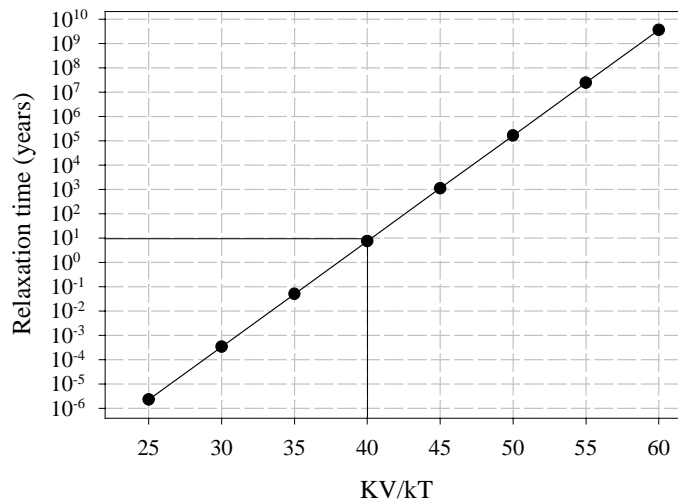


Fig. 3.1.3. Relaxation time as a function of the ratio  $KV/kT$ . Note that the vertical scale is logarithmic.

In practice, however, recording media consist of interacting particles. The reversal mode of the particles is commonly incoherent rotation. In this case, the volume  $V$  is no longer the particle (or grain) volume but an effective volume  $V_{\text{eff}}$ . The effective volume can be either smaller or larger than the physical volume of the particles. In many cases, this effective volume is identical to the activation volume. We will come back to this volume later in this chapter.

To increase the stability of the media, the product  $KV_{\text{eff}}$  should be increased. We can increase  $K$  or/and  $V_{\text{eff}}$ . To increase  $V_{\text{eff}}$ , we have to increase either the physical (particle) grain size, or the interaction between the particles [Rodé-87]. However, both of these attempts result in a decrease in recording density and an increase in recording noise. Therefore, the particle size of the media should be optimized so that it is small but not too close to the superparamagnetic limit. At the same time, the anisotropy should be as large as possible.

The superparamagnetic limit is also the limit of the magnetic recording technology. As far as the magnetic recording method is still used, the bit size of the media cannot be smaller than  $V_{\text{critical}}$ .

#### **3.1.4. From non-interacting Stoner-Wolffarth particles to practical recording media**

In Section 3.1.1 and 3.1.2, we only dealt with the time-dependence phenomena of media consisting of non-interacting S-W particles. In practice, recording media are much more complicated. One particle (or grain) could be single or multi-domain, and its reversal mode could be coherent or incoherent. The entirety of the particles, as they are together to form a medium, could have weak or strong intergranular interactions. The reversal modes and the interactions between particles affect directly the energy barrier and thus, affect the stability of the media. Figure 3.1.4 classifies several cases which are often observed in practice. The classification is only relative, because an exact comparison needs more parameters. Here, we only consider media consisting of particles having comparable  $K$  and sizes.

First, we start with the wall-motion case. This kind of media is a continuous film, without many defects and voids between crystallites. The reversal mechanism of these media is the wall-motion mode. The energy barrier is generally very low because the walls can move easily in the media. This kind of media is very unstable and not suitable for recording.

Next, in the second case, the medium consists of weakly interacting particles, switching by incoherent rotation mode (for instance, curling mode). This medium has better stability compared to the first case, however  $V_{\text{eff}}$  is smaller than the physical particle volume  $V$ , therefore the ratio  $KV_{\text{eff}}/kT$  is not very high.

### 3.1. Some basics about the time-dependence effect

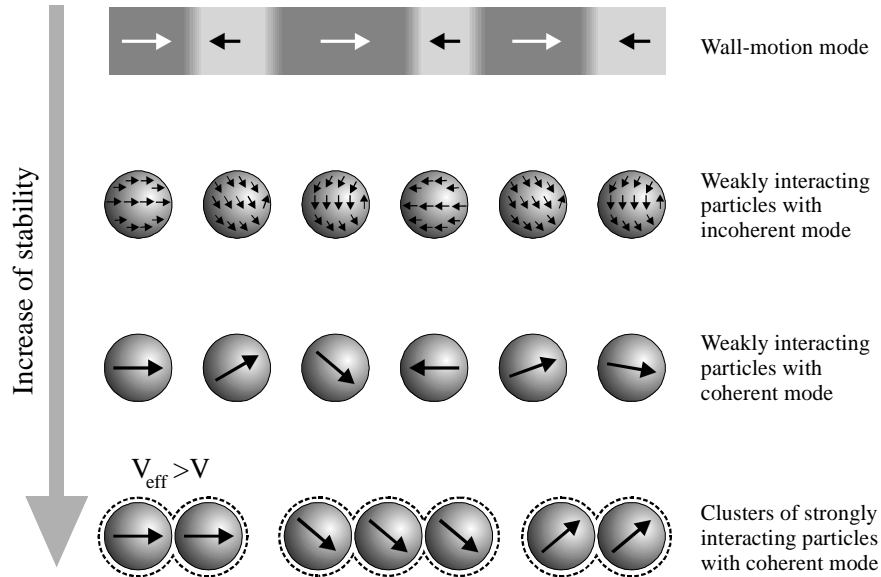


Fig. 3.1.4. Influences of reversal modes and interactions on the stability of recording media.

The most desirable medium is the one consisting of weakly interacting S-W particles (switching by coherent mode - the third case). The stability of each particle is rather high because  $V_{\text{eff}}$  is identical to the physical particle volume  $V$ . Moreover, since the interactions between particles are weak, the coercivity of this medium is quite high and recording noise is low. This medium is very close to the ideal case of non-interacting S-W particles mentioned in Section 3.1.1 and 3.1.2.

In the fourth case, the exchange interaction between S-W particles is strong enough to form clusters of several particles. The particles inside a cluster switch collectively and thus  $V_{\text{eff}}$  in this case is larger than the physical volume  $V$  of one particle. Rodé et al. [Rodé-87] found by simulation that  $V_{\text{eff}}$  could vary from  $V$  to  $2V$ , depending on the interaction strength. This leads to a higher energy barrier. Obviously, this kind of media has the best storage stability (among those classified). However,  $H_c$  of this medium is lower than the third case and the recording noise is higher. In addition, simulation results of Chantrell et al. [Chantrell-97] showed that the interactions between particles slow down the relaxation at short time scale, which means that it is difficult to record with high frequency. This kind of media is therefore not desirable for recording.

## 3.2. Analytical model for the time-dependence effect

After the studies of Street and Woolley [Street-49] - the pioneers of the time-dependence effect in magnetic materials - numbers of works have been devoted to this intriguing subject. Some models and calculations have been proposed [Gaunt-76, Wohlfarth-84, Charap-88, Lottis-90, Lyberatos-91, Chantrell-94, Folks-94] to interpret the time-dependence effect. Each model or calculation often focuses on a certain particular problem. Generally, they always accompany some assumptions which are only applicable in limited cases and conditions. In spite of variety of calculations, the models eventually come to more or less the same results. Among those models, an analytical model of Chantrell [Chantrell-94] and his co-workers has been adopted in this thesis.

The model starts with a differential equation describing the variation of the magnetization of a system:

$$\frac{dM(t)}{dt} = -\frac{M(t) - M_e}{\tau} \quad (3.2.1)$$

where  $M_e = M(t=\infty)$  (magnetization at equilibrium state). In the case of non-interacting system having a *distribution function  $f$  of the energy barrier*, the solution of Eq. (3.2.1) gives:

$$M(t) = B + A \int_0^{\infty} e^{-t/\tau(y)} f(y) dy \quad (3.2.2)$$

where  $B=M(t=\infty)$ ,

$$A=M(t=0)-M(t=\infty),$$

$y=\Delta E/\Delta E_m$ , the reduced energy barrier.  $\Delta E_m$  is the median energy barrier of the particles,

$$\tau^{-1}(y)=f_0 \exp(-y \Delta E_m/kT) \quad (3.2.3)$$

$$f(y) = \frac{1}{\sqrt{2\pi} \times y \times \sigma} \exp\left[-\frac{1}{2} \left(\frac{\ln(y/y_m)}{\sigma}\right)^2\right] \quad (3.2.4)$$

This function is called the *log-normal distribution*;  $y_m$  is the median reduced energy barrier, and therefore  $y_m=1$ ;  $\sigma$  is the standard deviation of the distribution.

### 3.2. Analytical model for the time-dependence effect

---

The distribution of energy barrier comes chiefly from the distribution of particle size and the distribution of anisotropy constant of the particles. The log-normal distribution has been found empirically as a typical distribution in nature [Granqvist-76, Battle-97]. The difference between the log-normal and the normal distribution is that the log-normal distribution is not symmetric around the maximum and the median value does not coincide with the value at which the maximum occurs.

The essential point of the model is the assumption of a critical energy barrier  $\Delta E_c$ . It is assumed that:

- if a particle has an energy barrier  $\Delta E < \Delta E_c$  or equivalently,  $y < y_c = \Delta E_c / \Delta E_m$ , the relaxation time  $\tau$  of the magnetization is so short that one can consider:  $\exp[-t/\tau(y < y_c)] \approx 0$ ;
- and if a particle has an energy barrier  $\Delta E > \Delta E_c$  (or  $y > y_c$ ), the relaxation time  $\tau$  is considered infinitely long and thus:  $\exp[-t/\tau(y > y_c)] \approx 1$ .

The above assumption is equivalent to the following argument: At the time  $t$  since the relaxation starts, all magnetic moments of the particles having the relaxation time  $\tau$  shorter than  $t$  have switched to the opposite direction while the moments of the particles having  $\tau$  longer than  $t$  still remain in their original direction.

With the above assumption, Eq. (3.2.2) becomes:

$$\begin{aligned} M(t) &= B + A \int_0^{y_c(t)} e^{-t/\tau(y)} f(y) dy + A \int_{y_c(t)}^{\infty} e^{-t/\tau(y)} f(y) dy = B + A \int_{y_c}^{\infty} f(y) dy \\ &= B + A \int_0^{\infty} f(y) dy - A \int_0^{y_c} f(y) dy \end{aligned}$$

And finally:

$$M(t) = M(t=0) - A \int_0^{y_c(t)} f(y) dy \quad (3.2.5)$$

$$\text{where: } y_c(t) = kT \ln(tf_0) / \Delta E_m \quad (3.2.6)$$

Using the differential calculus:  $\frac{d}{dp} \int_{p=\text{const}}^q f(x) dx = f(q)$  to differentiate Eq.(3.2.5),

we obtain the formula for calculating the viscosity  $S$  of a system at a time  $t$ :

$$S = \frac{dM(t)}{d \ln(t)} = - \frac{AkT}{\Delta E_m} f(y_c) \quad (3.2.7)$$

It is clear from Eq. (3.2.7) that if the distribution function  $f$  is so wide that it can be considered constant, the viscosity  $S$  will be a constant with respect to time, or in other words, the relaxation curve is logarithmic. Conversely, if  $f$  is a very narrow function,  $S$  will change with time and the relaxation curve is considered exponential. In practice, normal cases lie between these two extremes, in which the relaxation curve is quasi-logarithmic.

### 3.3. Fluctuation field and activation volume

Because the net contribution to the magnetic viscosity due to the activation of the reversible processes is zero [Street-52], the magnetic viscosity is only related to the irreversible reversal of the sample. Street and Woolley [Street-49] proposed a relationship between  $S$  and the irreversible susceptibility  $\chi_{\text{irr}}$ :

$$S = \chi_{\text{irr}} H_f \quad (3.3.1)$$

where  $H_f$  is a fictitious field called the *fluctuation field*. The bearing of this field is that, the thermal energy  $kT$  is imagined to be equivalent to a fictitious energy caused by a magnetic field  $H_f$  acting in the opposite direction of the initial magnetization (i.e.  $M_s$ ), trying to force the magnetic moments out of their original direction. This energy is able to switch a certain volume, which is a part of the whole magnetic body. We call this volume *activation volume* ( $V_{\text{act}}$ ). The fictitious energy is in fact the Zeeman energy caused by  $H_f$  acting on  $M_s V_{\text{act}}$ . Therefore the fictitious energy is:  $\mu_0 H_f M_s V_{\text{act}}$  which is equal to the thermal energy  $kT$ . From this, we obtain the formula for the activation volume:

$$V_{\text{act}} = \frac{kT}{\mu_0 H_f M_s} \quad (3.3.2)$$

$V_{\text{act}}$  presents the volume of material covered by a single jump of the domain wall between pinning centers in case of materials switching by domain wall motion or the volume that nucleates the magnetization reversal in other cases [Street-52].

### 3.4. Demagnetization corrections for perpendicular measurements

When the demagnetizing effect arising from the shape of the sample is involved, for instance in the case of perpendicular measurements, the calculation of  $H_f$  will be more complicated. A. Lyberatos and R. W. Chantrell [Lyberatos-97] have

### 3.4. Demagnetization corrections for perpendicular measurements

---

developed theoretically the relationships between the intrinsic and the observed values of  $\chi_{\text{irr}}$ ,  $S$  and  $H_f$ :

$$\chi_{\text{irr}}^i = \frac{\chi_{\text{irr}}}{1 - D\chi} \quad (3.4.1)$$

$$S_0 = S \left[ \frac{1 - D \partial M_{\text{rev}} / \partial H \Big|_{M_{\text{irr}}}}{1 - D\chi} \right] \quad (3.4.2)$$

$$H_f^i = H_f \left( 1 - D \frac{\partial M_{\text{rev}}}{\partial H} \Big|_{M_{\text{irr}}} \right) \quad (3.4.3)$$

where  $\chi_{\text{irr}}^i$  and  $\chi$  are the *intrinsic irreversible susceptibility* and the *intrinsic total susceptibility* (the total susceptibility is equal to irreversible + reversible susceptibilities), respectively;  $D$  is the demagnetization factor;  $S_0$  and  $S$  are the *intrinsic* and *observed viscosities*, respectively;  $\partial M_{\text{rev}} / \partial H \Big|_{M_{\text{irr}}}$  is the reversible susceptibility measured at constant irreversible magnetization and  $H_f^i$  is the *intrinsic fluctuation field*. It should be noted here that the intrinsic parameters (such as intrinsic viscosity, intrinsic fluctuation field, etc.) are parameters that one would observe if the demagnetizing effect were eliminated.

From the above calculations it is concluded that if the reversible susceptibility can be ignored,  $H_f = H_f^i$ , i.e. no demagnetization correction is needed for this particular case.

## 3.5. Experimental methods

### 3.5.1. Magnetic viscosity measurements

In this thesis, time-dependence effect measurements were carried out with an combined Oxford Instruments and Aerosonic VSM (see Section 4.2). The magnetic viscosity is measured as follows:

- First, the sample is saturated by a negative field of -1200 kA/m for 10s to ensure that the magnetization of the sample reaches its equilibrium state.
- The field is then increased to a positive field  $H_{\text{app}}$  with the fastest ramping rate available (16 kA/m per second).
- At the stabilized applied field  $H_{\text{app}}$ , the magnetization of the sample is recorded for 2000 seconds. The sampling rate is about 3 points/s at the beginning then

becomes more scattered with increasing measuring time, and ending up with one point every five seconds.

- After the measurement, the magnetization of the sample is plotted versus  $\ln(t)$ . This curve is called the *relaxation curve*. In general, the relaxation curve is linear as formulated in Eq. (3.1.4). The magnetic viscosity  $S$  is calculated by fitting this curve to a line. Note that the time range is shifted so that the first point of the measurement is at one second. An example is given in Fig. 3.5.1.a.

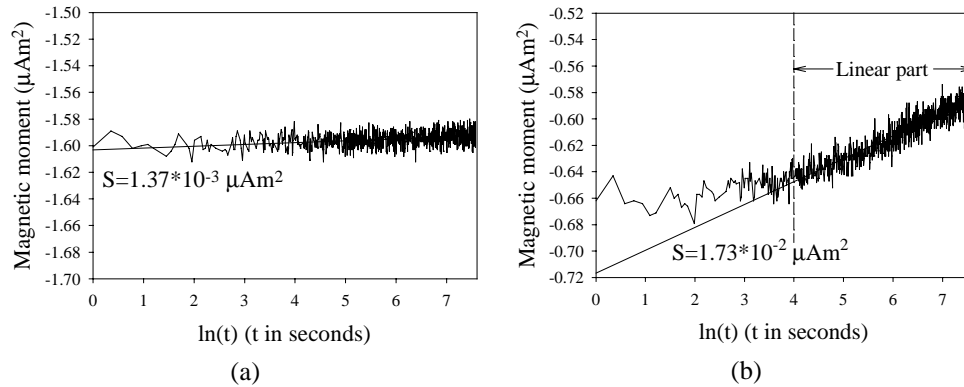


Fig. 3.5.1: Relaxation curves of Co-Cr-Ta/Cr thin film. (a) linear curve, measured at  $H_{app} = 20$  kA/m; (b) non-linear curve, measured at  $H_{app} = 75$  kA/m.

In some cases (especially at applied fields near coercivity), the relaxation curves are found not linear in the region close to the origin, from 1 to at most 100s. In these cases, the viscosity is calculated from the linear part of the curves. For example, in Fig. 3.5.1.b, the linear part from  $\ln(55\text{s})=4$  to the end of the relaxation curve is used to do the linear regression.

## 3.5.2. Fluctuation field measurements

There are two methods to determine the fluctuation field, namely the *DCD method* and the *waiting time method*. These methods will be presented below.

### 3.5.2.1. The DCD method

#### Principle of the method

This method [Street-49, Lyberatos-97], based on Eq. (3.3.1), is widely used to determine the fluctuation field  $H_f$  due to its ease of handling.  $\chi_{irr}$  is calculated from the derivation of the irreversible magnetization  $M_{irr}$  with respect to the applied field:

$$\chi_{\text{irr}} = \frac{dM_{\text{irr}}}{dH} \quad (3.5.1)$$

$M_{\text{irr}}$  is defined by the DC-demagnetization (DCD) measurement. In the DCD measurement, the sample is first negatively saturated, then a positive field is applied. After that the field is removed and the remanence is measured. This remanence is equal to  $M_{\text{irr}}$ , reflecting the irreversible component of the magnetization. The above actions are repeated for progressively increasing applied field, starting from zero and ending up with positive saturation field [Mayo-91].  $M_{\text{irr}}$  is finally plotted against the applied field which is known as the DCD curve. Remanence coercivity ( $H_{\text{cr}}$ ) is defined as the field at which the DCD curve crosses zero magnetization.

#### **The influence of the time-dependence effect on the DCD measurements**

Generally, the DCD measurements are time-dependent so the measurement set-up should be properly designed to give the correct values of  $H_f$  and  $V_{\text{act}}$ . In principle,  $M_{\text{irr}}$  should be measured at the equilibrium state at every applied field, i.e. at infinite time. In practical DCD measurements, before being removed for measuring the remanence, the applied field must remain for a sufficiently long *delay time*. In [Crew-96], it was proposed that  $M_{\text{irr}}$  should be measured at the end of the viscosity measurement. However, at fields at which the viscosity is negligibly small, i.e. the magnetization is almost time-independent, the choice the delay time is no longer important. For these cases, a short delay time is preferable to reduce the measuring time. In our experiments, the DCD measurements are divided into several sections, different in applied field ranges. At the field ranges where the viscosity  $S$  is zero and relatively small, the delay time is 10s and 60s, respectively. The delay time is the longest (5 minutes) at the fields where  $S$  is maximum. After the delay time, the field is ramped fast to zero at which the remanence is measured instantaneously. There should not be any delay here because by removing the applied field, we only want to remove the reversal component of the magnetization which is generally not time-dependent and at the same time to keep the irreversible component as it was before the field removal. The remanence must be measured right after the field is removed to reflect correctly the number of irreversible reversals which have been occurred after the delay time. Any delay at this point might result in an undesired relaxation due to the change in the energy barrier.

A thorough study of the influence of the delay time on the DCD measurements and obtained values of  $\chi_{\text{irr}}$ ,  $H_f$ ,  $V_{\text{act}}$  will be presented later in Chapter 7 (Section 7.1.3).

In normal DCD measurements in which the time-dependence effect is ignored, there is no need to re-saturate the sample before each field step. Several tests have been done to conclude that this way can also be applied to the time-dependence

DCD measurements. There is no significant difference in the relaxation curves between the measurements with and without the re-saturation action.

### 3.5.2.2. The waiting time method

Following the work of Oseroff et al. [Oseroff-87] who have measured the time taken for the magnetization to decay to zero in a negative applied field after previous saturation in a positive field, Chantrell et al. [Chantrell-88, Witte-93] developed a relation between the "waiting time"  $t$  and the fluctuation field:

$$t = t_0 \exp(-\Delta H / H_f) \quad (3.5.2)$$

where  $t_0$  is the time needed for the magnetization to decay to a certain value  $I_0$  at a positive applied field  $H_0$ , after a previous saturation in the negative direction;  $t$  is the time needed for the magnetization to decay to  $I_0$  at a field  $H_0 + \Delta H$ , after a saturation in the negative direction. Several measurements of  $t$  with field steps  $\Delta H$  of about 0.2 kA/m should be done to obtain the linear plot  $\ln(t/t_0)$  versus  $\Delta H$ , from which  $H_f$  at  $H_0$  can be derived according to Eq. (3.5.2).

$$H_f = -(\ln(t/t_0)/\Delta H)^{-1} \quad (3.5.3)$$

In practice, due to the limited resolution of the field control of the Oxford-Aerosonic VSM, the field step  $\Delta H$  cannot be smaller than 0.8 kA/m. It was found that measurements of 4 points at field values 0.8 kA/m apart can result in the value of fluctuation field with acceptable errors. At each measuring field, the relaxation curve is recorded for 15 minutes. After the measurement, the relaxation curves are extrapolated to intersect a horizontal line  $I=I_0$  (Fig. 3.5.2.a). The plot  $\ln(t/t_0)$  versus  $\Delta H$  is then plotted and fitted to a line. Finally, the fluctuation field  $H_f$  is calculated from the slope of this line (Fig. 3.5.2.b).

In perpendicular measurements, the applied field  $H_0$  must be corrected for the demagnetizing effect. There is no need to correct for  $\Delta H$  because it is small enough that the measurements can be considered as being made at constant internal field [Chantrell-98].

In references [Witte-93, Chantrell-98], the authors tried to convince that the waiting time method gives the best estimate of  $H_f$ . This is true as long as  $H_f$  is measured at several particular points. However we found that this method has some disadvantages:

- The determination of  $H_f$  at  $H_0$  around two sides of the viscosity peak, where  $S$  changes abruptly, is not precise. As described above,  $H_f$  is obtained from several measurements which cover a certain "field-width", at least as wide as 1-1.5 kA/m [Witte-93]. Within this field-width, the slope of the viscosity curve, or in other

### 3.5. Experimental methods

words, the value of  $S$  may change so much that the linear fit  $\ln(t/t_0)$  versus  $\Delta H$  does not give any good solution. This problem is even more severe if the measurements are carried out on the Oxford-Aerosonic VSM. Because the resolution of the field control of this equipment is limited, we have to use a field-width of 2.5kA/m in order to get enough 4 measurement points (see Fig. 3.5.2.b).

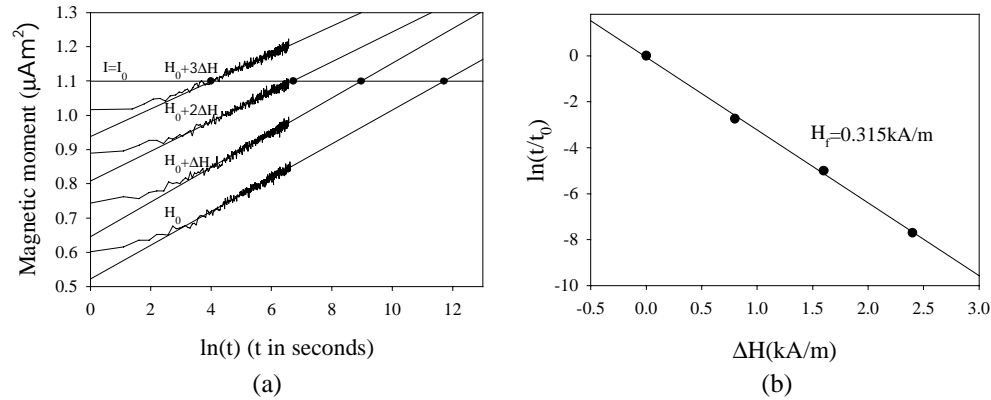


Fig. 3.5.2. An example of waiting time measurement on a CoCrTa/Cr in-plane sample. The measuring field  $H_0=85 \text{ kA/m}$ ,  $I_0= 1.1 \mu\text{Am}^2$ ,  $\Delta H=0.8 \text{ kA/m}$ . (a) Four relaxation curves measured at fields  $\Delta H$  apart; (b)  $H_f$  is calculated as  $-1/\text{slope}$  of the linear plot  $\ln(t/t_0)$  vs.  $\Delta H$ .

- To measure  $H_f$  as a function of applied field, we have to measure  $H_f$  at different  $H_0$  values. In this case another disadvantage emerges. Due to the existence of the field-width at each  $H_0$ , the measurement points (each point corresponds to an  $H_0$ ) cannot be too close to each other to avoid overlapping. This will reduce the number of points of the measurement.

### 3.6. Fitting procedures

In Chapter 7, we will present some fitting results of viscosity as a function of magnetic field using the analytical model of Chantrell [Chantrell-94] with the aim of linking viscosity curves to other magnetic characteristics of the media such as hysteresis loops, anisotropy constants, etc. The fit is based on Eq. (3.2.7). It requires a number of inputs. Fig. 3.6.1 shows the diagram describing briefly the fitting procedures.

The black boxes at the upper and left sides of the diagram are the main inputs of the fitting procedures, including single parameters (for example, fitting parameter  $F$ , sample volume  $V_{\text{sample}}$ , switching volume  $V_{\text{switching}}$ , etc.) or sets of data (torque coefficients, hysteresis loop). The gray boxes are where the calculations are done.

### 3. Time-dependence effect in magnetic recording media

Main formulae of the calculations are shown in each box. At the borders of each box, the symbols inside circles or hexagons represent inputs or outputs of the calculation, respectively.

Box 7 is the final calculation which calculates the curve  $S$  vs.  $H$ . It requires several inputs (such as  $\Delta E_m$ ,  $f(y_c)$ , etc.) which are provided by other boxes in the neighborhood. These boxes are linked together and affect mutually.

To calculate  $\Delta E_m$  (Box 2), the internal field ( $H_i$ ) is required.  $H_i$  is calculated in Box 4 from the generated applied field ( $H_a$ ) and the magnetization  $M$  obtained from the hysteresis loop. Other important inputs of  $\Delta E_m$  calculation are the anisotropy constant  $K$  and the anisotropy field  $H_k=2K/(\mu_0 M_s)$ .  $K$  is derived from the Fourier coefficients of the torque curve after the correction for the demagnetizing field:

$$K = \pm(K_d - R_1) - 2R_2 \quad (3.6.1)$$

where  $R_1$ ,  $R_2$  are the first and the second Fourier coefficients;  $K_d = 0.5 \mu_0 M_s^2 N$  is the demagnetizing anisotropy component. The sign (+) or (-) is used for perpendicular or in-plane case, respectively. For detailed formation of the formulae, see Section 4.2.2.

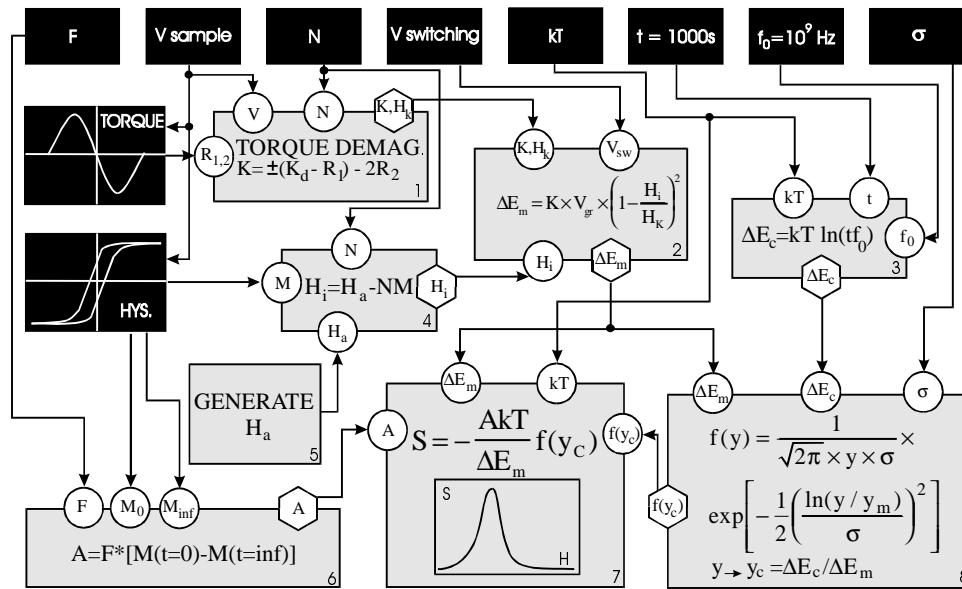


Fig. 3.6.1. Diagram of fitting procedures for viscosity curves using the analytical model. The fitting program is written in LabView language.

### 3.6. Fitting procedures

---

The values of  $\Delta E_m$  at each field  $H_a$  are fed to the calculation of viscosity  $S$  (Box 7) and the distribution function  $f(y)$  (Box 8).

In Box 8, the distribution function is calculated. The variable  $y$  of  $f(y)$  is replaced by the critical reduced  $y_c$  which is the ratio  $\Delta E_c/\Delta E_m$ .

#### **About factor A (Box 6)**

Factor  $A=M(t=0)-M(t=\infty)$  in practice is hard to define. In principle it is equal to the difference between the magnetization at the beginning of the relaxation curve,  $M(t=0)$ , and the equilibrium magnetization, i.e. the magnetization at infinite time  $M(t=\infty)$ .  $M(t=0)$  is in fact  $-M_s$ , because the sample is initially negatively saturated.

On the other hand, the theoretical value of  $M(t=\infty)$  is  $M_s$ , because under any positive field, all particles of the sample will eventually switch their magnetization to the field direction. However, the magnetization at  $t=0$  is never known, due to the limited ramping speed of the field. The magnetization at  $t=\infty$  is either undefined in practice. The only solution is to approximate  $M(t=0)$  to  $-M_s$  and approximate  $M(t=\infty)$  to the value of magnetization on the hysteresis loop at the field ( $H_a$ ) of interest. This assumption is based on the fact that there is only few percent (in our cases) difference between the magnetization on the hysteresis loop, which is measured at normal field rate, and the magnetization after a very long time, and this difference is very small compared to the value  $A$  calculated by the above approximation. This assumption is only valid in practice where the viscosity is calculated from a restrictedly long measurement and where the logarithmic assumption [Eq.(3.1.4)] is valid.

In Box 6, factor  $A$  is set to  $F*[M(t=0)-M(t=\infty)]$ , where the *fitting parameter*  $F$  is introduced. The analytical model is applicable only to perfectly aligned systems, where all reversal events contribute the same change in magnetization. However, the real materials generally have a distribution of orientation which effects not only the energy barrier distribution, but also means that not all reversal events contribute the same change in magnetization [Chantrell-98]. Therefore,  $F$  is introduced to represent the fraction of particles having the easy axis in the direction of the applied field. Besides,  $F$  is treated as fitting parameter, to correct for all errors due to assumptions and approximations of the calculations.

### **3.7. Definitions of the confusing volumes**

So far, we have talked about several kinds of volumes, namely, sample volume, particle volume, physical particle volume, effective particle volume, activation volume, switching volume, critical volume, etc. The picture of them is rather

complicated and confusing. The aim of this section is to give clearer definitions and comparison of all of these volumes.

- *Sample volume* is the magnetic volume of the whole sample, i.e. the total magnetic volume of all particles (or grains) in the sample. This volume is used to calculate the magnetization (A/m) from the magnetic moment ( $\text{Am}^2$ ) which is measured by a VSM. It is also used to calculate the torque values (in  $\text{J/m}^3$ ) from the raw torque data (in J).
- *Physical particle volume (or physical grain volume)* is the magnetic volume of one particle (or grain) in the sample. In some cases like in S-W particles, it can also be called particle volume, for short.
- *Switching volume*,  $V_{\text{switching}}$  is the volume of a switching unit. A switching unit is defined as a certain portion of the sample which switches its magnetization coherently. In a S-W particle, switching volume is identical to the physical particle volume. In other reversal modes rather than coherent (S-W) mode, switching volume could be smaller or larger than the physical particle volume. In our fitting procedures presented in the previous section, switching volume is not the physical particle volume but it is treated as a fitting parameter. For instance, if  $V_{\text{switching}}$  is found to be smaller than the physical particle volume, it means that by fitting, we suppose that the magnetic reversal takes place coherently at small switching units ( $V_{\text{switching}}$ ) inside a particle. When  $V_{\text{switching}}$  is smaller than the physical particle volume, the reversal mode of the particle is certainly incoherent. Conversely, when  $V_{\text{switching}}$  is larger than the physical particle volume, the interactions between particles must be rather strong so that they can switch collectively.
- *Effective volume* proposed by [Rodé-87] has the same meaning as the switching volume. However, we are not using this term in the rest of the thesis.
- *Activation volume* is slightly different from the switching volume (or the effective volume). Activation volume is derived from viscosity and susceptibility measurements, therefore, it is also a fictitious quantity like the fluctuation field. It is supposed to represent the volume that nucleates the magnetization reversal [Lyberatos-94]. The main difference between the activation volume and the switching volume is that the switching mechanism of the activation volume is not necessarily coherent whereas that of the switching volume must be coherent. In a S-W particle, the switching volume is identical to the physical volume of the particle whereas the activation volume is not necessarily equal to it. In some cases, the activation volume is equal to the switching volume. In most cases, they are comparable.
- *Critical volume*  $V_{\text{critical}}$  is the volume below which the magnetic material is no longer ferromagnetic but superparamagnetic. It is equal to  $\Delta E_c/K$ , where  $\Delta E_c$  is the

critical energy barrier (see Section 3.2) and  $K$  is the anisotropy constant. It is straightforward that the switching volume, effective volume and activation volume can not be smaller than the critical volume. They are equal to  $V_{\text{critical}}$  in case of exchange coupling between magnetic spins of the material is extremely weak. Commonly, they are a few orders of magnitude larger than  $V_{\text{critical}}$ .

## 3.8. Conclusion

Some basics about the time-dependence effect, experimental methods and simulation procedures have been presented. Studying the time-dependence effect is an important task for workers in the field of magnetic recording media. This effect reveals information about storage stability of the media and especially the switching mechanisms and switching volumes of the media. Definitions of magnetic viscosity  $S$ , energy barrier, fluctuation field and activation volume have been introduced.

In this thesis, we concentrate more on the value of magnetic viscosity  $S$  as a function of magnetic field. An analytical model proposed by R. Chantrell [Chantrell-94] has been cited. This model finally leads to a formula which allows to calculate the viscosity as a function of magnetic field. To investigate the time-dependence properties of perpendicular media, correction for the demagnetizing effect is required. A method by Lyberatos [Lyberatos-97] has been given, which allows to calculate the intrinsic viscosity, fluctuation volume, etc. as a function of internal field from data of normal measurements in external field.

In Section 3.5, we presented the experimental methods used in this thesis. Some remarks about how to measure in order to give good results and some comparisons between several measurement methods have been discussed.

In Section 3.6, fitting procedures based the analytical model of Chantrell have been presented. We will use this fit to study the time-dependence effect of several recording media. These studies will be presented in Chapter 7.

Finally, clear definitions of several types of volumes which are used in this thesis have been given. The definitions will help readers to understand better our discussions in Chapter 7.

## 3.9. References

- [Battle-97] X. Battle, M. Garcia del Muro and A. Labarta. "Interaction effects and energy barrier distribution on the magnetic relaxation of nanocrystalline

### 3. Time-dependence effect in magnetic recording media

---

- hexagonal ferrites". Phys. Rev. B, Vol 55(10) (1997), 6440.
- [Brown-63] W. F. Brown Jr., Phys. Rev. 130, (1963) 1677.
- [Chantrell-88] R. W. Chantrell, G. N. Coverdale and K. O'Grady. "Time dependence and rate dependence of the coercivity of particulate recording media". J. Phys. D. Appl. Phys. 21 (1988), 1469.
- [Chantrell-94] R. W. Chantrell, A. Lyberatos, M. El-Hilo and K. O'Grady. "Models of slow relaxation in particulate and thin film materials (invited)". J. Appl. Phys. 76(10) (1994), 6407.
- [Chantrell-97] R. W. Chantrell and J. Hannay. "Thermally activated magnetisation reversal at high frequencies". J. Magn. Soc. Of Japan 21 (Supp S2) (1997), 283.
- [Chantrell-98] Private communications.
- [Charap-88] S. H. Charap, "Magnetic viscosity in recording media". J. Appl. Phys. 63(6) (1988), 2054.
- [Crew-96] D. C. Crew, S. H Farrant, P. G. McCormick and R. Street. "Measurement of magnetic viscosity in a Stoner-Wohlfarth material". J. Magn. Magn. Mat. 136 (1996), 299
- [Cullity-72] B. D. Cullity. "Introduction to magnetic materials". Addison-Wesley (1972).
- [Folks-94] L. Folks and R. Street. "Analysis and interpretation of time dependent magnetic phenomena (invited)". J. Appl. Phys. 76(10)(1994), 6391.
- [Gaunt-76] P. Gaunt. "Magnetic viscosity in ferromagnets - I. Phenomenological theory". Physiosophical Magazine, 34 (1976), 775.
- [Granqvist-76] C. G. Granqvist and R. A. Buhrman. "Ultrafine metal particles". J. Appl. Phys, Vol. 47(5) (1976), 2200.
- [Lyberatos-94] A. Lyberatos, R. W. Chantrell and K. O' Grady. "Activation volumes and magnetization reversal in fine particles". Nato ASI Series E: Applied Sciences, Vol. 260 (1994) 653.
- [Lyberatos-91] A. Lyberatos, R. W. Chantrell, E. R. Sterringa and J. C. Lodder. "Magnetic viscosity in perpendicular media". J. Appl. Phys 70(8) (1991), 4431.
- [Lyberatos-97] A. Lyberatos and R. W. Chantrell. "The fluctuation field of ferromagnetic materials". J. Phys: Condens. Matter. 9 (1997), 2623.
- [Mayo-91] P.I. Mayo, K. O'Grady, R.W. Chantrell, J.A. Cambridge, I.L. Sanders, T. Yogi and J.K. Howard, "Magnetic measurement of interaction effects in CoNiCr and CoPtCr thin film media". J. Magn. Magn. Mat. 95(1991), 109

### 3.9. References

---

- [Neel-51] L. Néel, *J. Phys. Rad.* 12 (1951), 339.
- [Oseroff-87] S. B. Oseroff, D. Franks, V. M. Tobin and S. Schultz. "Magnetization time decay in particulate media". *IEEE Trans. Magn.* MAG-23 (1987), 2871.
- [Rodé-87] D. Rodé, H. N. Bertram and D. R. Fredkin. "Effective volume of interacting particles". *IEEE Trans. Magn.* MAG-23 (1987), 2224.
- [Stoner-48] E. C. Stoner, and E. P. Wohlfarth. "A mechanism of magnetic hysteresis in heterogeneous alloys". *Phil. Trans. Roy. Soc. A-240* (1948), 599.
- [Street-49] R. Street and J. C. Woolley. "A study of magnetic viscosity". *Proc. of Phys. Soc. A62* (1949), 562.
- [Street-52] R. Street, J. C. Woolley and P. B. Smith. "Magnetic viscosity under discontinuously and continuously variable field conditions". *Proc. of Phys. Soc. B.65* (1952), 679.
- [Witte-93] A. M. de Witte, K. O'Grady and R. W. Chantrell. "The determination of the fluctuation field in particulate media". *J. Magn. Magn. Mat.* 120 (1993), 187.
- [Wohlfarth-84] E. P. Wohlfarth. "The coefficient of magnetic viscosity". *J. Phys. F: Met. Phys.* 14(1984), L155

# Chapter 4

---

## Sample preparation and experimental methods

The research carried out in this thesis requires a number of experimental techniques and methods, ranging from preparation techniques to characterizing and measuring methods. This chapter gives some descriptions and important remarks on these methods and the equipment. To start with, we will discuss about the sputtering process, one of the most important techniques in the thesis. Next, we will present some magnetic and structural characterization methods.

### 4.1. Preparation of sputtered samples: sputter deposition

#### 4.1.1. RF sputtering system

To produce a thin metal film, evaporation or sputtering method is commonly utilized. The sputtering method is preferably used because it provides sputtered particles with much higher energy than the evaporation method, thus producing a denser and better film. To know in detail the sputtering technology, the readers are recommended to read [Chapman-80 and Wasa-92]. The sputtering technology is divided into two main categories: DC sputtering and RF sputtering. The RF sputtering is commonly used because it can work with both conducting and non-conducting materials. In addition, it creates more stable plasma and can operate at lower Ar pressure.

In this thesis, the RF sputtering technique is used. The schematic diagram of the Leybold - Heraeus Z400 sputtering system is shown in Fig. 4.1.1. In the vacuum chamber, there are three substrate holders mounted on the base flange. Above the substrate holders, three targets are mounted on the target mushroom which can rotate to arrange any target to face a desired substrate holder. Besides the three

#### 4.1. Preparation of sputtered samples: sputter deposition

targets, there is a blind flange which is used when the substrate is sputter cleaned. A perspective view of the targets and substrate holders is shown in the inset of Fig. 4.1.1. Under each target and substrate holder, there is a cooling system. One of the substrate holders is equipped with a resistance heater. The temperature of the heater can be adjusted by setting the heater voltage (see Section 4.1.3). All the targets and substrate holders are connected to the target and substrate switching boxes, respectively (in the diagram of Fig. 4.1.1, only four connections are shown, but in fact, there are six connections for three targets and three substrate holders). The task of the switching boxes is to connect any target or substrate holder to either RF voltage or earth. The RF voltage ( $V_{rf}$ ) inputs of the switching boxes are connected in series with a blocking capacitor, a matching network and an RF generator. In our system, the matching network is not adjustable. It is designed to match the most common impedance of the plasma.

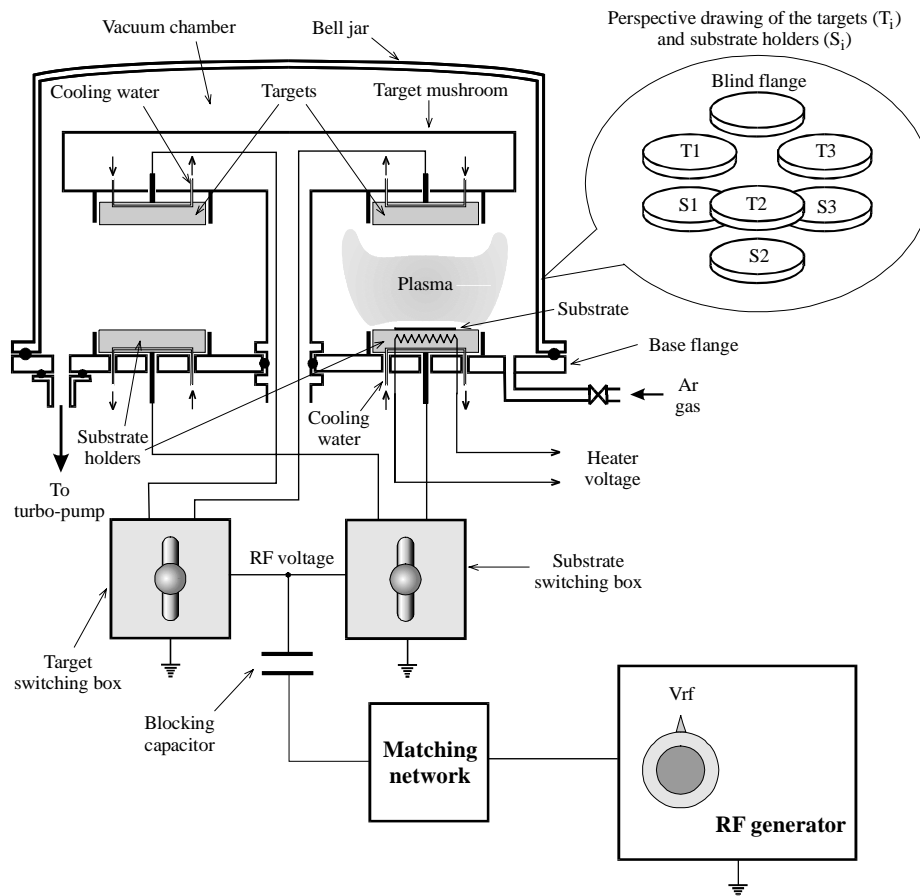


Fig. 4.1.1. Schematic diagram of the Leybold-Heraeus Z400 sputtering system.

The vacuum chamber is connected to the vacuum system that uses two pumps: a turbo molecular pump and a rotary pump. On the bell jar there is a cold finger which is filled with liquid nitrogen before a sputtering run. The ultimate vacuum of the system is about  $1.5 \times 10^{-7}$  mbar with liquid N<sub>2</sub>. When the heater is used, the ultimate pressure is slightly higher, due to degassing. Ar gas is admitted through a regulated valve controlled by a stepper motor.

### 4.1.2. Operation of the system

After loading the substrate, the system is pumped for at least six hours. Just before a sputtering run, the cold finger is filled with liquid nitrogen. Ar gas is then admitted at a constant flow rate, which keeps the Ar pressure in the chamber at a stable value. Prior to the sputtering process, the targets and the substrate are subsequently sputter-cleaned. To clean the targets, the cleaned target is connected to high RF voltage while an unused substrate holder, facing the cleaned target, is grounded. Generally, as experience, the cleaning step of each target lasts for 15 minutes at  $V_{rf}$  of 1.6kV, which ensures to remove the oxide and contamination layer on the surface of the target. The substrate is cleaned by back sputtering for about three minutes: it is connected to a low RF voltage while the blind flange facing it is grounded. After the cleaning steps, sputter deposition of the film starts. In between the steps, the target mushroom is rotated manually to an appropriate position.

The thickness of the sputtered layer can be controlled by the sputtering time calculated from the deposition rate. The deposition rate under certain sputtering conditions is defined in advance by depositing a test film under the same conditions and measuring its thickness.

### 4.1.3. Substrate heating

During sputtering runs, the substrate temperature is controlled by setting the heater voltage  $V_{heater}$ , without measuring the temperature *in-situ*. The temperature versus heater voltage is calibrated in advance. At a fixed voltage, temperature of the heater will be saturated at a certain value, after about half an hour or more, depending on the voltage. The dependence of the saturation temperature on the heater voltage has been investigated. The substrate temperature was measured by a thermocouple attached to the surface of the substrate. The substrate was mounted on the substrate holder with silver paste\*. Figure 4.1.2.a shows an example of the time-dependence of substrate temperature, when  $V_{heater} = 95V$ , and Ar pressure

---

\* Silver paste is a heat conducting paste consisting of vacuum grease and silver powder.

## 4.1. Preparation of sputtered samples: sputter deposition

(PAr) =  $2 \times 10^{-2}$  mbar, which is the most common value used in our experiments. It can be seen that the temperature gets saturated after about 30-35 minutes. The higher the heater voltage, the faster the temperature gets saturated. At a fixed voltage, the saturation temperature does not change significantly with PAr within the working range (from  $1 \times 10^{-2}$  to  $5 \times 10^{-2}$  mbar). Figure 4.1.2.b shows the dependence of the saturation temperature on the heater voltage. This curve is used as the calibrated curve for setting the heater voltage in our experiments.

About half an hour before a sputtering run, the heater is switched on. It is first set to the highest possible voltage (110V) for 5-10 minutes to speed up the heating process, and then an appropriate voltage, according to Fig. 4.1.2.b, is applied.

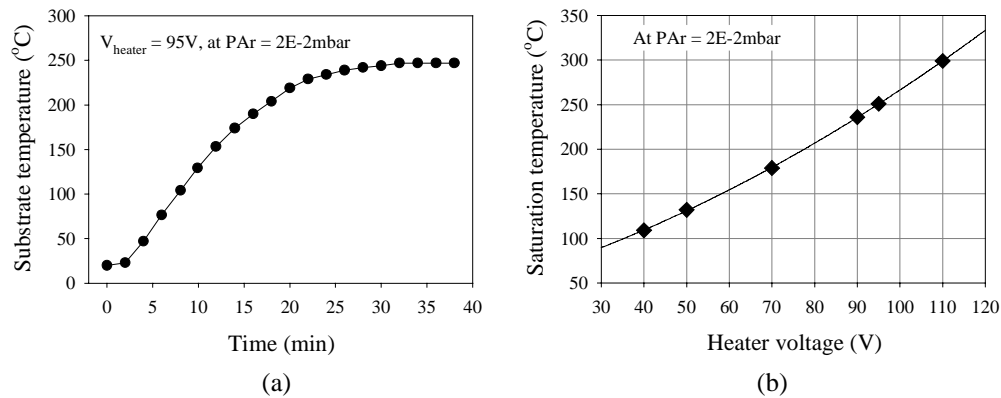


Fig. 4.1.2. (a) Behavior of substrate temperature with time, when  $V_{heater} = 95V$  and  $PAr = 2 \times 10^{-2}$  mbar. The temperature gets saturated after 30-35 minutes. (b) Saturation temperature as a function of heater voltage.

Some temperature measurements during sputtering have been done. It was found that normally after 10-15 minutes of sputtering, substrate temperature rises by about 30-50°C from the temperature measured before sputtering. This is because the substrate is exposed to the hot plasma and due to the bombardment of electrons coming from the plasma.

## 4.2. Magnetic characterization

### 4.2.1. VSM measurements

In magnetic thin film research, the Vibrating Sample Magnetometer (VSM) method is the most important method for magnetic characterization. In a VSM, a magnetic sample is vibrating at the center of a set of detection coils. The vibration

of the sample causes the flux through the coils to change, which induces a voltage on the terminals of the set of coils. This voltage is proportional to the magnetic moment of the sample, and thus can be determined by calibration. An electromagnet is used to apply a magnetic field on the sample, which allows to measure the magnetic moment of the sample at varied applied field. Details about the VSM technique can be found in [Foner-59 and Foner-96].

In this thesis, we used two VSMs:

One is the DMS 880 made by Digital Measurement Systems Inc. This VSM has a sensitivity of  $1 \times 10^{-5}$  mAm<sup>2</sup>, equipped with an electromagnet which can produce a maximum field of 1050kA/m (1.3T). The VSM has a vector coil system, allowing to measure magnetic moment along the field direction as well as perpendicular to it. The VSM can measure a sample at different angles with respect to the field direction.

Another is the combined Oxford Instruments and Aerosonic VSM. This VSM has a superconducting magnet which is capable to produce a maximum field of 2400kA/m (3T). This VSM has also a vector coil system and angle rotation mechanism. The sensitivity is  $1 \times 10^{-6}$  mAm<sup>2</sup>.

Details about VSM measurements are presented elsewhere (in Chapters 3, 6, 7).

### 4.2.2. Torque measurements

The torque magnetometer is used to determine the anisotropy constants of magnetic samples. Its operation is based on a principle that when an anisotropic sample is placed in a magnetic field at a certain angle, the field tries to force the magnetization of the sample to align along its direction, whereas the anisotropy energy of the sample tries to keep the magnetization in the easy-axis direction. The consequence is that the field exerts a torque on the sample. The torque  $L$  is proportional to the derivative of the anisotropy energy  $E_a$  with respect to the angle  $\theta$  between the magnetization and the easy-axis:

$$L = -\partial E_a / \partial \theta \quad (\text{J/m}^3) \quad (4.2.1)$$

In the torque measurement, the sample is rotated in a plane containing the easy-axis in a magnetic field. The torque, which is a function of  $\theta$ , can be expressed by a Fourier series:

$$L(\theta) = \sum_n [R_n \sin(2n\theta) + Q_n \cos(2n\theta)] \quad (\text{J/m}^3) \quad (4.2.2)$$

## 4.2. Magnetic characterization

In practice, the angle  $\theta$  can always be defined so that at  $\theta=0$ ,  $L=0$ ; therefore  $Q_n = 0$ . In the case of uniaxial anisotropy, as in the samples investigated in this thesis, the terms of order higher than 2 can be ignored. Equation (4.2.2) can be written as:

$$L(\theta) = R_1 \sin(2\theta) + R_2 \sin(4\theta) \quad (\text{J/m}^3) \quad (4.2.3)$$

Generally, the anisotropy energy of a thin film sample consists of two components:

$E_a = E_c + E_d$ ; in which,  $E_c$  is the crystalline anisotropy energy and  $E_d$  is the demagnetizing energy coming from the shape of the thin film. The anisotropy energy  $E_c$  can be expressed as:

$$E_c = K_1 \sin^2\theta + K_2 \sin^4\theta \quad (\text{J/m}^3) \quad (4.2.4)$$

where  $K_1$  and  $K_2$  are the first and the second anisotropy constants

In a real torque measurement, because the direction of the magnetization is unknown, we can only determine the torque as a function of the angle  $\alpha$  between the field and the normal direction of the film sample. Suppose that the field is high enough to saturate the sample to  $M_s$  and the direction of  $M_s$  almost coincides with that of the field (see Fig. 4.2.1). The demagnetization energy can be written as:

$$E_d = 1/2 \mu_0 M_s^2 N_d \cos^2\alpha = K_d \cos^2\alpha \quad (\text{J/m}^3) \quad (4.2.5)$$

in which  $\mu_0$  is the permeability of empty space, which is equal to  $4\pi \times 10^{-7} \text{ J/A}^2\text{m}$ ;  $N_d$  is the perpendicular demagnetizing factor and  $K_d$  is called the shape anisotropy constant.

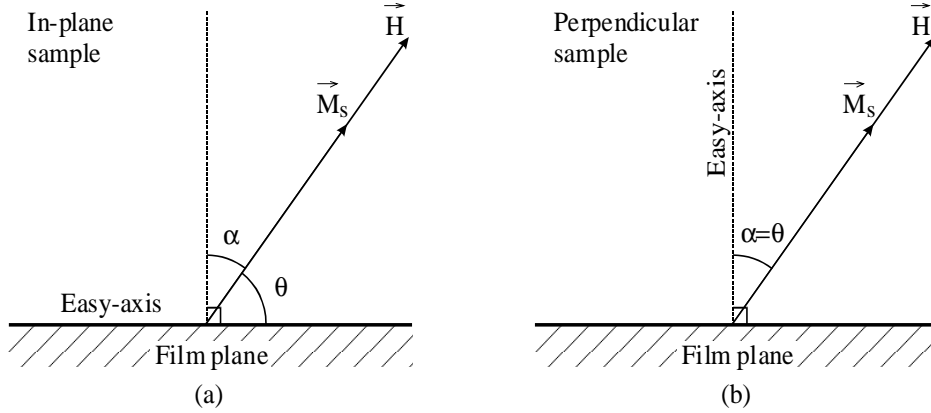


Fig. 4.2.1. (a) In-plane and (b) perpendicular samples in a torque measurement.

Now the torque in Eq. (4.2.3) can be expressed as a Fourier series of angle  $\alpha$ , instead of  $\theta$ :

$$L(\alpha) = R_1 \sin(2\alpha) + R_2 \sin(4\alpha) \quad (\text{J/m}^3) \quad (4.2.6)$$

The analysis of a torque curve depends on whether the sample has in-plane or perpendicular anisotropy:

- In-plane sample: From Eq. (4.2.4) and Fig. 4.2.1.a we have:

$$E_c = K_1 \sin^2(\pi/2-\alpha) + K_2 \sin^4(\pi/2-\alpha) \quad (4.2.7)$$

Finally, from Eqs. (4.2.7), (4.2.5) and (4.2.6) we obtain:

$$K_1 = R_1 - K_d - K_2 \quad \text{and} \quad K_2 = 2 R_2 \quad (4.2.8)$$

- Perpendicular sample: From Eq. (4.2.4) and Fig. 4.2.1.b we have:

$$E_c = K_1 \sin^2\alpha + K_2 \sin^4\alpha \quad (4.2.9)$$

Similar calculation leads to:

$$K_1 = K_d - R_1 - K_2 \quad \text{and} \quad K_2 = 2 R_2 \quad (4.2.10)$$

It could be summarized here that to obtain the anisotropy constants  $K_1$  and  $K_2$ , first we have to find the Fourier coefficients  $R_1$  and  $R_2$  of the torque curve, then calculate  $K_d$  using a known  $M_s$  and finally use Eqs. (4.2.8) or (4.2.10). However, because in practice, the field is not high enough to force the magnetization  $M_s$  exactly in the direction of the field, i.e.  $\alpha$  is not the same as  $\pi/2-\theta$  or  $\theta$ , for in-plane or perpendicular cases, respectively, we have to extrapolate to obtain the right  $R_1$  and  $R_2$  as they would be if the field were infinity. To do that, several torque curves at different high fields are measured. After that,  $R_1$  and  $R_2$  of each measurement are calculated by Fourier analysis. The values of  $R_1$  and  $R_2$  are then plotted against  $1/H^2$  and  $1/H$ , respectively. The right values of  $R_1$  and  $R_2$  can be obtained by extrapolating these graphs to infinity field. The physical meaning of the extrapolation has been described in [Burd-77]. Finally, the anisotropy constants  $K_1$  and  $K_2$  can be obtained from the values of extrapolated  $R_1$  and  $R_2$ ,  $K_d$  and Eq. (4.2.8) or (4.2.10).

Torque measurements in the thesis were carried out on a homemade torque-magnetometer having a maximum field of 1350kA/m and a sensitivity of  $1 \times 10^{-9}$  J.

## 4.3. Structural characterization

### 4.3.1. X-ray diffraction

To determine the crystalline structure of thin films, the most popular tool is the *X-ray diffractometer (XRD)*. All XRD results reported in this thesis were carried out on the Philips X-ray diffractometer. The specifications of the equipment are as follows: goniometer PW 1820, angular accuracy:  $0.005^\circ$ ; detector PW 1711; generator PW 1830, 3kW, Tube PW 2273 (Cu), 2.2kW; equipped with an attachment for measuring thin films. The followings are descriptions of three types of XRD measurements used in the thesis.

#### 4.3.1.1. High-angle measurements

The *high-angle measurement* is also called the  $\theta$ - $2\theta$  high-angle measurement. A narrow and parallel X-ray comes from an X-ray source to a sample at an angle  $\theta$  with respect to the film normal. A detector is placed at an angle  $2\theta$  with respect to the incident ray (Fig. 4.3.1). During the measurement, the source is fixed while the sample and the detector are rotated so that the configuration  $\theta$ - $2\theta$  is preserved. In the high-angle measurement, normally  $2\theta$  is scanned from about  $20^\circ$  to  $100^\circ$ , depending on the sample and the aim of the measurement. The recorded signal from the detector is plotted versus  $2\theta$ , which is called the high-angle XRD spectrum (see the inset of Fig. 4.3.1).

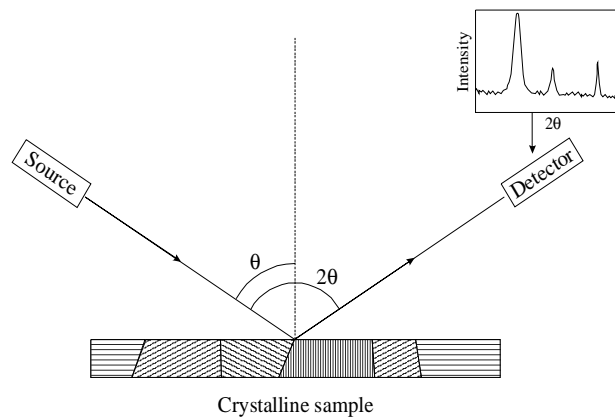


Fig. 4.3.1. Configuration of a  $\theta$ - $2\theta$  high-angle measurement. The crystalline sample consists of various textures with different orientations. The inset shows an example of a high-angle XRD spectrum recorded in the detector.

During the measurement, a peak is recorded at a certain angle  $2\theta$  when the Bragg condition is satisfied:  $2d \sin\theta = n\lambda$ , where  $d$  is the lattice spacing of a set of crystallographic planes (in  $\text{\AA}$ ), which is parallel to the film plane;  $n\lambda = 1.54056 \text{ \AA}$  for our equipment. From all peaks in the spectrum, we can get information about which textures of the sample are parallel to the film plane. The intensity of the peaks reveals the amount and quality of the texture. The higher the intensity, the better the texture is oriented.

#### 4.3.1.2. Rocking curve measurements

For a better evaluation of the quality of film textures, *rocking curve measurements* are employed. The measurement is only applicable to the samples that contain  $c$ -axes dispersing symmetrically around the normal direction of the film plane. To measure the rocking curve of a texture which is corresponding to a peak at certain angle  $2\theta_1$  in the high-angle XRD spectrum, the detector is first fixed at the angle  $2\theta_1$  with respect to the incident ray. Then the angle  $\theta$  between the incident ray and the normal direction of the film plane is scanned around the value  $\theta_1$ . This means that the sample is rotated around the symmetric position as shown in Fig. 4.3.1 while the source and the detector are fixed.

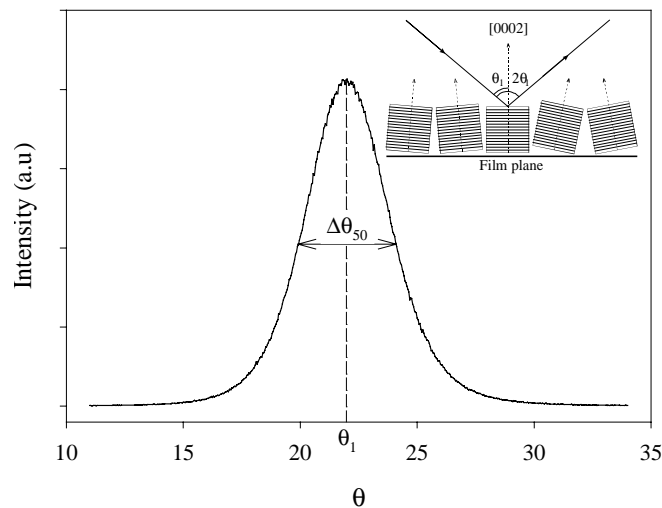


Fig. 4.3.2. An example of the rocking curve measured at  $2\theta_1 = 44^\circ$  ( $\theta_1 = 22^\circ$ ). This angle is corresponding to the CoCrTa (0002) texture. The inset shows a schematic drawing of the crystallites in the sample. The parallel lines in the crystallites indicate the (0002) planes of the crystallites, which disperse around the film plane. The width at half height of the peak,  $\Delta\theta_{50}$ , indicates the degree of dispersion.

### 4.3. Structural characterization

It should be noted here that the angle  $\theta$  in this case is used by convention and it is not the same as the Bragg angle  $\theta$  in high angle XRD measurements. An example of the rocking curve versus  $\theta$  is given in Fig. 4.3.2. The width at half height of the peak,  $\Delta\theta_{50}$ , indicates the degree of dispersion of the investigated texture. The smaller the  $\Delta\theta_{50}$ , the better the texture is oriented.

#### 4.3.1.3. Low-angle measurements

The *low-angle measurement* is used to determine the thickness of thin films. The low-angle measurement is in fact the  $\theta$ - $2\theta$  measurement but performing at low angles  $2\theta$ , typically from  $1^\circ$  to  $3^\circ$ . In the obtained spectrum, we can see regular peaks (Fig. 4.3.3). The peaks are equidistant from each other. These peaks are not due to the diffraction of lattice planes, but due to the interference between the reflected ray from the film surface and that from the interface between the film and the substrate (see the inset of Fig. 4.3.3). Therefore, the distance between the peaks reveals information about the thickness of the sample. Simple calculation leads to the following equation, which is similar to the Bragg equation:  $2t \sin(\Delta_{2\theta}/2) = n\lambda$ , in which  $t$  is the film thickness in  $\text{\AA}$ ;  $\Delta_{2\theta}$  is the distance between the adjacent peaks;  $n\lambda=1.54056\text{\AA}$ , for our equipment. In practice,  $\Delta_{2\theta}$  is obtained by averaging the distances between the peaks (or the valleys).

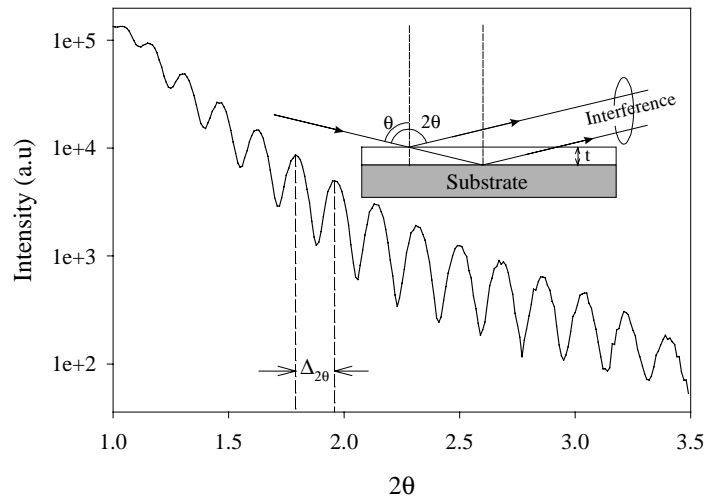


Fig. 4.3.3. An example of the low-angle measurement. The inset shows a diagram of the interference occurring during the low-angle measurement.

The low-angle measurement is one of the most accurate methods to determine thin film thickness, especially for metal thin film case, in which, other methods like ellipsometry are difficult. The typical error of the low-angle XRD measurement is

about  $\pm 2\text{nm}$ , for our equipment. However, this method has a disadvantage that to have an accurate measurement, the film to be measured should have a thickness of less than about 100nm, otherwise the peaks will be too close together.

Besides determination of film thickness, the low-angle measurement also gives some information about the film roughness. The intensity recorded at the lower bound of the  $2\theta$  range, i.e. about  $1^\circ$  or less, is chiefly the normal mirror reflection on the film surface. The higher the intensity at this bound, the smoother the surface is.

### 4.3.2. Microscopy

#### 4.3.2.1. SEM

*SEM* stands for *Scanning Electron Microscopy*. In a SEM, a fine beam of high energy electrons coming from an electron gun is scanned across the sample by the scan coils, while a detector counts the number of low energy secondary electrons or back-scattered electrons given off from each point on the scanned surface. The signal obtained from these types of electrons conveys information on the topology of the sample. SEM technique does not require any special preparations of the sample.

#### 4.3.2.2. TEM

The *Transmission Electron Microscopy (TEM)* is a powerful tool for the material science research. An electron beam emitted from a gun goes through a system of condenser lenses then enters the sample, in which it is scattered by the sample atoms. A contrast aperture, centered about the optical axis, is placed behind the sample to block partly the scattered electrons and allow the unscattered or less scattered electrons going through. The electrons leaving the aperture pass an objective lens, then a series of projector lenses and finally create a *bright-field image* on a fluorescent screen. The bright-field images were chiefly investigated in this thesis. They reveal information on the morphology of the sample, such as grains, columnar structures, stacking faults, textures, etc. Details about analyzing TEM images can be found in [Reimer-97].

The equipment used in this thesis is a Philips CM30 Twin/STEM, which operates at an accelerating voltage of 300kV.

It is very essential that the sample be thin enough for the electrons to penetrate. For instance, it should not be thicker than 300nm, for a TEM having an electron gun of 300kV. In this thesis, we made two types of TEM bright-field images: *Plane-view* and *cross-sectional images*.

### Plane-view images

*Plane-view images* allow to observe grains, faults and partly textures of a thin film, if the resolution is high enough. To prepare a plane-view sample of a thin film, we used a special  $\text{Si}_3\text{N}_4$  chip as the substrate (Fig. 4.3.4). The  $\text{Si}_3\text{N}_4$  chip consists of a Si wafer chip covered at both sides with 50nm-thick  $\text{Si}_3\text{N}_4$  layers. At the center of the chip, there is a small window in the Si wafer, on which the  $\text{Si}_3\text{N}_4$  layer at one side becomes a bare  $\text{Si}_3\text{N}_4$  membrane. The size of the chip fits the sample chamber of the TEM; i.e. its diagonal dimension is 3mm. The investigated film is deposited on the upper side of the membrane. The film thickness should not be thicker than about 200nm. After that the  $\text{Si}_3\text{N}_4$  chip containing the film is observed under the TEM. Because the  $\text{Si}_3\text{N}_4$  membrane is amorphous and relatively thin, it is electron-transparent and therefore, the obtained image of the sample is the plane-view image of the investigated film, containing information on the morphology of the film.

This method has an advantage that it is simple and cheap. However, its disadvantage is that the films deposited on the  $\text{Si}_3\text{N}_4$  membrane cannot be reproduced exactly the same as they are deposited on a normal substrate, chiefly due to the difference in the surface temperature. In experiments, we tried to keep their conditions as alike as possible by mounting both, the chip and the normal substrate, very well and close together on the substrate holder.

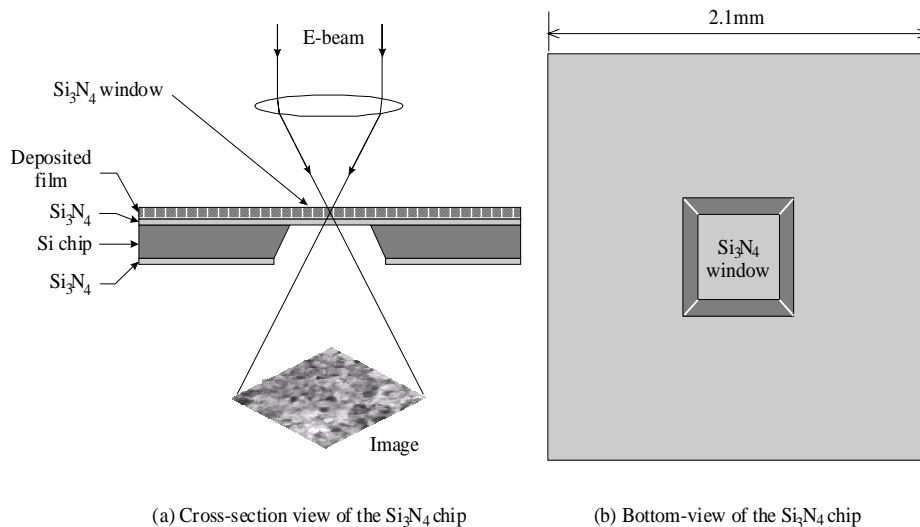


Fig. 4.3.4. Diagram of a  $\text{Si}_3\text{N}_4$  chip, (a) cross-section view and (b) bottom-view.

### Cross-sectional images

*Cross-sectional images* reveal information about columnar structure, grains, faults, partly textures, interfaces between layers, etc. of the cross-section of the thin film. The sample preparation of this method is difficult and time-consuming. Preparation procedure of a cross-section is described in Fig. 4.3.5. After step 4, the sample may be finally coated with a thin carbon layer to reduce the electron charge on the sample during observation. Then the sample can be observed on the TEM. The image is taken from the thinnest part of the cross-section, i.e. at the center of the sample.

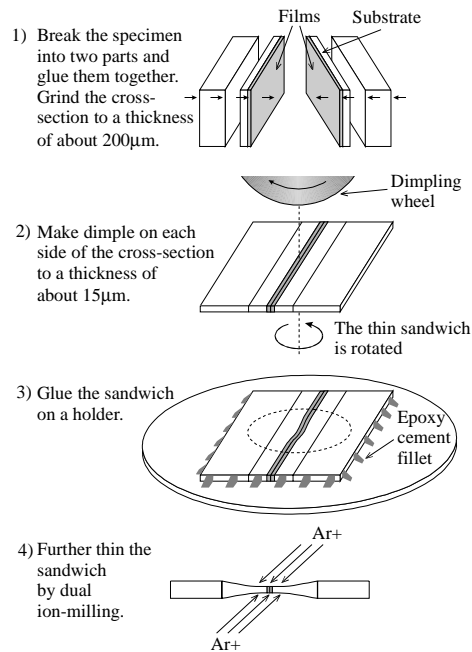


Fig. 4.3.5. Preparation procedure of a cross-section.

#### 4.3.2.3. AFM

*Atomic Force Microscopy (AFM)* belongs to the Scanning Probe Microscopy (SPM) technique in which a fine tip is brought into atomically close contact with a sample surface without actually touching the surface. This is done by sensing the repulsive force between the probe tip and the surface. The forces are extremely small (about 1 nN). The tip is then moved back and forth over the sample surface

### 4.3. Structural characterization

---

and can measure the topography with almost atomic resolution. To create an image, the tip is scanned over the area of interest on the sample and the image is reproduced in the computer.

AFM technique requires no sample preparation, and it can operate in the atmosphere. However, to obtain a good image, a lot of effort is needed. Besides, one should be aware that sometimes, one might get false images if the tip is not correctly selected. Figure 4.3.6 shows two AFM images produced on the same Cr thin film sample. In case (a), a low-resolution (i.e. blunt) tip was used, showing cube-like grains, elongated in one direction. This is the false image because the dimension of the tip is larger than that of the roughness on the sample. Therefore, in this case, the tip is scanned by the sample roughness but not vice versa and the cube-like grains in the image reflect the shapes of the tip. The elongation direction is the scan direction. In contrast, in case (b), a high-resolution (i.e. sharp) tip was used, which results in a strikingly different image, which is closer to the real topology of the sample.

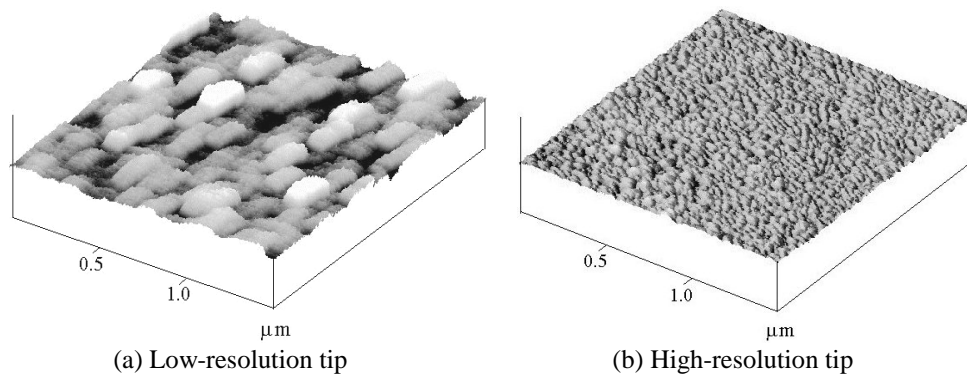


*Fig. 4.3.6. AFM images on the same Cr thin film sample by using (a) a low-resolution tip and (b) a high-resolution tip.*

#### 4.3.2.4. Comparison between AFM and TEM plane-view images

To determine the grain size of thin films, TEM plane-view image is preferably used, due to its accuracy. However, this method is rather complicated. AFM method is sometimes an alternative, which is much simpler. This method is based on the fact that the grains (or columns) of thin films appear on the surface as humps (see Fig. 4.3.7), which has been proven elsewhere [Honda-94]. By measuring the sizes of the humps, we can estimate the grain sizes of the sample. If we use an AFM to observe the surface of this sample (Fig. 4.3.7), the apparent image would look like the dashed curve as indicated in the figure. The hump size calculated from this image is certainly larger than the actual grain size. This is

because the tip has a certain dimension, which is added to the dimension of the hump as the tip scans. The problem is even more severe when the tip scans over small grains (like the grains 3 and 4) or bicrystal grains (like the grains 5 and 6). In the image, these two grains seem to merge together. Jones [Jones-99] has studied the grain size distributions in sputtered thin films obtain by TEM and by AFM and found that AFM gives an error of a factor of 2 in diameter, compared to TEM. We have tried the same experiments on CoCrTa thin films deposited on the  $\text{Si}_3\text{N}_4$  chips. A TEM plane-view image was taken on the film on  $\text{Si}_3\text{N}_4$  membrane inside the window whereas an AFM scan was carried out just outside the window (see Fig. 4.3.4). We found that the error could be from 2 to 3. Though, if we only need to compare grain sizes between several samples and a non-destructive method is required, AFM is the solution.

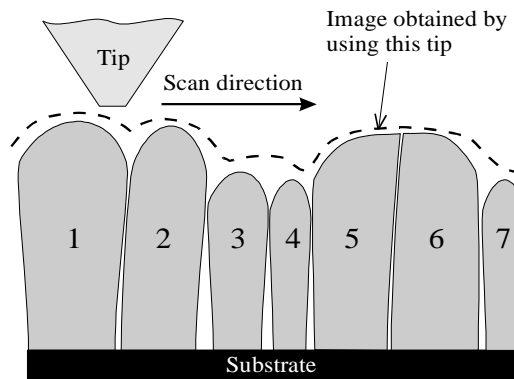


*Fig. 4.3.7. Diagram of a cross-section of a thin film in an AFM measurement. The roughness of the film is exaggerated. When the tip scans over the surface, it creates an image that shows hump sizes larger than the actual grain sizes.*

### 4.3.3. XRF

*X-Ray Fluorescence spectrometry (XRF)* is a nondestructive method for the elemental analysis of solids and liquids. It provides information about the composition, mass and mass-density of the sample. The sample is irradiated by an intense X-ray beam which causes the emission of fluorescent X-rays. The spectrum of emitted x-rays is detected using either an energy-dispersive or wavelength-dispersive detector. The elements in the sample are identified by the wavelengths of the emitted X-rays while the concentrations of the elements are determined by the intensity of those X-rays. XRF is a bulk analysis technique with the depth of sample analyzed varying from less than 1mm to 1cm depending on energy of the emitted X-ray and the sample composition. This technique therefore can be applied to thin films, provided that the spectrum of a bare substrate should

be subtracted from the total spectrum of the sample. The elements commonly detected range from sodium to uranium. To have accurate values of compositions, standard elements are needed for calibration. For elements without standards, only relative concentrations can be obtained, like the case of Ar, which will be discussed in Chapter 5.

#### 4.3.4. AES and depth profiling measurements

*Auger Electron Spectroscopy (AES)* is a popular technique for determining the composition of the top few layers of a surface. It is sensitive to all elements, except hydrogen and helium, but being most sensitive to the low atomic number elements.

A conducting sample is bombarded by electrons of energy 3-20keV. These electrons cause core electrons from atoms of the sample to be ejected, resulting in a photoelectron and an atom with a core hole. The atom then relaxes via electrons with a lower binding energy dropping into the core hole. The released energy can be converted into an X-ray or emit an Auger electron. The energy of the Auger electron is characteristic of the element that emitted it, and can thus be used to identify the element. AES technique has been described in detail in [Briant-88].

AES technique is used in combination with ion beam sputter-etching to measure the depth profile of composition of thin films. In this measurement, a thin film sample is gradually sputter-etched and measured alternatively. One cycle of a typical depth profile consists of sputtering a small increment in depth, stopping, measuring relevant portions of the Auger spectrum. Finally, the contents of the elements calculated from the Auger spectra are plotted versus the depth.

## 4.4. Conclusion

This chapter described several important experimental methods and techniques used in the thesis. In Section 4.1, we presented the sputtering system Leybold-Heraeus Z400. To sputter at elevated temperature, a substrate heater is used. Temperature behavior of the heater under different conditions and with different voltages has been investigated. We finally found a procedure to set the substrate temperature to a desired value without monitoring it *in-situ*. VSM and torque measurements have been discussed in Section 4.2. Torque analyses for in-plane and perpendicular samples have been given in detail. In the last part of the chapter, we introduced several methods for structural characterization. The most important and frequently used is the X-ray diffraction (XRD). There are three types of XRD measurements, namely high-angle, low-angle and rocking curve measurements. While the high-angle measurement reveals information about textures in thin films,

the rocking curve measurement evaluates the quality of each existing texture. Besides, film thickness cannot be determined precisely without using the low-angle measurements. Next, three methods of microscopy have been mentioned: SEM, TEM and AFM. Descriptions of sample preparation for TEM plane-view and cross-sectional images were given. It was found that to obtain a good and reliable AFM image, care must be taken when selecting a tip and when analyzing an image. Generally it has been found that grain size estimated by AFM images is considerably larger than TEM plane-view images, with a factor of 2 to 3. However, AFM can be used when one wants to compare relatively between samples. Finally we gave some brief definitions of the XRF and AES methods.

### 4.5. References

- [Briant-88] C. L. Briant and R. P. Messmer. "Auger electron spectroscopy. Treatise on materials science and technology". Vol. 30, Academic press, inc. (1988).
- [Burd-77] J. Burd, M. Huq and E. W. Lee. "Determination of magnetic anisotropy constants from torque curves". *J. Magn. Magn. Mat.* 5 (1977), 135.
- [Chapman-80] B. Chapman. "Glow discharge processes". John Wiley & Sons (1980).
- [Foner-59] S. Foner. "Versatile and sensitive Vibrating-Sample Magnetometer". *The review of scientific instruments*, 30 (1959), 548.
- [Foner-96] S. Foner. "The vibrating sample magnetometer: Experiences of a volunteer (invited)". *J. Appl. Phys.* 79(8) (1996), 4740.
- [Honda-94] N. Honda and K. Ouchi. "Low-temperature deposition of high-coercivity Cr-Cr films for perpendicular recording". *J. Appl. Phys.* 75(10) (1994), 5984.
- [Jones-99] G. R. Jones, M. Jackson and K O'Grady. "Determination of grain size distributions in thin films". *J. Magn. Magn. Mat.* 193 (1999), 75.
- [Reimer-97] L. Reimer. "Transmission electron microscopy - Physics of image formation and microanalysis". Springer series in optical sciences (1997), Vol. 36.
- [Wasa-92] K. Wasa and S. Hayakawa. "Handbook of sputter deposition technology: Principles, technology and applications". Noyes publications (1992).



# Chapter 5

---

## Experimental results of sputtered CoCrTa thin films

CoCrTa magnetic layer is the vital part of a recording medium. To prepare knowledge for further studies of recording media, a separate study of this layer is therefore necessary. Experimental results of single  $\text{Co}_{82}\text{Cr}_{13}\text{Ta}_5$  magnetic layers on Si substrates will be presented. Growing directly on Si substrates, CoCrTa thin films are expected to have c-axes perpendicular to the film plane. Therefore, the studies in this chapter seek for sputtering conditions that favor this texture. In order to control properties of the media, at first, the influences of sputtering conditions should be studied. In the first part of the chapter, we will deal with the influences of Ar pressure and substrate temperature on the magnetic and structural properties of CoCrTa thin films grown on Si substrate. From these results, optimum conditions to realize a good film can be obtained. The second part of the chapter will show an investigation into the variation of CoCrTa thin film properties with film thickness. In the last part of the chapter, we will present a study of the influence of the film composition. This study compares two series of films of different compositions, namely,  $\text{Co}_{86}\text{Cr}_{12}\text{Ta}_2$  and  $\text{Co}_{82}\text{Cr}_{13}\text{Ta}_5$ .

### 5.1. Influences of sputtering conditions

#### 5.1.1. Influence of Ar pressure at room temperature

The first parameter chosen for tuning is Ar pressure (PAr). The samples discussed in this section were produced at different PAr's from  $1.2 \times 10^{-2}$  to  $5.0 \times 10^{-2}$  mbar, RF voltage = 1.6kV and at room temperature. The voltage  $V_{rf}$  is fixed at 1.6kV because it has been found to be optimum for Co-alloy thin films produced by the same sputtering system (Leybold-Heraeus Z400) [Lodder-93].

## 5.1. Influences of sputtering conditions

When  $P_{Ar}$  changes, mean free path  $\lambda$  is changed, given by [Brunner-65, p. 7 and 162]:

$$\lambda(\text{cm}) = \frac{0.005}{0.75 \times P(\text{mbar})} \quad (5.1.1)$$

Figure 5.1.1 gives an impression of this relation. In our experiments,  $P_{Ar}$  was varied from 1.2 to  $5 \times 10^{-2}$  mbar (within the working range indicated in the plot), at which, the mean free path ranges from 0.56 to 0.13 cm. These values are about one order of magnitude smaller than the distance between the substrate and the target.

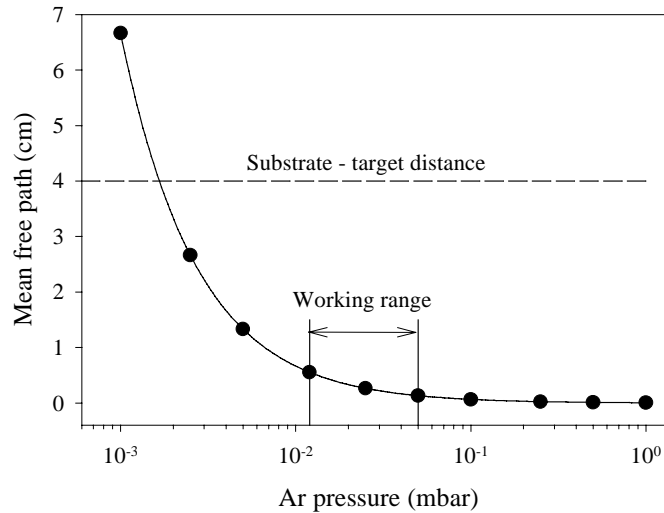


Fig. 5.1.1. Mean free path of Ar gas at different pressures. The variation of  $P_{Ar}$  in our experiments is within the working range. The distance between the substrate and the target is about one order of magnitude larger than the mean free path at the working range.

When  $P_{Ar}$  is varied, for instance it is decreased, the Ar ions, traveling to the target under the electric force between the target and the substrate, will cover longer distances before collisions. This results in higher kinetic energy of the ions, therefore higher kinetic energy of the sputtered atoms. Consequently, the film is better. However, at too low  $P_{Ar}$ , the mean free path is too large and number of ions per unit volume is so small that the number of collisions is not enough to sustain the plasma.

Our sputtering system does not allow to operate at  $P_{Ar}$  lower than  $1.2 \times 10^{-2}$  mbar since this value is very close to the critical  $P_{Ar}$ , below which the plasma is not stable. One should not, otherwise, increase  $P_{Ar}$  further than the upper bound of the working range ( $5 \times 10^{-2}$  mbar) because over this value, the plasma is observed to

change its color from purple to pink, which indicates that the energy of the bombarding particles is remarkably reduced. This situation will certainly result in bad films.

### 5.1.1.1. Deposition rate

Five test samples were prepared to measure the deposition rate at different Ar pressures. The thickness of the samples was measured by low angle XRD method (see Section 4.3.1) and the rate was obtained by dividing the thickness by the deposition time. A nearly linear dependence of deposition rate on PAr was found (Fig. 5.1.2.a). This dependence is caused by the linear dependence of Ar concentration on Ar pressure. Therefore, the cathode current, a measure of Ar ions taking part in the discharge, was found to be proportional to PAr (Fig. 5.1.2.b). Consequently, the deposition rate is also linearly dependent on the cathode current (Fig. 5.1.2.c).

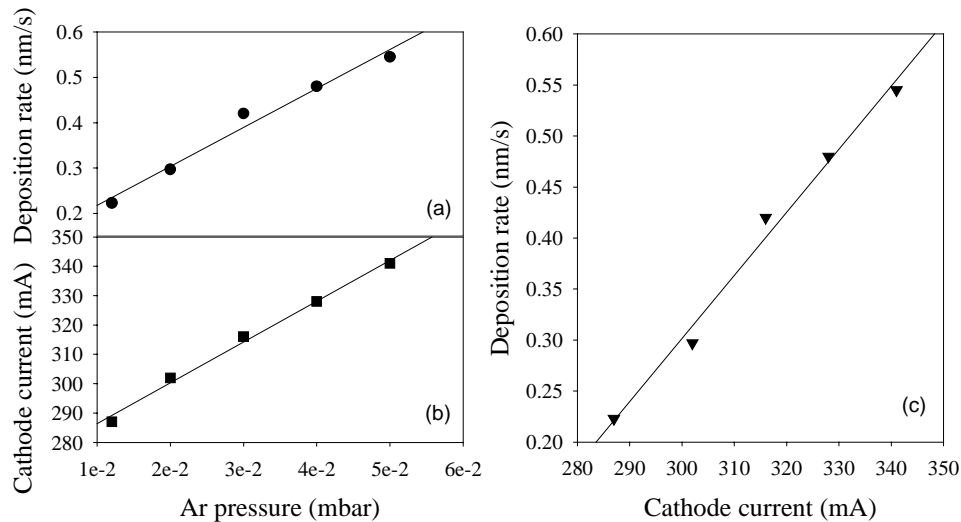


Fig. 5.1.2. Linear relations between the deposition rate, cathode current and Ar pressure.

### 5.1.1.2. Texture

Five samples of thickness of 200nm were prepared at different PAr's. Their names are indicated in Fig. 5.1.3. The deposition time of these samples was regulated according to the deposition rates found above in order to keep the film thickness constant. Figure 5.1.3 shows high-angle XRD spectra of the samples (see also Section 4.3.1 and Appendix). Generally, CoCrTa thin films grown directly on Si substrate are expected to have (0002) texture (c-axes perpendicular to the film plane). However, a small amount of other orientation can be found in some cases.

## 5.1. Influences of sputtering conditions

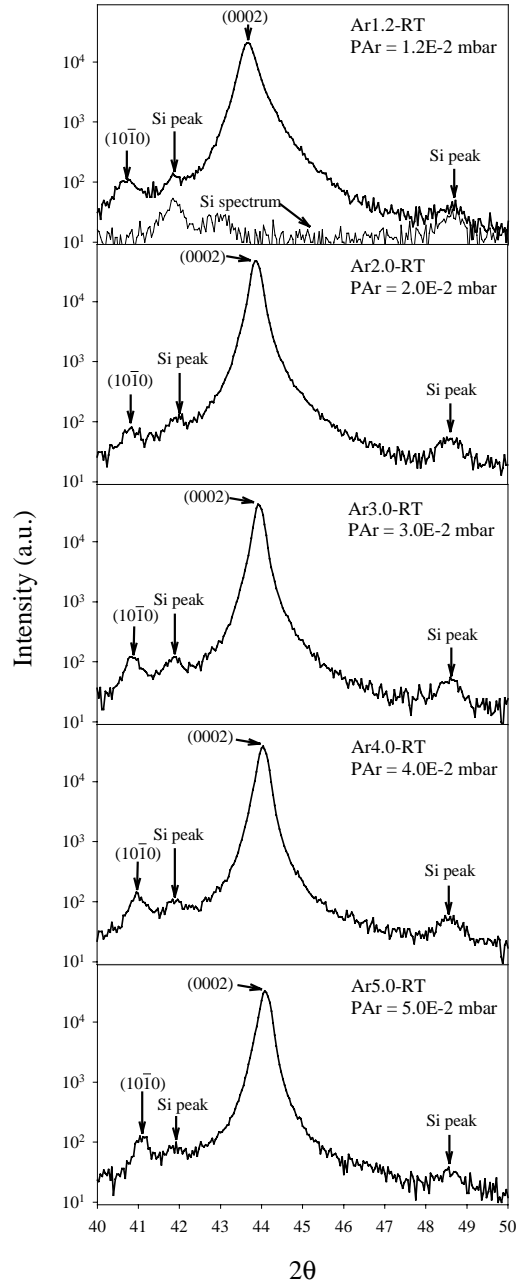


Fig. 5.1.3. XRD spectra of the CoCrTa films at various PAr's. The Si substrate contributes two peaks to the samples' displayed spectra.

In our investigated samples, two peaks were found, namely the  $(10\bar{1}0)$  peak (in-plane orientation) at about  $2\theta = 41^\circ$  and the  $(0002)$  peak at about  $44^\circ$ . The Si substrate contributes two other peaks to the spectra, which are ruled out from our consideration. The spectrum of the Si substrate is shown in the first graph of Fig. 5.1.3, for ease of comparison.

Figure 5.1.4 and 5.1.5 give close up views of the  $(0002)$  and  $(10\bar{1}0)$  peaks. Analysis of the  $(0002)$  peak intensities reveals that the  $(0002)$  texture is best oriented at  $PAr = 2.0 \times 10^{-2}$  mbar and becomes worse at lower and higher PAr (Fig. 5.1.4). On the other hand, the  $(10\bar{1}0)$  texture appears to be minimum at  $PAr = 2.0 \times 10^{-2}$  mbar (Fig. 5.1.5). The behavior of  $(10\bar{1}0)$  peak intensity is reverse to that of  $(0002)$  peak, meaning that when sputtered at  $PAr = 2 \times 10^{-2}$  mbar, the perpendicular  $(0002)$  texture is the strongest one, prevailing over other in-plane textures. In these two figures, we can also notice that the peak positions of the textures  $(0002)$  and  $(10\bar{1}0)$  tend to shift to higher angles with increasing PAr. This phenomenon will be discussed later in Section 5.1.1.4.

To have more precise information about the quality of the  $(0002)$  texture, rocking curves

## 5. Experimental results of sputtered CoCrTa thin films

measurements at the (0002) peak are required (see Section 4.3.1 for the description of the method). The values  $\Delta\theta_{50}$  of the rocking curves indicate orientation quality of the texture. The smaller the  $\Delta\theta_{50}$ , the better the texture is. Figure 5.1.6 shows the variation of  $\Delta\theta_{50}$  with PAr. As expected, the behavior of  $\Delta\theta_{50}$  is exactly reverse to that of the peak intensity shown in Fig. 5.1.4.b. This fact means that the measurements of rocking curves give consistent information with the XRD spectra. Now it can be surely concluded that the optimum PAr is  $2 \times 10^{-2}$  mbar, at which the CoCrTa films exhibit the best (0002) texture.

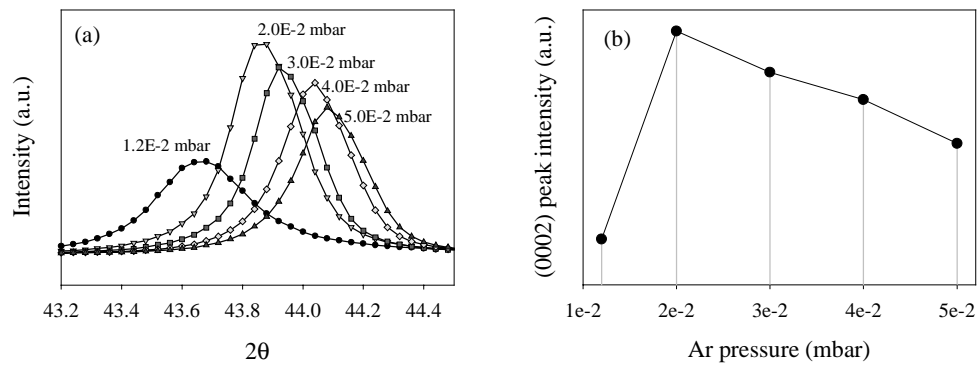


Fig. 5.1.4. (a): XRD spectra around the (0002) peak. (b): (0002) peak intensity at different PAr's.

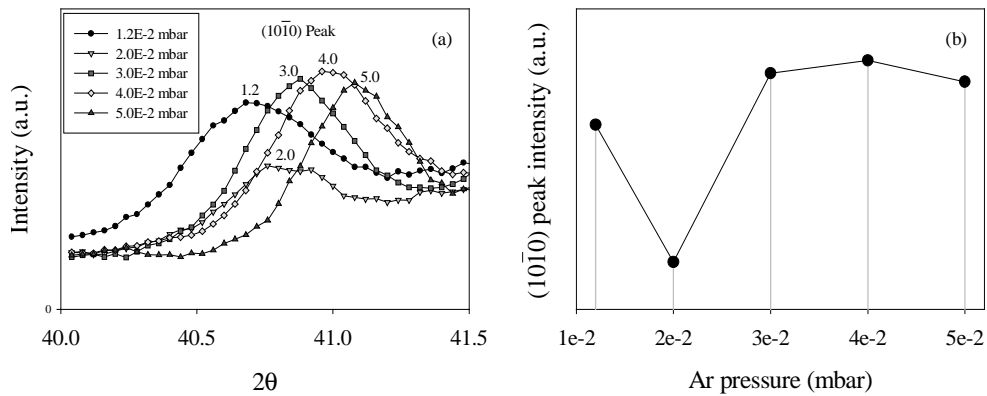


Fig. 5.1.5. (a): Smoothed XRD spectra around the (10 $\bar{1}$ 0) peak. (b): (10 $\bar{1}$ 0) peak intensity at different PAr's.

## 5.1. Influences of sputtering conditions

---

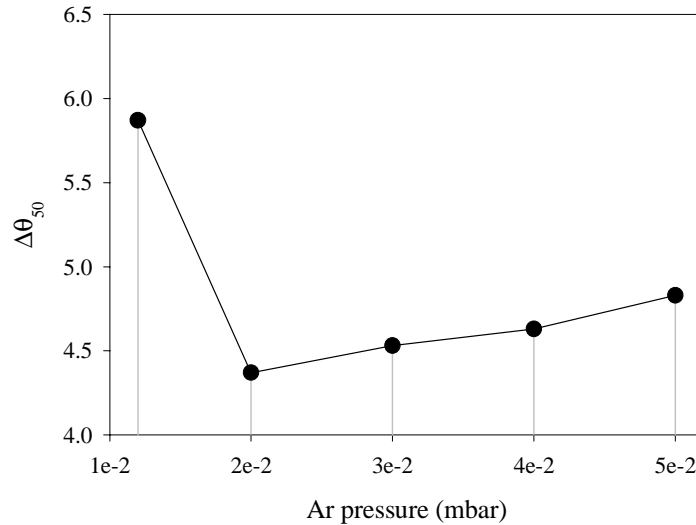


Fig. 5.1.6.  $\Delta\theta_{50}$  of the peak (0002) of the samples at different PAr's.

There are two possible opposite trends causing the existence of the optimum Ar pressure:

- On the one hand, when PAr increases, the mean free path is reduced, resulting in low kinetic energy of the particles. Consequently, the adatoms moving on the surface of the growing film have low mobility. This does not favor the attainment of equilibrium state of the islands, and thus leading to a worse oriented film.
- On the other hand, the worse orientation at low PAr could be attributed to the film defects caused by sputtered particles with too high energy [Feng-94].

### 5.1.1.3. Composition

In general, there is always a difference between composition of a sputter deposited alloy film and that of the target [Chapman-80, p.241], caused by the difference in sputter yields of the elements in the alloy. However, in most cases, the difference is not very much. The compositions of our samples have been examined by X-Ray Fluorescence (XRF) method (see Section 4.3.3). The results are shown in Table 5.1.1.

On average, the Ta content was found to deviate least from the target composition, whereas the Co content is always smaller and the Cr content is larger than that of the target composition. Figure 5.1.7 gives better illustration of the change in composition at different PAr's. In the figure, the contents of the elements are normalized on those of the target. It can be seen clearly that when PAr increases,

## 5. Experimental results of sputtered CoCrTa thin films

the Cr content increases, the Ta content decreases and the Co content is almost unchanged.

*Table 5.1.1. Compositions of films made from the  $Co_{82}Cr_{13}Ta_5$  target at different Ar pressures and at room temperature.*

Sample names	PAr (mbar)	Co (% at.) (±2%)	Cr (% at.) (±3%)	Ta (% at.) (±3%)
Ar1.2-RT	$1.2 \times 10^{-2}$	77.84	16.54	5.62
Ar2.0-RT	$2.0 \times 10^{-2}$	77.78	17.09	5.13
Ar3.0-RT	$3.0 \times 10^{-2}$	77.83	17.26	4.91
Ar4.0-RT	$4.0 \times 10^{-2}$	77.68	17.56	4.76
Ar5.0-RT	$5.0 \times 10^{-2}$	77.53	17.78	4.69

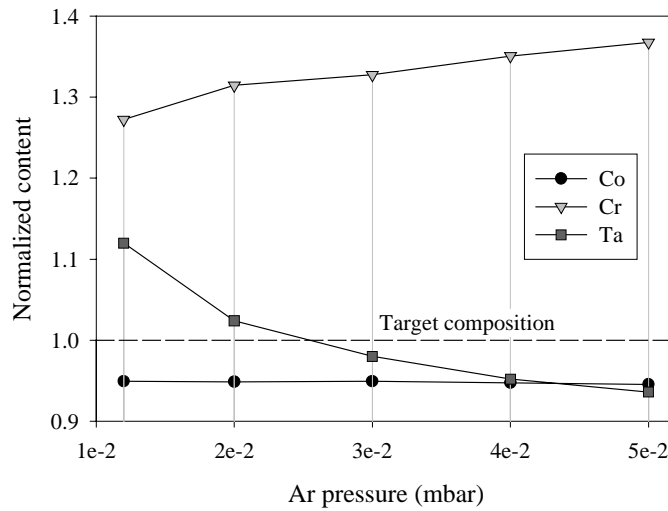


*Fig. 5.1.7. Variation of film composition with Ar pressure. The contents of the elements are normalized on those of the target  $Co_{82}Cr_{13}Ta_5$ .*

The change in sputtering yield of the three elements in different ways may account for this change in composition. This change in sputtering yield could be due to:

- a change in the energy of bombarding Ar ions with PAr. Sputter yield rises with increasing Ar ion energy [Wasa-92, p.56],
- a change in the incident angle of the bombarding Ar ions with PAr. Higher PAr means Ar ions suffer from more collisions and thus the average incident

## 5.1. Influences of sputtering conditions

---

angle\* increases. The sputter yield increases with increasing incident angle, exhibiting a maximum at about 60-80° [Wasa-92, p.57].

The combination of these two effects is very complicated and will not be fully investigated here.

We have also examined the content of Ar in the films. The XRF technique requires standard samples for all investigated elements. Because there was not such a standard sample for Ar, we could not determine the absolute content of Ar. The result shown in Fig. 5.1.8 is only relative. We found that the Ar content decreases as PAr increases. It has been estimated [Chapman-80, p.206] that at about  $2.6 \times 10^{-2}$  mbar, the Ar flux would be about  $10^4$  times greater than the arrival rate of the sputtered material. Therefore, it is not surprising if Ar is entrapped in the growing film. The entrapment of Ar is more sensitive to the small flux of high energy Ar ions (i.e. at low PAr) rather than large flux of low energy Ar ions (high PAr). This could account for the behavior of Ar content at different PAr's as observed. Our result is consistent with the work of Winters et al. [Winters-67], in which, it was found that the Ar content entrapped in sputtered Ni films decreases with increasing PAr.

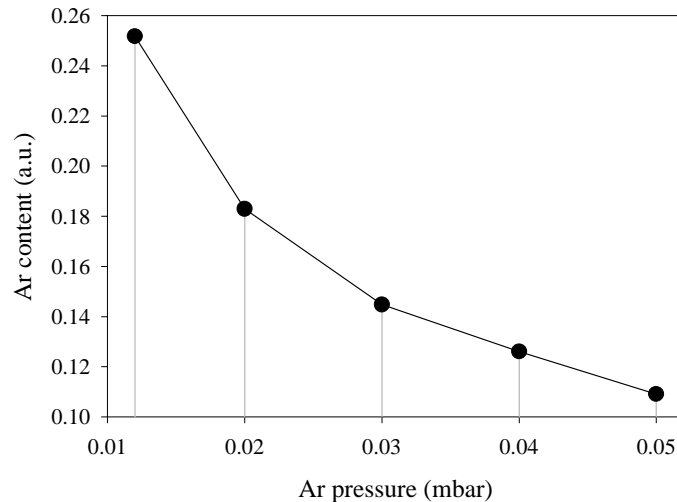


*Fig. 5.1.8. Relative Ar content versus Ar pressure*

---

\* Angle between the direction normal to the substrate and the direction of the incident atom.

#### 5.1.1.4. Lattice spacings

By XRD measurements, lattice spacings of two set of planes, namely the (0002) and (10 $\bar{1}$ 0), can be determined from the positions of the diffraction peaks (see Section 4.3.1 for the description of the method). In Fig. 5.1.4.a and 5.1.5.a, it can be clearly seen that with increasing PAr, the positions of the (0002) and (10 $\bar{1}$ 0) peaks shift to higher angles, indicating that the corresponding lattice spacings are reduced. Figure 5.1.9 plots the calculated spacings of these two sets of planes. Interestingly, both spacings of the (0002) and (10 $\bar{1}$ 0) set of planes tend to contract as PAr increases. The behaviors of both spacings versus PAr are almost similar. When PAr increases from  $1.2 \times 10^{-2}$  mbar to  $5.0 \times 10^{-2}$  mbar, the (0002) spacing contracts by 0.91% and the (10 $\bar{1}$ 0) spacing contracts by 0.88%.

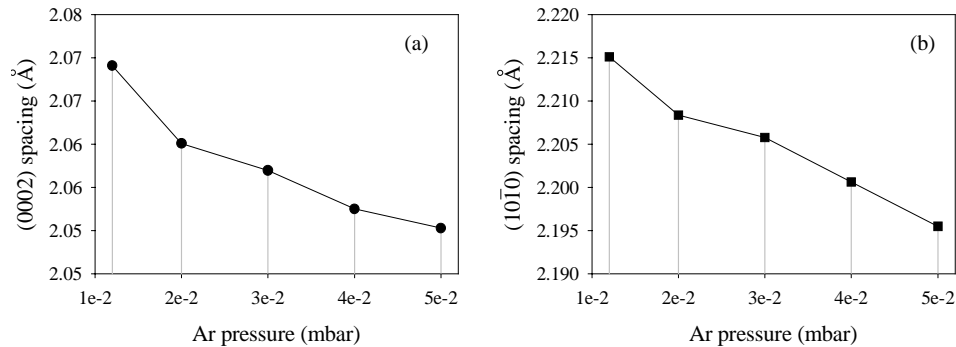


Fig. 5.1.9. Lattice spacings of (a) (0002) and (b) (10 $\bar{1}$ 0) sets of planes versus Ar pressure.

There are two possible reasons for the contraction of the spacings:

- First, because Ta has a larger atomic radius than Co or Cr\*, if Ta inserts into hcp lattice, the lattice spacings should be expanded [Hwang-93, Deng-93]. Therefore, the contraction of the (0002) and (10 $\bar{1}$ 0) spacings could be associated with the decrease in the Ta content when PAr increases as discussed above (Fig. 5.1.7). One may wonder that while the Ta content decreases, the Cr content otherwise increases, causing an opposite effect. To explain this, we have to consider the segregation of the elements (see Section 2.2). Cr is supposed to segregate. The change in Cr content does not mean that its solubility in Co matrix changes, thus it does not contribute to the change in lattice spacings [Hwang-93, Hwang-94]. Differently, because Ta does not

\* Empirical atomic radii of Ta is 1.45Å, of Co is 1.35Å and of Cr is 1.40Å [Winter-98].

## 5.1. Influences of sputtering conditions

segregate itself but stays homogeneously in the entire film, a change in the Ta content may cause the lattice spacings to change.

- Second, the contraction may also be attributed to the decrease in the Ar content when PAr increases (Fig. 5.1.8) or/and film stress. Deng et al. [Deng-93] worked out that if the entrapment of Ar has been subtracted, the increasing rate of (0002) spacing is  $10.26 \times 10^{-3} \text{ \AA}$  per 1at % of Ta. However, in our films, without knowing whether Ar plays any role in the contraction, we found that the rate is about  $20.6 \times 10^{-3} \text{ \AA}$  / 1at % of Ta. This value is about double that found by Deng, which could be contributed to the existence of Ar in films or film stress.

### 5.1.1.5. Magnetic properties

Coercivity  $H_c$  of the investigated samples is low, due to low substrate temperature. Both in-plane and perpendicular coercivities tend to increase with increasing PAr (Fig. 5.1.10). This increase in  $H_c$  is possibly due to the rise in temperature on the film surface with increasing Ar pressure. We have observed that when PAr is increased from about  $1 \times 10^{-2}$  mbar to  $5 \times 10^{-2}$  mbar, surface temperature could rise by about 20-30°C. Moreover, we will prove later that  $H_c$  of CoCrTa films is very sensitive to the substrate temperature.

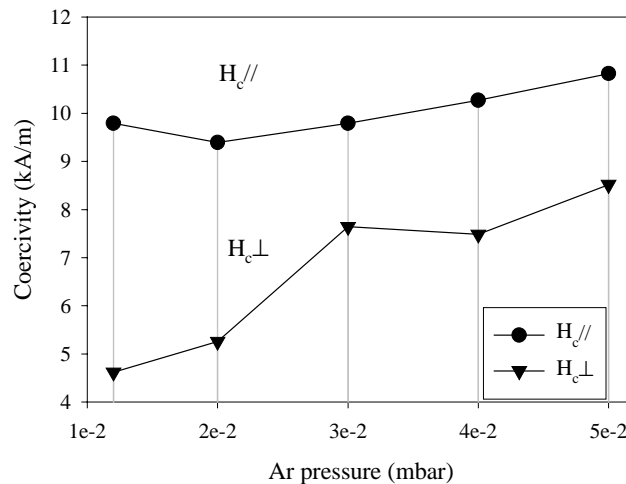


Fig. 5.1.10. In-plane and perpendicular coercivities as a function of Ar pressure.

Saturation magnetization  $M_s$  was generally found to decrease with increasing PAr (Fig. 5.1.11). In the XRF measurements (see Section 5.1.1.3), besides deriving the film composition, we could also determine the density of the films. The film density decreases with increasing PAr (Fig. 5.1.11). The behavior of  $M_s$  and that of the film density are almost identical, suggesting that the change in the film density

is the reason for the change in  $M_s$ . When PAr increases, the deposition rate increases (see Section 5.1.1.1), the films are more porous and thus leading to the decrease in density as seen in Fig. 5.1.11.

In spite of a considerable change in lattice spacings with PAr, as discussed in the previous section, we could not find any evidence for the correlation between this phenomenon and the magnetic properties.

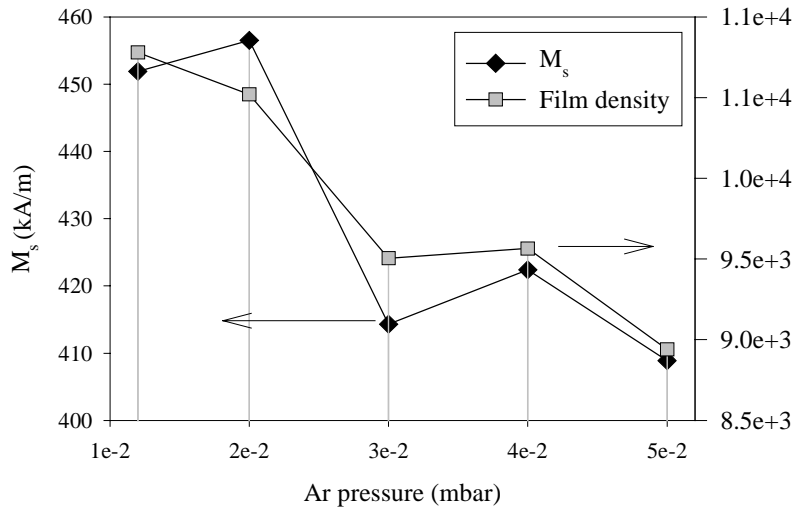


Fig. 5.1.11. Saturation magnetization and film density (derived from XRF measurements) as a function of PAr.

## 5.1.2. Influence of Ar pressure at high temperature

Five other samples were produced at substrate temperature  $T_s$  of 150°C at various Ar pressures, from  $1.5 \times 10^{-2}$  to  $5.0 \times 10^{-2}$  mbar. Names of the samples are PAr1.5-150, PAr2.0-150,..., PAr5.0-150.

### 5.1.2.1. Texture

X-ray diffraction measurements revealed that the (0002) is the only texture existing in the samples (see Fig. 5.1.12, in which only (0002) peaks are selected for plotting). Intensity of the (0002) peak is maximum at  $3.0 \times 10^{-2}$  mbar (Fig. 5.1.13.a). Note that in the previous series, at room temperature, the maximum appears at a lower value of  $2.0 \times 10^{-2}$  mbar. Rocking curves provide similar information: the half-width angle of these curves,  $\Delta\theta_{50}$  value, is the smallest at  $3.0 \times 10^{-2}$  mbar. There is a convenient way to judge the quality of crystallographic textures that is to plot the reverse value of  $\Delta\theta_{50}$ . Figure 5.1.13.b plots  $1/\Delta\theta_{50}$  as a

## 5.1. Influences of sputtering conditions

---

function of PAr. This curve has a similar shape as the (0002) peak intensity curve versus PAr, indicating that at  $3.0 \times 10^{-2}$  mbar and  $T_s = 150^\circ\text{C}$ , the (0002) texture of CoCrTa films has the best quality.

Similarly to the series produced at room temperature (the previous section), spacing of the (0002) set of planes tend to contract with increasing PAr (Fig. 5.1.13.c). The contraction is also thought to be due to the entrapment of Ar in the films and/or the decrease in Ta content, if we assume that the trend of composition change occurs at high  $T_s$  is similar to that at room temperature.

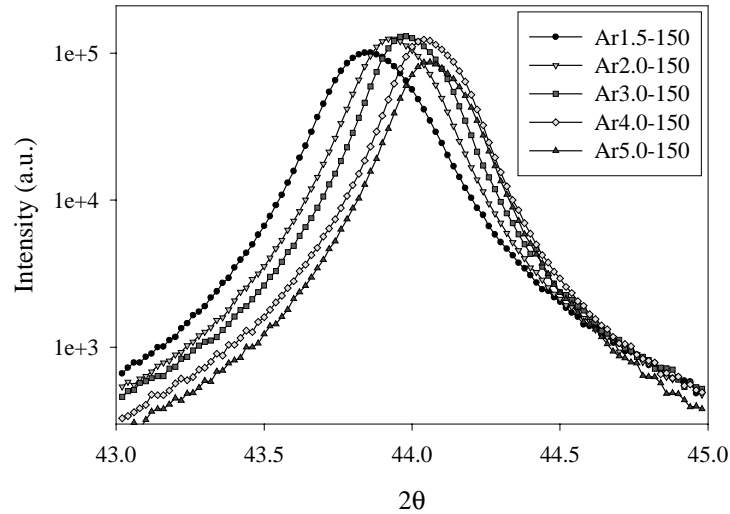


*Fig. 5.1.12. XRD spectra of the CoCrTa samples produced at  $150^\circ\text{C}$ , at various PAr's. The spectra are plotted around only the (0002) peaks.*

## 5. Experimental results of sputtered CoCrTa thin films

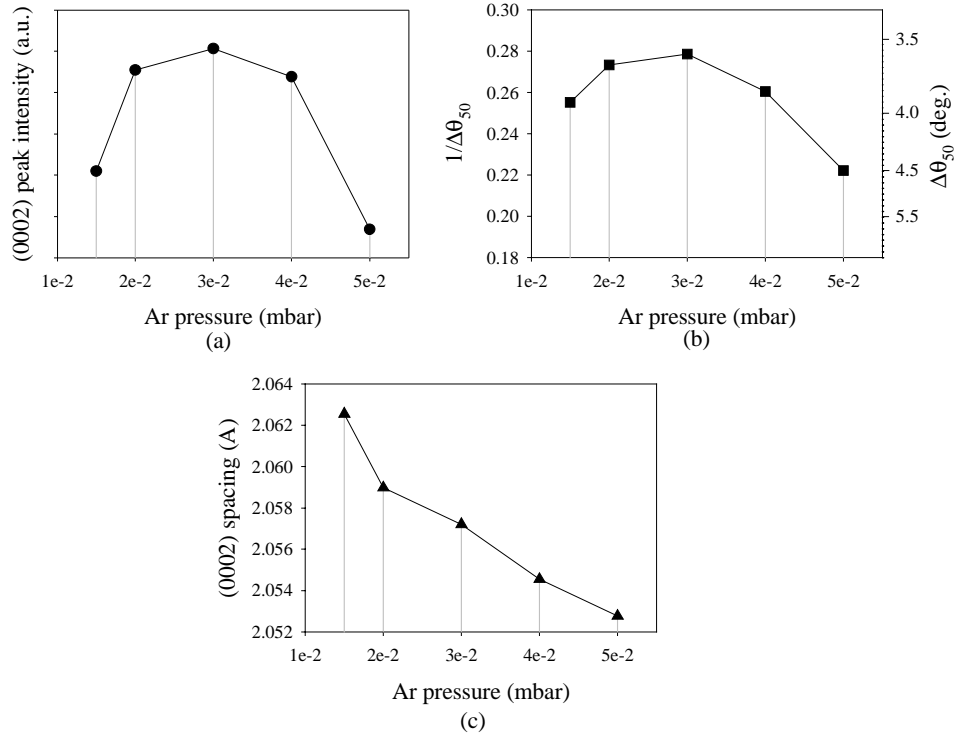


Fig. 5.1.13. (a) (0002) peak intensity. (b) reverse  $\Delta\theta_{50}$  value ( $1/\Delta\theta_{50}$ ) as functions of PAr. The right axis of (b) presents the corresponding values of  $\Delta\theta_{50}$ . (c) Spacing of (0002) crystallographic planes vs. PAr.

### 5.1.2.2. Coercivities

At high  $T_s$ , coercivities are higher than the case produced at RT. Perpendicular coercivity is substantially higher than in-plane coercivity at all PAr values. More extensive study of the influence of substrate temperature will be presented in the next section. Similarly to the RT case reported earlier, both perpendicular and in-plane coercivities increase slightly with increasing PAr (fig. 5.1.14). This is thought to be due to the increase in the temperature on the surface of the growing film when PAr increases.

## 5.1. Influences of sputtering conditions

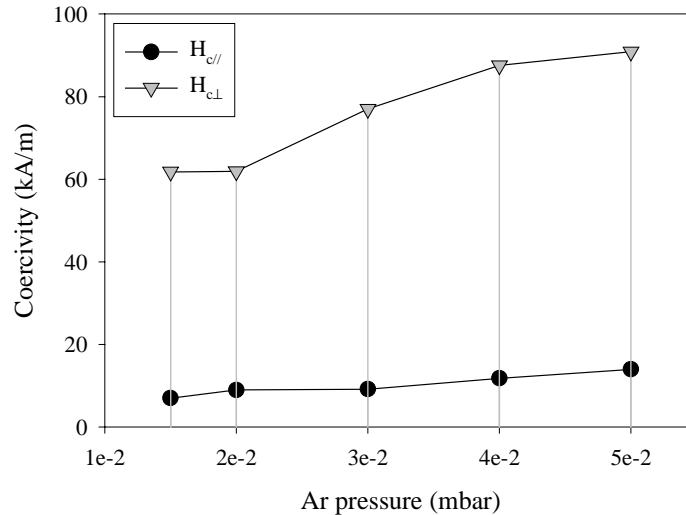


Fig. 5.1.14. Perpendicular and in-plane coercivities vs. PAr.

### 5.1.3. Influence of substrate temperature

Another series of samples were produced at fixed PAr= $2.0 \times 10^{-2}$  mbar,  $V_{rf} = 1.6$  kV. The varied parameter now is the substrate temperature,  $T_s$ , which was varied from room temperature (RT) to 250°C. The deposition rate was found unchanged at different  $T_s$ 's. Thicknesses of the samples were kept at 100nm. The sample names are Ts-RT, Ts-100, Ts-150, Ts-200 and Ts-250. The suffixes of the names indicate the substrate temperatures.

#### 5.1.3.1. Textures

Crystalline orientations of the samples were measured by XRD. Unfortunately, sample Ts-150 was lost; therefore, there is a missing point in the XRD measurements. In all spectra, only (0002) peaks appear. The (10 $\bar{1}$ 0) peak is almost invisible, suggesting that in this series, the (0002) texture is the only texture existing in the films. Intensity of the (0002) peak is given in Fig. 5.1.15.a. Rocking curves were also measured to verify the results of XRD spectra. Sample RT-250 appears to be polycrystalline. To avoid plotting an infinite value of  $\Delta\theta_{50}$  of this sample, we use again the reverse values of  $\Delta\theta_{50}$ ,  $1/\Delta\theta_{50}$  (Fig. 5.1.15.b). This quantity reflects directly the quality of the texture. From Fig. 5.1.15 we can conclude that at around  $T_s = 100$ -200°C, the (0002) texture is best oriented.

## 5. Experimental results of sputtered CoCrTa thin films

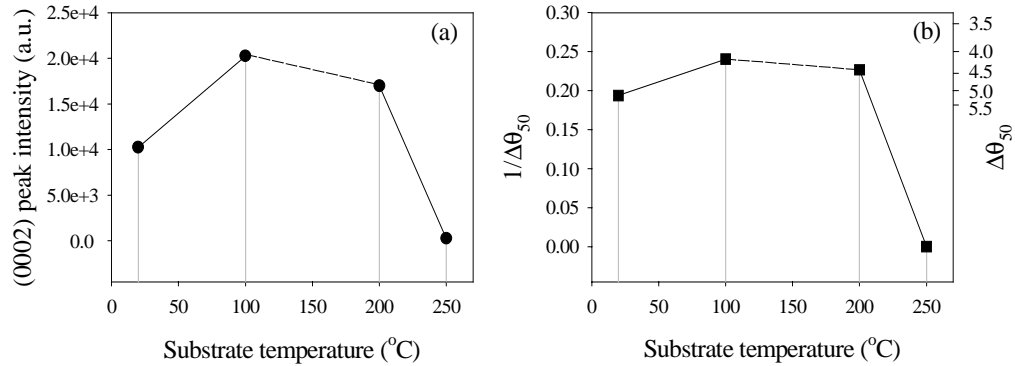


Fig. 5.1.15. (a) Intensity of (0002) peak and (b) corresponding  $1/\Delta\theta_{50}$  values of CoCrTa samples at different substrate temperatures. Corresponding  $\Delta\theta_{50}$  values are also given on the right axis of graph (b).

### 5.1.3.2. Roughness

Surface roughness of the samples was found to increase with increasing substrate temperature. Figure 5.1.16 shows SEM images of three samples as examples, namely, samples Ts-RT, Ts-150 and Ts-250. During the observation, the sample surface is tilted 45° with respect to the direction of the electron detector. The surface of sample Ts-RT is almost smooth, under the available resolution (Fig. 5.1.16.a). When  $T_s$  is higher, at 150°C, sample surface is rougher (Fig. 5.1.16.b). Sample Ts-250, produced at 250°C, appears to be the roughest (Fig. 5.1.16.c). The humps seen on the surface of sample Ts-250 seem to correspond to columnar structure of the sample.

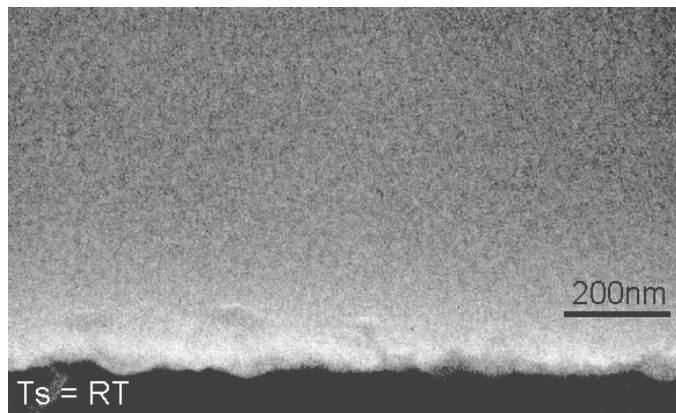
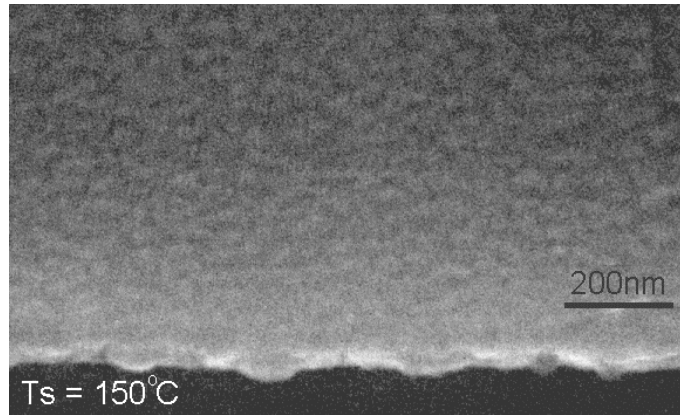


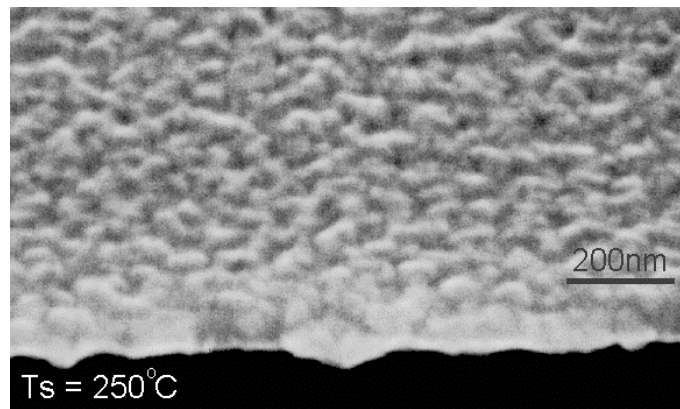
Fig. 5.1.16.a (see Caption on the next page)

## 5.1. Influences of sputtering conditions

---



(b)



(c)

*Fig. 5.1.16. SEM images of surface of samples (a) Ts-RT, (b) Ts-150 and (c) Ts-250. The sample surface is tilted 45° with respect to the direction of the electron detector. It is shown that the roughness increases with increasing  $T_s$ .*

### 5.1.3.3. Depth profile of composition

To investigate the influence of substrate temperature on the change in composition along the depth of the CoCrTa thin films, Auger Electron Spectroscopy method (AES) was utilized (see Section 4.3.4 for detailed description of the method). Figure 5.1.17 shows the results of the AES measurements of two samples: samples Ts-RT and Ts-250, being the two extreme cases of the series. There are three regions to be discussed:

## 5. Experimental results of sputtered CoCrTa thin films

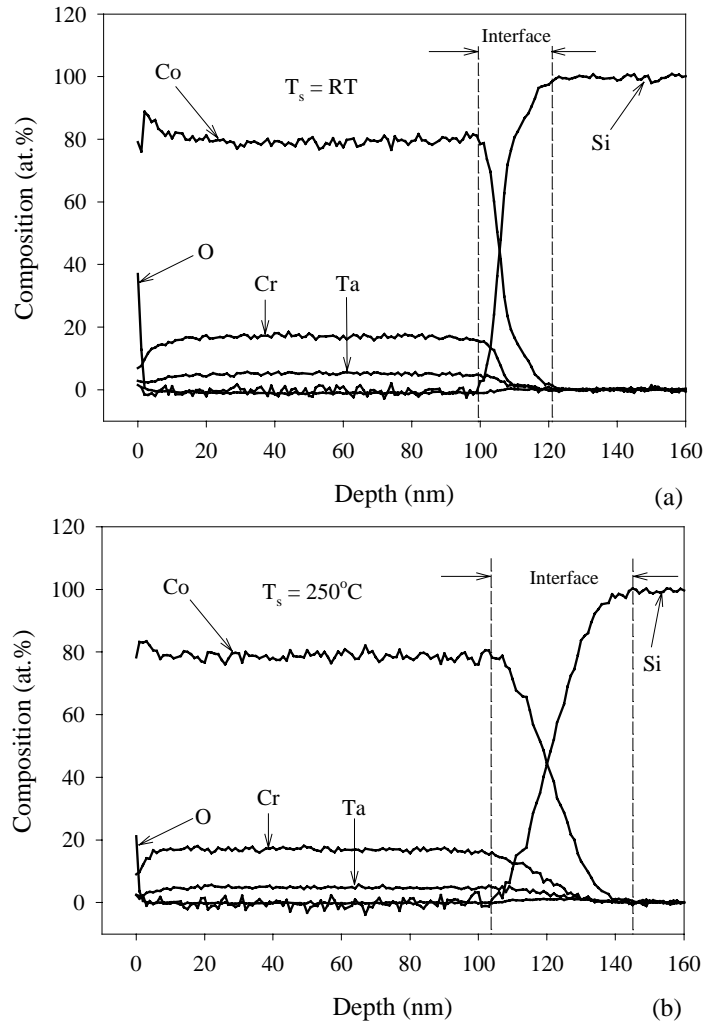


Fig. 5.1.17. Depth profile of composition of CoCrTa samples produced at RT and 250°C, measured by Auger Electron Spectroscopy. The depth of zero nm is corresponding to the film surface. The left part of the interface region is the film and the right part is the Si substrate.

- The region near the film surface: The profiles reveal that in both samples, oxidation occurs at the surface, within a depth of less than 10nm from the surface. Furthermore, to investigate the relation between the contents of each element in the alloy, we plot the ratio of Co content to Cr and Ta contents (Fig. 5.1.18) and found that this ratio increases significantly near the film surface. This indicates that Co tends to accumulate to the surface, probably in form of

## 5.1. Influences of sputtering conditions

Co oxide, whereas Cr and Ta become less. Masuda et al. [Masuda-91] has thoroughly studied the surface chemical state of sputtered CoCr films and found a high concentration of CoO at the surface, to a depth of about 5-10nm, which is consistent with our result. Besides, the authors found that below this CoO-rich region,  $\text{Cr}_2\text{O}_3$  enrichment occurs. According to them, the main reason is that the diffusion of Co cations into CoO is about 1000 times higher than that of Cr into  $\text{Cr}_2\text{O}_3$ . Therefore, after an initial oxidation of the first atom layers on the surface of both elements, the oxidation process is governed by the selective diffusion of Co to the surface and thus the CoO-rich region at the surface is formed.

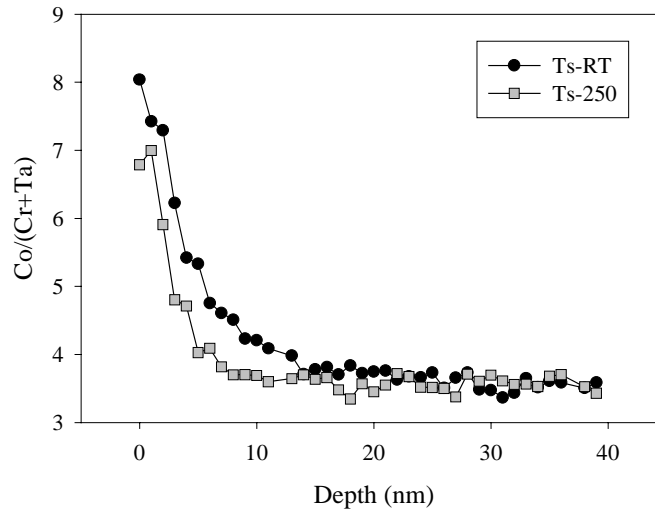


Fig. 5.1.18. Ratio of Co content to Cr and Ta contents near the film surfaces.

- The region at the interface between the film and the substrate: There is a clear diffusion of Co, Cr and Ta into the Si substrate. However, Si does not clearly diffuse into the film. Note that both films are about 100nm thick; the Si profiles do not extend into the region of depth less than 100nm, which is the region of CoCrTa film. The region marked "Interface" is the transition region between the film and the substrate, where the diffusion occurs. It can be clearly seen that the interface thickness increases with substrate temperature. It increases from about 20nm (in sample Ts-RT) to about 40nm (in sample Ts-250).
- The region in between the surface and the interface: The contents of all present elements are stable.

#### 5.1.3.4. Magnetic properties

Substrate temperature plays a significant role in the magnetic properties of CoCrTa thin films. We found that with increasing  $T_s$ , coercivities, especially perpendicular coercivity, drastically increase (Fig. 5.1.19). The perpendicular coercivity  $H_{c\perp}$  increases steadily from a few kA/m at RT up to 152 kA/m at 200°C and then is saturated. In a different way, the in-plane coercivity  $H_{c\parallel}$  does not increase until  $T_s$  exceeds 150°C. The increase and saturation of  $H_c$  in the direction of  $c$ -axes with increasing  $T_s$  is a well known phenomenon not only for perpendicular media but also for in-plane media [Howard-87, Nakagawa-89, Uchiyama-92, Honda-96, Duan-90]. In some papers [Howard-87, Nakagawa-89], only an increase in  $H_c$  with temperature up to about 200°C was reported, while in some other papers, the authors observed the saturation of  $H_c$  at above 200°C [Uchiyama-92] or even higher  $T_s$ , at 400°C [Honda-96]. The variation of the temperature at which  $H_c$  is saturated has been proven to depend on the Ar pressure during sputtering [Honda-96]. The difference in PAr used by different authors is the cause of the temperature difference mentioned above. Besides, this temperature is certainly dependent also on the composition and other sputtering conditions.

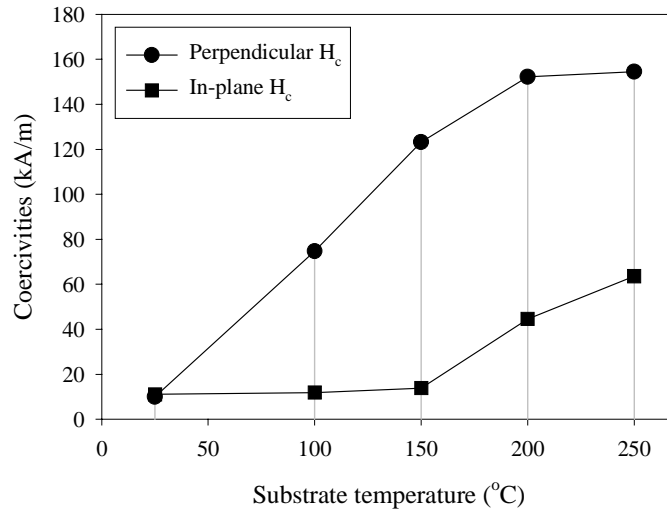


Fig. 5.1.19. Perpendicular and in-plane coercivities as a function of  $T_s$ .

At elevated temperature, thermal vibration of the substrate causes high mobility of adatoms, which favors surface diffusion. A bit differently from the low PAr case discussed in Section 5.1.1, high mobility in the high  $T_s$  case is sustained longer. As a consequence, segregation of Cr at grain boundaries is enhanced, which leads to a decrease in exchange coupling, expressed apparently by an increase in coercivities.

## 5.1. Influences of sputtering conditions

However, at  $T_s$  higher than  $150^\circ\text{C}$ , only  $H_{c\perp}$  is improved, because at this range of temperature, the perpendicular c-axis orientation has been proven to develop, which promotes the increase in  $H_{c\perp}$  while suppressing  $H_{c\parallel}$ .

The ratio of  $H_{c\perp}$  to  $H_{c\parallel}$  can be used as an evaluation of perpendicular anisotropy. This ratio is plotted together with the first anisotropy constant  $K_1$  and the (0002) peak intensity in Fig. 5.1.20. The behavior of  $H_{c\perp}/H_{c\parallel}$  matches exactly that of  $K_1$ , suggesting that this ratio indicates truly the magnetic anisotropy. It is also clear that the improvement of the perpendicular c-axis orientation is the cause of the increase in the ratio  $H_{c\perp}/H_{c\parallel}$ .

At the end of this section, it can be concluded that the substrate temperature of  $150^\circ\text{C}$  has been found to be the optimum temperature, at which crystalline orientation, anisotropy and perpendicular coercivity are the best.

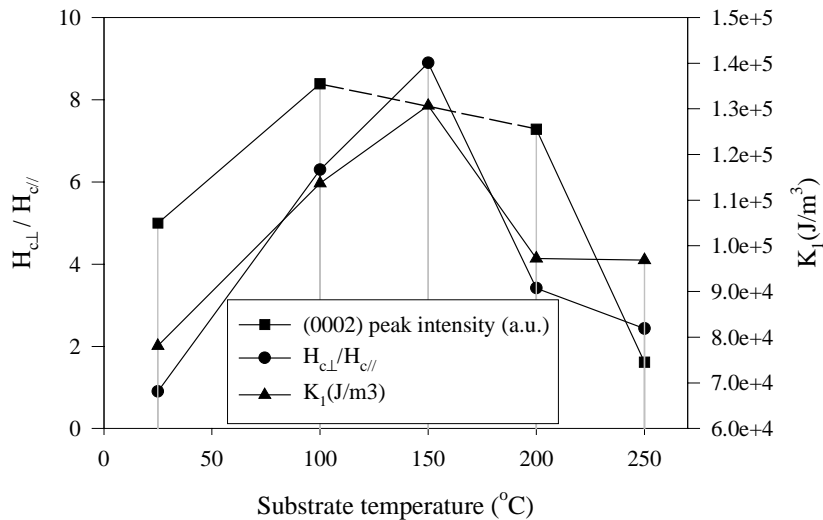


Fig. 5.1.20. (0002) peak intensity, ratio of  $H_{c\perp}$  to  $H_{c\parallel}$ , and the first anisotropy constant ( $K_1$ ) versus  $T_s$ .

## 5.2. CoCrTa thin films versus film thickness

### 5.2.1. Initial layer

Generally, Co-alloy thin films grown on a non-epitaxial substrate are not homogeneous along the film thickness. They normally have two sublayers [Wuori-84, Futamoto-85] (see Fig.5.2.1):

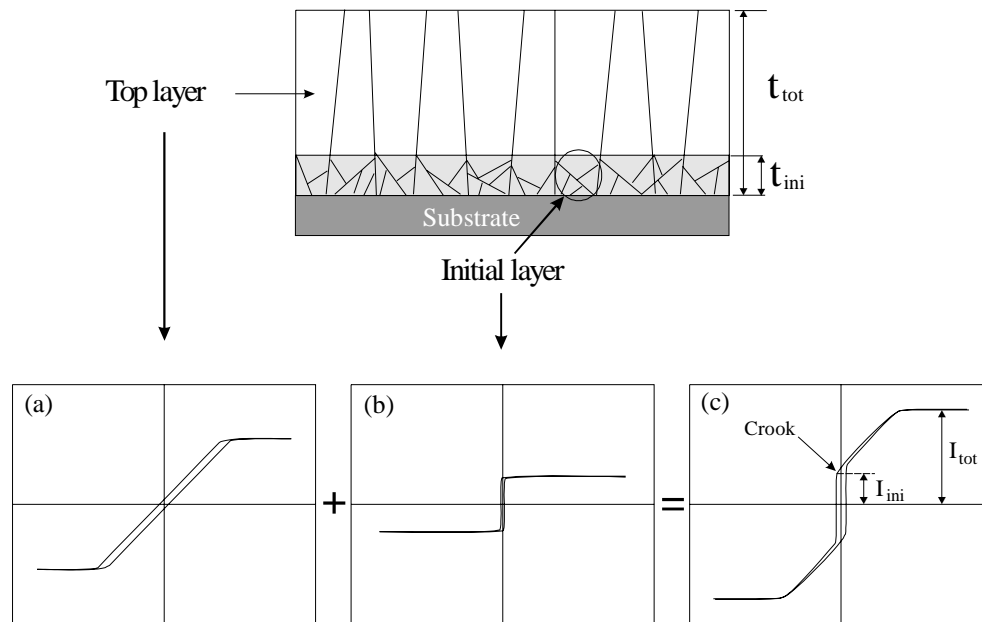


Fig. 5.2.1. Schematic cross-section of a Co-alloy thin film, consisting of an initial layer and a top layer. The thicknesses of the entire film and of the initial layer are denoted as  $t_{tot}$  and  $t_{ini}$ . Graph a is the in-plane hysteresis loop of the top layer, Graph b is the in-plane hysteresis loop of the initial layer, if they would be measured separately. Graph c is the resultant in-plane hysteresis loop of the entire film. The crook shown in the graph indicates the existence of the initial layer. The values of corresponding saturation magnetic moment of the entire film and of the initial layer are  $I_{tot}$  and  $I_{ini}$ , which can be determined from Graph c.

- 1- A top layer where the c-axes are well oriented perpendicular to the film plane. The anisotropy of this layer is expected to be perpendicular to the film plane; therefore, the in-plane hysteresis loop of this layer would be like Graph a (Fig. 5.2.1), if we could measure it separately.

## 5.2. CoCrTa thin films versus film thickness

2- An *initial layer*, closest to the substrate, where the c-axes are randomly distributed in-plane. The in-plane hysteresis loop of this layer would look like Graph b (Fig. 5.2.1), which indicates that the initial layer is a soft layer, switching by domain-wall motion with low coercivity and having in-plane anisotropy. In this initial layer, the film composition might be altered due to mutual diffusion of the film and the substrate. The thickness of this layer should be reduced to improve the quality of the Co-alloy film.

The resultant in-plane hysteresis loop of the entire film, which is the sum of the above two loops, has a shape like Graph c (Fig. 5.2.1). This is the curve that we can observe in reality by VSM measurements. The crook of this curve as indicated in Graph c is a typical feature of a Co-alloy film having an initial layer.

With experiments presented below, we investigated the relation between the thickness of the initial layer and the magnetization of the crook. Four samples were prepared under the same conditions ( $V_{rf} = 1.6\text{kV}$ ,  $P_{Ar} = 5 \times 10^{-2}$  mbar,  $T_s = \text{RT}$ ), but with varied deposition time to have films of different thicknesses, from 12 to 77nm. The in-plane hysteresis loops of these samples are shown in Fig. 5.2.2.

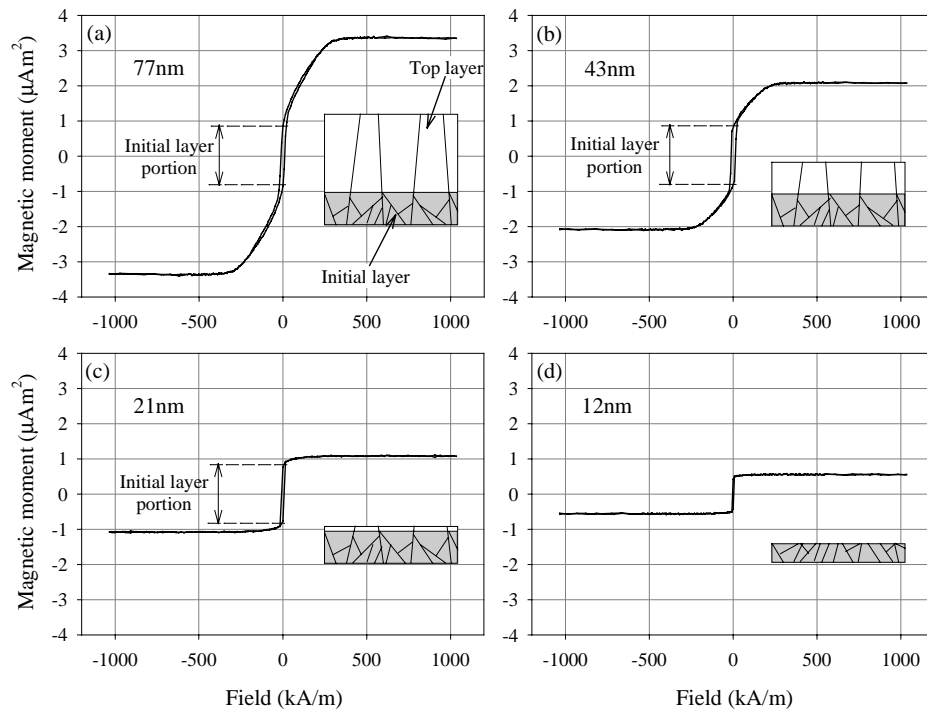


Fig. 5.2.2. In-plane hysteresis loops of CoCrTa samples of different thicknesses. The insets show schematic cross-sections of the corresponding films.

The difference in sputtering time of the samples is not much, about 1-2 minutes, therefore, the surface temperatures during deposition of the four samples can be considered the same. The 77-nm thick sample (Graph a) shows a typical hysteresis loop with a crook at  $I_{ini}$  of about  $0.9\mu\text{Am}^2$ . With decreasing the film thickness, the total magnetic moment,  $I_{tot}$ , of the film is reduced but the magnetic moment of the crook,  $I_{ini}$ , seems not to change (Graph b). This implies that the crook corresponds to the initial layer and by reducing the film thickness, only the top layer is reduced, but the initial layer thickness is unchanged (see the insets). When the film thickness is 21nm (Graph c), the thickness of the initial layer is almost reached. Its hysteresis loop looks almost like the loop in Fig. 5.2.1.b. The magnetic moment  $I_{ini}$  is slightly smaller than  $I_{tot}$ . When the layer thickness is further reduced, the top layer disappears (Graph d). The film thickness is now even thinner than the natural thickness of the initial layer that would be if the film grew thicker.

The samples in Graph c and d have lower coercivity than those in Graph a and b, suggesting that the initial layer has lower coercivity than the top layer.

Now it can be estimated that the initial layer of CoCrTa thin film deposited under the mentioned conditions has a thickness of about 20nm. This thickness is much thinner than that found by Futamoto et al. [Futamato-85], which is 100nm. The difference is thought to be due to the difference in deposition conditions and probably, substrate materials.

From the hysteresis loops (Fig. 5.2.2) we found that the saturation magnetization values ( $M_s$ ) of the top and the initial layers are not the same. Figure 5.2.3 plots  $M_s$  versus thickness of the samples, which shows clearly that  $M_s$  exhibits a maximum around 20nm, which is the thickness of the initial layer. This result is consistent with that of Uchiyama et al. on CoCr films [Uchiyama-92]. The authors also found that  $M_s$  peaks at the same thickness. According to them, the decrease in  $M_s$  in the region of less than 20nm might be due to the fact that the film is partly superparamagnetic. We suggest another possible reason that the thinnest film (12nm) is still not completely continuous, therefore it has low density, thus low  $M_s$ . When the film grows thicker, coalescence occurs and the film becomes more and more continuous, resulting in an increase in  $M_s$ . At a thickness of around the initial layer thickness (as the 21nm-thick sample), the density and  $M_s$  are highest. When the film is thicker than the initial layer, it becomes more porous again due to the formation of columns, with micro-voids in between, which consequently leads to a decrease in  $M_s$ . The above arguments have been proven by Lee et al. [Lee-87] who observed the formation of CoCr films at different thicknesses using TEM.

Sometimes, if we want to determine approximately the thickness of the initial layer from the in-plane hysteresis loop and  $t_{tot}$ , the following equation can be used:

## 5.2. CoCrTa thin films versus film thickness

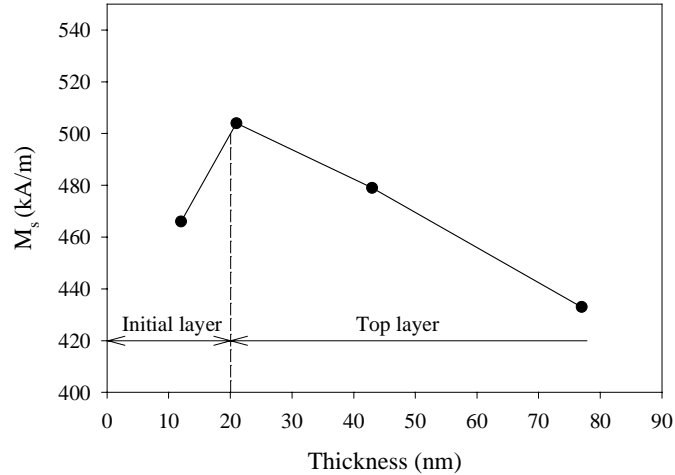


Fig. 5.2.3. Saturation magnetization of CoCrTa films versus thickness.

$$\frac{t_{\text{ini}}}{t_{\text{tot}}} = \frac{I_{\text{ini}}}{I_{\text{tot}}} \quad (5.2.1)$$

This equation is only true if  $M_s$  is constant along the film thickness. However, as shown above, it is not the case. The initial thickness calculated from Eq. (5.2.1) is overestimated, with an error of about 15%, due to the difference between  $M_s$  of the total film and that of the initial layer.

In some cases, to compare the initial thickness between samples produced under more or less the same conditions, it is more convenient to use the *relative initial thickness*,  $t_{\text{relative}} = t_{\text{ini}}/t_{\text{tot}}$ , which characterizes the quality of the c-axis orientation of the samples. Using  $t_{\text{relative}}$  allows us to avoid errors due to the difference in  $M_s$  of the samples.

### 5.2.2. Dependence of grain size on film thickness

When a CoCrTa film is growing, its grain size increases with thickness. Within the thickness range of interest, i.e. smaller than about 100-200nm, grain size was found to increase drastically with film thickness. We prepared two samples on  $\text{Si}_3\text{N}_4$  chips (see Section 4.3.2) under the same sputtering conditions, except that their thicknesses are different (20nm and 100nm). Plane-view images of the samples were taken using a TEM. The images are shown in Fig. 5.2.4. The contrast between the grains is the diffraction contrast, arising from the difference in orientation of the single crystallites. Clearly, grain size of the 100nm-thick sample

is much larger than that of the 20nm-thick one. We estimated that the grain size of the thin sample is about 5nm and of the thick one is about 23nm. The increase in grain size with film thickness is generally found in all kinds of thin films. In Chapter 6, we will show that this phenomenon also occurs in Cr thin films.

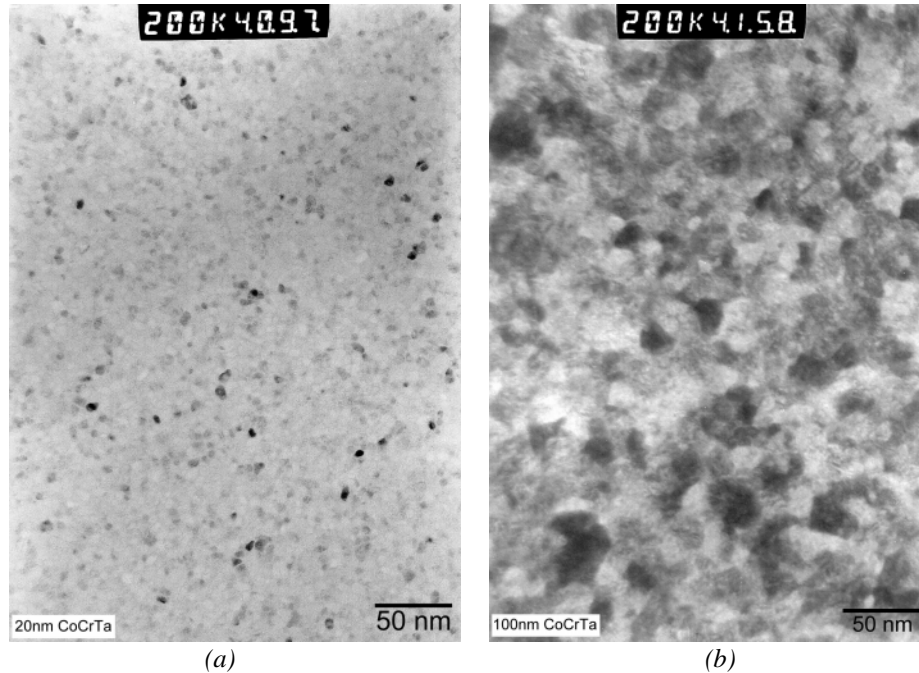


*Fig. 5.2.4. Bright-field plane-view images of (a) 20nm-thick and (b) 100nm-thick CoCrTa thin films. The images show that grain size of the 20nm-thick sample is about 5nm and of the 100nm-thick sample is about 23nm.*

## 5.3. Influences of alloy composition

### 5.3.1. The roles of Cr and Ta in the CoCrTa films

In sputtered Co-Cr-Ta magnetic thin films, the roles of Cr and Ta are reportedly different. In the olden days, only Cr was added to Co because besides increasing  $H_c$ , the composition CoCr has better c-axis orientation and higher anisotropy field than other Co-M alloys\* [Lodder-93]. Chromium, whose content is about 10 to 20

---

\* M = Rh, Pd, Mo, W, V, Ti, etc.

### 5.3. Influences of alloy composition

at.%, was observed to segregate at the grain boundaries and inside the grains [Maeda-85, 94]. This mechanism is often called the compositional separation (CS). The compositional separation is the main reason for the reduction of intergranular interaction, which causes the coercivity to increase (see Section 2.2 for more information).

Later, a third element has been added, such as Ta, Pt. Tantalum is commonly used today. By adding Ta into CoCr alloy, coercivity increases remarkably [Hwang-93]. Small addition of Ta (typically less than 5at.%) is more effective in raising  $H_c$  than further addition of Cr to Co alloy films [Hwang-93]. To date, the role of Ta in the ternary alloy CoCrTa has been investigated and interpreted [Tamai-88, Hwang-93 and Rogers-94]. It has been observed by Energy Dispersive X-ray Spectrometer (EDS) that Ta does not segregate but stays homogeneously in the grains [Nakai-94]. The role of Ta was thought to enhance the segregation of Cr due to the chemical affinity difference between the atoms [Hwang-93]. Therefore, the addition of Ta makes the coercivity to increase. However, too much Ta may result in worse magnetic properties [Tamai-88] (see Section 2.2 for more information).

#### 5.3.2. Experiments

In this section, we investigate the difference in properties between  $\text{Co}_{86}\text{Cr}_{12}\text{Ta}_2$  and  $\text{Co}_{82}\text{Cr}_{13}\text{Ta}_5$  thin film media (hereafter called CoCrTa<sub>2</sub> and CoCrTa<sub>5</sub>, respectively). The significant difference between these two compositions is the difference in Ta content. All samples were deposited on Si substrates, at different substrate temperatures,  $T_s$ . The Ar pressure was set at  $2.0 \times 10^{-2}$  mbar and the film thickness was 100nm for all samples. The names and other specifications of the samples are listed in Table 5.3.1.

Table 5.3.1. Names and other specifications of the samples.

Compositions	Names	$T_s$ (°C)	Compositions	Names	$T_s$ (°C)
$\text{Co}_{86}\text{Cr}_{12}\text{Ta}_2$	Ta2-RT	RT	$\text{Co}_{82}\text{Cr}_{13}\text{Ta}_5$	Ta5-RT	RT
	Ta2-100	100		Ta5-100	100
	Ta2-150	150		Ta5-150	150
	Ta2-200	200		Ta5-200	200
	Ta2-250	250		Ta5-250	250

In principle, the series Ta5 should be similar to the series presented in Section 5.1.3. However, due to some improvements of the sputtering system after the last series of samples, to have appropriate results of this section, we had to prepare again the series Ta5 in order to ensure the identity of the sputtering conditions between the samples of the series Ta2 and Ta5. We will later see that the results of

the series Ta5 produced in this section differ slightly from those of the series in Section 5.1.3. Nevertheless, this difference does not change the physical meaning of the research and therefore can be ignored.

### 5.3.3. Results and discussion

Varying  $T_s$ , we found that the perpendicular coercivity,  $H_{c\perp}$ , of both compositions increases fast when  $T_s$  is higher than  $100^\circ\text{C}$ , peaking at about  $200^\circ\text{C}$  (see Fig.5.3.1), before a slight decrease. Differently, the in-plane coercivity,  $H_{c\parallel}$ , does not change very much with  $T_s$ . The explanation for this behavior could be as follow: Increasing  $T_s$  causes higher mobility of adatoms, which stimulates the surface diffusion. Due to the compositional separation (CS) of Cr [Maeda-87], with the help of Ta, the exchange coupling decreases, which is expressed apparently by an increase in perpendicular coercivity. When  $T_s$  exceeds a certain value, about  $200^\circ\text{C}$  in our case, the perpendicular c-axis orientation becomes worse, leading to a decrease in  $H_c$ . It will be shown later that the expansion of the initial layer and the decrease in the (0002) XRD intensity at high  $T_s$  confirm this worsening of perpendicular c-axis orientation.

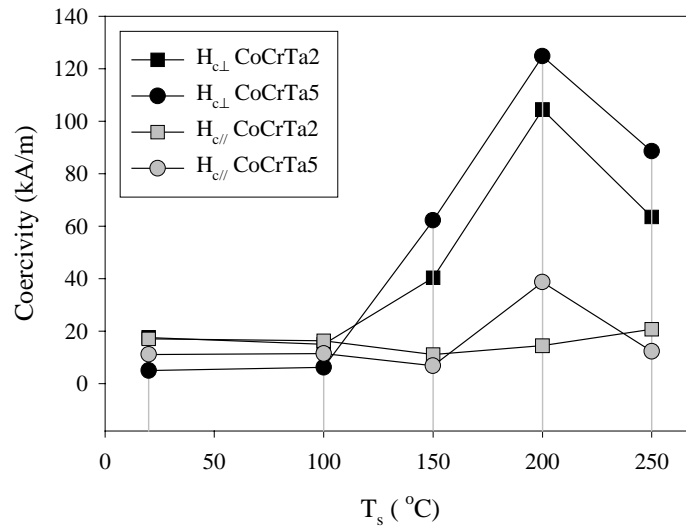


Fig. 5.3.1. Perpendicular and in-plane coercivities of samples of the two compositions at different  $T_s$ .

In spite of the same behaviors of  $H_c$  versus  $T_s$  of the series Ta2 and Ta5, there is a difference between their coercivities at each value of  $T_s$ . Figure 5.3.1 shows that  $H_c$  of samples Ta5 is mainly higher than that of samples Ta2 at  $T_s$  of above  $100^\circ\text{C}$ . This is undoubtedly caused by the difference in the compositions in which Ta is

### 5.3. Influences of alloy composition

thought to play the main role. Higher content of Ta in samples Ta5 may cause higher degree of CS, which therefore finally leads to higher coercivity, especially at elevated  $T_s$  [Maeda-87].

By the method described in Section 5.2.1, the relative initial thickness of the investigated samples was calculated. Figure 5.3.2 shows that  $t_{\text{relative}}$  of the two compositions decreases slightly as  $T_s$  increases from room temperature to about 150-200°C and then drastically increases at higher  $T_s$ . Minima of those curves indicate that the best perpendicular c-axis orientation is formed at  $T_s$  of about 150 to 200°C.

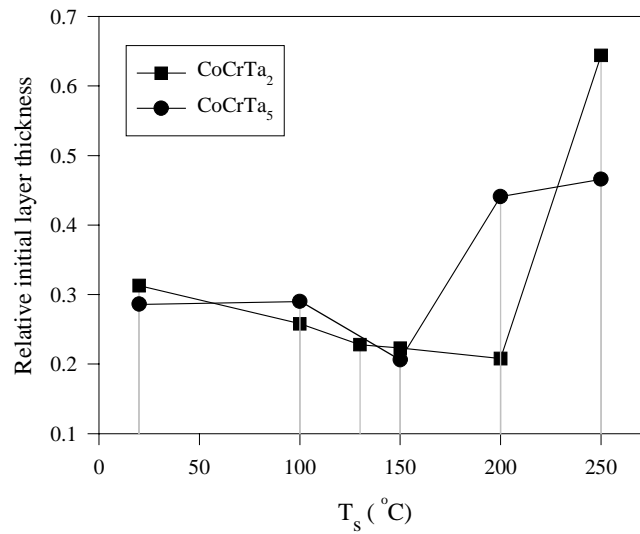


Fig. 5.3.2. Relative initial layer thicknesses of samples at different  $T_s$ 's. They exhibit minima at around 150-200 °C.

AFM images of the film surface were taken from the most four interesting samples: Ta2-RT, Ta5-RT, Ta2-200 and Ta5-200 (Fig. 5.3.3). Round caps of grains are seen clearly, based on which their sizes could be estimated. Note that grain sizes estimated by AFM images are generally larger than those obtained by TEM, which are the real sizes (see Section 4.3.2). Therefore, we can only compare relatively the grain sizes between the samples but any statement of an absolute value is not reliable. We have analyzed scan lines of the images to estimate the average grain sizes of the samples. When  $T_s$  increases from RT to 200°C, grain sizes of both compositions increase by about double. Grain sizes of samples Ta2 are slightly larger than those of samples Ta5 in both RT and 200°C cases. This could partly contribute to the higher coercivities of the series Ta5 than those of the series Ta2.

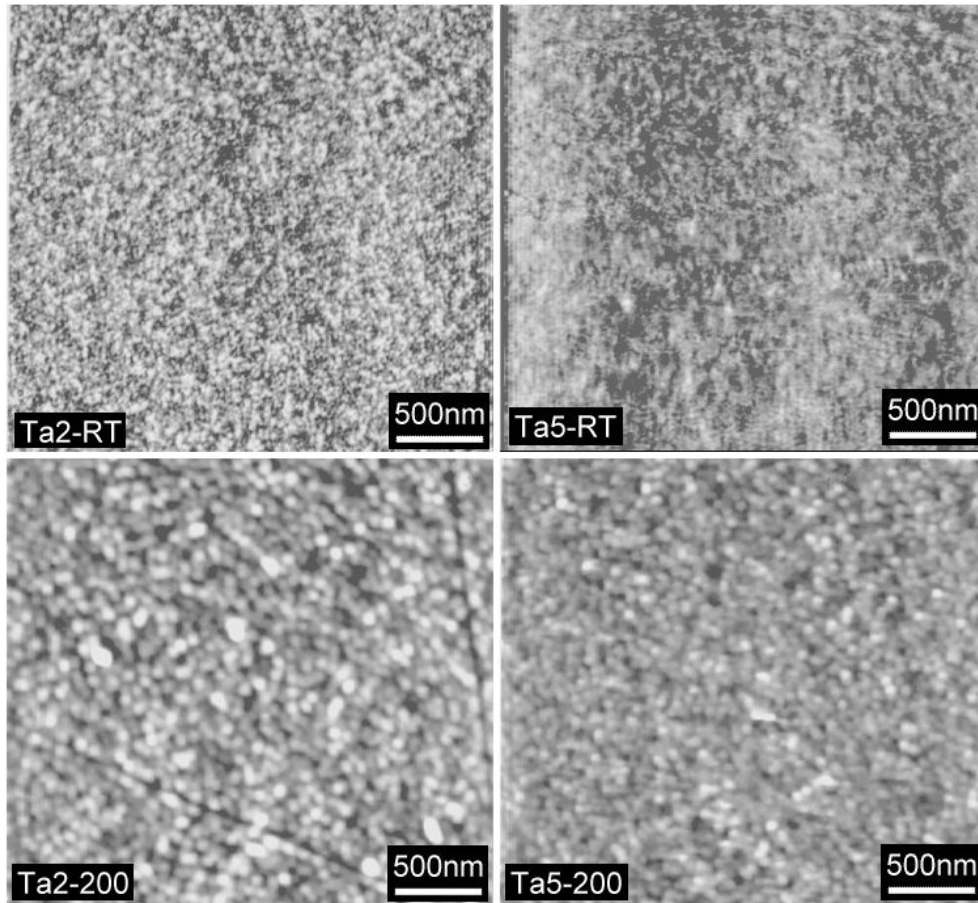


Fig. 5.3.3. AFM images of the surface of samples Ta2-RT, Ta5-RT, Ta2-200 and Ta5-200.

Crystalline orientation of the samples was examined by XRD. The XRD spectra show that only (0002) texture appears at all samples. Comparing the heights of these peaks one can see that the perpendicular c-axis orientation of the samples of both compositions seems to be the best at  $T_s$  of about 100°C to 150°C (Fig. 5.3.4). At  $T_s$  higher than about 150 to 200°C, the (0002) peak intensity of both compositions drops drastically. The behaviors of c-axis orientation versus  $T_s$  of the samples can be understood if we consider the role of the mobility of adatoms. Higher  $T_s$  and thus higher mobility of adatoms enables them to reach the equilibrium state more easily, at which the growing crystallites have the lowest potential energy. The crystallites are therefore in a better order, or in other words, they have better crystalline orientations. This argument accounts for the improvement of the (0002) texture which is the most favorable growth direction (Fig. 5.3.4) and the decrease in initial layer thickness (Fig. 5.3.2) with increasing

### 5.3. Influences of alloy composition

$T_s$  up to about 150°C. When  $T_s$  is further increased, the rate of defect formation increases, which hinders the growing crystals from being well crystallized [Glocker-86, Uchiyama-92]. Therefore, at excessively high  $T_s$ , the c-axis orientation becomes worse, resulting in the drop of the (0002) peak intensity of both samples at  $T_s$  higher than about 150 to 200°C (Fig. 5.3.4). The above argument also explains the expansion of the initial layer when  $T_s$  is higher than 200°C (Fig. 5.3.2).

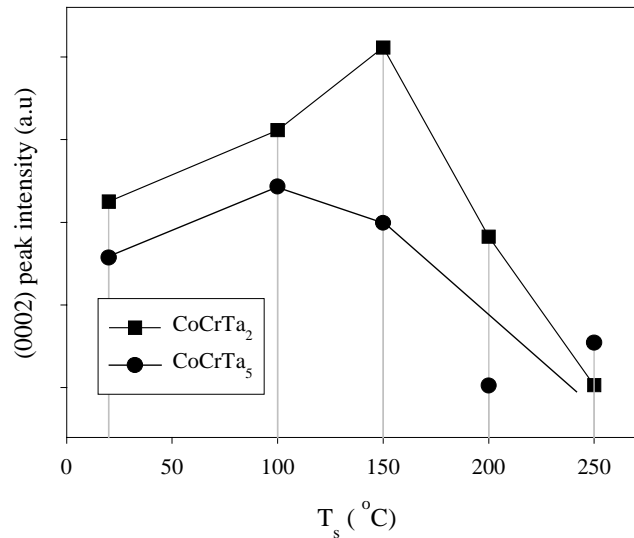


Fig. 5.3.4. Variation of (0002) peak intensity with  $T_s$ .

Comparing Fig. 5.3.4 to Fig. 5.3.1, we can notice that the temperature at which  $H_c$  of both composition peaks is 200°C, which is higher than the temperatures at which the maxima of (0002) peak intensity occur. This fact suggests that crystalline orientation is not the only factor governing  $H_c$ .

In addition, Fig. 5.3.4 reveals that Ta2 samples have better c-axis orientation than Ta5 samples. Additions of alien elements to a crystal always influence its orientation. In our case, these are the additions of Cr and Ta to the hcp Co crystal. In thin films made of Co-alloy material consisting of sufficiently small percentage of Cr and Ta, the hcp structure is still preserved. The better c-axis orientation of samples Ta2 compared to that of samples Ta5 could be attributed to the smaller amount of Ta and Cr in  $\text{Co}_{86}\text{Cr}_{12}\text{Ta}_2$  samples than that in  $\text{Co}_{82}\text{Cr}_{13}\text{Ta}_5$ .

From the above structural and magnetic studies, it could be concluded that generally,  $H_c$  of  $\text{CoCrTa}_5$  is higher than that of  $\text{CoCrTa}_2$ . Contrary to the behavior of  $H_c$ , c-axis orientation of  $\text{CoCrTa}_2$  films was found to be better than that of  $\text{CoCrTa}_5$  films. To get an optimum material, suitable for making magnetic

recording media, we suggest that Ta content should be in between 2 to 5 at.% to compromise the two contrary trends as mentioned above.

Besides the worsening of the crystalline orientation, the additions of Ta and Cr may expand the lattice spacings due to the strain caused by lattice inclusion. Lattice spacing calculations of the bulk samples (derived from the peak position of the XRD spectra of the target materials) show that (0002) spacing of the material having 18 at. % of Cr and Ta (in  $\text{CoCrTa}_5$ ) is larger than that of the material having 14 at. % of Cr and Ta (in  $\text{CoCrTa}_2$ ). These spacing values of bulk are marked as the lines "Bulk" in Fig. 5.3.5.

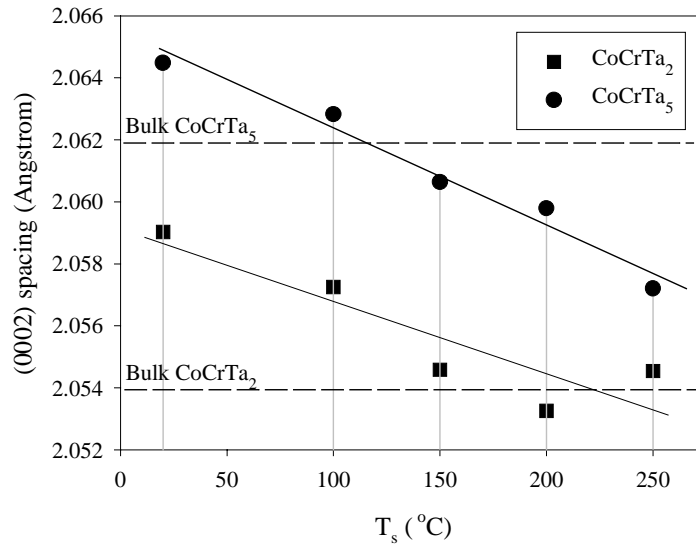


Fig. 5.3.5. Lattice spacing of (0002) set of planes as a function of  $T_s$  of Series Ta2 and Ta5.

Similarly to the bulk case, spacing values of Ta5 films are larger than those of Ta2 films at all temperatures (Fig. 5.3.5). The (0002) spacing of thin films of both compositions was found to decrease with increasing  $T_s$ . It is obvious that the peak (0002) comes from the hcp structure of the Co-rich regions in the film. When  $T_s$  is increased, as discussed above, CS between Co and Cr is enhanced. As a result, the Co-rich regions become richer and contain less Cr and Ta atoms, causing the average (0002) spacing measured on the whole sample to contract. This can account for the decrease in the (0002) spacing with increasing  $T_s$ . Another possible reason for this decrease is that when growing at high  $T_s$ , the lattice is more relaxed while being formed therefore the lattice strain and thus the lattice spacing is reduced.

## 5.4. Conclusion

In this chapter, we have shown the studies of the CoCrTa single layer thin films having *c*-axes perpendicular to the film plane, grown on Si substrate. One of the aims of the studies is to prepare knowledge for further studies of CoCrTa/Cr thin films, which will be presented in the next chapter.

In the first part of the chapter, the influences of sputtering conditions on properties of the CoCrTa thin films have been studied. Besides studying various properties, we sought for the conditions that support the (0002) texture growth. First of all, Ar pressure (PAr) was varied while other parameters were fixed. Substrate temperature was set at room temperature. We found that in all examined films at different PAr's, the (0002) texture is dominant. The sample produced at  $2 \times 10^{-2}$  mbar was found to have the strongest (0002) texture. Measurements of film compositions showed that when PAr increases, the Cr content increases, the Ta content decreases and the Co content is almost unchanged. Besides, we found that Ar atoms are entrapped inside the films and the Ar content decreases with increasing PAr. Concerning the crystallographic spacings, we observed that both (0002) and  $(10\bar{1}0)$  spacings contract when PAr increases, which is associated with the decrease in the Ta and Ar contents. Both in-plane and perpendicular coercivities increase slightly with PAr. Saturation magnetization decreases with increasing PAr, which is proven to be caused by the decrease in the film density. In the second series of samples, we varied Ar pressure while setting substrate temperature  $T_s$  at 150°C. We found that the optimum PAr in this case is about  $3 \times 10^{-2}$  mbar, instead of  $2 \times 10^{-2}$  mbar in the case at room temperature.

The second parameter to be tuned is the substrate temperature  $T_s$ . It was found that the optimum  $T_s$  to obtain good (0002) texture is about 150°C. Surface roughness increases with  $T_s$ . Depth profiles of the composition of the samples at RT and 250°C have been studied. From the profiles, we found that both samples are oxidized from the surface to the depth of about 5-10nm. Co seems to accumulate to the surface. The interface region between the film and the substrate, where Co, Cr and Ta diffuse into the Si substrate, extends as  $T_s$  increases. Regarding magnetic properties, we found that the perpendicular coercivity increases drastically with  $T_s$  and becomes saturated at  $T_s$  higher than 200°C. The ratio  $H_{c\perp}/H_{c\parallel}$  and the first anisotropy constant, characterizing the perpendicular anisotropy, are maximum at 150°C. From the studies in this section, it could be concluded that 150°C is the optimum substrate temperature.

The second part of the chapter presented some studies of the CoCrTa film of various thicknesses. By making several films of different thicknesses and

comparing the in-plane hysteresis loops, we estimated that the initial layer in our films has a thickness of about 20nm. From two plane-view TEM images we found that the grain size increases with increasing film thickness.

In the last part of the chapter, we dealt with the influences of CoCrTa alloy composition on the properties of CoCrTa film. Magnetic and structural properties of perpendicular media samples made of two different compositions ( $\text{Co}_{86}\text{Cr}_{12}\text{Ta}_2$  and  $\text{Co}_{82}\text{Cr}_{13}\text{Ta}_5$ ) deposited on Si substrates and at different substrate temperatures from room temperature to 250°C have been studied and interpreted. It was found that perpendicular  $H_c$  of the two compositions reaches maximum at  $T_s$  of about 200°C. Generally,  $H_c$  of  $\text{CoCrTa}_5$  is higher than that of  $\text{CoCrTa}_2$ . Contrary to the behavior of  $H_c$ , c-axis orientation of  $\text{CoCrTa}_2$  samples was found to be better than that of  $\text{CoCrTa}_5$  samples. C-axis orientation was observed to be the best at  $T_s$  of about 100°C to 150°C. When  $T_s$  increases, (0002) spacing of the samples contracts. Moreover, (0002) spacing of the  $\text{CoCrTa}_5$  samples is always larger than that of  $\text{CoCrTa}_2$  samples. To get an optimum material, suitable for making magnetic recording media, we suggest that Ta content should be in between 2 and 5 at.% to compromise the two contrary trends as mentioned above and  $T_s$  should be about 150 to 200°C.

## 5.5. References

- [Brunner-65] W. F. Brunner and T. H. Batzer. "Practical vacuum techniques". New York: Reinhold Pub. Corp. (1965).
- [Chapman-80] B. Chapman. "Glow discharge processes: sputtering and plasma etching". A Wiley-interscience publication - John Wiley & Sons (1980).
- [Deng-92] Y. Deng, D. N. Lamberth and D. E. Laughlin. "The effects of substrate and bias on CoNiCr/Cr thin films". IEEE Trans. Magn. 28 (1992), 3096.
- [Deng-93] Y. Deng, D. N. Lamberth and D. E. Laughlin. "Structural characteristics of bias sputtered CoCrTa/Cr films". IEEE Trans. Magn. 29 (1993), 3676.
- [Deng-93] Y. Deng, D. N. Lamberth, X. Sui, L. L. Lee and D. E. Laughlin. "Substrate bias effects on composition and coercivity of CoCrTa/Cr thin films on canasite and glass". J. Appl. Phys. 73(10) (1993), 5557.
- [Duan-89] S. L. Duan, J. O. Artman, J. W. Lee, B. Wong and D. E. Laughlin. "Effect of sputtering conditions, annealing and the microstructure of Cr underlayer on the magnetic properties of CoNiCr/Cr thin films". IEEE Trans. Magn. 25 (1989), 3884.
- [Duan-90] S. L. Duan, J. O. Artman, B. Wong and D. E. Laughlin. "The dependence of the microstructure and magnetic properties of CoNiCr/Cr

## 5.5. References

---

- thin films on the substrate temperature". IEEE Trans. Magn. 26 (1990), 1587.
- [Feng-94] Y. C. Feng, D. E. Laughlin and D. N. Lamberth. "Formation of crystallographic texture in RF sputter-deposited Cr thin films". J. Appl. Phys. 76(11) (1994), 7311.
- [Futamoto-85] M. Futamoto, Y. Honda, H. Kakibayashi, T. Shimotsu and Y. Uesaka. "Microstructure of CoCr thin films prepared by sputtering". Jap. J. Appl. Phys. 24 (1985), L460.
- [Glocker-86] D. A. Glocker, W. E. Yetter and J. S. Gau. "The role of atomic mobility during film growth in the structural and magnetic properties of CoCr". IEEE Trans. Magn. MAG-22 (1986), 331.
- [Honda-96] N. Honda, S. Yanase, K. Ouchi and S. Iwasaki. "High recording performance of Co-Cr medium sputter-deposited at high Ar pressure and high substrate temperature". J. Appl. Phys. 79(8) (1996), 5362.
- [Howard-87] J. K. Howard, R. Ahlert and G. Lim. "Effect of polycrystalline sublayer films on the magnetic and structural properties of CoCr films". J. Appl. Phys. 61(8) (1987), 3834.
- [Hwang-93] C. H. Hwang, Y. S. Park, P. W. Jang and T. D. Lee. "Magnetic properties and structures of CoCrTa films for wide range of Cr variation". IEEE Trans. Magn. 29 (1993), 3733.
- [Hwang-94] C. H. Hwang, T. D. Lee, K. H. Shin and Y. S. Park. "A study of redistribution phenomenon of solute atoms in CoCrTa and CoCr perpendicular recording films by annealing". J. Magn. Soc. of Japan 18 (Supp. No. S1) (1994), 83.
- [Lee-87] J. W. Lee, B. G. Demczyk, K. R. Mountfield and D. E. Laughlin. "Microstructural development in Co-Cr films for perpendicular recording media". IEEE Trans. Magn. MAG-23 (1987), 2455.
- [Lodder-93] J. C. Lodder. "Chapter 6: Preparation, microstructure, and magnetic properties of Co-Cr thin films". High density digital recording, Nato ASI Series E: Applied Sciences, Vol. 229 (1993), 161.
- [Maeda-85] Y. Maeda, S. Hirono and M. Asahi. "TEM observation of microstructure in sputtered Co-Cr film". Jap. J. Appl. Phys. 24, No. 12 (1985), L951.
- [Maeda-87] Y. Maeda and M. Asahi. "Segregation in sputtered Co-Cr films". IEEE Trans. Magn. MAG-23 (1987), 2061.
- [Maeda-94] Y. Maeda, K. Takei and D. Rogers. "Compositional microstructures in Co-Cr films for magnetic recording". J. Magn. Magn. Mat. 134 (1994), 315.
- [Masuda-91] T. Masuda, W. J. M. A Geerts and J. C. Lodder. "Surface chemical state

## 5. Experimental results of sputtered CoCrTa thin films

---

- of sputtered Co-Cr films". *J. Magn. Magn. Mat.* 95 (1991), 123.
- [Nakagawa-89] S. Nakagawa, J. Park and M. Naoe. "Columnless structure of Co-Cr thin film deposited at ultra-low Ar gas pressure on high temperature substrate". *J. Magn. Soc. of Japan* 13 (Supp. No. S1) (1989), 639.
- [Nakai-94] J. Nakai, E. Kusumoto, Kuwabara, T. Miyamoto, M. R. Visokay, K. Yoshikawa and K. Itayama. "Relation between microstructure of grain boundary and the intergranular exchange in CoCrTa thin film for longitudinal recording media". *IEEE Trans. Magn.* 30 (1994), 3969.
- [Rogers-94] D. J. Rogers, Y. Maeda, K. Takei, Y. Shen and D. E. Laughlin. "Investigations of compositional separation in Co-Cr-Ta/Cr thin film recording media". *J. Magn. Magn. Mat.* 135 (1994), 82.
- [Tamai-88] H. Tamai, K. Tagami and H. Hayashida. "Ta additive effect on RF magnetron sputtered CoCr films". *IEEE Trans. Magn.* 24 (1988), 2347.
- [Uchiyama-92] Y. Uchiyama, H. Sato and Y. Kitamoto. "Effect of substrate temperature on magnetic and microstructural properties of sputtered Co-Cr films with perpendicular magnetic anisotropy". *IEEE Trans. Magn.* 28 (1992), 2010.
- [Wasa-92] K. Wasa and S. Hayakawa. "Handbook of sputter deposition technology: principles, technology and applications". Noyes Pub. (1992).
- [Winter-98] M. Winter. "WebElements". University of Sheffield, England (Copyright 1993 - 1998). Website: [www.shef.ac.uk/chemistry/web-elements/](http://www.shef.ac.uk/chemistry/web-elements/)
- [Winters-67] H. F. Winters and E. Kay. "Gas incorporation into sputtered films". *J. Appl. Phys.* 38(10) (1967), 3928.
- [Wuori-84] E. R. Wuori and J. H. Judy. "Initial layer effects in Co-Cr films". *IEEE Trans. Magn.* MAG-20 (1984), 774.

## 5.5. References

---

# Chapter 6

---

## CoCrTa/Cr thin films for longitudinal recording

Most hard disks currently installed nowadays in PCs are based on longitudinal media consisting mainly of a Co-alloy layer grown epitaxially on a Cr underlayer. The role of this underlayer is to induce *c*-axes of the upper magnetic layer to grow in or near to the direction of the film plane. The first section of this chapter will discuss about some basics of crystallographic textures of a CoCrTa layer grown on a Cr underlayer. In the second section, we will present experimental results about the influences of substrates and sputtering conditions on the structural properties of single Cr films. The next two sections of the chapter will show subsequent studies of CoCrTa/Cr double layers with varying thickness of each layer.

### 6.1. About the Cr underlayer and its crystallographic textures

#### 6.1.1. The role of the Cr underlayer and crystallography of Co-alloy layer grown on Cr underlayer

It has been 30 years since the discovery of the chromium underlayer in longitudinal recording media. Lazzari et.al. [Lazzari-67] first reported a study of Co/Cr evaporated double layers on various types of substrates. They could achieve a rather high in-plane coercivity (compared to the technique at that time) of about 30-50kA/m. They had not then known why the coercivity could increase by using the underlayer until a thorough study of Daval and Randet [Daval-70] reported in the *Intermag*, 1970. This study investigated electron diffraction patterns of Co on Cr underlayer, which revealed that the increase in  $H_c$  in Co/Cr thin films is caused by polycrystalline epitaxial growth of the Co layer on the Cr underlayer. Later on,

## 6.1. About the Cr underlayer and its crystallographic textures

---

many works have tried to look for all possible epitaxial relationships between the Co and Cr layers.

### 6.1.1.1. Crystal structures of Cr and Co-alloys

Chromium is a nonferromagnetic metal. At 20°C, the crystal structure of Cr is body-centered cubic (bcc) with lattice constant  $a=2.8844 \text{ \AA}$  [ASM-90]. Crystallographic X-ray diffraction data of bcc Cr are shown in the Appendix.

Cobalt is a typical ferromagnetic metal. At room temperature, the crystal structure of Co could appear as two phases [ASM-90]:

- $\alpha$  phase: close-packed hexagonal (hcp) with lattice constants  $a=2.5071 \text{ \AA}$  and  $c=4.0686 \text{ \AA}$ , which is chiefly observed in sputtered Co films. Crystallographic X-ray diffraction data of hcp Co are shown in the Appendix.
- $\beta$  phase: face-centered cubic (fcc) with lattice constant  $a=3.5441 \text{ \AA}$ . This phase is not often observed in sputtered films so it will not be discussed in this section.

When Co is alloyed with a sufficiently small amount of other metals, like in the alloy of  $\text{Co}_{82}\text{Cr}_{13}\text{Ta}_5$  which is used in this thesis, the hcp structure is still preserved, however, the lattice constants are altered slightly.

### 6.1.1.2. Epitaxial relationships between Co-alloy layer and Cr underlayer

It has been found that there are six possible types of epitaxial relationships between hcp Co (or Co-alloy) layer and bcc Cr underlayer:

1.  $\text{Co}(10\bar{1}1)$  planes on  $\text{Cr}(110)$  planes (Potter type) [Hsu-90, Wong-92]. This type promotes the c-axis orientation of the hcp Co layer tilting  $28^\circ$  out of the film plane.

And the following types promote c-axis orientation parallel to the film plane:

2.  $\text{Co}(11\bar{2}0)$  planes on  $\text{Cr}(200)$  planes (Pitsch-Schrader type) [Wong-92, Huang-96].
3.  $\text{Co}(11\bar{2}0)$  planes on  $\text{Cr}(111)$  planes (Burgers type) [Wong-92].
4.  $\text{Co}(10\bar{1}0)$  planes on  $\text{Cr}(110)$  planes [Hsu-90].
5.  $\text{Co}(10\bar{1}0)$  planes on  $\text{Cr}(112)$  planes [Hono-90, Huang-96].
6.  $\text{Co}(10\bar{1}0)$  planes on  $\text{Cr}(113)$  planes [Hono-90].

(Note that the above crystallographic planes are planes parallel to the film plane. The relationships are listed in the order of probability observed in practice).

Figure 6.1.1 shows the schematic diagrams of the most two common types of epitaxial relationships between hcp Co-alloy layer and bcc Cr layer. The lattice constants are obtained from XRD measurements on  $\text{Co}_{82}\text{Cr}_{13}\text{Ta}_5$  and Cr thin films on Si substrates.

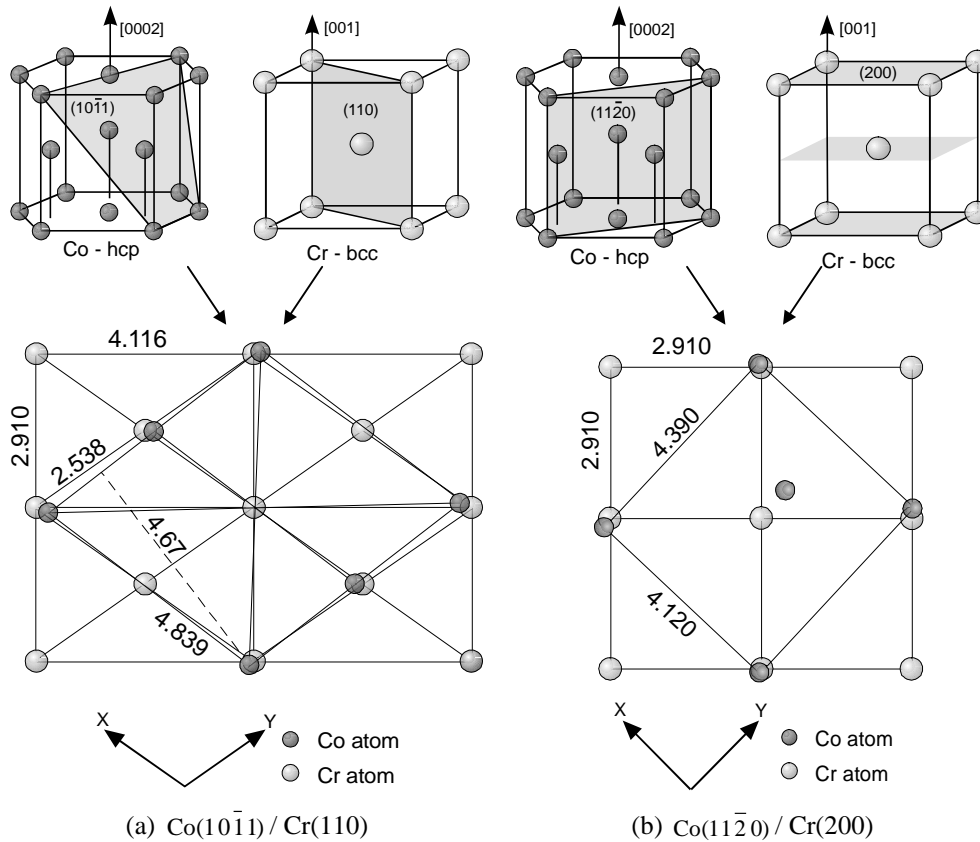


Fig. 6.1.1. Schematic diagrams of the two most common types of epitaxial relationships between Co and Cr layers. The spacing values are in Å and they are taken from data of bulk materials. The directions  $x$  and  $y$  are used to calculate the misfit.

The quality of epitaxy is characterized by the measure of misfit  $P_i$ , expressed by the formula [Howard-87]:

$$P_i = [(b_i - a_i) / \frac{1}{2}(b_i + a_i)] \times 100\% \quad (6.1.1)$$

where  $P_i$  is the percentage of misfit along a certain direction  $i$ ;  $b_i$  and  $a_i$  are the cell dimensions along  $i$  direction of the upper and the underlayer, respectively.

## 6.1. About the Cr underlayer and its crystallographic textures

---

Table 6.1.1 gives some values of misfit of types 1 and 2 of epitaxial relationships, calculated for two cases:

- 1, pure Co grown on pure Cr with lattice constants taken from bulk material data (see Section 6.1.1.1),
- 2,  $\text{Co}_{82}\text{Cr}_{13}\text{Ta}_5$  layer grown on Cr layer with lattice constants calculated from XRD data measured on single  $\text{Co}_{82}\text{Cr}_{13}\text{Ta}_5$  and Cr thin films deposited on Si substrates.

*Table 6.1.1. Values of misfit of type 1 and type 2, calculated for pure bulk Co/Cr and  $\text{Co}_{82}\text{Cr}_{13}\text{Ta}_5/\text{Cr}$  thin films.*

	Pure Co/Cr (bulk data)		$\text{Co}_{82}\text{Cr}_{13}\text{Ta}_5/\text{Cr}$ thin films	
	$P_x$	$P_y$	$P_x$	$P_y$
$\text{Co}(10\bar{1}1)/\text{Cr}(110)$	-4.46%	+0.36%	-4.06%	+0.75%
$\text{Co}(11\bar{2}0)/\text{Cr}(200)$	+3.07%	+3.07%	+3.39%	+3.39%

### 6.1.1.3. Optimum texture for longitudinal recording media

All epitaxial relationships listed in the previous section are suitable for longitudinal recording because they create the c-axis orientation of the magnetic Co-alloy layer parallel or nearly parallel to the film plane. However, there should be an optimum texture that gives the best recording performances, which has been a subject of much debate.

On the one hand, some researchers tried to produce the texture of Co-alloy  $(11\bar{2}0)/\text{Cr}(200)$  because they believe that with the in-plane c-axis orientation, this texture can result in high  $H_c$  and high in-plane anisotropy [Mirzamaani-91, Tsai-92, Lal-94]. On the other hand, other research groups found that the texture of Co-alloy  $(10\bar{1}1)/\text{Cr}(110)$  is more suitable for longitudinal recording [Chen-86, Ohno-89] even though it makes the c-axis orientation  $28^\circ$  out of plane. Their explanation was that this texture gives better signal-to-noise ratio [Shen-92, Shen-94]. At the middle ground, Lyakhovich [Lyakhovich-96] proved that a mixed texture is the optimum configuration to give maximum  $H_c$ .

### 6.1.2. Model for the formation of crystallographic texture of Cr thin films

When sputter-deposited onto a substrate, commonly, Cr thin films have either (110) or (200) crystallographic textures or a mixture of these two textures,

depending on the type of the substrate and sputtering conditions [Duan-90, Laughlin-91, Feng-94, Shen-94, Rogers-94, Lyakhovich-96]. Although some researchers have tried to explain the growth mechanisms of Cr films [Duan-90, Parker-91], their explanations were not sufficient to understand the dependence of the texture on the sputtering conditions. To cope with that, Feng et al. [Feng-94] proposed a model for the formation of the crystallographic texture of Cr thin films based on minimization of the surface energy.

In summary, two mechanisms of the formation of texture have been proposed in this model.

**Mechanism I:** During the film growth, if the islands can reach their equilibrium shape before they impinge to each other to form a continuous film, the islands prefer the (200) orientation and eventually the (200) texture forms. This mechanism occurs in several circumstances:

- a) When substrate temperature is high, which makes the adatoms more mobile and thus the equilibrium state is created more easily and faster.
- b) When the deposition rate is low, the islands have more time to reach their equilibrium state.
- c) When the Ar pressure is relatively low, the Ar ions have high kinetic energy, which also make the adatoms more mobile and thus the equilibrium state is created more easily.

**Mechanism II:** If the islands cannot obtain their equilibrium shape before impingement, the (110) texture will develop due to the faster growth mechanism because for bcc Cr, the {110} planes have the lowest surface energy. During the development of the (110) texture after impingement, the smaller the impingement island size (higher concentration of islands), the easier the (110) texture develops. This mechanism takes place in the following circumstances:

- a) When the substrate temperature is low, in contrast to the case (a) of mechanism I. In this case, the atoms are “quenched” onto the substrate. The islands are small and their concentration is high. They cannot reach their equilibrium orientation before impingement, therefore, after a continuous film is formed, the (110) texture will develop by faster growth mechanism.
- b) When the deposition rate is high, however this case will also create high surface temperature, which makes the formation of the (110) texture not obvious.
- c) When the Ar pressure is very low, it means that the Ar ions have very high kinetic energy. This causes sputtered particles to have very high energy. When arriving on the growing islands, they create a lot of defects. Hence, the

## 6.1. About the Cr underlayer and its crystallographic textures

---

concentration of islands is increased, and therefore the (110) texture can develop easily.

- d) When substrate bias is applied. In this case, Ar ions bombard the film surface, having the same effect as in the case (c).

## 6.2. Experimental results on Cr thin films

In order to prepare some knowledge for the disposition of CoCrTa layer on Cr underlayer, the growth of single Cr films were studied. The aim of this study is to find a way to control the crystallographic texture of the Cr film and to optimize the sputtering conditions to make a desired Cr underlayer. This section presents our study of Cr films on different types of substrates, at different Ar pressures, substrate temperature  $T_s$  and with various thicknesses.

### 6.2.1. Cr films on different types of substrates

In non-textured longitudinal media\* like our samples, the substrate plays no important role in the texture of the deposited layers. However, some small effects of the types of substrates are sometimes reported [tenBerge-92]. The effects could be due to the difference in interfacial energy at the interface between the substrate and the Cr layer and/or the difference in heat conductivity of the substrates, which eventually causes a difference in the substrate temperature. This section will report experimental results of Cr films deposited on Si(100), Si(111) wafers,  $\text{Si}_3\text{O}_4/\text{Si}(100)$ ,  $\text{SiO}_2/\text{Si}(100)$  and Corning glass substrates.

In the first series of samples, we compared 100nm Cr films deposited on four types of substrates, namely Si (100), Si(111) wafers,  $\text{Si}_3\text{O}_4/\text{Si}(100)$ ,  $\text{SiO}_2/\text{Si}(100)$  (which will be called  $\text{Si}_3\text{O}_4$  and  $\text{SiO}_2$  substrates for short) at several  $T_s$ 's.

The  $\text{Si}_3\text{O}_4$  substrates were produced by coating a Si(100) wafer with a 45nm-thick amorphous  $\text{Si}_3\text{O}_4$  layer. The amorphous layer was formed by reaction of ammonia with an excess dichlorosilane by low pressure chemical vapor deposition [tenBerge-92]. The  $\text{SiO}_2$  substrates were produced by oxidation of Si(100) wafers at 1100-1150°C in oxygen atmosphere. The thickness of the  $\text{SiO}_2$  layer is about 65nm.

In the sputtering process of the Cr films, besides varying  $T_s$  from room temperature (RT) to 250°C, other sputtering parameters were kept constant. Four 2 by 2cm

---

\* Textured longitudinal media are media deposited on a pre-grooved substrate, which causes the direction of the easy axis to lie along the grooves.

substrates of the above types were put close together in every sputtering run. A conducting paste was applied in between the substrates and the heater to create uniform temperature of the samples.

After analyzing XRD spectra, we found that the peak intensities of the samples are not significantly different. Measurements of  $\Delta\theta_{50}$  are therefore necessary to compare them. The (110) peak (at around  $2\theta = 44^\circ$ ) is chosen for these measurements because it produces larger signal. The results are given in Table 6.2.1. From Table 6.2.1 we can conclude that generally, there is no remarkable difference in the  $\Delta\theta_{50}$  values between the Cr films deposited on different types of substrates at a fixed  $T_s$ . However, at most substrate temperatures, the Cr film on  $\text{Si}_3\text{N}_4$  seems to have the smallest  $\Delta\theta_{50}$ , which means that on this type of substrate, Cr film has the best (110) texture.

Table 6.2.1.  $\Delta\theta_{50}$  of Cr(110) peak of Cr films deposited on different types of substrates and substrate temperature.

	$\Delta\theta_{50}$ of Cr on Si(100)	$\Delta\theta_{50}$ of Cr on Si(111)	$\Delta\theta_{50}$ of Cr on $\text{Si}_3\text{N}_4/\text{Si}(100)$	$\Delta\theta_{50}$ of Cr on $\text{SiO}_2/\text{Si}(100)$
$T_s = 100^\circ\text{C}$	7.2°	7.1°	6.7°	11.1°
$T_s = 150^\circ\text{C}$	10.0°	9.9°	8.6°	8.9°
$T_s = 200^\circ\text{C}$	6.3°	6.5°	6.3°	6.6°
$T_s = 250^\circ\text{C}$	6.2°	6.9°	6.4°	6.2°

Note: Shading levels indicate approximately values of  $\Delta\theta_{50}$ :

□ :  $<6.5^\circ$       □ :  $6.5\text{--}7.0^\circ$       □ :  $>7^\circ$

Later, we compared Cr films deposited on  $\text{Si}_3\text{N}_4$ , Si(100) with Corning glass substrates and found that in general, Cr films on Corning glass substrates exhibit even better orientation, especially the (110) texture. There is no general rule for the (200) texture, which is sometimes stronger in Corning glass case, sometimes it is otherwise weaker. Figure 6.2.1 gives an example of these comparisons. The figure shows that the intensity of the (110) peak of the Corning glass case is substantially higher than that of the  $\text{Si}_3\text{N}_4$  case. Rocking curve measurements at this peak revealed that  $\Delta\theta_{50}$  of Cr/glass is slightly smaller than that of Cr/ $\text{Si}_3\text{N}_4$ , which means the (110) texture of Cr film on glass is better than on  $\text{Si}_3\text{N}_4$ . However, intensity of the (200) peak of Cr on  $\text{Si}_3\text{O}_4$  substrate is slightly higher. After weighting pros and cons, we came to a conclusion that Corning glass is the optimum substrate in our case. Moreover, Corning glass substrates have another advantage: it is easier to analyze XRD spectra of samples deposited on glass because there is no background spectrum of the substrate which is largely observed

## 6.2. Experimental results on Cr thin films

in samples deposited on any Si-wafer-based substrates. In all samples reported later in this section, only glass substrates were used.

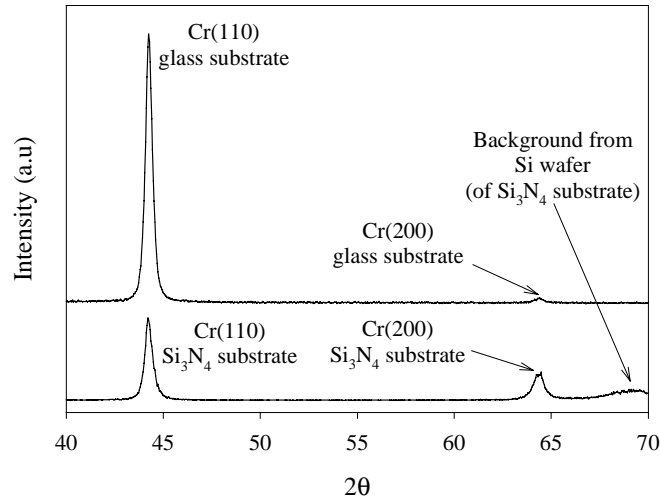


Fig. 6.2.1. XRD spectra of 200nm thick Cr films on Corning glass and on  $\text{Si}_3\text{N}_4$  substrates.  $T_s = 250^\circ\text{C}$ .

### 6.2.2. Cr films produced at various substrate temperatures

Substrate temperature  $T_s$  is always considered one of the most important parameters. To study the influence of  $T_s$  on the texture of Cr films, a series of Cr film samples at different  $T_s$ 's (from RT to  $320^\circ\text{C}$ ) was made. The thickness of these samples was kept at about 100nm. Ar pressure was  $3 \times 10^{-2}$  mbar and  $V_{rf}$  was 1.6kV. Care is needed when mounting the substrate on the substrate heater because an inappropriate way of mounting can cause rather large error of temperature.

We analyzed XRD spectra of the samples and found that in most samples, both (110) and (200) textures appear. However, peak intensities of these textures follow opposite trends (Fig. 6.2.2). Note here that the intensity scale is relative, i.e. the peak intensity values have been normalized on the corresponding peak intensities of the Cr powder sample, which are 100 and 16 for (110) and (200) peaks, respectively (see the Appendix). At  $T_s$  less than  $150^\circ\text{C}$ , only the (110) texture is observed. The peak intensity of the (110) texture decreases with increasing  $T_s$ . On the other hand, at  $T_s$  higher than  $150^\circ\text{C}$ , the (200) texture starts growing. The peak intensity of this texture increases when  $T_s$  is raised from  $150$ - $320^\circ\text{C}$ . At about  $200$ - $250^\circ\text{C}$ , the (200) texture is comparable to the (110) texture and it becomes

dominant at 250-320°C. This is consistent with experimental results obtained by some other authors [Duan-90, Hono-90, Feng-94]. This phenomenon can be interpreted using the model of [Feng-94] as presented in Section 6.1.2.

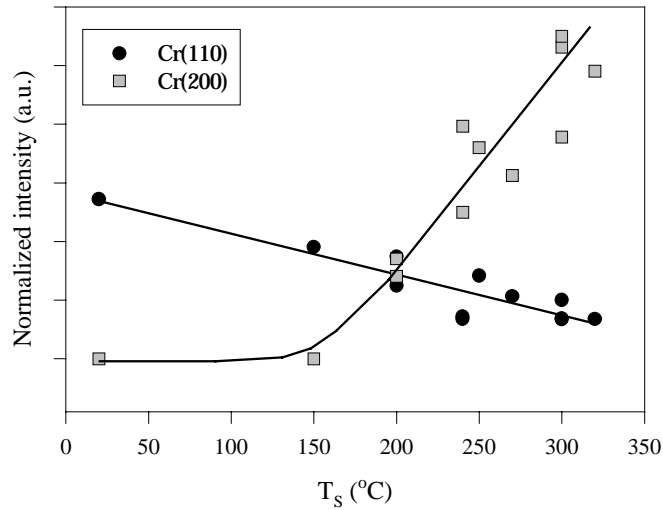


Fig.6.2.2. Peak intensities of Cr samples at different  $T_s$ 's. The solid lines are guides for the eyes.

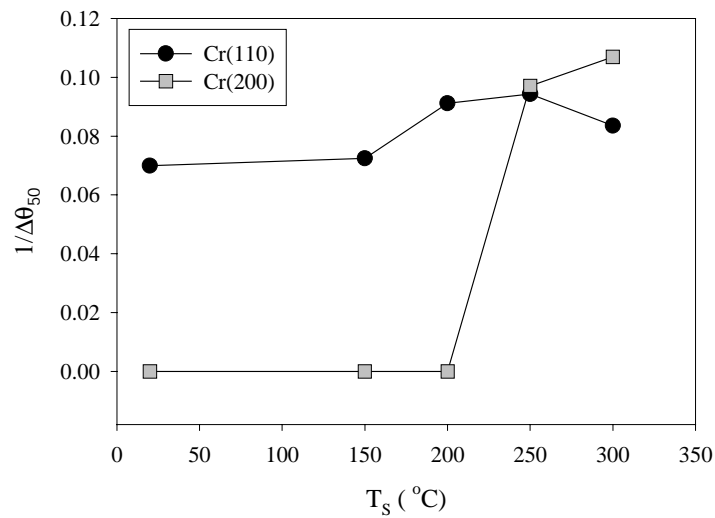


Fig. 6.2.3.  $1/\Delta\theta_{50}$  of Cr thin films at various substrate temperature  $T_s$ .

To have better evaluation of the textures, rocking curves of Cr samples at several  $T_s$ 's have been measured. From these measurements,  $\Delta\theta_{50}$  of the textures were

calculated (Fig. 6.2.3). Because the (200) peak of the samples at low  $T_s$  does not exist, the corresponding  $\Delta\theta_{50}$  value is considered infinity. To avoid plotting infinity values, we used the reverse value of  $\Delta\theta_{50}$ , which is a convenient way to plot. The larger the  $1/\Delta\theta_{50}$  quantity, the better the orientation quality of the texture is. The values of  $1/\Delta\theta_{50}$  in Fig. 6.2.3 indicate that the orientation of the (110) texture is slightly improved at high  $T_s$  ( $>200^\circ\text{C}$ ). At about  $200\text{-}250^\circ\text{C}$ , it reaches a maximum. Similarly to the graph of intensity versus  $T_s$  (Fig. 6.2.2), the quality of the (200) texture drastically increases at  $T_s$  higher than about  $250^\circ\text{C}$ .

### 6.2.3. Cr films of various thicknesses

Another series of Cr samples was made in order to investigate the development of the (110) and (200) textures as a function of film thickness. For all samples,  $T_s$  was set at  $250^\circ\text{C}$ , other sputtering conditions were kept the same as in the series presented in the previous section, except for the deposition time. According to the previous study, at this substrate temperature, both (110) and (200) textures are comparably strong, which is convenient for  $\Delta\theta_{50}$  measurements at the two peaks. Three samples with thickness ranging from 27 to 200nm have been realized.

#### 6.2.3.1. Development of film textures

XRD spectra of these samples are plotted in Fig. 6.2.4. From the figure, we can see that in the 27nm-thick sample, only the (110) texture exists. When the Cr film becomes thicker (100nm), the (110) texture develops and the (200) texture starts to grow. When the Cr thickness increases further (to 200nm), the (110) texture stops growing but the (200) texture still develops drastically. The inset of Fig. 6.2.4 shows the normalized peak intensity of the sample (on peak intensities of the standard Cr powder sample) as a function of Cr thickness. At a thickness of 27nm, the Cr film can be considered (110) textured. When the film is growing, the (110) and (200) textures are comparable at about 100nm and at a higher thickness, the (200) texture wins out and becomes dominant. This behavior of the Cr texture is not consistent with the works of [Shen-92 and Feng-94], probably due to the difference in sputtering conditions of the equipment (between theirs and ours) or due to the fact that not all parameters, except the Cr thickness, are fixed. For instance, the thicker sample, which is exposed for a longer time to the plasma, has higher surface temperature. We have observed this effect when depositing CoCrTa layers (see Section 4.1). If this is the case, the interpretation for the behavior of the Cr textures in our case could be as follows. At small thickness (27nm), the Cr film is growing at the initial stage, therefore, it could be polycrystalline, meaning that both textures equally exist. In the XRD spectrum (Fig. 6.2.4), only a weak (110) peak is visible. This is because the sample is too thin and the intensity the (200)

texture is only 16% of that of the (110) peak (see the Appendix), which is too weak to appear in the spectrum. At larger Cr thicknesses, both textures develop and probably the (110) texture develops faster than the (200) texture, according to the other works [Shen-92 and Feng-94], provided that  $T_s$  is fixed. However, as said above, the thicker sample may have higher  $T_s$ , and according to our results on the previous series, this fact promotes strongly the (200) texture and therefore, the (200) texture may grow even faster than the (110) texture when the film is thicker. Eventually, we can observe the phenomenon as shown in Fig. 6.2.4.

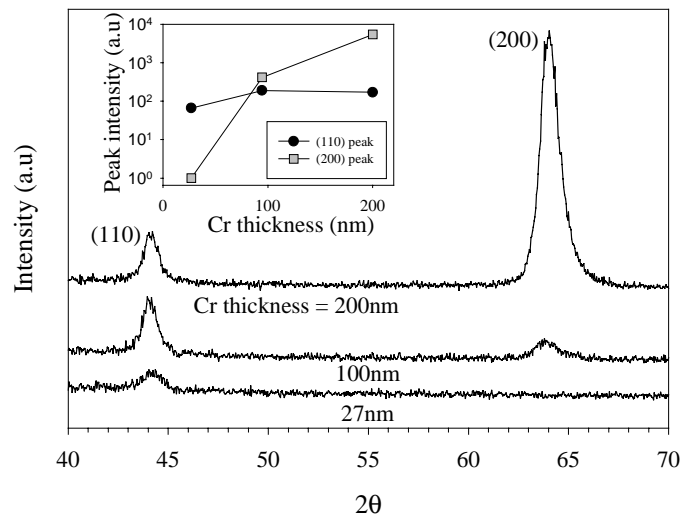


Fig. 6.2.4. XRD spectra of Cr thin films with various thicknesses. (110) and (200) peaks appear at about  $44.1^\circ$  and  $64^\circ$ . The inset shows normalized peak intensity (on intensity of powder sample) as a function of Cr thickness.

To have better evaluation of the textures, rocking curves of the Cr samples have been measured. Similarly to Fig. 6.2.3, we use again the reverse value of  $\Delta\theta_{50}$ . The results are shown in Fig. 6.2.5. For ease of evaluation, another scale of  $\Delta\theta_{50}$  (in degrees) is shown on the right vertical axis. Information obtained from Fig. 6.2.5 is almost consistent with Fig. 6.2.4. As the Cr film thickness increases, orientation quality of the (110) texture is almost constant while that of (200) gets better.

## 6.2. Experimental results on Cr thin films

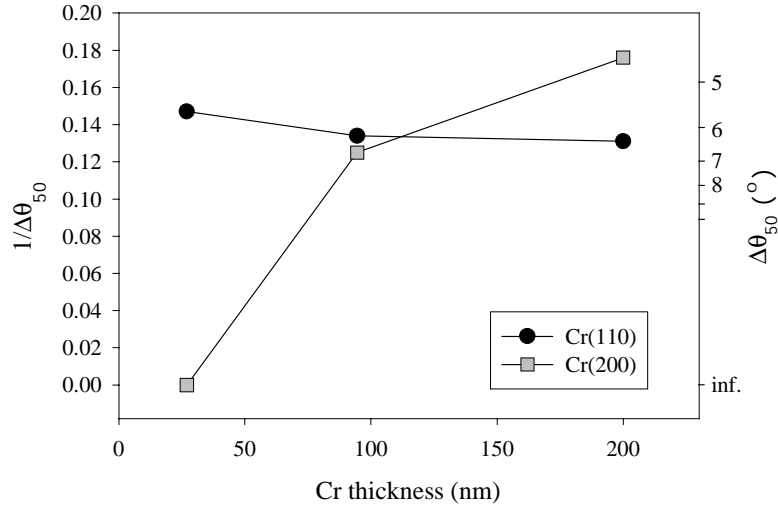
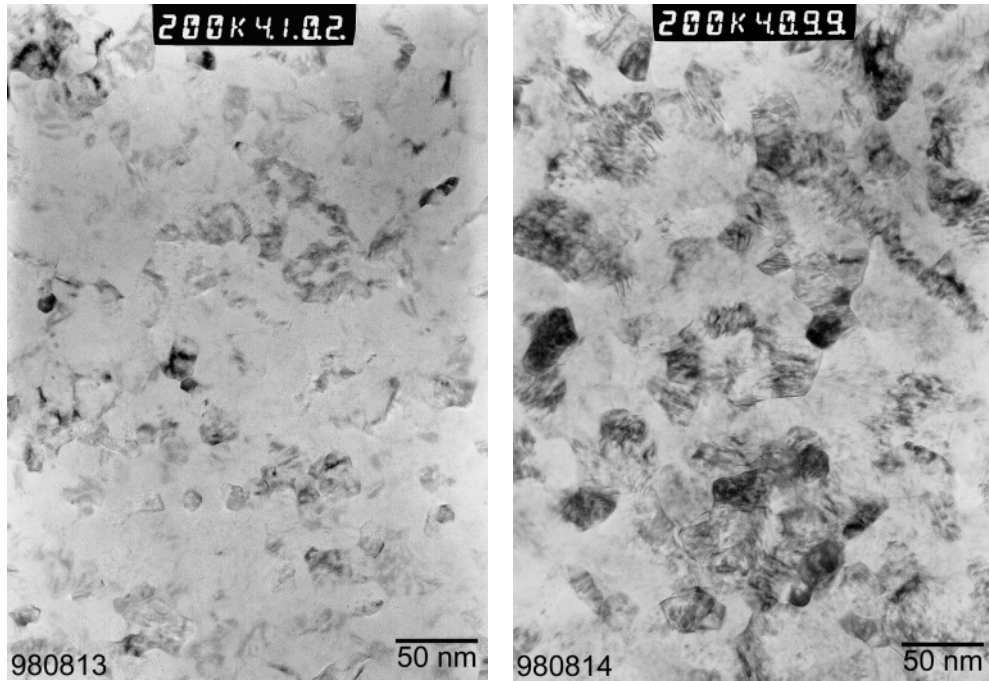


Fig. 6.2.5.  $1/\Delta\theta_{50}$  (left vertical axis) and  $\Delta\theta_{50}$  (right vertical axis) of Cr samples of various thicknesses.

### 6.2.3.2. Development of morphology

Morphology of Cr thin films of different thicknesses has been investigated. Two Cr films of thicknesses of 15 and 75nm were sputtered on  $\text{Si}_3\text{N}_4$  chips (see Section 4.3.2 for more detail of the method) at  $T_s$  of 200°C, PAr of  $3 \times 10^{-2}$  mbar and  $V_{rf}$  of 1.6kV. Bright-field plane-view images of the samples were observed using TEM (Fig. 6.2.6). Obviously, grain size of Cr films increases double (from 15 to 30nm) when the film thickness increases from 15 to 75nm. This is a well-known phenomenon, not only for Cr thin film case [Lee-88, Tang-93], but also for many other materials, for instance CoCr thin films [Zhang-94], or CoCrTa thin films (Section 5.2.2).

To have more information of the surface, AFM observations of these two samples were carried out. Figure 6.2.7 shows 3D-view of AFM images of the samples. It is clear that the 15nm-thick sample contains small domes, which are the appearance of the grains. On the other hands, the AFM images of the 75nm-thick sample indicate that the film surface is more continuous.



(a) Thickness = 15nm. Grain size  $\approx$  15nm      (b) Thickness = 75nm. Grain size  $\approx$  30nm

Fig. 6.2.6. Plan-view TEM images of Cr films of different thicknesses.

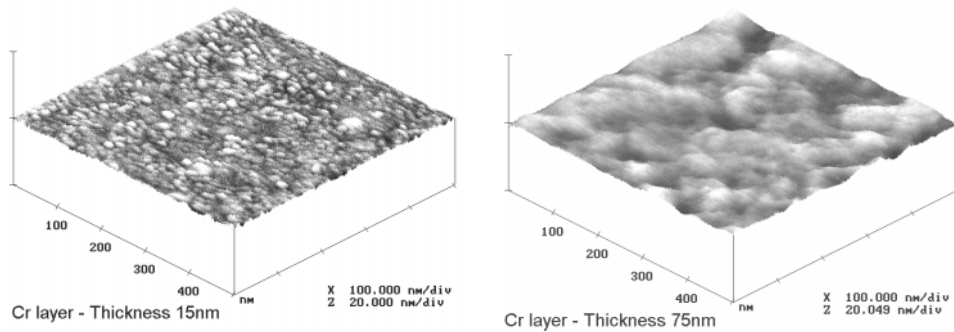


Fig.6.2.7. AFM images of the surface of the Cr films of different thicknesses.

### 6.2.4. Cr films produced at various Ar pressures

Another series of Cr samples were made to investigate the influence of Ar pressure on the texture of the films. Three samples were made at various PAr's, from  $2 \times 10^{-2}$  to  $4 \times 10^{-2}$  mbar. For our sputtering system (L-H Z400), an Ar pressure of less than about  $2 \times 10^{-2}$  mbar is not possible because the plasma is unstable. Substrate temperature was kept at  $250^\circ\text{C}$ , as the series of various thicknesses reported above. Thickness of all samples was fixed at about 100nm, of which, according to the previous section, the Cr films have comparable two textures (110) and (200). This choice of thickness enables us to study easily the behaviors of both textures. Because the deposition rate depends on PAr, three other test samples have been made in advance. Their thicknesses were then measured by low-angle XRD method (see Section 4.3.1), from which the deposition rates were calculated. Other sputtering parameters were kept the same as the previous series of Cr samples. Figure 6.2.8 shows the XRD spectra of the samples. It is obvious that PAr affects equally the (110) and (200) textures. At  $\text{PAr} = 3 \times 10^{-2}$  mbar, both textures appear to be the best.

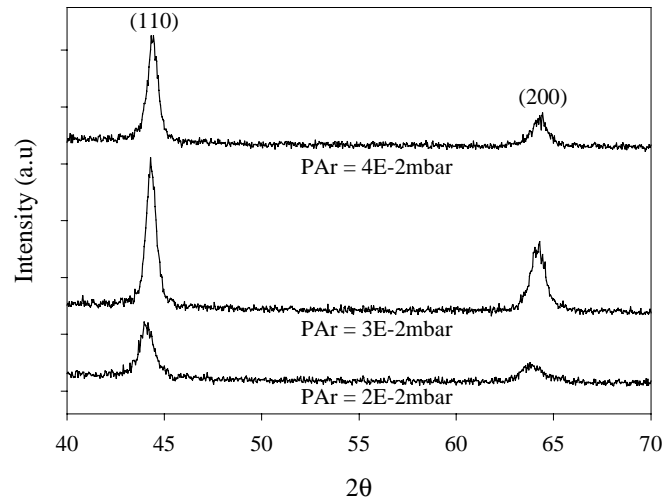
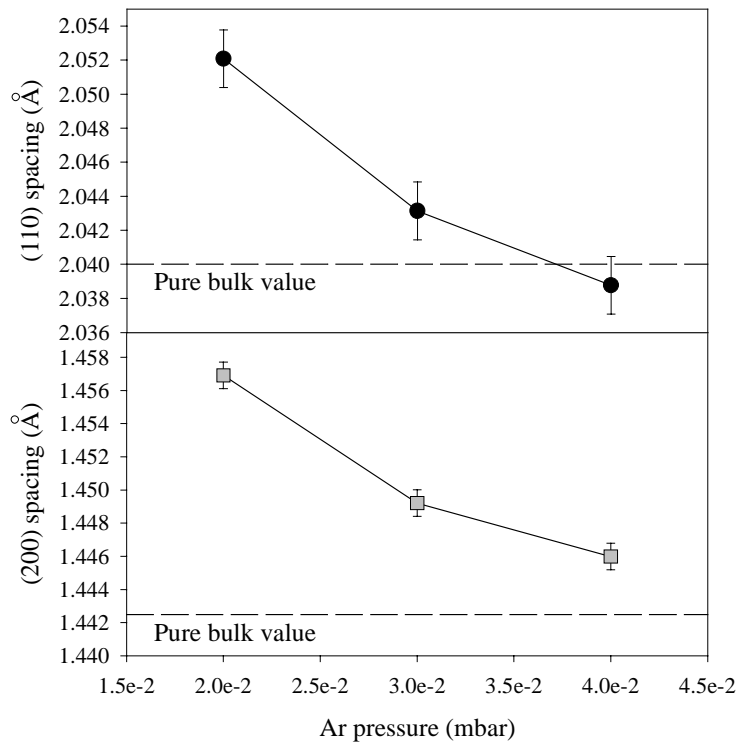


Fig. 6.2.8. XRD spectra of Cr films at different PAr.

Another effect of Ar pressure is illustrated in Fig. 6.2.9, in which the lattice spacings of the (110) set of planes and that of the (200) set of planes are calculated from the  $2\theta$  values of the corresponding peaks\*. Both two spacings (110) and (200) follow a common trend: they contract when PAr increases. This effect has also

\* Spacing  $d$  is calculated from Bragg equation:  $n\lambda = 2d \sin\theta$ ; in which  $n\lambda = 1.54056 \text{ \AA}$

been observed in CoCrTa films (Section 5.1). In the mentioned section, we have shown that the contraction of the lattice spacings when PAr increases could be associated with the decrease in Ar content which is entrapped in the film during deposition. Although Ar content entrapped in the Cr films was not measured, we can suppose that a similar phenomenon could also happen in Cr films, which results in the contraction of the (110) and (200) spacings as plotted in Fig. 6.2.9. Spacing values of pure Cr bulk material are also indicated in the graphs. It is logical that these pure bulk values are commonly smaller than measured values. If the above supposition is true, when PAr increases, Ar content decreases and tends to approach zero at high PAr, at which the measured spacings of the films are expected to be close to the spacings of pure bulk material.



6.2.9. Lattice spacings calculated from XRD spectra. Dashed lines are spacings of pure Cr bulk material.

## 6.2.5. Discussion and summary

A rather broad picture about the influences of substrates and sputtering conditions on the structures and morphology of Cr thin films has been made. This will be the

## 6.2. Experimental results on Cr thin films

---

key to control properties of Cr underlayers when we study later the CoCrTa/Cr media.

For our case, it was found that Corning glass substrate is more suitable for Cr films.

To investigate the influences of sputtering conditions, three important parameters, namely  $T_s$ , thickness and PAr, were scanned over rather broad ranges in the manner that one parameter is varied while the rest is fixed. Because it is time consuming to scan the whole ranges, we tried to reduce the number of experiments by the following way. First, we set the unvaried parameters to the most commonly used values, suitable for the system (e.g.  $V_{rf}$ , PAr) or values often found in literature (e.g. thickness), while scanning the investigated parameter (e.g.  $T_s$ ). Then we choose the value of the investigated parameter at which both peaks of (110) and (200) textures obtained from this experiment are equally strong for the setting of the next experiments, and so on.

In the first series, we found that when  $T_s$  increases, the (110) texture of Cr films of thickness of 100nm becomes weaker, whereas, the (200) texture becomes stronger. The (110) texture is dominant at  $T_s$  lower than about 100°C while the (200) texture is prevailing at  $T_s$  higher than about 250°C. In between, from 200-250°C, both textures comparably exist. The rocking curve measurements revealed that even when the intensity of the (110) peak becomes slightly weaker at high  $T_s$ , its orientation quality, however, is slightly improved at high  $T_s$ , and is the best at about 200-250°C. The quality of the (200) texture drastically increases at high  $T_s$ .

Fixing  $T_s$  at 250°C, where both peaks can be seen clearly in the XRD spectra, we tried to change the film thickness of the second series, from 27 to 200nm. The (200) texture develops drastically with the Cr thickness, whereas, the (110) does not change significantly. At about 100nm, the two textures are comparable. Besides, grain size of the Cr films was found to increase with thickness. In the last series of sample,  $T_s$  was fixed at 250°C and the thickness was kept at 100nm while PAr was varied from  $2 \times 10^{-2}$  to  $4 \times 10^{-2}$  mbar. The Ar pressure seems to affect equally the (110) and (200) textures. The optimum PAr is about  $3 \times 10^{-2}$  mbar. In addition, we found that the increase in PAr causes the lattice spacings to contract.

Now we have the key to control the texture of Cr underlayers. In experiments with CoCrTa/Cr that will be presented in the next section, the sputtering process of the Cr underlayer is controlled so that its texture is commonly a mixture of (110) and (200). Substrate temperature is set at about 200-250°C, PAr is always at  $3 \times 10^{-2}$  mbar and  $V_{rf}$  is 1.6kV. Except for the series of samples with different thicknesses of Cr underlayer, all samples consist of a CoCrTa layer deposited on 100nm-thick Cr underlayer.

### 6.3. Experiments on CoCrTa on Cr underlayer: varying CoCrTa thickness

Having the key to control texture of the Cr underlayer (Section 6.2) and properties of CoCrTa single layer (Chapter 5), in the next step, which will be dealt in this section, we place a CoCrTa magnetic layer on top of a Cr underlayer. The Cr underlayer is first deposited on a glass substrate and then, just after finishing this layer, the CoCrTa layer is sequentially deposited. In this section, we investigated CoCrTa layers of various thicknesses deposited on Cr underlayers of fixed thickness.

#### 6.3.1. Sputtering process

**Substrate:** Commercial Corning glass substrates were cut into 2.5×2.5 cm and they were cleaned with ethanol in an ultrasonic cleaner for 20 minutes. In each sputtering run, a substrate was mounted onto the substrate heater with silver glue.

**Vacuum system:** We used the Leybold-Heraeus Z400 sputtering system equipped with a resistance substrate heater. After loading sample, the system is pumped down to  $4 \times 10^{-7}$  mbar. A few hours before sputtering, the heater is switched on for 1 hour to degas. Before sputtering, liquid N<sub>2</sub> is filled to the cold trap to get the vacuum down to about  $3 \times 10^{-7}$  mbar.

**Sputtering conditions:** To have a Cr underlayer with mixed textures of (110) and (200), the Cr underlayer should be deposited at  $T_s = 250^\circ\text{C}$ ,  $V_{rf} = 1.6\text{kV}$  and  $P_{Ar} = 3 \times 10^{-2}$  mbar (see Section 6.2). On the other hand, it has been shown that (Section 5.1) the CoCrTa layer has the best performance at  $T_s$  of about  $150\text{-}200^\circ\text{C}$ ,  $V_{rf} = 1.6\text{kV}$  and  $P_{Ar} = 2 \times 10^{-2}$  mbar. However, it is difficult to set  $T_s$  differently at two successive deposition steps of Cr and CoCrTa because of the thermal inertia. This problem will be mentioned below.

**Sputtering process** consists of four main steps (Fig. 6.3.1). Before the first step, the heater is switched on and set to 94V. At this voltage, according to the calibrated temperature curve (see Section 4.1.2), the substrate temperature will be saturated at  $250^\circ\text{C}$  within half an hour. Because it takes more than half an hour to clean the targets and the substrate, when the first layer is deposited, this saturation temperature will be established.

### 6.3. Experiments on CoCrTa on Cr underlayer: varying CoCrTa thickness

In Step 1 and Step 2, the Cr and CoCrTa targets are successively cleaned for 900s. An unused substrate holder (grounded) is arranged to face the cleaned target (connected to high RF voltage). Between the steps, the target mushroom containing the three target holders and the blind flange is rotated to an appropriate

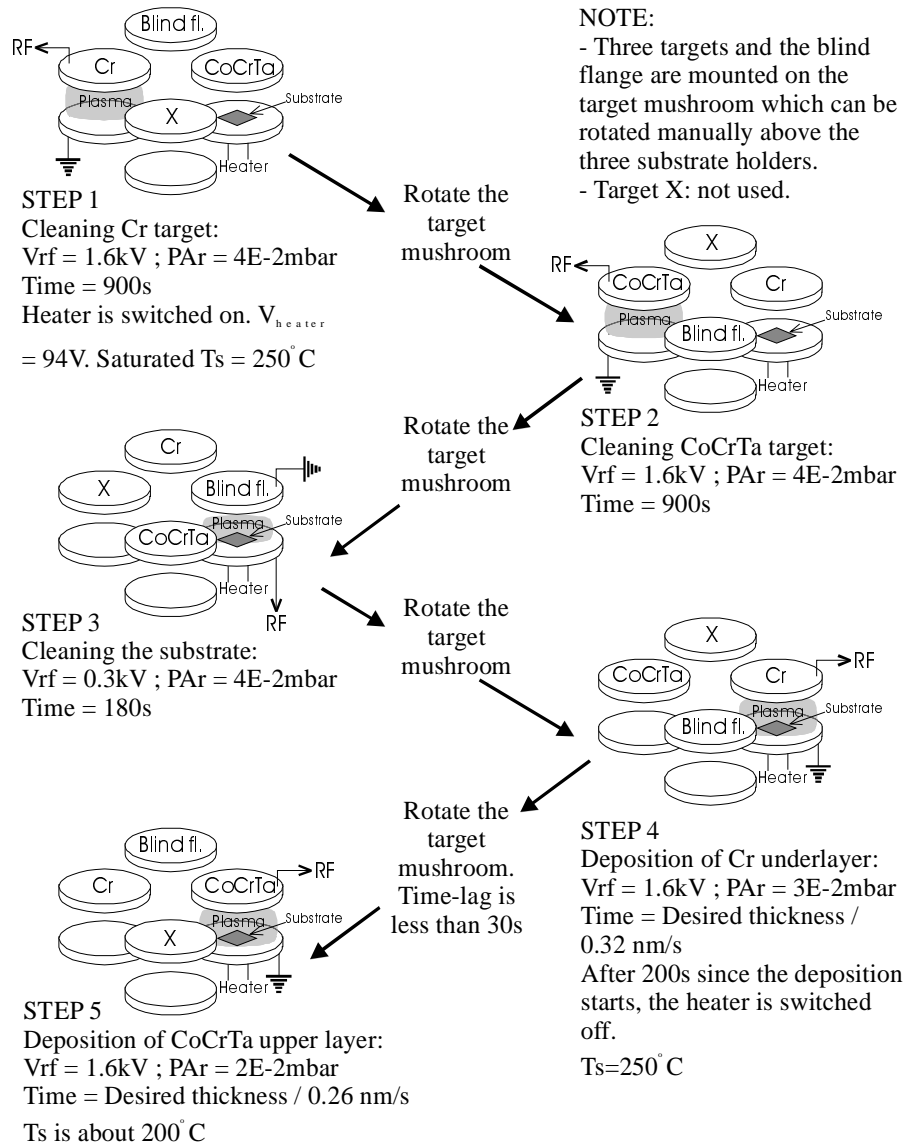


Fig. 6.3.1 Diagram of sputtering process of CoCrTa/Cr media

position. In step 3, the substrate is cleaned for 180s by connecting it to a low RF voltage (0.3kV). A blind flange facing the substrate is grounded.

After the cleaning steps (Step 1-3), the Cr underlayer is deposited (Step 4). The Cr target is connected to high RF voltage while the substrate is grounded. As mentioned above, there is a problem that the Cr underlayer and the CoCrTa layer are supposed to be deposited at 250°C and about 150-200°C, respectively. The temperature can not be change abruptly and the time lag between two steps should be as short as possible to avoid contamination between the layers. The only way to solve this problem is to change the substrate temperature gradually from 250°C to about 200°C. To do that, after 200s since the deposition of Cr starts, the heater is switched off. According to a prior measurement of cooling down process,  $T_s$  must decrease to about 200°C after 2-3 minutes. After this duration, the cooling rate is slower, therefore during the deposition of the successive CoCrTa layer, which takes about a few minutes further,  $T_s$  does not change very much.

After completing the deposition of the Cr underlayer. The high voltage is switched off, the target mushroom is rotated to a new position, in which the CoCrTa target faces the substrate (indicated in Step 5, Fig. 6.3.1), PAr is adjusted to  $2 \times 10^{-2}$  mbar. The above actions take less than 30s. Now the high voltage is switched on again and the deposition of the CoCrTa layer starts (Step 5). The substrate temperature at Step 5 is about 200°C. This  $T_s$  is reproducible if all of the actions are carried out exactly the same in different runs. Names and specifications of the samples are presented in Table 6.3.1.

*Table 6.3.1. Names and specifications of the samples*

Sample names *	Thickness of CoCrTa layer	Thickness of Cr underlayer
UP10	10 nm	100 nm
UP20	20 nm	100 nm
UP40	40 nm	100 nm
UP60	60 nm	100 nm
UP100	100 nm	100 nm

### 6.3.2. Texture

Textures of the samples were analyzed by XRD. The obtained spectrum of a sample is a superposition of two spectra from the CoCrTa layer and the Cr underlayer. Figure 6.3.2 gives examples of the three strongest spectra. Because in

\* The names UPxxx mean variation of UPper layer thickness.

### 6.3. Experiments on CoCrTa on Cr underlayer: varying CoCrTa thickness

most samples, the CoCrTa layer is thinner than the Cr underlayer, diffraction signal from the CoCrTa layer is generally weaker than signal from the Cr underlayer, and sometimes, it is even smaller than background noise. Spectra of Sample UP10 and UP20 are not presented here because the signal from the CoCrTa layer is too weak to appear in the spectra. A general remark from Fig 6.3.2 is that in all samples, the Cr layer has two textures: Cr(110) at about  $44.2^\circ$  and Cr(200) at about  $64.4^\circ$ . This causes the epitaxial growth of the CoCrTa layer which has two corresponding textures: CoCrTa(10 $\bar{1}$ 1) at about  $46.2^\circ$  and

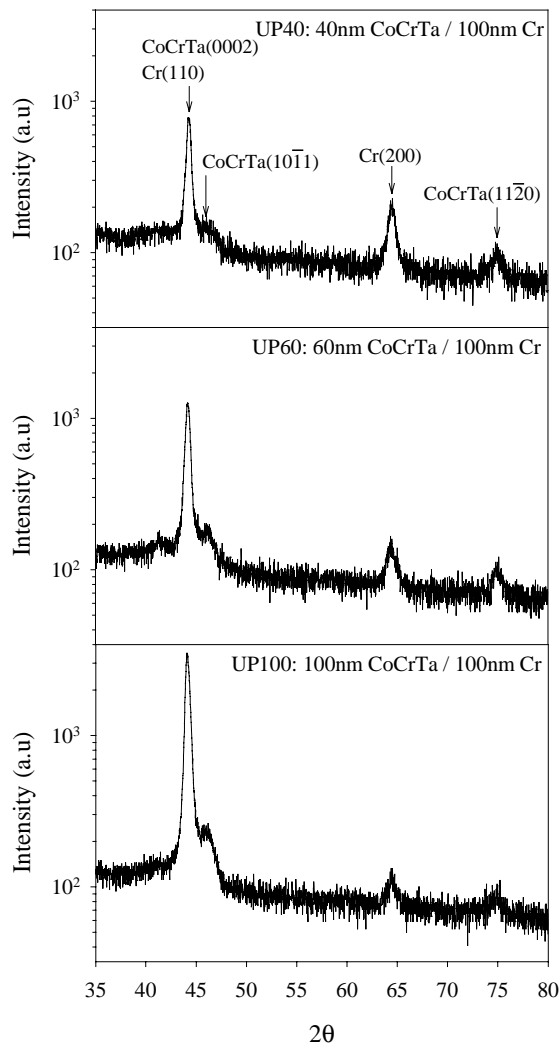


Fig. 6.3.2. XRD spectra of three samples UP40, UP60 and UP100.

CoCrTa(11 $\bar{2}$ 0) at about  $74.9^\circ$ .

These two textures seem not to develop when the CoCrTa film is thicker, at least for the three samples presented here.

Besides the above textures, the CoCrTa layers have also the CoCrTa(0002) texture whose peak overlaps the Cr(110) peak. They are almost at the same position of  $2\theta \approx 44.2^\circ$ . Therefore, from Fig. 6.3.2, it is difficult to tell about the amounts of contribution of CoCrTa(0002) and Cr(110) to the peak at  $44.2^\circ$ . However, from the increase in the intensity this peak with increasing CoCrTa layer thickness, we can deduce that the CoCrTa(0002) texture develops remarkably when the CoCrTa layer becomes thicker. In other words, c-axis orientation is gradually changing from in-plane (or nearly in-plane) direction to perpendicular direction when the layer becomes thicker. This can be explained as follows: the intensity of the peak at  $44.2^\circ$  is a summation of the intensities of the CoCrTa(0002) and the Cr(110) peaks. More over, the contribution of the unchanged 100nm Cr layer

should be slightly decreased with increasing the CoCrTa layer thickness since the signal from the Cr underlayer is screened by the CoCrTa upper layer. Therefore, from the increase in the  $44.2^\circ$  peak intensity, we can safely deduce that the CoCrTa(0002) texture develops.

Now it could be concluded that when the CoCrTa thickness increases from 40 to 100nm, the CoCrTa( $10\bar{1}1$ ) and CoCrTa( $11\bar{2}0$ ) textures do not develop, whereas, there is a significant development of the CoCrTa(0002) texture. This can be explained by the competition between the epitaxial growth and the minimization of surface energy of the CoCrTa layer. When the CoCrTa grows thicker, the epitaxial influence of the Cr underlayer becomes weaker. Hence, in samples with thick CoCrTa layer, the CoCrTa(0002) texture, which has the lowest surface energy, will gradually displace and eventually prevail over the other textures.

### 6.3.3. General magnetic properties

#### 6.3.3.1. Hysteresis loops

By employing a Cr underlayer, hysteresis loops of a CoCrTa layer are drastically changed. Figure 6.3.3 shows two cases: two graphs on the left are in-plane and perpendicular loops of a 20nm-thick CoCrTa single layer sample (which is named UN0<sup>\*</sup>) and two graphs on the right are in-plane and perpendicular loops of Sample UP20 (20nm CoCrTa / 100nm Cr). The sputtering conditions of the CoCrTa single layer sample are the same as those of the CoCrTa layer of Sample UP20. Sample UN0 has almost no hysteresis and coercivity at all measuring directions, probably because this sample is still thinner than the thickness of the initial layer (see Section 5.2). However, when this layer is deposited onto a Cr underlayer of a thickness of 100nm, the in-plane and perpendicular coercivities abruptly increase, from almost zero to 152 and 63 kA/m, respectively. The sample becomes an in-plane media with in-plane anisotropy.

---

<sup>\*</sup> This sample belongs to another series which will be discussed in Section 6.4. UN0 means the UNderlayer thickness is zero. Now we only use this sample for comparison.

### 6.3. Experiments on CoCrTa on Cr underlayer: varying CoCrTa thickness

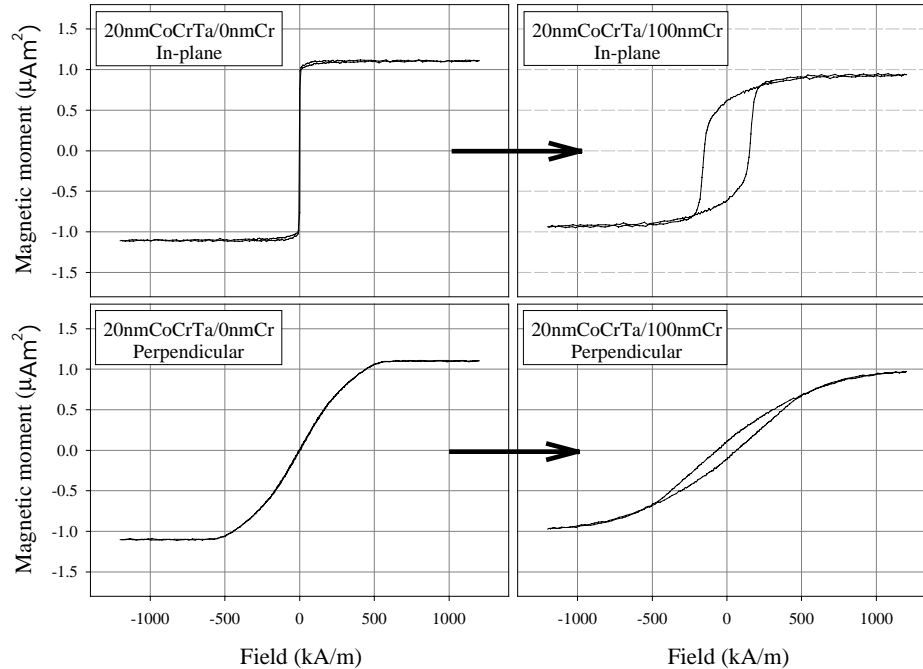


Fig. 6.3.3. With a Cr underlayer, hysteresis loops of a CoCrTa layer change drastically (from the left graphs to the right graphs)

#### 6.3.3.2. Coercivities

Figure 6.3.4 plots the behaviors of the in-plane and perpendicular coercivities as a function of CoCrTa layer thickness. The in-plane coercivity  $H_{c//}$  reaches a maximum when the CoCrTa thickness is 20nm and monotonously decreases at higher CoCrTa thickness. This is a well-known behavior [Lu-89, Hsu-89, Hsu-90] which has been reported as a feature of longitudinal media made of Co-alloy layer on an underlayer. In contrast, perpendicular coercivity  $H_{c\perp}$  increases with increasing CoCrTa thickness. Particularly, from 20 to 60nm,  $H_{c\perp}$  increases slightly.

To interpret the behavior of in-plane coercivity versus CoCrTa thickness, data of the variation of  $H_c$  with particle size obtained by Luborsky et al. [Luborsky-61] were used. In this reference, the authors presented data of  $H_c$  measured on several magnetic materials including pure Co particles of different sizes at temperature of 76°K. According to these data, there is a general behavior for all materials:  $H_c$  increases with increasing particle diameter, reaching a maximum and then decreases. The increase in  $H_c$  at small diameter is attributed to the gradual change of the material from superparamagnetic state to single domain state. And the decrease in  $H_c$  at large diameter is due to the change of the particle from coherent

rotation to incoherent rotation mode and from single domain to multi-domain state [Lodder-98].

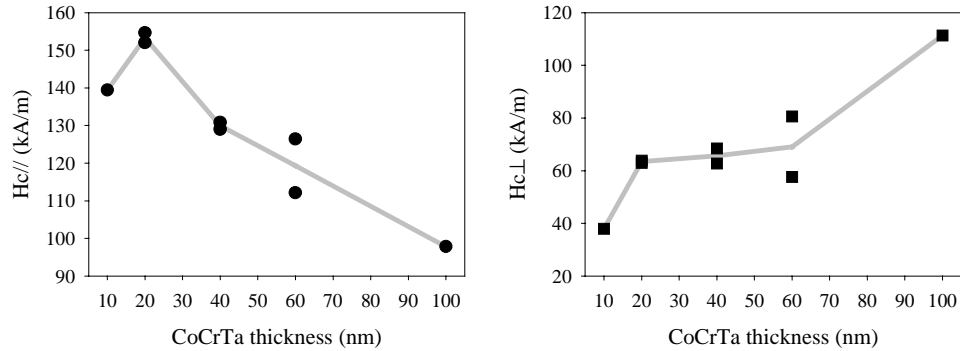


Fig. 6.3.2. In-plane and perpendicular coercivities as a function of CoCrTa thickness.

To compare this behavior to our case, we have to modify the data of Luborsky found for Co particles at 76°K to the case of CoCrTa particles at room temperature. According to Lodder [Lodder-98], the values of particle diameters at the transitions between coherent and incoherent rotation, and between single domain and multi-domain state are proportional to  $\sqrt{A / (N_{\perp} \mu_0 M_s^2)}$ , in which  $A$  is the exchange constant,  $M_s$  is the saturation magnetization. Because  $A \propto kT_c/a$  [Cullity-72, p.395], in which  $T_c$  is the Curie temperature and  $a$  is the lattice parameter, we can estimate that in the case of CoCrTa alloy, the mentioned diameters increase with a factor of about 1.7\*. This means that to have data for CoCrTa particles, the data of the variation of  $H_c$  with Co particle size of Luborsky have to shift to higher values of diameter, with a factor of 1.7, as plotted in Fig. 6.3.5 (solid circle symbols). These data is be called the Luborsky's modified data. We do not take into account the shift of  $H_c$  because it is not important in this case. The curve of in-plane  $H_c$  versus thickness of CoCrTa/Cr thin films (Fig. 6.3.4) is converted to the curve of  $H_c$  versus particle diameter and plotted in the same graph of the Luborsky's modified data with an assumption that the grain size of CoCrTa layer is about 45nm in average†. From the comparison in Fig. 6.3.5, we can easily see that the peak of  $H_c$  of the CoCrTa/Cr films almost coincides with the peak of

\* The Curie temperature was estimated based on data of [Wijn-91];  $M_s$  changes from 1400kAm (for Co) to about 450kA/m (for CoCrTa) and does not change significantly with increasing temperature from 76°K to room temperature; “ $a$ ” is considered constant.

† This assumption is based on TEM cross-section images of CoCrTa/Cr thin films (see Section 6.4). The grain is supposed to have cylindrical shape with diameter is the grain size and length is the layer thickness.

### 6.3. Experiments on CoCrTa on Cr underlayer: varying CoCrTa thickness

the Luborsky's modified data. This suggests that the observed peak is due to the transition of CoCrTa grains from coherent rotation to incoherent rotation and the peak occurs in the middle of the coherent rotation mode region. This is only true if we assume that the exchange coupling between CoCrTa grains is sufficiently small.

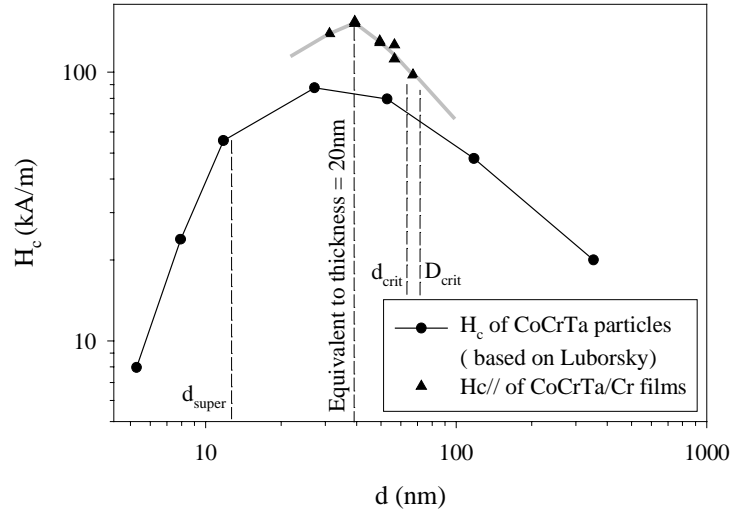


Fig. 6.3.5. Variation of  $H_c$  with particle diameter, for the case of CoCrTa particles (Luborsky's modified data - lower curve) and for the case of CoCrTa/Cr thin film with thickness converted to CoCrTa particle diameter (upper curve) Note that both axes are in log scale.  $d_{super}$ : diameter of superparamagnetic particle.  $d_{crit}$ : diameter at the transition between coherent and incoherent rotations.  $D_{crit}$ : diameter at the transition between single domain and multi-domain states.

Values of diameter of superparamagnetic particle ( $d_{super}$ ), diameter at the transition between coherent and incoherent rotations ( $d_{crit}$ ) and that between single domain and multi-domain states ( $D_{crit}$ ) for CoCrTa are also given in Fig. 6.3.5. We can easily notice that the grain diameter of the thinnest sample is about a few times larger than the superparamagnetic limit. Moreover, the CoCrTa magnetic layer is supposed to change from coherent to incoherent rotation mode at a thickness of about 79nm (equivalent to  $d_{crit}=62.2$ nm) and from single domain to multi-domain state at a thickness of about 119.8nm (equivalent to  $D_{crit}=71.4$ nm).

Another reason for the decrease in  $H_c$  with increasing CoCrTa thickness is the gradual change of easy-axis from in-plane (or nearly in-plane) to perpendicular direction when the CoCrTa layer becomes thicker. This change is indicated by the decrease in  $H_{c//}$  and the increase in  $H_{c\perp}$  when the CoCrTa thickness is above 20nm

(Fig. 6.3.4). The ratio  $H_{c//} / H_{c\perp}$  can be used to evaluate the in-plane easy-axis (Fig. 6.3.6). This ratio decreases as the CoCrTa thickness increases.

As said above, in the Luborsky's modified data, the shift of  $H_c$  values (from pure Co to CoCrTa) were not taken into account. The curve of these data is therefore substantially lower than the curve of CoCrTa/Cr films. This is straightforward because by adding Cr and Ta into Co, the compositional separation occurs leading to an increase in coercivity.

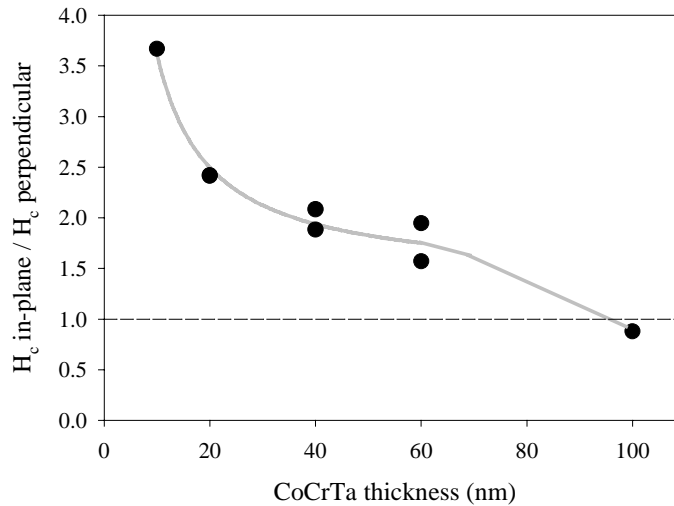


Fig. 6.3.6. Variation of the ratio  $H_{c//} / H_{c\perp}$  with CoCrTa thickness

Looking more carefully at Fig. 6.3.4, one can see that when the CoCrTa layer grows from 10 to 20nm, both in-plane and perpendicular coercivities increase. At this stage of the film growth, the thermal energy is still comparable to the in-plane anisotropy energy, the existence of an in-plane easy-axis has not taken effect and therefore, the increase in both  $H_c$ 's is merely due to the gradual transition from superparamagnetic to coherent rotation state. When the thickness increases from 20 to 60nm,  $H_{c\perp}$  does not change very much, probably because at this stage, only the in-plane texture develops. When the film is thicker than about 60nm, c-axis orientation of the upper part near the surface changes from in-plane (or nearly in-plane) to perpendicular direction, which is confirmed by XRD spectra (see the previous section). This leads to the fast increase in  $H_{c\perp}$  and probably also partly leading to the decrease in  $H_{c//}$ . At about 100nm, the film is considered isotropic, because the ratio  $H_{c//} / H_{c\perp}$  approaches one (Fig.6.3.6).

### 6.3.3.3. Squareness

Squareness  $S$  of the investigated samples was found to decrease with increasing thickness (Fig. 6.3.7.a). However, the coercivity squareness  $S^*$ , a measure of SFD, exhibits a peak at 20nm (Sample UP20) (Fig. 6.3.7.a). It could be concluded that UP20 is the best sample of the series because it has the highest  $H_{c//}$  and  $S^*$ . The mechanism governing  $S^*$  is rather complicated. The value of  $S^*$  could be influenced by the following factors:

- Exchange coupling strength tends to increase  $S$  and  $S^*$  [Zhu-88, Sanders-89, Dean-96].
- Narrow distribution of anisotropy field also increases  $S$  and  $S^*$  [Speliotis-90].
- Degree of perpendicular anisotropy can reduce  $S^*$  [Sanders-89].

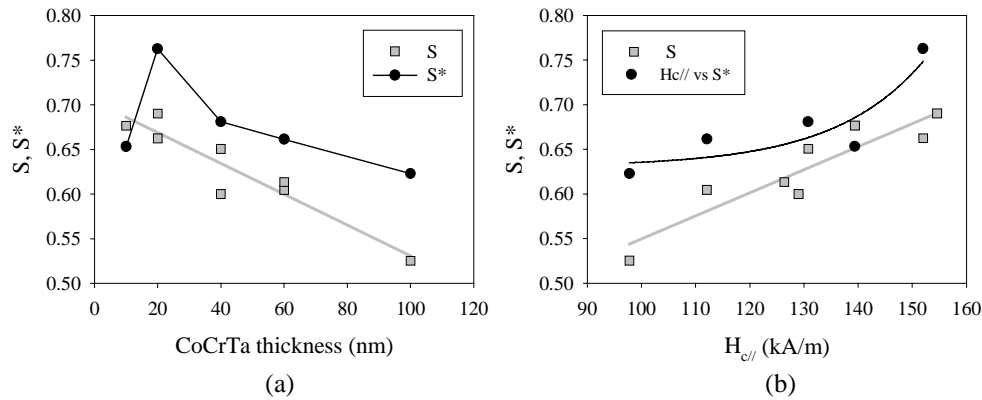


Fig. 6.3.7. Variation of squareness ( $S$ ) and coercive squareness ( $S^*$ ) with CoCrTa layer thickness (a) and with in-plane coercivity (b). The lines are guides for the eyes.

In our case, it is difficult to interpret the behavior of  $S$  and  $S^*$  with a single factor. When the CoCrTa layer thickness increases from 10 to 20nm,  $S^*$  rises probably due to an increase in exchange coupling caused by coalescence of islands [Ross-98]. At 20nm, the sample has the highest in-plane anisotropy and probably narrow distribution of anisotropy field, leading to the highest values of  $S$  and  $S^*$ . The general decrease in  $S$  and  $S^*$  with increasing CoCrTa layer thickness above 20nm could be attributed to the increase in perpendicular  $c$ -axis orientation and thus the increase in perpendicular anisotropy.

### 6.3.3.4. Effective anisotropy constants

Torque measurements were carried out in the plane perpendicular to the film plane. The first Fourier coefficients  $R_1$  ( $J/m^3$ ) derived from the torque measurements can be used as a measure of effective in-plane anisotropy constant

(Fig. 6.3.8). The first Fourier coefficient  $R_1$  gets maximum at a thickness of 60nm. This maximum does not coincide with the maximum of  $H_{c//}$  (Fig. 6.3.4), suggesting that high in-plane anisotropy is not the only cause of high coercivity. From the 10nm-thick sample (UP10) to the 60nm-thick sample (UP60), the in-plane anisotropy increases due to the development of the in-plane (or nearly in-plane) texture. When the CoCrTa layer grows thicker than 60nm, c-axis orientation of the growing film changes rapidly from in-plane (or nearly in-plane) to perpendicular direction, resulting in a sharp decrease in  $R_1$ . This agrees with the XRD measurements and the arguments in Section 6.3.3.2 about the relationship between  $H_c$ 's and texture of the CoCrTa layer.

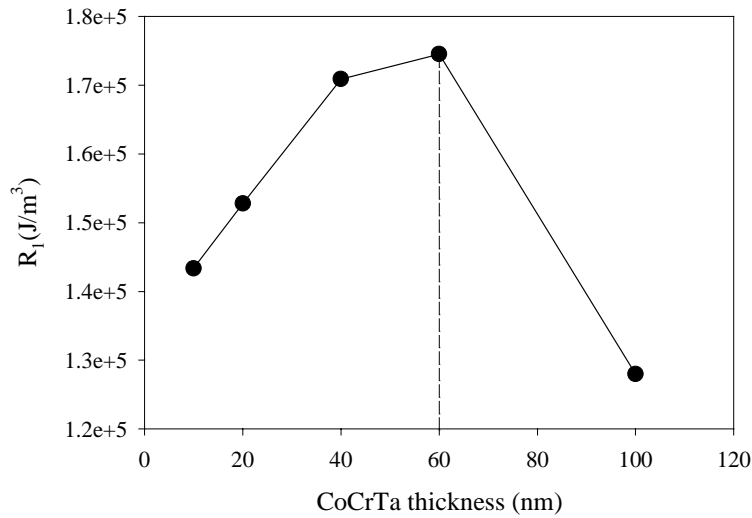


Fig. 6.3.8. First Fourier coefficient  $R_1$  as a function of CoCrTa thickness.

### 6.3.4. Viscosity

Magnetic viscosity has been measured as a function of applied field. For all samples, viscosity exhibits a peak near  $H_c$ . An example is given in Fig. 6.3.9.a. The shape of the viscosity versus field curve (viscosity curve) is not a subject of this chapter. An extensive study about viscosity curves of different types of recording media, including CoCrTa/Cr thin films, is presented in Chapter 7. Here we only concentrate on the values of the viscosity peak of the samples. The normalized values (on saturation magnetization moment  $I_s$ ) of viscosity peak,  $S_{max}$ , of the investigated samples were plotted against CoCrTa layer thickness and  $H_{c//}$  (Fig. 6.3.9.b). Except Sample UP10 (thickness = 10nm),  $S_{max}$  generally decreases with increasing layer thickness. This behavior was also observed by Suzuki et al. [Suzuki-96]. Moreover, we observed that there is a correlation between  $S_{max}$  and

### 6.3. Experiments on CoCrTa on Cr underlayer: varying CoCrTa thickness

$H_{c//}$  as plotted in Fig. 6.3.9.b (lower axis):  $S_{max}$  increases with increasing  $H_{c//}$ . This is certainly because of the difference in grain sizes and exchange coupling between grains. In thin samples, small grain size and weak exchange coupling between grains, leading to a small ratio  $KV/kT$  (see Section 3.1) could be the reason for the relatively high  $S_{max}$ . This case may fall into the second or the third type of recording media as shown in Fig. 3.1.4. When the layer becomes thicker, grain size and probably the exchange coupling increase, which leads to collective switching of magnetization (the fourth type in Fig. 3.1.4). This is equivalent to a higher ratio  $KV/kT$ . The stability of this case is therefore higher, which is observed as the decrease in  $S_{max}$  of thicker samples.

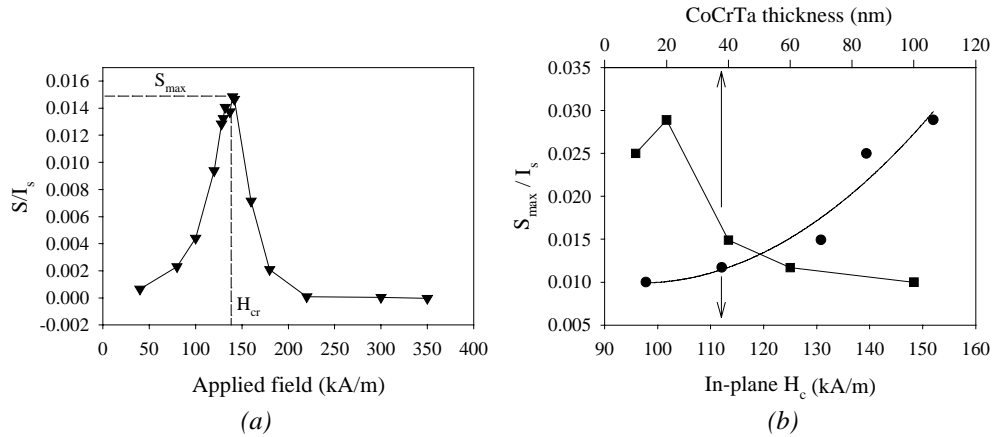


Fig. 6.3.9. (a) An example of viscosity vs. applied field (UP40); (b) Maximum viscosity  $S_{max}$  vs. CoCrTa thickness and  $H_{c//}$ .

### 6.3.5. Angular dependent measurements

This section presents some angular dependent measurements, namely angular dependence of coercivity and hysteresis loss, on the series UPxxx. Hysteresis loops were measured at various angles  $\theta$  from  $0^\circ$  (in-plane) to  $90^\circ$  (perpendicular), from which  $H_c$  and hysteresis loss (the area enclosed by the hysteresis loop) were calculated. Differently from other angular measurements (like torque, IRM or DCD measurements, etc.), the results of  $H_c$  and hysteresis loss versus angle are not affected by the demagnetization effect. This is because  $H_c$  is measured at zero magnetization where demagnetizing field is also zero and the area of a sheared loop is the same as a corresponding unsheared loop.

### 6.3.5.1. Angular dependence of coercivity

Figure 6.3.10 shows the coercivity normalized on the effective anisotropy field\* as a function of angle  $\theta$  of the investigated samples. On the same graph, theoretical angular dependence of  $H_c$  normalized on  $H_K$  of a Stoner-Wohlfarth elongated particle and of a sample switching by pure domain-wall-motion (DWM) is also plotted for comparison. It is clear that the samples do not switch either by wall motion mode or by S-W mode because there is an obvious lack of agreement between the experimental and theoretical curves. The experimental curves exhibit a peak at about 50-70°.

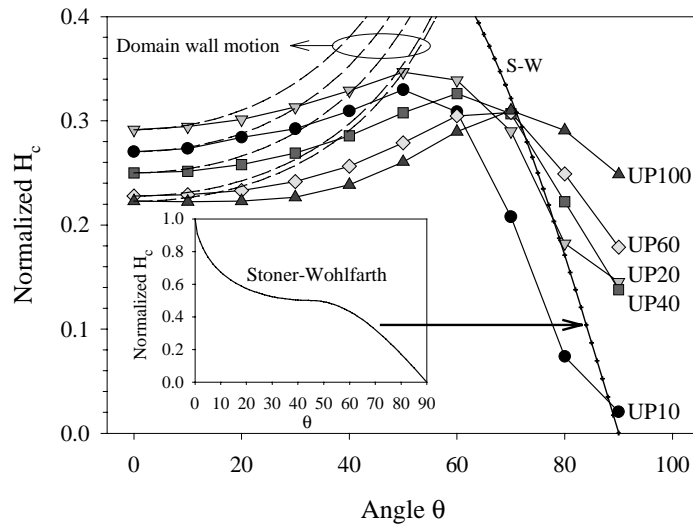


Fig. 6.3.10. Normalized coercivity (on effective anisotropy constant) as a function of measuring angle  $\theta$ . The dashed curves are normalized  $H_c$  curves calculated for domain wall motion mode and the cross-hair curve is the normalized  $H_c$  curve calculated for a Stoner-Wohlfarth particle, which is also shown as a whole in the inset.

In order to get information from the experimental curves, we refer to the theory of switching mechanisms. Figure 6.3.11 shows the calculated angular dependence of normalized coercivity for a particle of infinite cylinder (switching by S-W mode and curling mode) and a chain of spheres (switching by fanning mode) [Shtrikman-59, Luborsky-61, Lisfi-98]. According to the calculations, the particle switches by coherent mode (S-W) when  $s=1^\dagger$ . When  $s$  increases over one, the curling mode will

\* Effective anisotropy field  $H_{K,eff} = 2R_1/\mu_0 I_s$ , where  $R_1$  is the first Fourier coefficient (J) and  $I_s$  is the saturation magnetic moment of the sample ( $Am^2$ )

$^\dagger$  Normalized particle radius  $s=r/r_0$ , in which  $r_0 = A^{1/2}/M_S$ ;  $A$  is the exchange constant.

### 6.3. Experiments on CoCrTa on Cr underlayer: varying CoCrTa thickness

take place. However, the particle switches by curling only at low angle (lower than about  $60^\circ$ ). When the curling curve crosses the S-W curve at about  $60^\circ$ , the reversal mechanism changes from the curling mode to the S-W mode. The resultant  $H_c$  versus angle curve of the particle has a peak at the crossing point. When  $s$  is reduced towards one, the reversal mechanism is changing gradually from curling to S-W mode, which appears as a decrease in the peak height (compared to the value at  $0^\circ$ ) and a shift of the peak position to lower angles. Another possibility of reversal is fanning mode, which is independent of particle size. This mode has a small peak at about  $50^\circ$ . In reality, a magnetic thin film consists of grains with distribution of  $H_K$ , sizes, etc., and there are interactions between the grains. Therefore, the application of these theories to experimental cases has only qualitative meaning. Further calculations are not within the scope of this thesis.

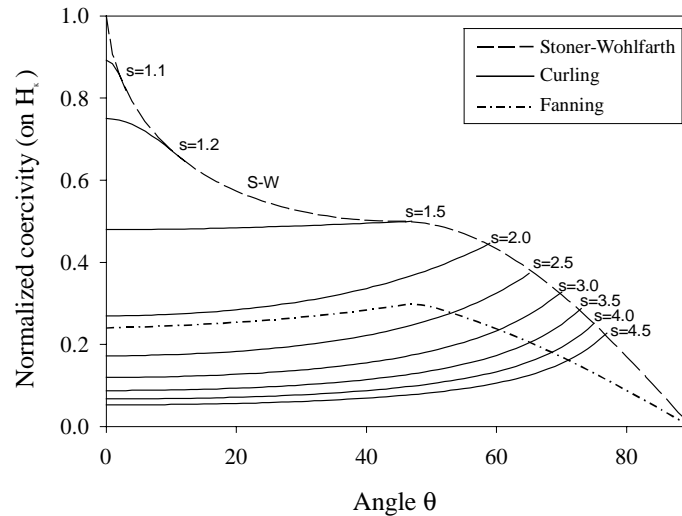


Fig. 6.3.11. Normalized coercivity (on  $H_K$ ) for S-W and curling modes in an infinite cylinder model and fanning in a chain-of-spheres model as a function of angle.

Figure 6.3.12.a shows the same curves of  $H_c$  versus angle of the samples but they are normalized on  $H_c$  at  $0^\circ$ , for ease of comparison. When the CoCrTa layer thickness is reduced (from 100 to 10nm), the peak of  $H_c$  shifts to lower angles and the maximum value of the peak tends to decrease (Fig.6.3.12.b). These facts suggest that the reversal mechanism of the thin samples is closer to S-W rotation than that of the thick samples. This is somewhat consistent with the discussions in Section 6.3.3.2, in which we suggested that the decrease in  $H_{c//}$  when the CoCrTa layer thickness increases is partially attributed to a gradual change of reversal mechanism from coherent to incoherent mode. If the curling mode is assumed to

take place, the shift of  $H_c$  peak to lower angles also indicates that the normalized particle radius  $s$  decreases. This implies that the grain size of the CoCrTa layer is reduced with decreasing layer thickness. We have not proven this; however, it is a well-known behavior [Hsu-90, Murata-93].

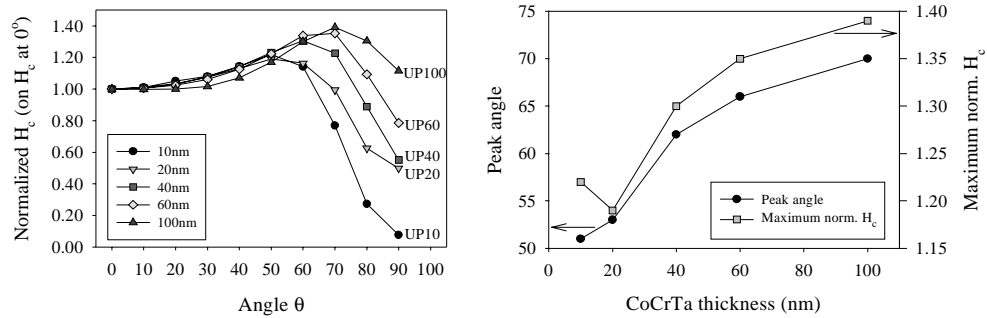


Fig. 6.3.12.  $H_c$  normalized on  $H_{c//}$  (a) and the behaviors of peak angle maximum values of  $H_c$  vs. angle curves (b).

Figure 6.3.13 shows an attempt to compare the angular dependence of  $H_c$  of Sample UP10 with that calculated for an elongated particle switching by curling and fanning modes. Apparently, the experimental curve is close to the fanning curve rather than the curling curve. The misfit between the calculated curves and the experiment curve is probably due to the fact that the practical sample consists of interacting grains with certain distributions of sizes and  $H_K$  whereas in the calculation, the sample is considered to be a single elongated particle.

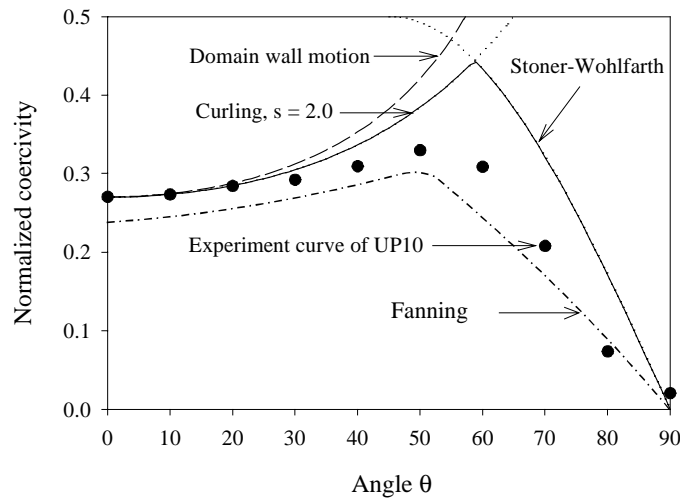


Fig. 6.3.13. Normalized  $H_c$  as a function of measuring angle of Sample UP10, compared to the calculations for an elongated particle.

### 6.3.5.2. Angular dependence of hysteresis loss

Angular dependence of hysteresis loss of the series UPxxx is plotted in Fig. 6.3.14. On the same graph, hysteresis loss of a DWM sample and of a S-W particle is also plotted for comparison. Similarly to the conclusion drawn from the angular dependence of  $H_c$ , from the dependence of hysteresis loss, we can see that the thinner the CoCrTa layer thickness, the closer to the S-W rotation the switching mechanism is. An additional information derived from these curves is that the sample having the thickest CoCrTa layer (UP100) seems to switch (probably partly) by DWM, because the hysteresis loss curve is close to that calculated for a DWM sample, which is angular independent.

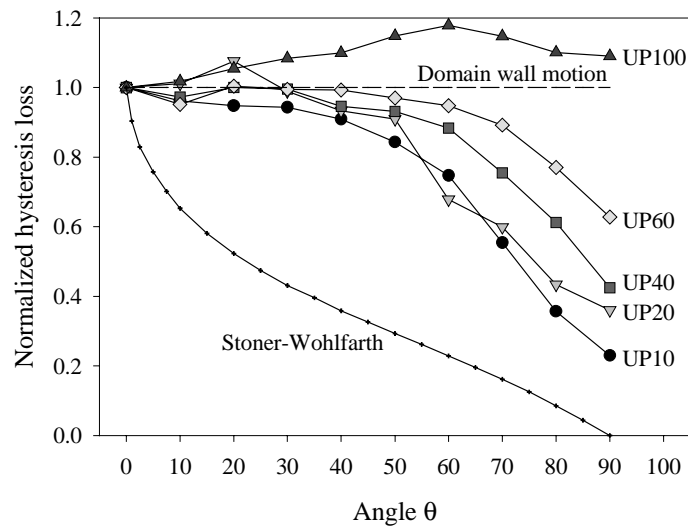


Fig. 6.3.14. Angular dependence of hysteresis loss of the series UPxxx. The dashed line represents the hysteresis loss of a sample switching by domain wall motion. The cross-hair curve is the hysteresis loss calculated for a S-W particle.

## 6.4. Experiments on CoCrTa on Cr underlayer: varying Cr thickness

In the previous section, we have investigated a series of samples (UPxxx) consisting of a Cr underlayer of fixed thickness (100nm) and a CoCrTa layer of various thicknesses. We found out that sample UP20 which has a 20nm-thick CoCrTa layer is the optimum sample in the series because it has the highest  $H_{c//}$ , high  $S$  and  $S^*$ . In the next step, which will be presented in this section, we kept the thickness of the CoCrTa layer at 20nm and varied the thickness of the Cr underlayer from 0nm to 250nm. This series is named UNxxx, which stands for variation of UNderlayer thickness.

### 6.4.1. Sputtering process

This series of samples were produced under almost the same conditions as the series UPxxx, except for the followings:

- The thickness of the Cr underlayer was varied from 0nm (i.e. no underlayer) to 250nm by changing deposition time. On top of the Cr underlayer, a CoCrTa layer of a fixed thickness of 20nm was deposited. The deposition rates of the layers are the same as the series UPxxx.
- Because the deposition time of the Cr underlayer was varied and can be very short, the setting of substrate temperature  $T_s$  as used for the series UPxxx is not suitable. For the series UNxxx,  $T_s$  was fixed at 200°C during the deposition of both Cr and CoCrTa layers. This temperature is reasonably close to the optimum temperatures of both layers.

Table 6.4.1 shows the names and general specifications of the samples.

*Table 6.4.1. Names and specifications of the samples*

Sample names	Thickness of CoCrTa layer	Thickness of Cr underlayer
UN0	20 nm	0 nm
UN15	20 nm	15 nm
UN45	20 nm	45 nm
UN75	20 nm	75 nm
UN100	20 nm	100 nm
UN150	20 nm	150 nm
UN200	20 nm	200 nm
UN250	20 nm	250 nm

## 6.4.2. Morphology

For this series, we focused on the development of morphology of the samples using TEM. To observe the development of grain size,  $\text{Si}_3\text{N}_4$  chips for TEM plane-view observation (see Section 4.3.2) were put close to the Corning glass substrate in every sputtering run. Films deposited on these membranes were used to observe TEM plane-view images.

### 6.4.2.1. Plane-view images

Bright field plane-view images of four samples, from UN0 to UN75 are given in Fig. 6.4.1. The contrast visible on the images is mainly diffraction contrast between crystalline grains. Some of them appear as black regions, because at these grains, a certain set of lattice planes lies in a proper direction that satisfies the Bragg condition, and hence, the emerging e-beam is deflected, resulting in a dark region on the bright field image. Sample UN0 contains only a single CoCrTa layer of thickness of 20nm. The grain size of this sample is only about 4nm. However, when the Cr underlayer is introduced, the grain size increases drastically with increasing the Cr thickness. Estimation of average grain sizes of these samples reveals that with an underlayer of thickness of 15, 45, and 75nm, the grain sizes are 19, 33 and 47nm, respectively. It should be mentioned here that the grains observed in these images are double grains, containing a Cr grain under a CoCrTa grain.

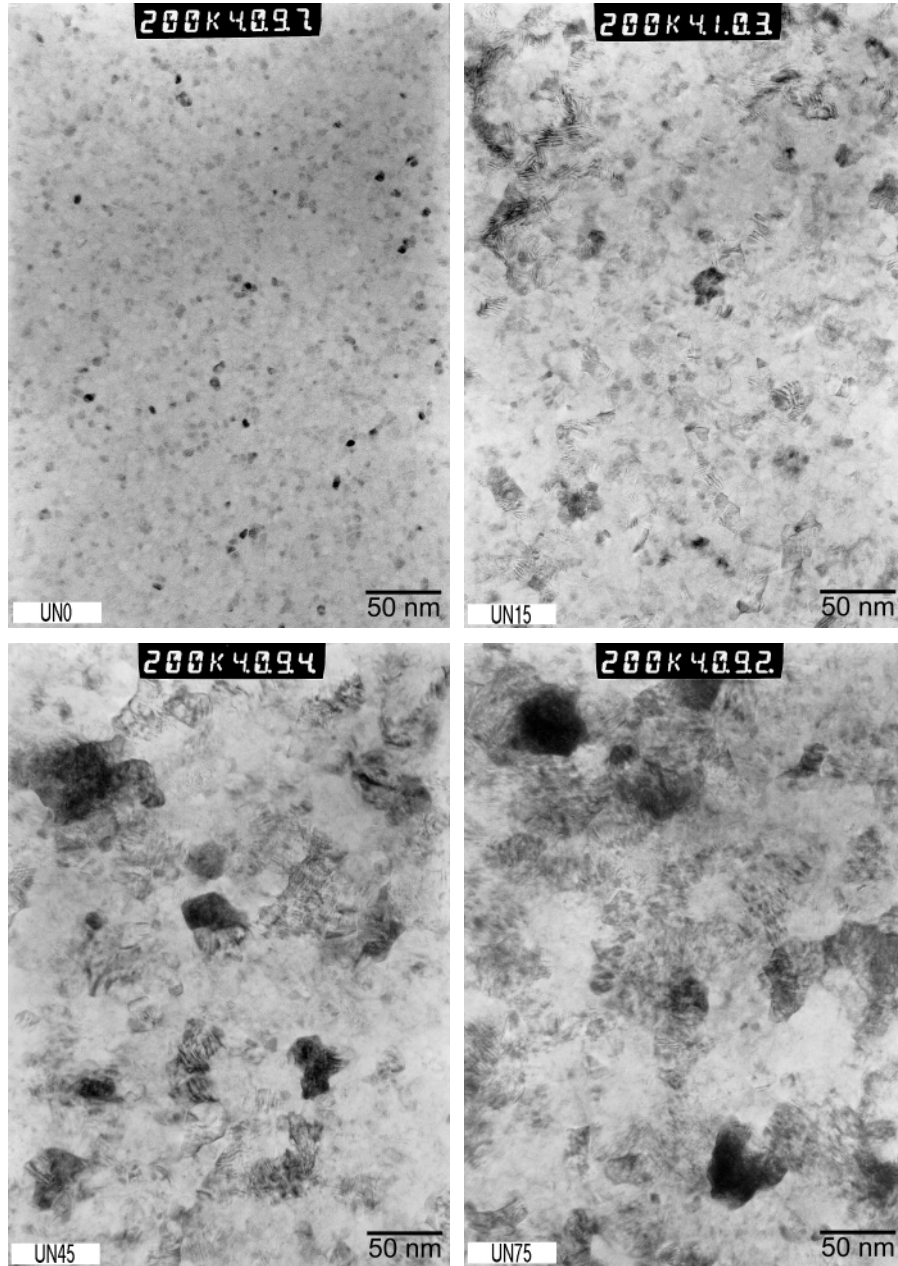


*Fig. 6.4.1. TEM plane-view images of samples UN0-UN75. Average grain sizes of samples UN0, UN15, UN45, UN75 are 4, 19, 33, 47nm, respectively.*

#### 6.4.2.2. Cross-sectional images

To have more information about the morphology of the samples, bright field images of cross-section of samples UN15 and UN75 have been taken (Fig. 6.4.2). The grains can be easily recognized by the contrast of their columnar structure. The columnar grains have almost vertical boundary. The contrast of the grains is the diffraction contrast caused by the difference in orientations of the grains, suggesting that the samples are polycrystalline and each grain appears to be a single crystal. It is obvious that commonly, a CoCrTa grain is grown on top of a Cr grain; they have the same size and form a double grain, which can also be seen on the corresponding plane-view images (Fig. 4.6.1). The interface between two layers is clear and rather smooth. Grain sizes estimated from the cross-sectional images are similar to those obtained from the plane-view images. The average grain sizes of samples UN15 and UN75 are 17 and 41nm, respectively. The columnar structure of the grains of sample UN75 is clearer than that of sample UN15. In the image of sample UN75 (Fig. 6.4.2), a bright line at the interface between two layer can be seen. This could be due to a thin layer of oxide formed at the interface and/or due to elastic strain between two layers due to lattice misfit between them [Wong-92].

Looking into detail of several double grains, we can observe the lattice fringes (caused by phase contrast) on both CoCrTa and Cr grains. Figure 6.4.3 shows a magnified image of sample UN75. Continuous lattice fringes running from the Cr grain to the CoCrTa grain indicate that in this double grain, epitaxial growth occurs between the CoCrTa grain and the Cr grain. To have such an epitaxial growth, the interface between two layers must be free of contamination. Therefore, we can deduce that the contrast at the interface between two layers of sample UN75 is mainly caused by the elastic strain between them [Wong-92].

6. CoCrTa/Cr thin films for longitudinal recording

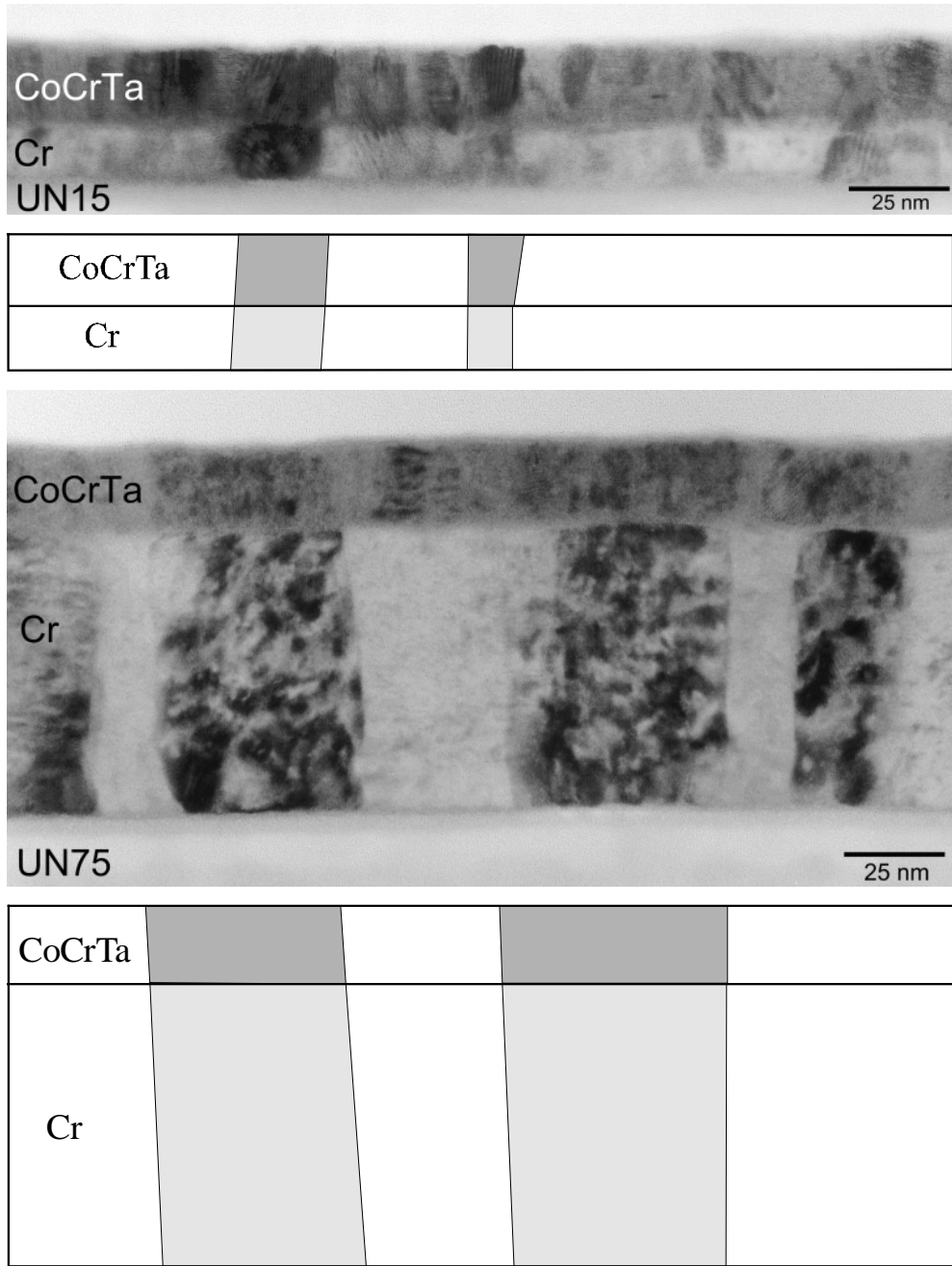


Fig. 6.4.2. Cross-section of samples UN15 and UN75. The corresponding schematic drawings under each TEM image are guides to indicate the possible grains observed in the images. Average column width of sample UN15 is 17nm and of sample UN75 is 41nm.

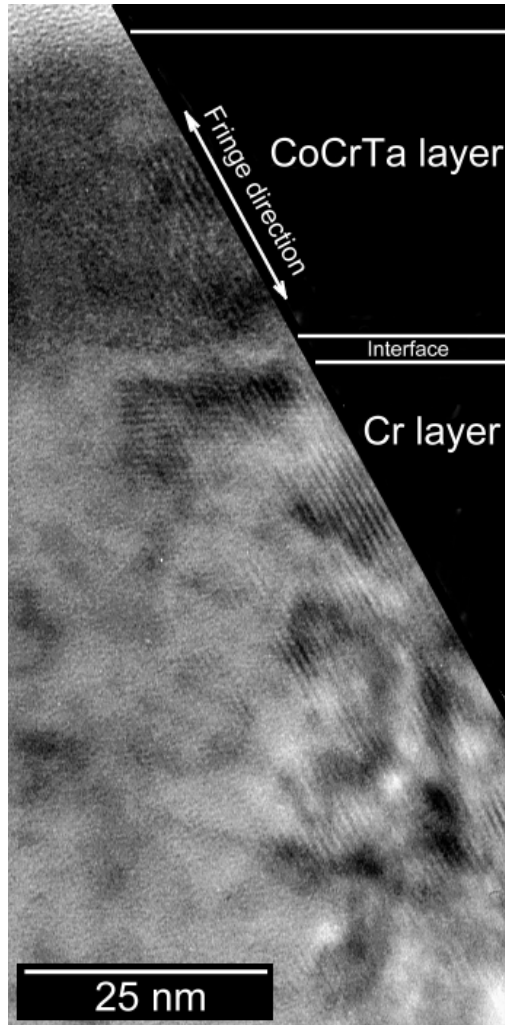
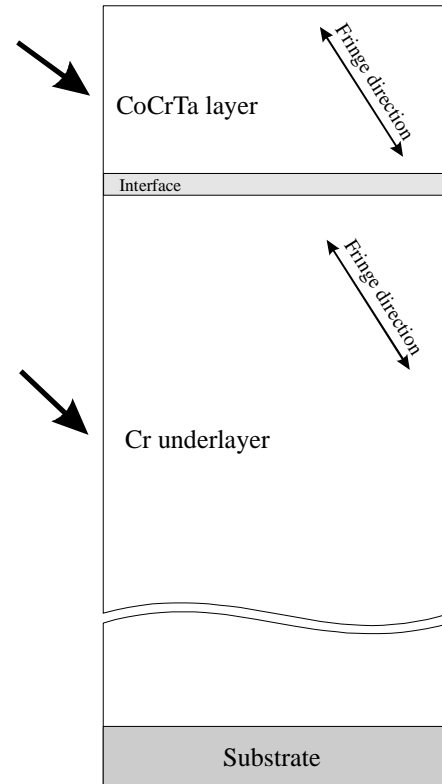


Fig. 6.4.3. A magnified image of sample UN75. Continuous lattice fringes running from the Cr grain to the CoCrTa grain suggest that epitaxial growth occurs. The drawing below helps readers to understand better the image.



Information from Fig. 6.4.1 and Fig. 6.4.2 allows us to say that with an underlayer, the CoCrTa grains, which would have small sizes if deposited directly on the substrate, become larger, comparable to the sizes of Cr grains. This phenomenon is probably accompanied by the formation of *bicrystal clusters*, which can be explained as follows. At the first stage of layer growth, small CoCrTa islands growing on top of a Cr grain may have c-axis orientation along two orthogonal directions due to the epitaxial relationship. For instance, growing on a Cr(200) grain, the c-axes of CoCrTa islands having the  $(11\bar{2}0)$  texture may be parallel to either  $[110]$  or  $[\bar{1}10]$  axis of the Cr grain [Wong-92, Hosoe-95]. The islands with parallel c-axes can merge together to become a larger single crystal. This

mechanism is suggested to form larger CoCrTa grains (compared to the case without an underlayer). Eventually, on top of a Cr grain, there could be a bicrystal cluster consisting of several grains with their  $c$ -axes perpendicular or parallel to each other [Hosoe-95, Ross-98]. A schematic diagram of the bicrystal structure is shown in Fig. 6.4.4. When the cross-section of the sample is observed in a TEM, the crystallites inside a bicrystal cluster produce the same diffraction contrast on the image because they belong to one texture [the  $(11\bar{2}0)$  texture, for instance]. Therefore, in the cross-sectional images, we do not observe clear evidence of the bicrystal structure.

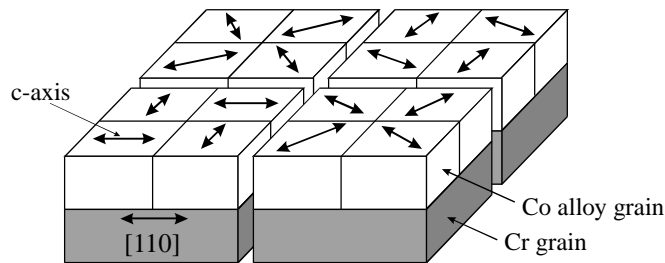


Fig. 6.4.4. Bicrystal structure of Co-alloy layer grown on Cr underlayer [Hosoe-95]

## 6.4.3. General magnetic properties

### 6.4.3.1. Coercivity

Hysteresis loops of the samples were measured and coercivities were calculated. Figure 6.4.5 plots the in-plane and perpendicular coercivity as a function of Cr underlayer thickness. The in-plane coercivity increases abruptly with increasing Cr layer thickness and tends to be saturated at a thickness of about 50nm. This is a well-known behavior, found in all kinds of Co-alloy layer grown on Cr underlayer [Allan-87, Yogi-88, Lee-88, Chen-86, Murata-93, Shen-94]. Differently from  $H_{c//}$ , perpendicular coercivity  $H_{c\perp}$  increases monotonously with the Cr thickness. The ratio of  $H_{c//}$  to  $H_{c\perp}$  is used to evaluate the in-plane anisotropy of the samples. This ratio increases very fast with increasing Cr thickness from 0 to 15nm, exhibiting a peak at about 75nm and then decreases (Fig. 6.4.6). This curve suggests that when the Cr underlayer thickness is from 15 to 75nm, the films have good in-plane anisotropy; and at 75nm, it is the best.

## 6.4. Experiments on CoCrTa on Cr underlayer: varying Cr thickness

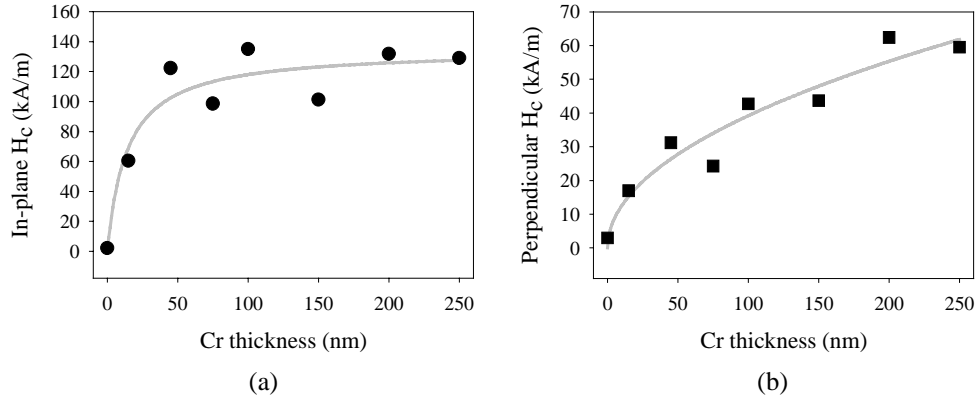


Fig. 6.4.5. Variations of (a) in-plane and (b) perpendicular coercivities with Cr underlayer thickness. The gray curves are guides for the eyes.

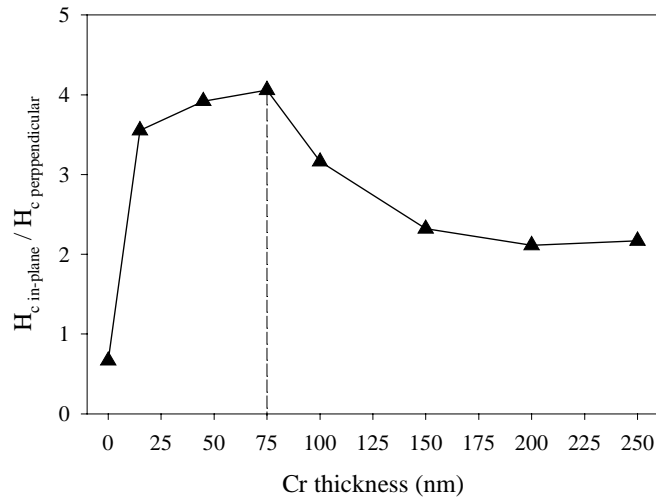


Fig. 6.4.6. The ratio  $H_{c//} / H_{c\perp}$  versus Cr underlayer thickness.

### 6.4.3.2. Squareness

Remanence squareness  $S$  of the series UNxxx behaves like the ratio  $H_{c//} / H_{c\perp}$ . It exhibits a peak at around 45-75nm. However, coercive squareness  $S^*$  seems to be saturated at a thickness of 45nm.

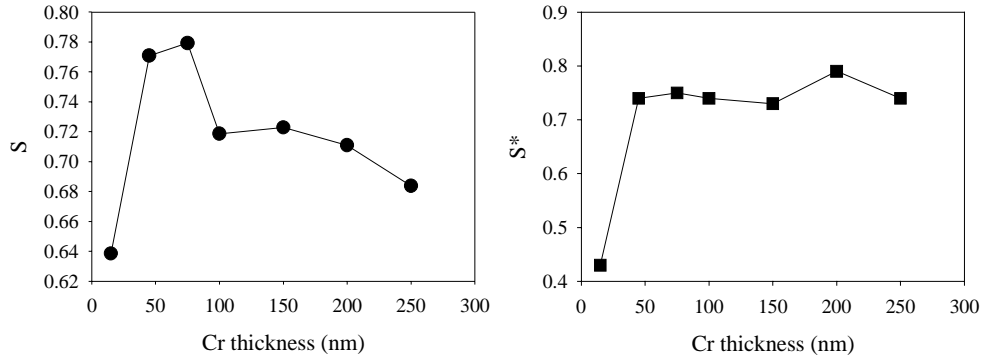


Fig. 6.4.7. Remanence squareness  $S$  and coercive squareness  $S^*$  versus Cr underlayer thickness.

### 6.4.3.3. Effective anisotropy constant

By dividing the first Fourier coefficient (from torque measurements) by the sample volume, the effective anisotropy constant  $R_1$  can be obtained. This quantity determines the degree of in-plane anisotropy, including shape anisotropy and crystalline anisotropy. Interestingly, the behavior of  $R_1$  is quite similar to that of  $H_{c\parallel}/H_{c\perp}$  and  $S$ . It increases fast to a maximum at a thickness of about 45-75nm and then decreases slowly with increasing Cr thickness.

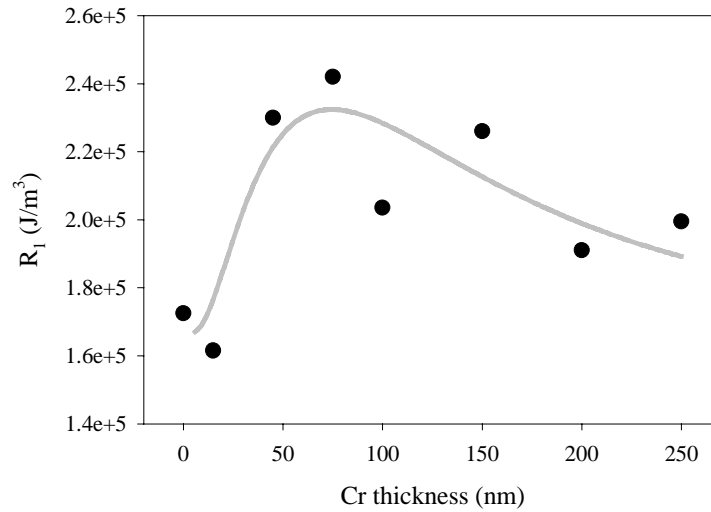


Fig. 6.4.8. Effective anisotropy constant  $R_1$  as a function of Cr underlayer thickness

### 6.4.3.4. Discussion

The general magnetic properties presented above are clearly affected by the Cr underlayer thickness. Without the Cr underlayer, sample UN0 has almost no hysteresis, due to the fact that the CoCrTa layer thickness of 20nm is still under the initial thickness (see Section 5.2.1). The reversal mechanism of this sample is mainly domain wall motion, as will be proven in the next section, which is the cause of low coercivity. An introduction of only 15nm-thick underlayer in sample UN15 drastically raises the coercivity, especially  $H_{c//}$  (Fig. 6.4.5). Further increase in the thickness of Cr underlayer to 75-100nm continues to increase  $H_{c//}$  to about 120kA/m and  $H_{c\perp}$  to about 40kA/m. This is undoubtedly caused by the improvement of the Cr(200) and Cr(110) textures when Cr underlayer thickness is increased, which has been discussed in Section 6.2.3. The development of the Cr(200) and Cr(110) textures causes the c-axes of the CoCrTa layer to grow in-plane, resulting in the increase in  $H_{c//}$ .

However, as observed, an increase in  $H_{c//}$  is always accompanied by an increase in  $H_{c\perp}$ . This is probably because when growing on the Cr underlayer consisting of well-defined columnar grains, the CoCrTa layer has also better defined grains. The intergranular interaction is weaker and therefore causes higher coercivity in the perpendicular direction, besides the in-plane coercivity. This explains the drastic increase in  $H_{c//}$  and  $H_{c\perp}$  when the thinnest Cr underlayer is introduced (sample UN15). Moreover, it is well-known that in the theory of reversal mechanism, Stoner and Wohlfarth [Stoner-48] proved that only for a particle or a system of easy-axis-aligned particles switching by coherent or incoherent mode, the coercivity measured at perpendicular direction (to the direction of easy-axis) is zero. In practice, the alignment is usually not perfect and therefore,  $H_{c\perp}$  can take up values comparable to  $H_{c\perp}$  [Wohlfarth-59]. In our case, because there is always a certain distribution of c-axes,  $H_{c\perp}$  can have a value up to a certain percentage of  $H_{c//}$ . When  $H_{c//}$  is increased due to any reason, statistically,  $H_{c\perp}$  is also increased to a certain extend.

Besides the increase in coercivity, the improvement of in-plane c-axis orientation also leads to the improvement of the effective anisotropy constant and consequently, of the squarenesses as well (Fig. 6.4.7).

When the Cr underlayer is further increased, beyond 100nm, there are two factors competing against each other. At one side, the slight decrease in the effective anisotropy constant (Fig. 6.4.8) and, probably, the increase in grain size of CoCrTa layer (Fig. 6.4.1), tend to reduce  $H_{c//}$ . At the other side, the improvement of in-plane c-axis orientation, due to better epitaxial growth, tends to increase  $H_{c//}$ . This competition finally results in the saturation of  $H_{c//}$  of the samples with thick Cr underlayer (Fig. 6.4.5).

A brief conclusion can be drawn from this section: an introduction of the Cr underlayer drastically increases  $H_{c//}$ ,  $S$ ,  $S^*$  and in-plane anisotropy. A Cr thickness of about 45-75nm is considered the optimum underlayer thickness, under our deposition conditions.

## 6.4.4. Initial susceptibility

### 6.4.4.1. Principle

Initial magnetization curve (initial curve) reveals some information about the switching mechanisms of magnetic samples. In the upper graph of Fig. 6.4.9, examples of three typical types of initial curve are given.

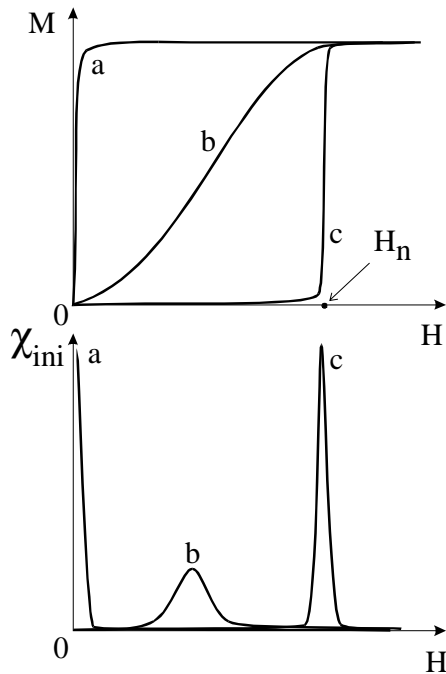


Fig. 6.4.9. Initial curves and initial susceptibility of three types of samples.

*a: typical domain-wall-motion sample.*

*b: normal sample, switching mainly by incoherent rotation mode.*

*c: typical Stoner-Wolhfarth sample, in this case,  $H_n$  is identical to  $H_K$ .*

If the initial curve starts with a steep slope at nearly zero field, the sample is said to switch by domain wall motion (curve a). In this sample, only a small field is able to move domain walls and to drive the sample quickly to the state of saturation magnetization. The initial susceptibility ( $\chi_{ini}$ ), which is the derivative  $dM/dH$ , is very large near zero field and vanishes abruptly with increasing field. In contrast, initial curve c comes from a typical Stoner-Wolhfarth sample. In this sample, magnetization of the sample remains zero until the field reaches a nucleation field  $H_n$ , at which the magnetization rises abruptly to the saturation

#### 6.4. Experiments on CoCrTa on Cr underlayer: varying Cr thickness

state. As a result, the initial susceptibility has a high and narrow peak at  $H_n$ . In the ideal case, it is a Dirac function and the nucleation field  $H_n$  is identical to the anisotropy field  $H_K$ . In between the two extreme cases mentioned above, magnetization of a sample having curve b switches by the incoherent rotation mode, or a combination of several modes. The initial susceptibility curve is a Gaussian curve with a moderate peak height. The height and the width of the peak are also considered as measures of SFD.

Using information from the initial susceptibility curves, we can judge whether the reversal mechanism of a sample is close to the domain wall motion mode or the coherent mode.

##### 6.4.4.2. Results

Initial magnetization curves of several samples UNxxx were measured after they were AC-demagnetized by rotating in a decreasing field. Only four interesting samples were selected for the measurements, namely UN0, UN15, UN75 and UN250. The initial susceptibility was then calculated and the results are shown in Fig. 6.4.10. It can be seen clearly that sample UN0 behaves like the case a in Fig. 4.6.9, which indicates that the reversal mechanism of this sample is mainly domain wall motion. When the Cr underlayer thickness increases to 15, 75 and 250nm,  $\chi_{ini}$  curves of all samples exhibit a peak near their  $H_{c//}$ 's, similar to the curve b as shown in Fig. 6.4.9 and the peaks tends to move to higher fields. This means there is a tendency of moving towards the S-W mode when the Cr thickness is increased.

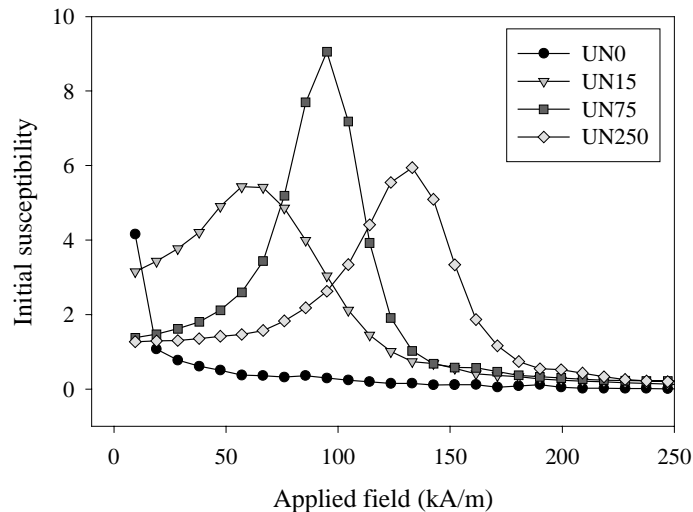


Fig. 6.4.10. Initial susceptibility curves of several samples with various Cr underlayer thickness.

To compare these  $\chi_{ini}$  curves to the S-W case, the field positions  $H_{sus-peak}$  of the  $\chi_{irr}$  peaks are normalized to the effective anisotropy field  $H_{K-eff}$ . Figure 6.4.11 shows normalized  $H_{sus-peak}$  and peak height  $\chi_{ini-max}$  versus Cr thickness of samples UN15, UN75 and UN250. In principle, a sample is said to be close to the S-W mode when the normalized  $H_{sus-peak}$  is close to one and  $\chi_{ini-max}$  is as large as possible. However, Fig. 6.4.11 shows that there is no such a unique tendency. Both samples UN75 and UN250 behave like they are closer to the S-W mode than the others. Sample UN75 has higher  $\chi_{ini-max}$  but lower normalized  $H_{sus-peak}$  than sample UN250. This is because in practical samples there always exists exchange coupling which tends to reduce SFD, which leads to higher and narrower  $\chi_{ini}$  peak of this case, and tends to decrease  $H_c$  which is closely correlated to  $H_{sus-peak}$ . It can be concluded here that sample UN75 has stronger exchange coupling than sample UN250.

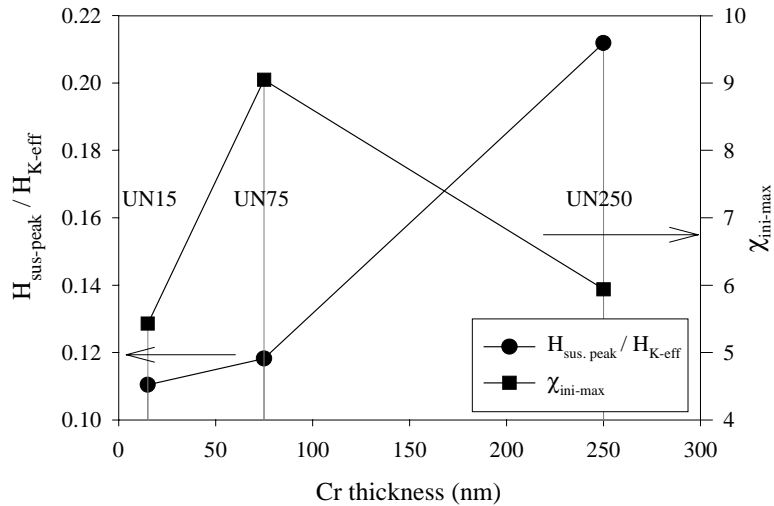


Fig. 6.4.11. Field positions of  $\chi_{ini}$  peaks normalized on  $H_{K-eff}$  and maximum values of  $\chi_{ini}$  peaks ( $\chi_{ini-max}$ ) versus Cr thickness.

### 6.4.5. Angular dependent measurements

Angular dependence of coercivity and hysteresis loss was measured for the series UNxxx. As expected, sample UN0 exhibits the domain-wall-motion (DWM) behavior. Its coercivity and hysteresis loss versus angle can be fitted pretty well to the DWM mode (Fig. 6.4.12). This result is consistent with initial magnetization measurements in the previous section.

The results of angular dependence of  $H_c$  of the other samples are depicted in Fig. 6.4.13. From Fig. 6.4.13.a, we can easily compare these curves to the theoretical

#### 6.4. Experiments on CoCrTa on Cr underlayer: varying Cr thickness

curves of the curling mode (see Fig. 6.3.11). Sample UN250 seems to be close to the fanning mode while the others probably switch by curling. Figure 6.4.13.b is used to see the tendency of the reversal modes. However, there is no clear difference between those curves. The peaks of  $H_c$  of samples UN75 and UN150 are slightly higher than that of the other samples. This phenomenon is not understood.

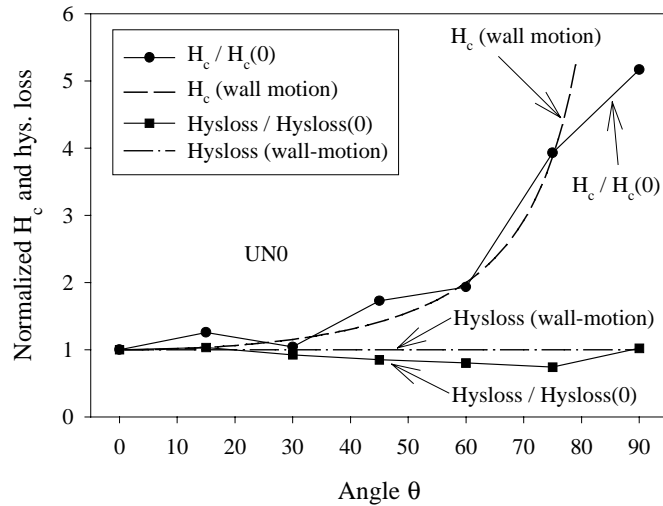


Fig. 6.4.12. Normalized  $H_c$  and hysteresis loss (on values at  $0^\circ$ ) of sample UN0. The experimental curves are fitted to the domain-wall-motion mode.

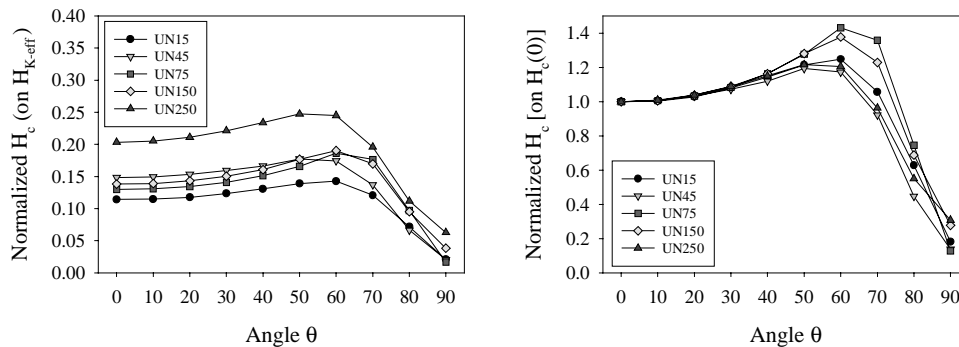


Fig. 6.4.13. Angular dependence of coercivity. (a)  $H_c$  is normalized on  $H_{K-eff}$  and (b)  $H_c$  is normalized on  $H_c$  at  $0^\circ$ . Samples UN100 and UN200 are omitted because there is no significant difference between them and samples UN150 and UN250.

Hysteresis loss measurements of the investigated samples (except sample UN0) are presented in Fig. 6.4.14.a. To compare these curves to S-W and DWM curves, they

are normalized on the values at  $0^\circ$  (Fig. 6.4.14.b). There seems to be no remarkable difference between the curves. Sample UN15 seems to be close to the DWM mode than the other, at  $\theta$  lower than  $50^\circ$ . This is reasonable because this sample is at the transition between pure DWM mode (sample UN0) and incoherent mode (the other samples).

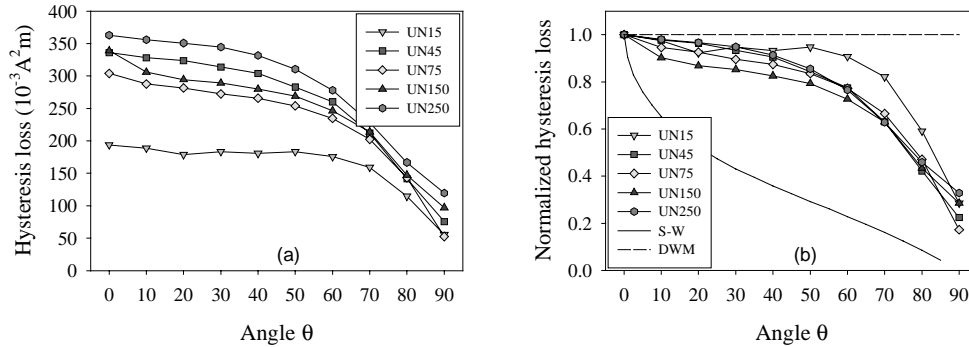


Fig. 6.4.14. Angular variation of hysteresis loss of samples UNxxx. (a) Measured hysteresis loss ( $10^{-3} A^2 m$ ). (b) Hysteresis loss normalized on values at  $0^\circ$ . Samples UN100 and UN200 are omitted because there is no significant difference between them and samples UN150 and UN250.

## 6.5. Conclusion

Chapter 6 began with an introduction to the role of Cr underlayer in CoCrTa/Cr longitudinal recording media and the epitaxial relationships between the Co-alloy magnetic layer and the Cr underlayer. There are six possible relationships, among which, CoCrTa(10 $\bar{1}$ 1) planes on Cr(110) planes and CoCrTa(11 $\bar{2}$ 0) planes on Cr(200) planes are the most common and important relationships.

In the first step, we studied single Cr layers on different types of substrates and under different sputtering conditions, in order to find a way to control and to optimize the texture of the Cr layer. Among several kinds of substrates, we found that Corning glass is the most suitable substrate for Cr films. A substrate temperature  $T_s$  of about 200-250°C was found to create a Cr film (100nm-thick) with both (110) and (200) textures. High  $T_s$  promotes the (200) texture, whereas at low  $T_s$ , only Cr(110) exists. Varying Cr film thickness, we found that 100nm-thick film has comparably strong (110) and (200) textures. Grain size increases with increasing layer thickness. Argon pressure has equal effects on both textures, and it was found to be optimum at  $3 \times 10^{-2}$  mbar.

## 6.5. Conclusion

---

In the next step, we deposited a CoCrTa layer of various thicknesses on a Cr underlayer of fixed thickness (series UPxxx). The in-plane coercivity exhibits a peak at 20nm whereas the perpendicular coercivity increases monotonously with CoCrTa thickness. Similarly, coercive squareness  $S^*$  was found to have the highest values at the thickness of 20nm, suggesting that 20nm is the optimum thickness for CoCrTa layer. Magnetic viscosity versus applied field of the samples was investigated. The maximum of viscosity has a correlation with  $H_{c//}$ : it increases with increasing  $H_{c//}$ . Finally, we studied angular dependence of coercivity and hysteresis loss of the samples UPxxx. Comparison between measurements and theories of reversal mechanisms indicates that the magnetization of the samples switch mainly by the incoherent rotation mode. There is a tendency to change from the incoherent to coherent rotation when the CoCrTa thickness is reduced.

Lastly, we deposited a CoCrTa layer of fixed thickness onto a Cr underlayer of various thicknesses (series UNxxx). In this series, we focused on the morphology of the layers. Plane-view TEM images show that grain size increases with increasing Cr underlayer thickness. From the cross-sectional images, it was found that the samples have clear columnar structure. Commonly, a CoCrTa grain grows epitaxially on top of a Cr grain. We suggested that the CoCrTa grain could be a bicrystal cluster consisting of several grains with their c-axes parallel or perpendicular to each other. Concerning magnetic properties, the in-plane coercivity increases abruptly when the Cr underlayer is introduced and tends to be saturated when the Cr layer is about 50nm thick. The squareness  $S$  and the in-plane anisotropy constant were found to increase with increasing Cr thickness and exhibit a peak at about 45-75nm. This suggested that a Cr underlayer of thickness within this range be considered the optimum thickness for longitudinal recording. Moreover, we investigated the initial susceptibility of the samples. From the results of these measurements, we found that sample UN0 (without an underlayer) switches by the domain wall motion mode. When the Cr underlayer is thicker, the reversal mode changes to incoherent and tends to move to coherent mode in the samples having thick Cr underlayer. Angular dependence of coercivity and hysteresis loss was also measured. The measurements revealed almost the same conclusions as the initial susceptibility measurements.

## 6.6. References

- [Allan-87] J. C. Allan and R. D. Fisher. "A comparison of magnetic and recording properties of sputtered ternary alloys for high density applications". IEEE Trans. Magn. MAG-23 (1987), 122.

## 6. CoCrTa/Cr thin films for longitudinal recording

---

- [ASM-90] ASM International. "Metal handbook". 10<sup>th</sup> edition. Vol. 2 (1990)
- [Chen-86] G. L. Chen. "New longitudinal recording media  $\text{Co}_x\text{Ni}_y\text{Cr}_z$  from high rate static magnetron sputtering system". IEEE Trans. Magn. MAG-22 (1986), 334.
- [Cullity-72] B. D. Cullity. "Introduction to magnetic materials". Addison-Wesley (1972).
- [Daval-70] J. Daval and D. Randet. "Electron microscopy on high-coercive force Co/Cr composite films". IEEE Trans. Magn. MAG-6 (1970), 4733.
- [Dean-96] C. Dean, R. W. Chantrell, H. Suzuki, N. Kodama and P. R. Bissell. "Simulations of highly anisotropic Co-Cr-Ta thin films". J. Appl. Phys. 79(8) (1996), 6467.
- [Duan-90] S. L. Duan, J. O. Artman, B. Wong and D. E. Laughlin. "The dependence of the microstructure and magnetic properties of CoNiCr/Cr thin films on the substrate temperature". IEEE Trans. Magn. 26 (1990), 1587.
- [Feng-94] Y. C. Feng, D. E. Laughlin and D. N. Lamberth. "Formation of crystallographic texture in RF sputter-deposited Cr thin films". J. Appl. Phys. 76(11) (1994), 7311.
- [Hono-90] K. Hono, B. Wong and D. E. Laughlin. "Crystallography of Co/Cr bilayer magnetic thin films" J. Appl. Phys. 68(9) (1990), 4734.
- [Hosoe-95] Y. Hosoe, Y. Yahisa, R. Tsuchiyama, A. Ishikawa, K. Yoshida, M. Igarashi and Y. Shiroyishi. "Bicrystal cluster structure and magnetic properties of CoCrTa/Cr thin film media". IEEE Trans. Magn. 31 (1995), 2824.
- [Howard-87] J. K. Howard, R. Ahlert and G. Lim. "Effect of polycrystalline sublayer films on the magnetic and structural properties of CoCr films". J. Appl. Phys. 61(8) (1987), 3834.
- [Hsu-89] Y. Hsu, J. M. Sivertsen and J. H. Judy. "Effective initial thickness of RF sputtered CoCrTa/Cr films". J. Magn. Soc. of Japan 13 (Supp. No. S1) (1989), 651.
- [Hsu-90] Y. Hsu, J. M. Sivertsen and J. H. Judy. "Texture formation and magnetic properties of RF sputtered CoCrTa/Cr longitudinal thin films". IEEE Trans. Magn. 26 (1990), 1599.
- [Huang-96] J. C. A. Huang, F. C. Tang, W. W. Fang, R. L. Liu, Y. M. Hu, C. K. Lo, Y. Liou, Y. D. Yao, W. T. Yang, C. P. Chang and S. Y. Liao. "Studies of the magnetic anisotropies of  $\text{Co}(1\bar{1}00)/\text{Cr}(211)$  and  $\text{Co}(11\bar{2}0)/\text{Cr}(100)$  multilayers". J. Appl. Phys. 79(8) (1996), 4790.
- [Lal-94] B. B. Lal, M. Tobise and Shinohara. "Effect of very thin Cr-underlayer

## 6.6. References

---

- on the magnetic and recording properties of CoCrTa thin film media". IEEE Trans. Magn. 30 (1994), 3954.
- [Laughlin-91] D. E. Laughlin and B. Y. Wong. "The crystallography and texture of Co-based thin film deposited on Cr underlayers". IEEE Trans. Magn. 27 (1991), 4713.
- [Lazzari-67] J. P. Lazzari, I. Melnick and D. Randet. "Thin evaporated films with high coercive force. IEEE Trans. Magn. MAG-3 (1967), 205.
- [Lee-88] H. Lee. "The crystal growth and magnetic properties of sputtered Co-Ni films on bcc polycrystalline underlayers". J. Appl. Phys. 63(8) (1988), 3269.
- [Lisfi-98] A. Lisfi. Unpublished.
- [Lodder-98] J. C. Lodder. "Magnetic recording hard disk thin film media". Handbook of magnetic materials. Vol. 11 (1998), edited by K. H. J. Buschow.
- [Lu-89] M. Lu, Q. Chen, J. H. Judy and J. M. Sivertsen. "Effects of Cr underlayers and CoCr thickness on the coercivity and the magnetization reversal mechanisms in CoCr/Cr films". J. Magn. Soc. of Japan 13 (Supp. No. S1) (1989), 435.
- [Luborsky-61] Luborsky, E. Fred. "Development of elongated particle magnets". J. Appl. Phys. 32 (1961), 171S.
- [Lyakhovich-96] T. Lyakhovich, A. Umpelev, G. Flerova. "Optimal texture of magnetic recording media". IEEE Trans. Magn. 32 (1996), 3629.
- [Maeda-91] Y. Maeda, K. Takei, S. Yamamoto and Y. Nakamura. "Compositional microstructures in Co-Cr films for perpendicular magnetic recording". J. Magn. Soc. of Japan 15 (Supp. No. S2) (1991), 457.
- [Mirzamaani-91] M. Mirzamaani, C. V. Jahnes and M. A. Russak. "Magnetic properties of CoPtCr thin films with  $(11\bar{2}0)$  crystal orientation". J. Appl. Phys. 69(8) (1991), 5169.
- [Murata-93] H. Murata, H. Kogure, K. Ichikawa and T. Shinohara. "Magnetic properties and microstructure of CoCrTa/Cr magnetic recording media". IEEE Trans. Magn. 8 (1993), 298.
- [Ohno-89] T. Ohno, Y. Shiroishi, S. Hishiyama, H. Suzuki and Y. Matsuda. "Modulation and crystallographic orientation of sputtered CoNi/Cr disks for longitudinal recording". IEEE Trans. Magn. MAG-23 (1989), 2809.
- [Parker-91] M. A. Parker, K. E. Johnson, C. Hwang and A. Bermea. "A cross-section TEM study of the microstructure evolution of CoPtCr/Cr thin films and the effect on magnetic properties". IEEE Trans. Magn. 27

- (1991), 4730.
- [Reimer-97] L. Reimer. "Transmission electron microscopy - Physics of image formation and microanalysis". Springer series in optical sciences, Vol. 36 (1997).
- [Rogers-94] D. J. Rogers, Y. Maeda, K. Takei, Y. Shen and D. E. Laughlin. "Investigations of compositional separation in Co-Cr-Ta/Cr thin film recording media". J. Magn. Magn. Mat. 135 (1994), 82.
- [Ross-98] C. A. Ross, F. M. Ross, G. Bertero and K. Tang. "Microstructural evolution and thermal stability of thin CoCrTa/Cr films for longitudinal magnetic recording media". IEEE Trans. Magn. 34 (1998), 282.
- [Sanders-89] I. L. Sanders, J. K. Howard, S. E. Lambert and T. Yogi. "Influence of coercivity squareness on media noise in thin film recording media". J. Appl. Phys. 65(3) (1989), 1234.
- [Shen-92] Y. Shen, D. E. Laughlin and D. N. Lamberth. "Effects of substrate temperature on magnetic properties of CoCrTa/Cr films". IEEE Trans. Magn. 28 (1992), 3261.
- [Shen-94] Y. Shen, D. E. Laughlin and D. N. Lamberth. "Materials and processing aspects of CoCrTa/Cr longitudinal recording media. I. Processing and magnetic properties". J. Appl. Phys. 76(12) (1994), 8167.
- [Shtrikman-59] S. Shtrikman and D. Treves. "The coercive force and rotational hysteresis of elongated ferromagnetic particles". Le journal de Physique et le Radium. 20(1959), 286.
- [Speliotis-90] D. E. Speliotis. "Coercive squareness and media noise in thin film magnetic recording media". J. Magn. Magn. Mat. 83 (1990), 79.
- [Stoner-48] E. C. Stoner and E. P. Wohlfarth. "A mechanism of magnetic hysteresis in heterogeneous alloys". Phys. Trans. of the Roal Soc. of London, series A: Math. and Phys. Sci. 240, A. 826 (1948), 74.
- [Suzuki-96] H. Suzuki, P. R. Bissell, R. W. Chantrell and N. Kodama. "In-plane time-dependent magnetisation and magnetic interactions of Co-Cr-Ta thin films". J. Magn. Magn. Mat. 155 (1996), 196.
- [Tang-93] L. Tang and G. Thomas. "Microstructure and texture evolution of Cr thin films with thickness". J. Appl. Phys. 74(7) (1993), 5025.
- [ten Berge-92] Peter ten Berge. "The effect of substrate materials on the structural and magnetic properties of Co-Cr recording media". Ph.D. thesis - University of Twente, the Netherlands, 1992.
- [Tsai-92] H. Tsai, B. B. Lal and A. Eltoukhy. "Preferred orientation in Cr- and Co-based thin films and its effects on the read/write performance of the

## 6.6. References

---

- media". J. Appl. Phys. 71(7) (1992), 3579.
- [Wielinga-82] T. Wielinga, J. C. Lodder and J. Worst. "Characteristics of RF-sputtered CoCr films". IEEE Trans. Magn. MAG-18 (1982), 1107.
- [Wijn-91] H. P. J. Wijn (editor). "Data in Science and Technology: Magnetic properties of metals: d-elements, alloys and compounds". Springer - Verlag (1991), 51.
- [Wohlfarth-59] E. P. Wohlfarth. "Fine particles. Angular variation of the coercivity of partially aligned elongated ferromagnetic particles". J. Appl. Phys. 30(4) (1959), 117S.
- [Wong-92] B. Y. Wong and E. E. Laughlin. "Cross-sectional structures of CoNiCr/Cr bilayer and multilayer thin films". Appl. Phys. Lett. 61(21) (1992), 2533.
- [Yogi-88] T. Yogi, G. Gorman, C. Hwang, M. Kakalec and S. Lambert. "Dependence of magnetic, microstructures and recording properties on underlayer thickness in CoNiCr/Cr media". IEEE Trans. Magn. 24 (1988), 2727.
- [Zhang-94] L. C. Zhang, J. C. Lodder and J. A. Szpunar. "The development of texture in Co-Cr films". IEEE Trans. Magn. 30 (1994), 1373.
- [Zhu-88] J. G. Zhu and H. N. Bertram. "Micromagnetic studies of thin metallic films (invited)". J. Appl. Phys. 63(8) (1988), 3248.

# Chapter 7

---

## Experimental and fitting results of the time-dependence effect in recording media

### 7.1. Time-dependence effect in in-plane media

This section reports the investigations of magnetic viscosity of some in-plane media as a function of applied field. The experimental curves will be fitted to the analytical model proposed by Chantrell et al. [Chantrell-94]. Furthermore, the fit will give more understanding of the nature of the viscosity curves, the switching mechanism and the behaviors of the energy barriers and relaxation times of the samples. The last part of the section will give some results about how the DCD measurements and thus the obtained values of  $\chi_{\text{irr}}$ ,  $H_{\text{f}}$ ,  $V_{\text{act}}$  are influenced by the delay time during the measurements.

#### 7.1.1. Experimental results and discussion

Samples used in this chapter are  $\text{Co}_{86}\text{Cr}_{12}\text{Ta}_2/\text{Cr}$  media samples with various magnetic properties. We used two sputtered samples which consist of 60 nm  $\text{Co}_{86}\text{Cr}_{12}\text{Ta}_2$  layer made at different substrate temperatures  $T_{\text{s}}$ , grown on top of 200 nm Cr underlayer. They have in-plane anisotropy. Figure 7.1.1 shows the in-plane hysteresis loops of these samples.

Some important parameters of the samples are listed in Table 7.1.1. Concerning the sputtering conditions, the only difference between the two samples is the substrate temperature. This leads to several differences in magnetic properties of the samples. The most significant difference is the difference in in-plane coercivities  $H_{\text{c}}$ : the sample prepared at higher  $T_{\text{s}}$  (CTT2) has higher  $H_{\text{c}}$  than the sample prepared at room temperature. The anisotropy constant  $K_1$  and anisotropy

## 7.1. Time-dependence effect in in-plane media

field  $H_K$  of sample CCT2 are also significantly higher than those of sample CCT1. Another important difference is the difference in switching field distributions (SFDs). The sample having higher  $H_c$ ,  $K_1$  (sample CCT2) also has higher SFD.

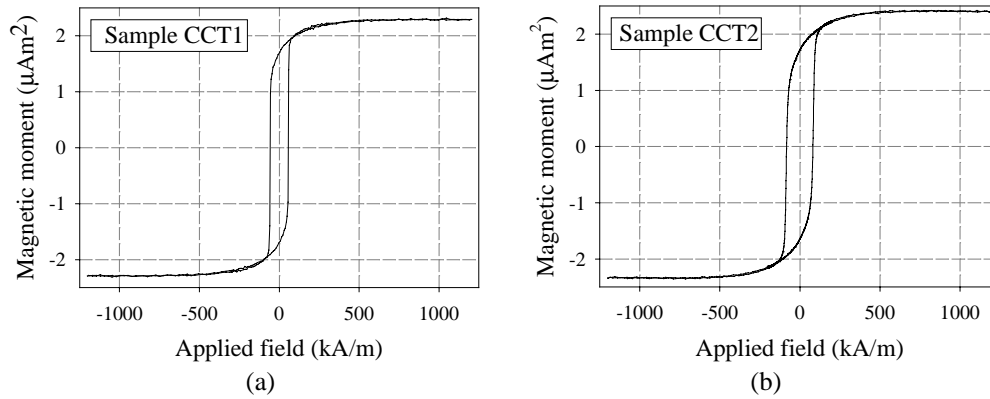


Fig. 7.1.1. In-plane hysteresis loops of sample CCT1 (a) and sample CCT2 (b).

Table 7.1.1. Some important parameters of the CoCrTa/Cr samples.

Parameters	Sample CCT1	Sample CCT2
CoCrTa thickness (nm)	60	60
Cr thickness (nm)	200	200
Substrate temperature (°C)	RT	150
$H_c$ in-plane (kA/m)	56	81
$H_{cr}$ in-plane (kA/m)	57	83
$M_s$ (kA/m)	523.6	573.6
Squareness	0.732	0.707
$K_1$ (J/m <sup>3</sup> )	2.49E+4	4.16E+4
$H_K$ (kA/m)	75.9	115.6
SFD	0.058	0.172
$S_{\text{half-width}}$	0.039	0.169

In Fig. 7.1.2, the measurements of magnetic viscosity  $S$  as a function of applied field are plotted (viscosity curve). These samples have almost the same  $M_s$  so their viscosities can be compared by normalizing all magnetization values on the saturation magnetization  $M_s$ . Both curves exhibit a high peak close to the remanence coercivity  $H_{cr}$  which is slightly higher than the coercivity  $H_c$  (see Section 3.5.2.1 for the definition of  $H_{cr}$ ). The positions of their remanence coercivities are marked by the dashed vertical lines. This well-known behavior

have been widely reported as a characteristic of in-plane magnetic thin films [Suzuki-96, Uwazumi-97].

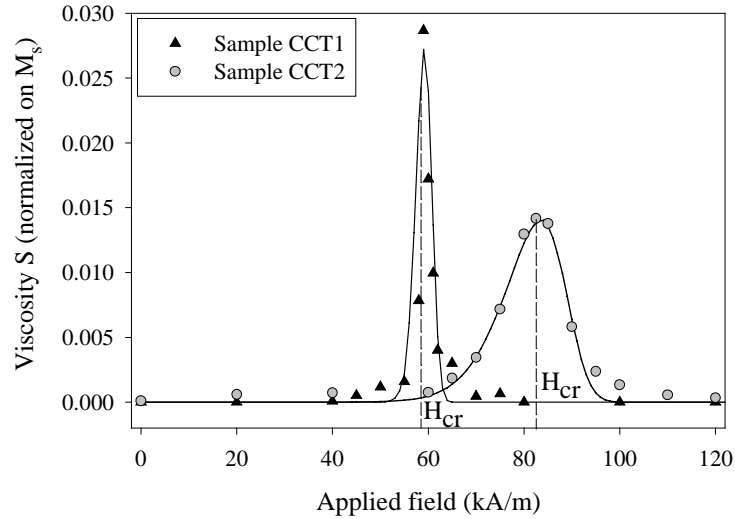


Fig. 7.1.2. Normalized viscosity as a function of applied field. The solid lines are fitted curves (see later in Section 7.1.2)

As mentioned above, sample CCT2 has a higher coercivity  $H_c$  and anisotropy constant  $K_1$  than those of sample CCT1. However, the viscosity peak of sample CCT2 is lower and wider than that of sample CCT1. To evaluate the width of the viscosity peak, we introduce a parameter called half-width of the viscosity peak ( $S_{\text{half-width}}$ ).  $S_{\text{half-width}}$  is defined as the ratio of the width at half height of the viscosity peak to  $H_c$ .

From Table 7.1.1, we can see that the two samples are clearly different in their switching field distributions (SFD). SFD of sample CCT2 ( $T_s=150^\circ\text{C}$ ) is about 3 times higher than SFD of sample CCT1. We found that there is a close correlation between the half-widths of the viscosity peaks  $S_{\text{half-width}}$  and the SFD values.

To calculate the fluctuation field and the activation volume by the DCD method, DCD measurements are required. The irreversible magnetization  $M_{\text{irr}}$ , which is actually the magnetization on the DCD curve, is plotted against applied field (Fig. 7.1.3). By taking the derivative of these curves, we obtain the irreversible susceptibility  $\chi_{\text{irr}}$  curves (Fig. 7.1.3, right scales). It is clear that the shapes (heights and widths of the peaks) of the  $\chi_{\text{irr}}$  curves correlate closely with the shapes of the viscosity curves (Fig. 7.1.2). Moreover, the peak positions of the  $\chi_{\text{irr}}$  curves which are at  $H_{\text{cr}}$  coincide with those of the viscosity curves.

### 7.1. Time-dependence effect in in-plane media

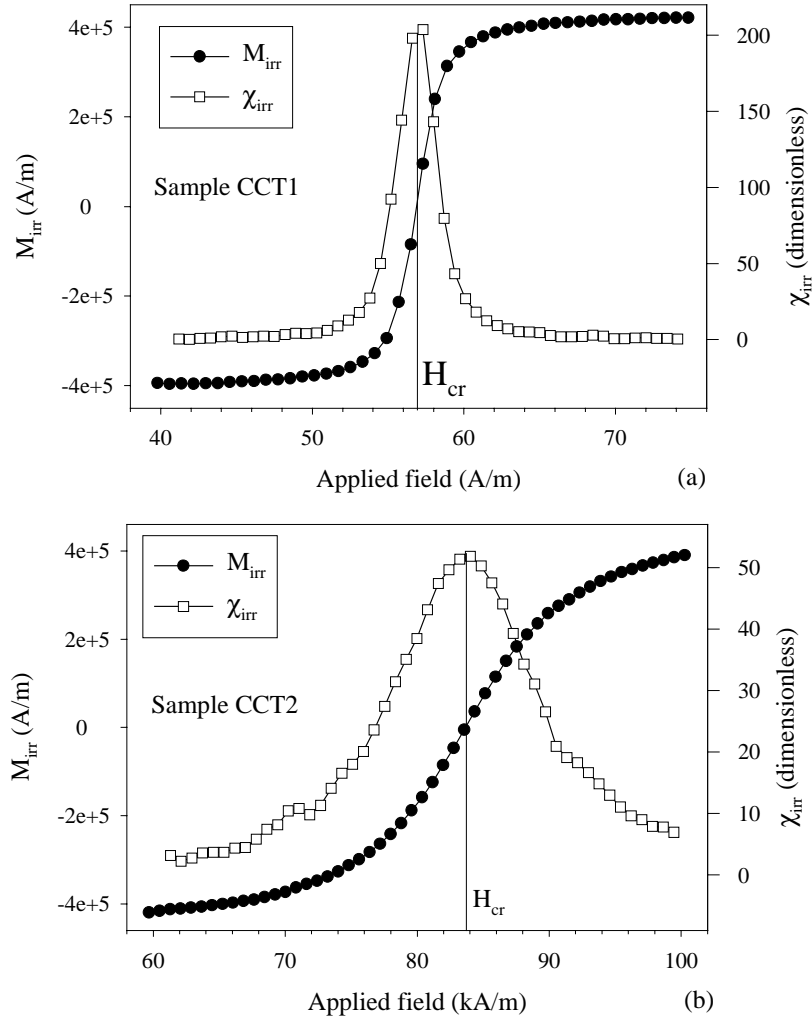


Fig. 7.1.3. Irreversible magnetization (from DCD measurements) and irreversible susceptibility curves of sample CCT1 (a) and sample CCT2 (b).

The fluctuation field of the samples was then obtained by two methods: the DCD and the waiting time method (Fig. 7.1.4). The values of fluctuation field near coercivity calculated from the waiting time method were found to be close to those obtained from the DCD method. In the DCD method,  $H_f$  values outside the plotted field range are not reliable due to large errors arising from the limit  $0/0$  of the ratio  $S/\chi_{irr}$  where both  $S$  and  $\chi_{irr}$  are small. Similarly, in the waiting time method, the limitation of the equipment does not allow to calculate  $H_f$  at field values far from coercivity. In these regions, the relaxation curves are so noisy that it is impossible

## 7. Experimental and fitting results of time-dependence effect in recording media

to extrapolate precisely to the value  $I_0$  (see detailed measurement procedure in Section 3.5.2.2). Now we can conclude that for the in-plane media case, where there is no demagnetizing field correction involved, the DCD method is better than the waiting time method, because in the DCD method, more points can be measured within the same range of applied field. Of course this conclusion is only valid for our experimental conditions. We think it might be better to rely on the DCD method because it gives better field resolution.

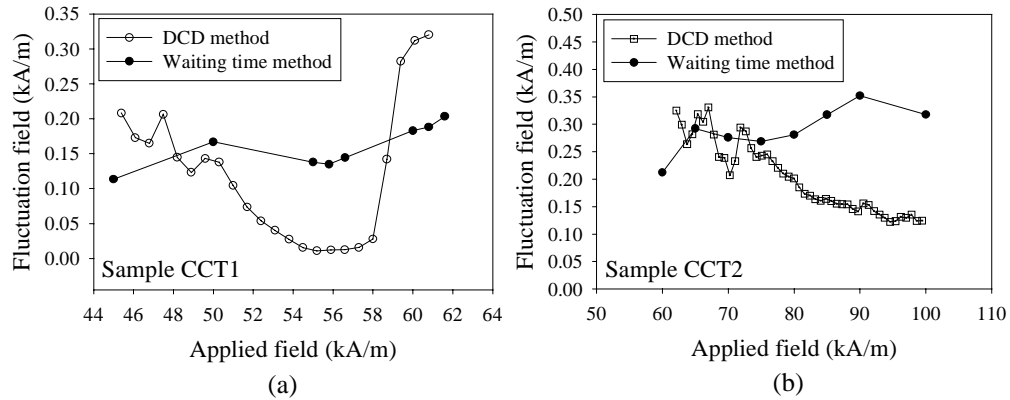


Fig. 7.1.4. Fluctuation field as a function of applied field obtained by the DCD ( $\square$ ) and the waiting time method ( $\bullet$ ) of the samples CCT1 (a) and CCT2 (b).

The  $H_f$  curves obtained by the DCD method of the two samples are clearly different:  $H_f$  of sample CCT1 has a minimum around  $H_c$  and  $H_{cr}$  whereas  $H_f$  of sample CCT2 seems to decrease monotonously with field.

From the fluctuation field, activation volumes  $V_{act}$  of the investigated samples were calculated (Fig. 7.1.5). As opposed to  $H_f$ ,  $V_{act}$  of sample CCT1 exhibits a clear peak around  $H_c$  and  $H_{cr}$ . Sample CCT2 however behaves differently around  $H_c$ . Its activation volume increases monotonously with increasing applied field.

The difference in the SFD of the two samples could be attributed to the difference in the distribution of the anisotropy fields and grain sizes or switching unit sizes. This causes the difference in the curves  $V_{act}$  vs. field. In the sample having narrow distribution (sample CCT1), a large number of switching units reverse at  $H_c$  resulting in a peak of  $V_{act}$  at this field. In the sample having wider distribution (sample CCT2), the reversal occurs over a wide range of switching unit sizes at different fields, therefore  $V_{act}$  changes monotonously with the field.

## 7.1. Time-dependence effect in in-plane media

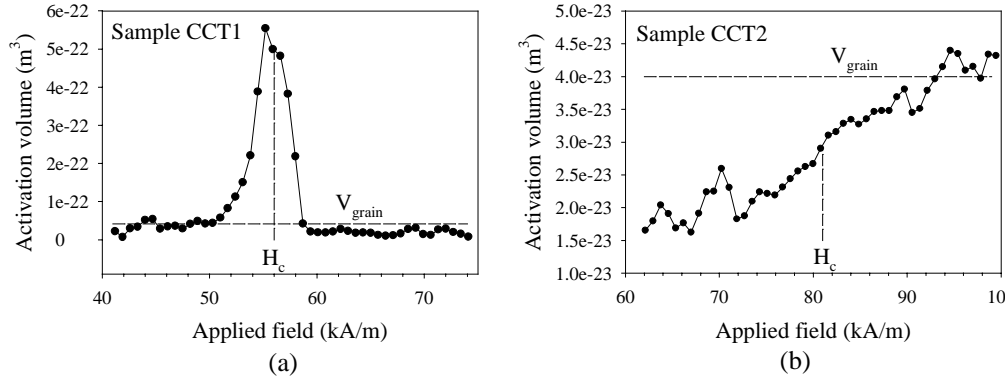


Fig. 7.1.5. Activation volume (derived from fluctuation field) versus applied field of samples CCT1 (a) and CCT2 (b). Average physical volumes of grains ( $V_{\text{grain}}$ ) are indicated by dashed lines.

From AFM surface images of the samples, average physical volumes of the grains,  $V_{\text{grain}}$ , could be estimated. They are approximately the same for both samples, which is about  $4 \times 10^{-23} \text{ m}^3$ . The values of  $V_{\text{grain}}$  are indicated by dashed lines in Fig. 7.1.5.

In sample CCT1,  $V_{\text{act}}$  is slightly smaller than  $V_{\text{grain}}$  in the regions far from  $H_c$ , while around  $H_c$ , it is substantially larger. It could be concluded here that in the regions far from  $H_c$ , the reversal is nucleated in a volume slightly smaller than  $V_{\text{grain}}$ . This reflects the fact that the reversal mechanism is probably incoherent or partly coherent rotation. On the other hand, in the region around  $H_c$ , the reversal is nucleated in a volume larger than the volume of the grains. This indicates that the intergranular exchange coupling is probably strong enough to force several grains to switch collectively.

Differently, in sample CCT2, the activation volume is smaller than the physical volume of grains at fields smaller than about 95 kA/m. With the same argument as given above, we can conclude that in sample CCT2, at fields lower than about 95 kA/m, the reversal mechanism is incoherent and above 95 kA/m, the grains could switch collectively due to large intergranular exchange coupling.

The above discussions leads to a remark that in average, intergranular exchange coupling of sample CCT1 is stronger than that of sample CCT2. It has been proved by theory [Zhu-88] and experiments [Dova-97] that  $H_c$  and SFD decrease with increasing intergranular exchange coupling. This is consistent with the data of the in-plane coercivities and SFDs of our samples (Table 7.1.1). Indeed,  $H_c$  and SFD of sample CCT1 are substantially smaller than those of sample CCT2.

## 7.1.2. Fitting results and discussion

The measured viscosity curves (Fig. 7.1.2) were fitted to the analytical model of Chantrell (see Section 3.2 and 3.6). The fits are pretty good, except for the part at the end of the slope on the right side of the peak. Some important input and output parameters of the fit are listed in Table 7.1.2.

Table 7.1.2. Some important input and output parameters of the fit. Parameters in italic are inputs, the others are outputs.

Parameters of the fit	Sample CCT1	Sample CCT2
<i>Fitting parameter F</i>	0.28	0.38
<i>Standard deviation <math>\sigma</math></i>	0.22	0.40
<i>Switching volume <math>V_{switching}</math> (<math>m^3</math>)</i>	9.0E-23	3.0E-23
Calculated critical volume $V_{critical}$ ( $m^3$ )	4.6E-24	2.7E-24
Calculated coercivity $H_c$ (kA/m)	58.7	80.6
Field at viscosity peak $H_{peak}$ (kA/m)	59.0	84.0
KV/kT	543	302
Relaxation time at zero field $\tau$ (years)	1.38E+219	4.39E+114

### 7.1.2.1. Discussion on the parameters of the fit

The fitting parameters  $F$  are smaller than one. This can be explained as follow: Although the samples have in-plane anisotropy, they are isotropic in all directions lying in the plane of the film. Only a small fraction of grains having easy axes aligned or nearly aligned with the field direction can contribute to the measured viscosity. The fitting parameters  $F$ , as described in Section 3.6, reflects this fraction and therefore they are smaller than one.

Coercivity can be calculated from the formula [Sharrock-90 and Cullity-72, p.415]:

$$H_c = H_K \left[ 1 - \left( \frac{\Delta E_c}{KV} \right)^{1/2} \right] \quad (7.1.1)$$

From Table 7.1.2, we can see that calculated coercivities of the samples are almost consistent with experimental coercivities as listed in Table 7.1.1. The calculated coercivities, like the experimental ones, are slightly lower than the fields at which the fitted viscosity peaks appear ( $H_{peak}$ ).

The standard deviations  $\sigma$  correlate closely with the half-width of the viscosity peak  $S_{half-width}$  and SFDs. This is due to the fact that these three parameters ( $\sigma$ ,  $S_{half-width}$  and SFD) are all attributed to the same factor that is the dispersion of sizes, anisotropy constants, etc. of grains of each sample. More dispersion means wider

## 7.1. Time-dependence effect in in-plane media

---

distribution function, and thus larger  $\sigma$ . The correlation between  $\sigma$  and  $S_{\text{half-width}}$  can be easily explained by fitting. The fitting results show that the shape (width and height) of the viscosity peak is mainly decided by the shape of the distribution function  $f$ . Later we will present in more details about this correlation.

### 7.1.2.2. Discussion on $V_{\text{switching}}$

Another important parameter is the switching volume  $V_{\text{switching}}$  (see Section 3.6 and 3.7). In the fit,  $V_{\text{switching}}$  is considered as the volume of a portion of the material which reverses its magnetization coherently (coherent rotation) as a Stoner-Wohlfarth particle. We assumed that this volume is constant with field and it is treated as a fitting parameter of the fit. From fitting results, we found that the values of  $V_{\text{switching}}$  are close to those of  $V_{\text{grain}}$  and also close to  $V_{\text{act}}$  near  $H_c$ . They are about one order of magnitude higher than the calculated critical volumes  $V_{\text{critical}}$  (see Section 3.7).

By fitting, we approximate the incoherent rotation which could happen in practice to a simpler coherent rotation of  $V_{\text{switching}}$ . The switching volume in this case is close to the physical volume of the grains, which indicates that the switching unit could be either a part of a grain or a cluster of a few grains. This agrees with the conclusions about the reversal mechanisms drawn from the measurements of activation volume (Section 7.1.1). Similar conclusions can be found in the anomalous Hall effect study of Co-Cr thin films with perpendicular anisotropy [Lodder-97]. Similarly, by studying the time-dependence of coercivity of CoCrTa/Cr media, Ross et al. [Ross-98] found that the switching volume is slightly larger than the physical volume of the grains.

### 7.1.2.3. What is the nature of the viscosity curve ?

By splitting Eq. (3.2.7) (as re-written below) into components, the nature of the viscosity curve can be understood.

$$S = \frac{dM(t)}{d \ln(t)} = -\frac{AkT}{\Delta E_m} f(y_c)$$

Figure 7.1.6 shows the formation of the viscosity curve  $S$  from its components, namely the factor  $A$ , the median energy barrier  $\Delta E_m$  and the distribution function  $f$  (Graphs 1,2 and 3, respectively). The arrows between the graphs show how the formula is built. For example, we divide Graph 3 ( $f$ ) by Graph 2 ( $\Delta E_m$ ) to create Graph 4 ( $f/\Delta E_m$ ).

7. Experimental and fitting results of time-dependence effect in recording media

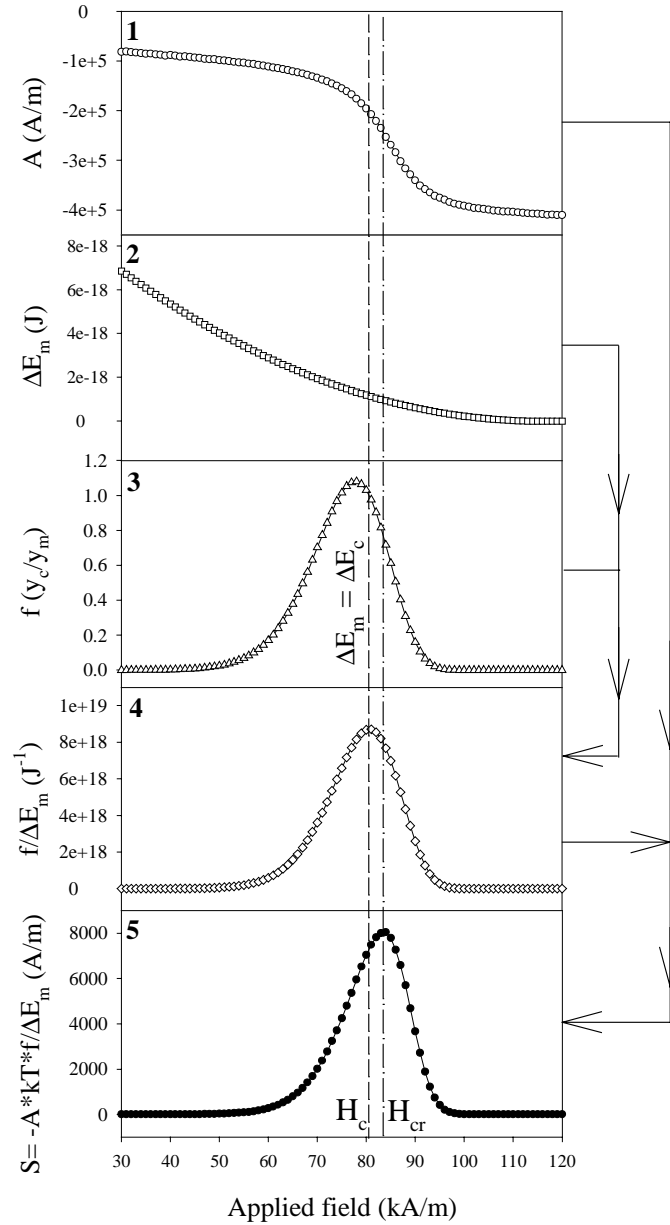


Fig. 7.1.6. Components forming the viscosity curve, calculated for sample CCT2, as an example.

It should be mentioned that  $f$  is now plotted against applied field  $H_{app}$ , not vs.  $\Delta E$  as in the original form of the distribution function. Therefore, the horizontal scale of the plot  $f$  versus  $H_{app}$  is altered (compared to the plot  $f$  vs.  $\Delta E$ ) according to the

## 7.1. Time-dependence effect in in-plane media

---

behavior of  $\Delta E$  vs.  $H_{app}$ . Generally, the position of the peak of  $f$  curve does not coincide with  $H_c$  where the median energy barrier equals to the critical energy barrier ( $\Delta E_m = \Delta E_c$ ), but is at a smaller field.

Now we move one step towards the final form of  $S$  by dividing  $f$  by  $\Delta E_m$  and we obtain the curve  $f/\Delta E_m$  versus  $H_{app}$  (Graph 4). The function  $f/\Delta E_m$  has the same shape as  $f$  but its peak is now shifted to  $H_c$ . It could be concluded here that the role of  $\Delta E_m$  curve is to shift the peak of  $f$  towards a higher field, at  $H_c$ .

Finally,  $f/\Delta E_m$  is multiplied by  $kT \times A$ , in which  $kT$  is constant, resulting in the final form of  $S$  versus  $H_{app}$  curve (Graph 5). Now we can say that the role of  $A$  is to shift the peak further to a position at which the maximum of viscosity occurs. Therefore,  $A$  is mainly responsible for the deviation of the viscosity peak from  $H_c$ .

If the sample had no reversible component of magnetization, the hysteresis loop would be square and consequently  $A$  would be a step function. This causes the viscosity peak to coincide with  $H_c$ . On the other hand, DCD measurement of this sample (having no reversible component) would certainly show that  $H_c$  equals to  $H_{cr}$ . The less square the  $A$  function, the further the viscosity peak position and  $H_{cr}$  deviate from  $H_c$ . Therefore, these facts indicate that there is a close correlation between the position of the viscosity peak and  $H_{cr}$ . That is the reason why in practice, their values are close together.

It is clear that the shape of the resulting viscosity curve (Graph 5) is mainly decided by the distribution function  $f$ . This is the reason why there is a correlation between the half-width of the viscosity peak and SFD and  $\sigma$ .

The deviation of the fitted curves from the experimental ones near the end of the slope (on the right of the viscosity peak - Fig. 7.1.2) is partly attributed to the limitation of the numeric calculations. In the calculation, we used only the average value of  $H_K$  and assume that  $f$  vanishes at  $H_K$ . This is probably not true because in practice, there is always a certain distribution of  $H_K$ .

### 7.1.2.4. Energy barrier and relaxation time as a function of applied field

The fit allows to calculate the median energy barrier  $\Delta E_m$  of the samples under the influence of applied field. According to Eq (3.1.10), we have:

$$\Delta E_m = K_1 \times V_{switching} \times \left(1 - \frac{H}{H_K}\right)^2 \quad (7.1.2)$$

in which  $\Delta E$ ,  $K$  and  $V$  are now replaced by  $\Delta E_m$ ,  $K_1$  and  $V_{switching}$ , respectively.

## 7. Experimental and fitting results of time-dependence effect in recording media

In Fig. 7.1.7, values of  $\Delta E_m$  versus applied field of the samples are plotted. At zero and low field, the squared term of Eq (7.1.2) is so close to one that only the factor  $K_1 V_{\text{switching}}$  influences chiefly  $\Delta E$ . Sample CCT1 has larger  $K_1 V_{\text{switching}}$  (Table 7.1.2), therefore,  $\Delta E_m$  of sample CCT1 is higher than that of sample CCT2 at zero and low field. When the field increases, especially near the anisotropy fields  $H_K^*$ , the squared term becomes more dominant. The behavior of  $\Delta E_m$  is now determined by  $H_K$ . As a result,  $\Delta E_m$  of sample CCT1 having smaller anisotropy field ( $H_{K1} < H_{K2}$ , see Table 7.1.1) decreases faster than  $\Delta E_m$  of sample CCT2 and vanishes earlier, at  $H_{K1}$ .  $\Delta E_m$  of sample CCT2 becomes zero at higher field  $H_{K2}$ .

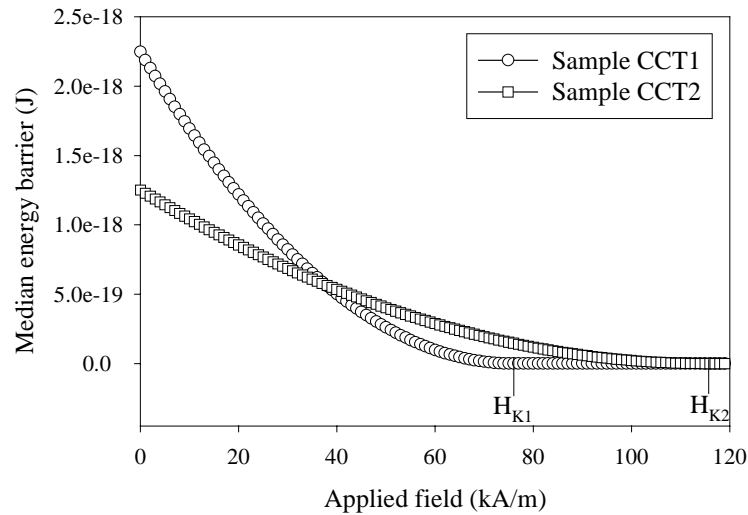


Fig. 7.1.7. Median energy barrier of samples CCT1 and CCT2 as a function of applied field.  $H_{K1}$  and  $H_{K2}$  are the anisotropy fields of samples CCT1 and CCT2, respectively.

Now we can conclude that the difference in the behaviors of the two samples at low and high field is attributed to the fact that  $V_{\text{switching}}$  of sample CCT1 is larger than  $V_{\text{switching}}$  of sample CCT2, whereas,  $K_1$  and  $H_K$  of sample CCT2 are higher than those of sample CCT1 (even though, the product  $K_1 V_{\text{switching}}$  of sample CCT1 is still larger than that of sample CCT2).

From  $\Delta E_m$ , the relaxation time  $\tau$  can be determined by Eq. (3.1.2). The relaxation times of the samples as a function of applied field are plotted in Fig. 7.1.8. The behaviors of the curves look similar to those of  $\Delta E_m$ . However, it should be

---

\* We are now talking about the general anisotropy  $H_K$  which appears in Eq. (7.1.2). When the real anisotropy values of the samples CCT1 and CCT2 are concerned,  $H_K$  will be replaced by  $H_{K1}$  and  $H_{K2}$ , respectively.

## 7.1. Time-dependence effect in in-plane media

mentioned that the vertical scale in Fig. 7.1.8 is logarithmic. At zero and low field, sample CCT1 is more magnetically stable than sample CCT2 because it has larger relaxation time. However, at higher field, similarly to the behavior of  $\Delta E_m$ ,  $\tau$  of sample CCT1 decreases faster than that of sample CCT2. They become zero at their anisotropy fields  $H_{K1}$  and  $H_{K2}$ . That means at high field (higher than about 35kA/m - the value at the crossing of two curves), sample CCT1 becomes less stable than sample CCT2, and consequently, it is easier to write magnetic information onto sample CCT1 than sample CCT2. The relaxation time at coercivities of the two samples are almost the same. They are about 3800s and 1500s (for sample CCT1 and CCT2, respectively).

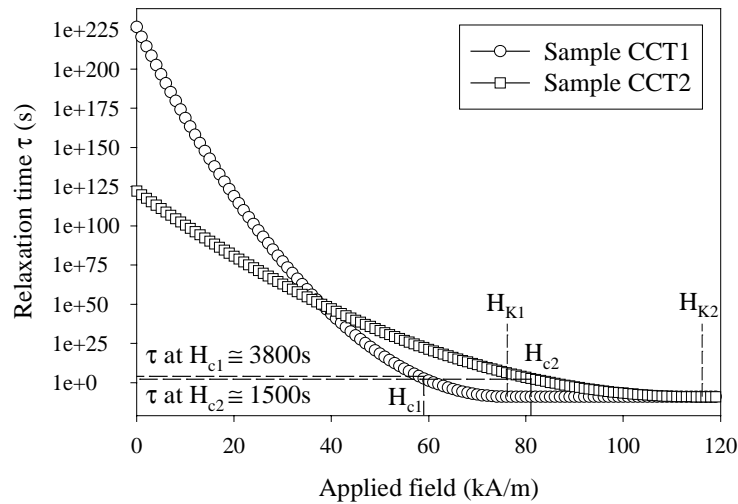


Fig. 7.1.8. Relaxation time  $\tau$  versus applied field of samples CCT1 and CCT2. The vertical scale is logarithmic.  $H_{c1}$  and  $H_{c2}$  are coercivities of samples CCT1 and CCT2.

### 7.1.3. Influence of the delay time on the DCD and $\chi_{irr}$ measurements of in-plane media

In Section 3.5.2.1 we have mentioned that there is an influence of the time-dependence effect on the DCD and  $\chi_{irr}$  measurements. In some cases, this influence can be ignored while in some others, it can be quite considerable. This section investigates in more details the influence of the delay time on the DCD and  $\chi_{irr}$  measurements of in-plane media.

Two DCD measurements have been made on sample CCT2 (Fig. 7.1.9). The first measurement was carried out with a delay time of 500s at every step. The second measurement was just a normal measurement, i.e. without delay time.

## 7. Experimental and fitting results of time-dependence effect in recording media

From Fig. 7.1.9, we can see that the difference between the two measurements is the largest around  $H_{cr}$  which is also close to the viscosity peak. At this field, the difference is as large as 4.7% of  $M_s$ . The two curves become indistinguishable at fields far from  $H_{cr}$ . The difference between two points at the same field on different curves is exactly the difference between  $M(t=0s)$  and  $M(t=500s)$  of the relaxation curve if it would be measured at this field.

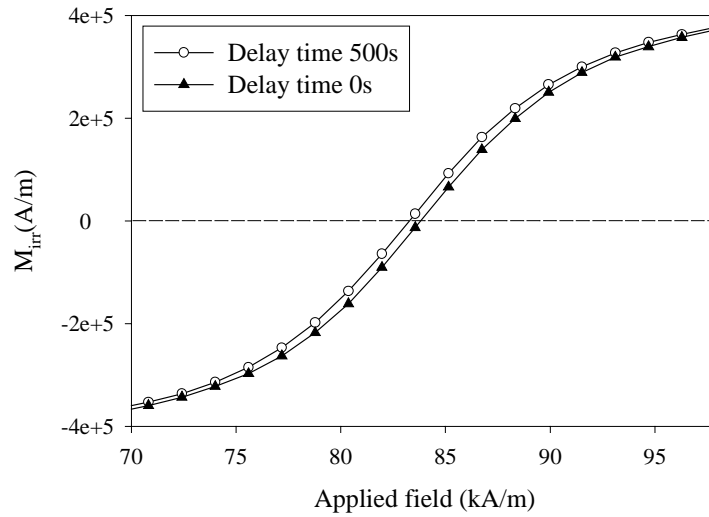


Fig. 7.1.9. Influence of the delay time on the  $M_{irr}$  measurement (DCD measurement).

In contrast, when the derivative of  $M_{irr}$  (i.e. magnetization on the DCD curve) is taken to get  $\chi_{irr}$  (Fig. 7.1.10), the difference in  $\chi_{irr}$  almost vanishes at field around  $H_{cr}$ , because around this field, two  $M_{irr}$  curves are almost parallel. On two sides of the maximum of  $\chi_{irr}$ , the curve with delay time=0s is shifted from that with delay time=500s: on the left side, at lower field, it shifts down whereas on the right side, at higher field, it shifts up. The difference in  $\chi_{irr}$  on these two sides is 6% of the maximum  $\chi_{irr}$ .

## 7.1. Time-dependence effect in in-plane media

---

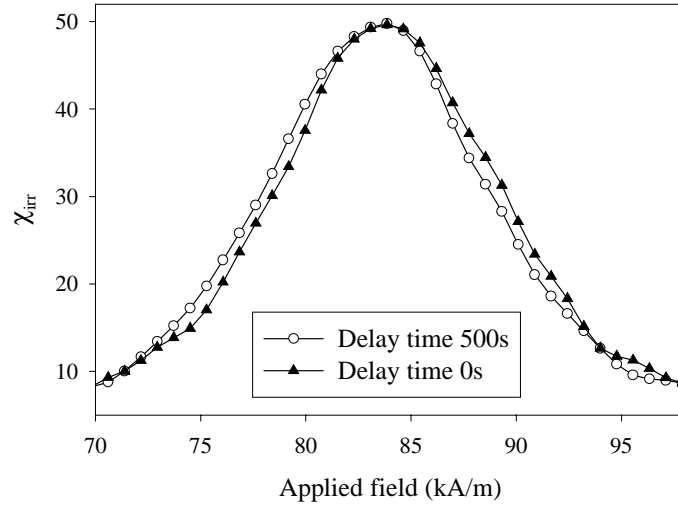


Fig. 7.1.10. Influence of the delay time on the irreversible susceptibility  $\chi_{irr}$ .

Now it can be concluded that to determine  $\chi_{irr}$  and consequently  $H_f$  and  $V_{act}$  of in-plane media within the region around  $H_{cr}$  and  $H_c$ , it is not necessary to include a delay time in the DCD measurement routine. However, if we are interested in the dependence of those parameters on the applied field at larger range, appropriate delay times should be taken into account.

## 7.2. Time-dependence effect in perpendicular media

### 7.2.1. Alumite media

In this section, we will present a study of the time-dependence effect in alumite perpendicular media. Although there is still much doubt about possible applications of this type of media, alumite media are often considered as a good model to study switching mechanisms. This is because their morphology is more regular and less complicated than sputtered continuous media. With the benefit of this study, the next section will investigate the time-dependence effect in CoCrTa single layer having perpendicular c-axis orientation.

#### 7.2.1.1. About the samples and their important parameters

To have better understanding about the time-dependence effect in perpendicular media, perpendicular alumite media are used. The advantages of using this type of media in our study are that:

- these media have large perpendicular anisotropy,
- they are particulate media having small magnetic interactions,
- their morphology are simple and regular so the switching mechanisms are simpler than thin film cases.

Alumite media consist of long separate Co (or Ni, Fe, etc.) columns perpendicular to the substrate (see Fig. 7.2.1). These columns are realized by depositing a desired magnetic material into micro-pores in an aluminum oxide layer. The aluminum oxide layer is made by anodic oxidation of aluminum substrate surface. This technique allows to realize an aluminum oxide layer with hollow pores perpendicular to the substrate, arranged in a nearly perfect hexagonal pattern. Details about fabrication method, morphology and other properties of the media can be found in [Tsuya-86, Shiraki-85 and Huysmans-88].

In this study, we used an experimental alumite hard disk made of Co-filled alumite with a thickness of 1 $\mu$ m. To have a systematic series of samples, the disk was sawn into several 1 $\times$ 1cm samples and they were thinned down to different thicknesses by mechanical polishing. There are four samples of thickness ranging from 0.23 to 0.50 $\mu$ m. The names of the samples are given in Fig. 7.2.1.

## 7.2. Time-dependence effect in perpendicular media

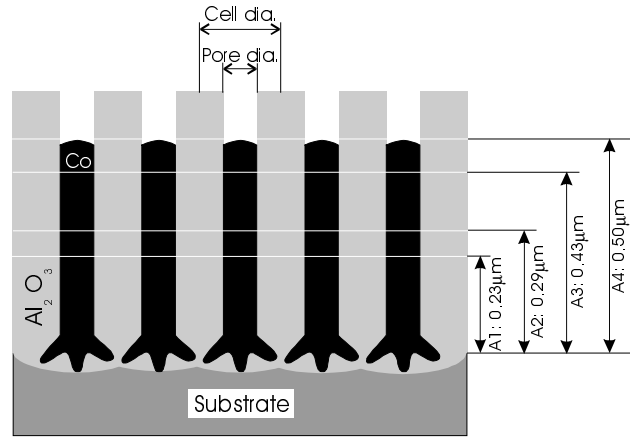


Fig. 7.2.1. Diagram of an original alumite hard disk sample. The black parts are the Co-filled columns surrounded by the aluminum oxide (gray parts). The sample was sawn into several  $1 \times 1$  cm pieces and then they were thinned down to four different thicknesses by polishing, indicated by 4 horizontal white lines. The polished samples are named as A1, A2, A3 and A4.

From torque measurement data, it could be concluded that the samples have perpendicular anisotropy. According to [vanDrent-91], the contribution of the shape anisotropy of the columns is dominant over the crystalline anisotropy of Co. Table 7.2.1 shows the most important parameters of the samples.

Table 7.2.1. Important parameters of the alumite samples.

Parameters	Sample A1	Sample A2	Sample A3	Sample A4
Cell diameter (nm)	95.7			
Pore diameter (nm)	40.0			
Packing density	0.16			
Thickness (col. length) ( $\mu\text{m}$ )	0.23	0.29	0.43	0.50
Total magnetic volume ( $\text{m}^3$ )	3.65E-11	4.72E-11	6.85E-11	8.04E-11
Column volume $V_{\text{col}}$ ( $\text{m}^3$ )	2.85E-22	3.69E-22	5.36E-22	6.29E-22
Saturation moment $I_s$ ( $\mu\text{Am}^2$ )	8.9	11.5	16.7	19.6
$M_s$ (kA/m)	243.8			
In-plane $H_c$ (kA/m)	27.02	28.2	30.1	34
Perpendicular $H_c$ (KA/m)	98.54	98.80	88.44	81.6
$K_1$ (J/m)	4.75E+4	4.98E+4	5.16E+4	5.08E+4

### 7.2.1.2. Viscosity and remanence measurements

Relaxation curves were measured on the alumite samples in the perpendicular direction at different applied fields. Viscosity  $S$  normalized on  $M_s$  of all samples as a function of applied field is illustrated in Fig. 7.2.2.

Generally, viscosity of the samples has a short plateau at low field and when the applied field increases further, it decreases monotonously with the field. Finally all of the  $S$  values vanish at above 500 to 600kA/m. This general behavior is different from that of in-plane media investigated in Section 7.1 where it was found that the viscosity always performs a peak near  $H_{cr}$  and in the regions near zero and high field, it vanishes. The difference between viscosity curves of perpendicular and in-plane media is attributed to the demagnetizing effect.

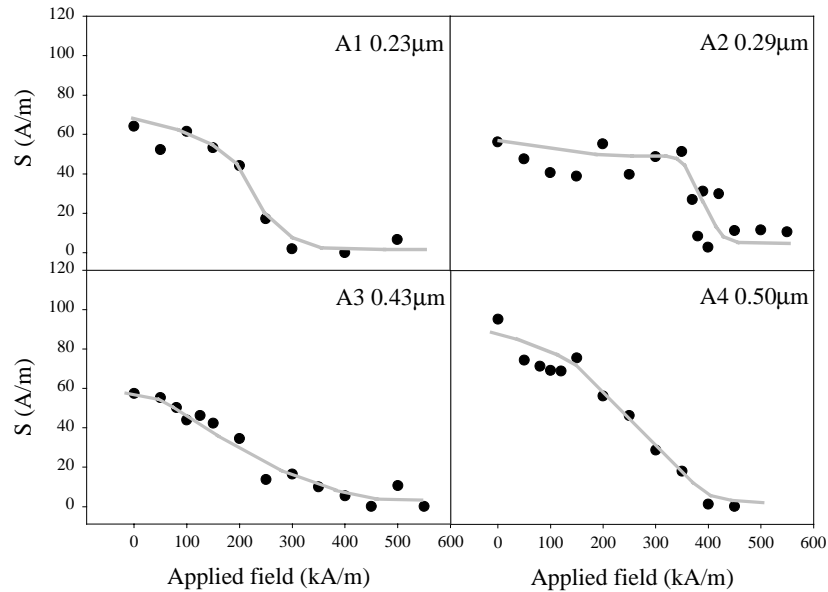


Fig.7.2.2. Viscosity as a function of applied field.

In order to correct for the demagnetizing effect of the viscosity measurements and furthermore, to calculate fluctuation field and activation volume (see Section 3.3 and 3.4), perpendicular DCD measurements were carried. The intrinsic viscosity versus internal field was obtained by correcting for the demagnetizing effect (Fig. 7.2.3). We used the measured viscosity versus applied field, the total susceptibility ( $\chi_{\text{tot}}=dM_{\text{hys}}/dH$ ) and the reversible susceptibility ( $\chi_{\text{ir}}=dM_{\text{DCD}}/dH$ ) for the correction, according to Eq. (3.4.2).

After correction, the shapes of the viscosity curves change totally: the viscosity values increase by a factor of about 10 while the field range of the curves is

## 7.2. Time-dependence effect in perpendicular media

compressed to a smaller range (for instance, from 500 to about 60 kA/m for sample A1). It can also be seen that after the correction, intrinsic viscosity curves exhibit a peak near the perpendicular coercivity (hereafter called  $H_c$ ), somewhat similar to the in-plane case. We cannot compare the position of the peak to  $H_{cr}$  as in the in-plane case, because a correction to get a real  $H_{cr}$  is needed. However, in general,  $H_{cr}$  should be very close to  $H_c$ . For sample A4 whose peak appears at a lower internal field, if more points were measured further at negative applied field, one would observe the downhill part on the left side of the viscosity peak.

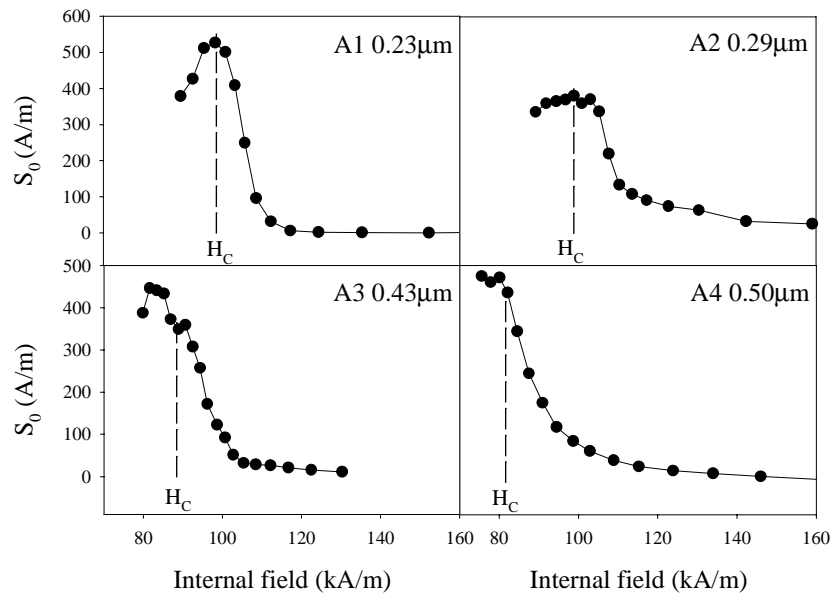


Fig. 7.2.3. Intrinsic viscosity versus internal field, obtained by correction for the demagnetizing effect of the measured viscosity curves

Among two components of susceptibility, the irreversible component,  $\chi_{irr}$ , is more significant in this chapter because the time-dependence effect is only attributed to the change in the irreversible component of magnetization. Figure 7.2.4.a shows  $\chi_{irr}$  versus applied field. The maximum value of  $\chi_{irr}$  decreases with increasing layer thickness. Using Eq.(3.4.1), the intrinsic irreversible susceptibility ( $\chi_{irr-i}$ ) is calculated. The intrinsic irreversible susceptibility  $\chi_{irr-i}$  is the susceptibility that one would observe if there were no demagnetizing effect involved.

Similarly to the in-plane case, there is a close correlation between the intrinsic irreversible susceptibility and the intrinsic viscosity curves: they both have a peak near  $H_c$ .

## 7. Experimental and fitting results of time-dependence effect in recording media

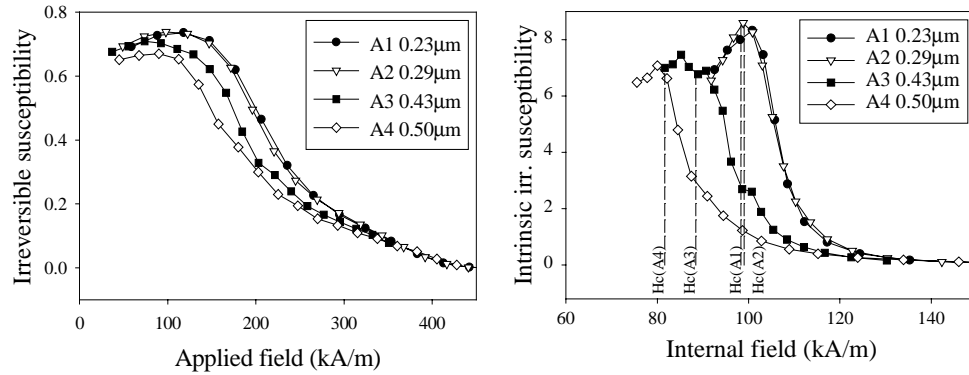


Fig. 7.2.4. (a) Irreversible susceptibility ( $\chi_{irr}$ ) calculated directly from the derivative of DCD curves. (b) Intrinsic irreversible susceptibility ( $\chi_{irr-i}$ ) calculated by Eq. (3.4.1). Values of corresponding  $H_c$  are also indicated by dashed lines.

### 7.2.1.3. Fluctuation fields and activation volumes

By using Eq. (3.3.1) and Eq. (3.3.2), fluctuation fields and activation volumes have been calculated (Fig. 7.2.5). In the graphs of activation volumes versus internal field, volumes of one column are indicated by the dashed lines. Table 7.2.2 shows the relations between the column volumes and the activation volumes at coercivities.

It could be seen at a glance that the activation volumes,  $V_{act}$ , are generally smaller than the column volumes,  $V_{col}$ . This phenomenon agrees with results of other researchers working on alumite media or in general, on particulate media. Studying  $\alpha$ -Fe filled alumite films, Li and Metzger [Li-97a, Li-97b] found that the activation volumes are an order of magnitude smaller than the experimentally measured average particle (or column) volumes. In another case, calculations of  $V_{act}$  of Co-epitaxial  $\gamma$ -Fe<sub>2</sub>O<sub>3</sub> particles revealed that the ratio  $V_{act}/V_{particle}$  is as small as 0.21 [Witte-90].

Another remark from Fig. 7.2.5 is that the curves of  $V_{act}$  versus  $H_i$  of all samples exhibit a peak. There seems to be no correlation between the position of this peak and coercivities as observed earlier in the in-plane media. The variation of  $V_{act}$  with field cannot be easily interpreted [Witte-90], especially in the case of perpendicular media where the demagnetizing field has a strong influence.

## 7.2. Time-dependence effect in perpendicular media

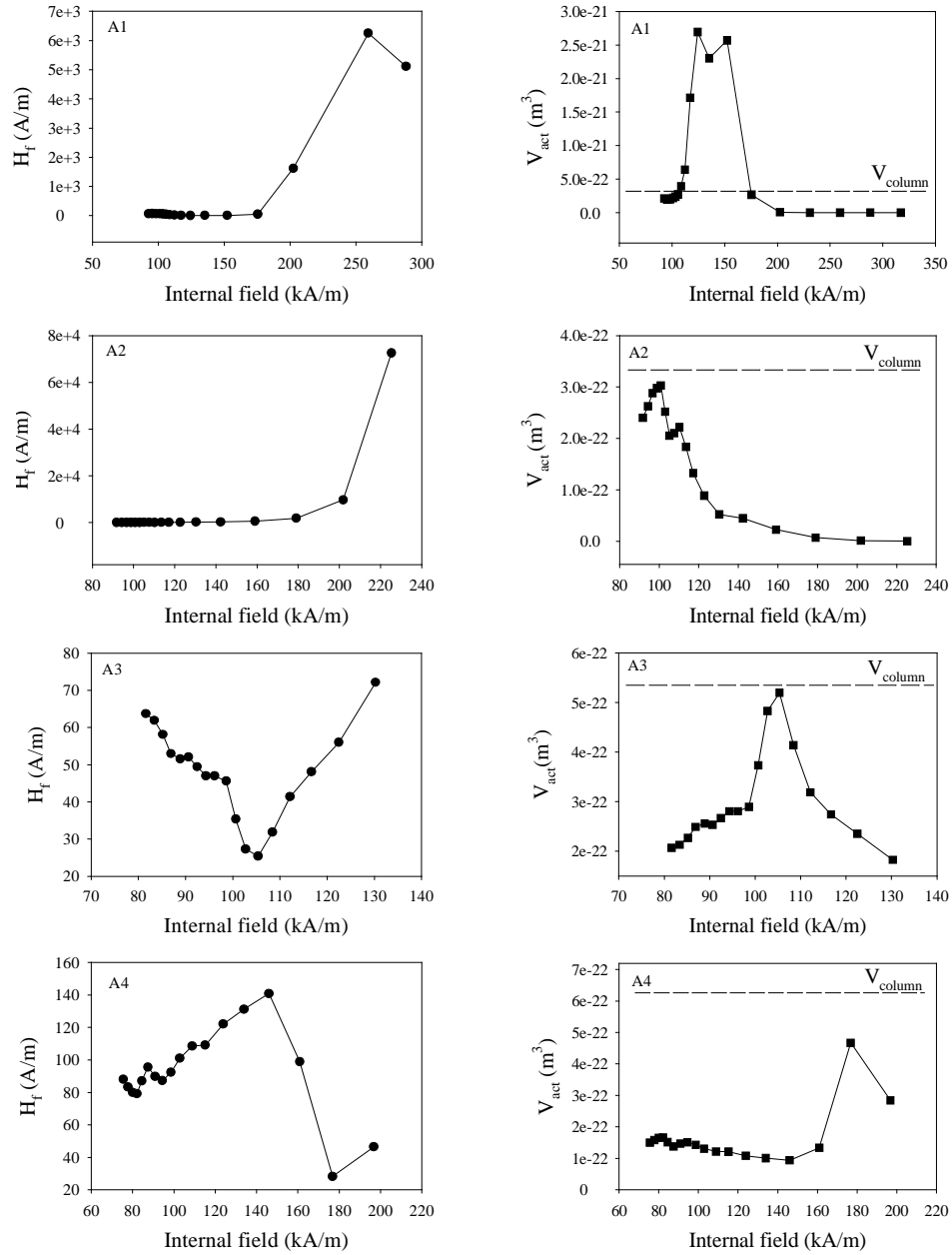


Fig.7.2.5. Calculated fluctuation field and activation volume versus internal field.

## 7. Experimental and fitting results of time-dependence effect in recording media

Table 7.2.2. Relations between column volumes and activation volumes at  $H_c$ .  $V_{act@H_c}$  is activation volume at  $H_c$ .

Parameters	Sample A1	Sample A2	Sample A3	Sample A4
Thickness (col. length) ( $\mu\text{m}$ )	0.23	0.29	0.43	0.50
$V_{act@H_c}$ ( $\text{m}^3$ )	2.00E-22	2.90E-22	2.56E-22	1.65E-22
Column volume $V_{col}$ ( $\text{m}^3$ )	2.85E-22	3.69E-22	5.36E-22	6.29E-22
$V_{act@H_c}/V_{col}$	0.702	0.786	0.478	0.262

In a Stoner-Wolffarth particle where the reversal mechanism is coherent rotation, the activation volume at switching field is identical to the particle volume at the switching field. The small ratios  $V_{act}/V_{particle}$  or  $V_{act}/V_{col}$  observed above reflect the existence of incoherent rotation in the sample. In this case, thermal activation takes place in tiny volumes ( $V_{act}$ ) and then propagating throughout the entire particle. By angle dependence of coercivity and hysteresis loss, Huysmans and Lodder [Huysmans-88, Lodder-89] have proven that the reversal mechanism of alumite media is curling rotation which belongs to incoherent mode. This conclusion agrees with the small ratio  $V_{act}/V_{col}$  found in our study.

Looking into more details in our case, one can see that  $V_{act}$  becomes closer to  $V_{col}$  with decreasing layer thickness, or in other words, with decreasing  $V_{col}$ . This fact is illustrated in Fig. 7.2.6, in which it is shown that the ratio  $V_{act@H_c}/V_{col}$  is approaching one with decreasing  $V_{col}$  (or thickness). It is straightforward that when the ratio  $V_{act}/V_{col}$  approaches one, it means the switching mechanism is closer the coherent rotation. By another approach, Chantrell [Chantrell-91] also supposed that the reversal mechanism tends toward coherent rotation in smaller particles. We can conclude here that the thinner the alumite film, the closer the switching mechanism to the coherent rotation is. If the trend in Fig. 7.2.6 is roughly extrapolated to smaller values of  $V_{col}$ ,  $V_{act@H_c}/V_{col}$  becomes one when the column volume is about  $5 \times 10^{-23} \text{ m}^3$  (or thickness is about  $0.04 \mu\text{m}$ ). At this point, the switching mechanism is supposed to be coherent. Unfortunately, we were not able to make such a thin sample because it is so thin that the polishing technique fails to keep the homogeneity of the thickness. Calculation of critical diameter  $d_{crit}$  between coherent and incoherent mode [Lodder-98] for Co revealed that the volume at which a Co particle changes its reversal mode from incoherent to coherent rotation is about  $2.6 \times 10^{-23} \text{ m}^3$  (equivalent to  $d_{crit} \approx 36.6 \text{ nm}$ ). This is very close to our mentioned value.

## 7.2. Time-dependence effect in perpendicular media

---

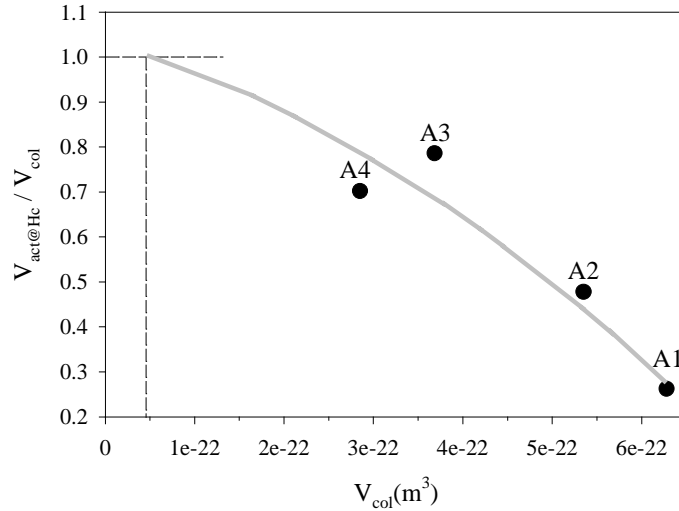


Fig. 7.2.6. Ratio of activation volume at  $H_c$  to column volume versus column volume.

### 7.2.1.4. Fitting results and discussion

The intrinsic viscosity,  $S_0$ , as a function of internal field of the alumite samples has been fitted to the analytical model of Chantrell [Chantrell-94] (see Section 3.2 and 3.6). The fit was carried out in the same manner as in the case of in-plane media (see also Section 7.1), except that in all calculations, external field is replaced by internal field. Figure 7.2.7 shows the fitting results.

The program starts with generating a number array of applied field  $H_a$ . This array is fed into Box 4 (Fig. 3.6.1), in which the internal field  $H_i = H_a - N \times M$  is calculated.  $M$  is assumed to be the magnetization on the hysteresis loop at the corresponding  $H_a$ . This assumption is acceptable because during the relaxation process,  $M$  changes only a little (less than few percent for our cases) thus causing the same little change in  $H_i$ . This change in  $H_i$  does not affect significantly the fitting results. After being calculated in Box 4,  $H_i$  is used to calculate the energy barrier  $\Delta E_m$  (Box 2). The rest of the calculations is similar to the in-plane case. Finally, viscosity  $S_0$  is plotted against  $H_i$ .

7. Experimental and fitting results of time-dependence effect in recording media

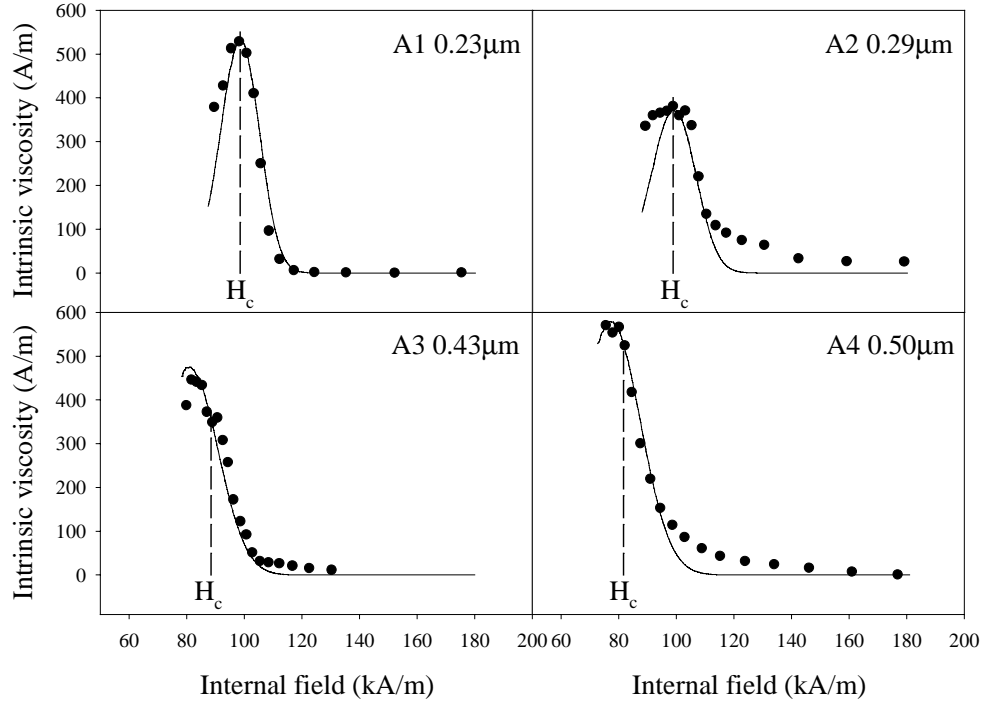


Fig. 7.2.7. Fitting results of the alumite samples. Back dots are  $S_0$  calculated from experiments and solid curves are the fitted curves. Positions of  $H_c$  are also indicated.

The fit is pretty good, except for some points at the end of the slopes. This misfit is similar to that observed in the in-plane case. The fitted curves reflect quite well the existence of the viscosity peak near coercivity as in the in-plane case.

Some important parameters of the fit are listed in Table 7.2.3.

Table 7.2.3: Some important input and out put parameters of the fit. Parameters in italic are inputs, the others are outputs. The switching volume is actually an effective volume found to fit to the model.

Parameters of the fit	Sample A1	Sample A2	Sample A3	Sample A4
Fitting parameter $F$	0.010	0.0076	0.017	0.02
Standard deviation $\sigma$	0.066	0.07	0.085	0.093
Switching volume, $V_{switching}$ ( $m^3$ )	5.073E-24	4.649E-24	3.698E-24	3.648E-24
$V_{switching}/V_{col}$	0.0180	0.0130	0.0069	0.0058
Critical volume ( $m^3$ )	2.406E-24	2.297E-24	2.219E-24	2.250E-24
Calculated $H_c$ (kA/m)	96.64	96.63	75.9	71.09
$KV_{switching}/kT$	58.3	55.9	46.1	44.8

- **The fitting parameter  $F$**  is found smaller than one, which is similar to the in-plane media case.
- **The standard deviations  $\sigma$**  are smaller than those found in the in-plane samples ( $\sigma$  values of CCT1 and CCT2 are 0.22 and 0.40). This is reasonable, due to the fact that morphology of alumite media is more regular than that of sputtered media. Another interesting fact is that  $\sigma$  of the alumite samples is found to increase almost linearly with increasing film thickness (Fig. 7.2.8). This phenomenon could be caused by the change of the column length distribution with thickness. Sterringa [Sterringa-90] observed several alumite samples with SEM and concluded that in many samples, a substantial part of the pores was not fully filled. Although SEM images of the samples used in this chapter were not taken, we can still predict that in the unpolished sample (A4), which is an “as-made” alumite sample, there is a certain distribution of column length, resulting in a relatively high standard deviation. When the “as-made” sample was polished to make thinner samples (A3-A1), the columns were gradually trimmed off. Therefore, in the thinned samples, column length is more uniform, which causes the standard deviation to decrease.

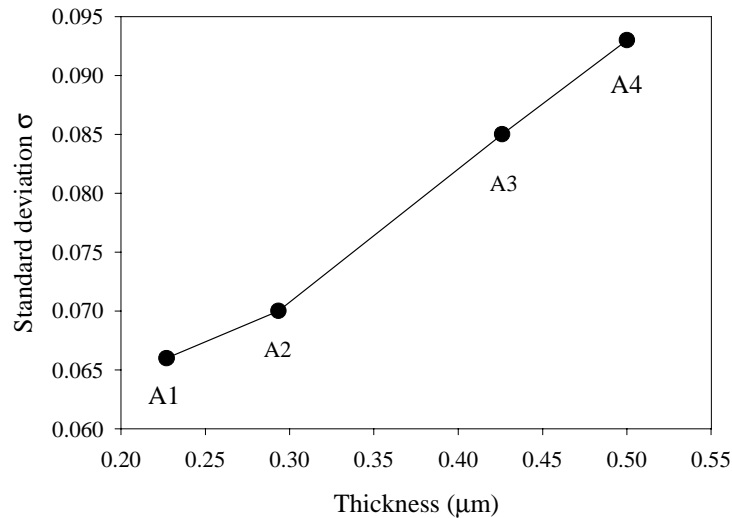


Fig. 7.2.8: Standard deviation  $\sigma$  found in the fit.

- **The switching volumes  $V_{\text{switching}}$**  are much smaller than  $V_{\text{col}}$  and  $V_{\text{act@Hc}}$ . This fact has been found by some other researchers who tried to fit experimental data to a theory using the Stoner-Wolhfarth model to calculate the energy barrier. Lyberatos and co-workers [Lyberatos-91] proposed a mean-field model to solve the demagnetizing field problem in alumite media. They tried to simulate temperature dependence of viscosity and found that the effective volume (similar to the switching volume in our case) involved in the switching process is only 5%

## 7. Experimental and fitting results of time-dependence effect in recording media

of the physical volume of the particles, which is probably attributed to the incoherent reversal mechanism. Their explanation is somewhat similar to the small ratio  $V_{\text{act}}/V_{\text{particle}}$  found by de Witte [Witte-90] as mentioned in the previous section. In our case, the switching volume is as small as about 1% of the column volume (see the ratio  $V_{\text{switching}}/V_{\text{col}}$  in Table 7.2.3).

Commonly, the switching volume should be close to the activation volume. In our case, they are not equal, because the model is based on coherent rotation whereas the activation volume, derived from experiments, probably switches by incoherent rotation. However, by fitting the theoretical viscosity curves to the experimental ones, we tried to make two phenomena equivalent: the incoherent rotation which happens in reality with the coherent rotation of the effective switching volume as found from the fit. This equivalence is just an assumption, still, it reflects, to a certain extent, the real reversal process.

The switching volume is considered as a small portion of a column which reverse coherently. These tiny volumes are slightly bigger than the critical volume (Fig. 7.2.9.a). Figure 7.2.9.b shows that the ratio of the switching volume to the column volume  $V_{\text{switching}}/V_{\text{col}}$  decreases with increasing film thickness. This behavior is similar to that of  $V_{\text{act@Hc}}/V_{\text{col}}$  (Fig. 7.2.6).

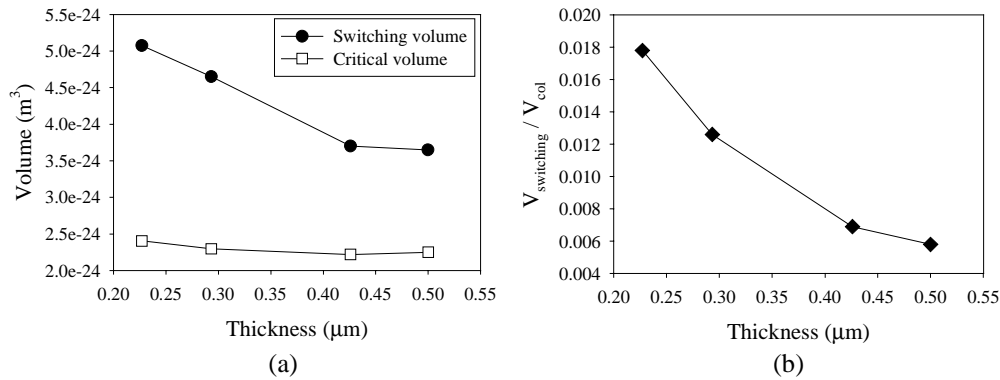


Fig. 7.2.9: (a) Switching volumes versus sample thickness, compared to critical volumes, below which the material is superparamagnetic. (b) Ratio of the switching volume  $V_{\text{switching}}$  to column volume  $V_{\text{col}}$ .

- **It is more reasonable to calculate the ratio  $KV/kT$  from the switching volume rather than from the column volume.** This ratio is around 50 (Table 7.2.3). Figure 7.2.10.a shows that the ratio  $KV/kT$  increases when the thickness of alumite film is reduced. Relaxation time  $\tau$  is calculated from these ratio (Fig. 7.2.10.b). By reducing film thickness from 0.5μm down to about half of that, the calculated relaxation time is enormously increased, from about 10<sup>3</sup> to 10<sup>8</sup> years.

## 7.2. Time-dependence effect in perpendicular media

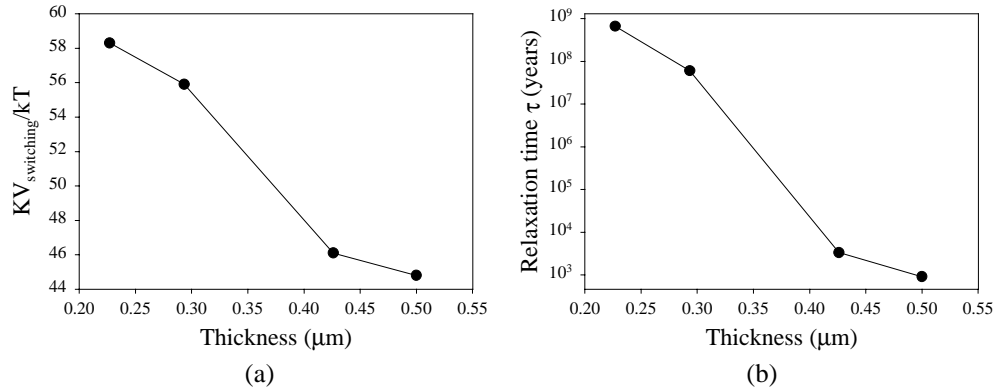


Fig. 7.2.10: (a) The ratio  $KV/kT$  with  $V$  is the switching volume found in the fit. From this ratio, the relaxation time  $\tau$  is calculated (b). Note that  $\tau$  is plotted in log scale.

### 7.2.2. CoCrTa single layers

CoCrTa single layer samples investigated in this section are those studied in Chapter 5, in which, we have shown the study about the influences of substrate temperature ( $T_s$ ) and Ta content on their structural and magnetic properties. Following Chapter 5 and Section 7.2.1, this section will present a study of the time-dependence effect in these CoCrTa single layer samples.

#### 7.2.2.1. Viscosity curves

We investigated two groups of CoCrTa samples corresponding to two target compositions of 2 and 5 at.% of Ta. They were produced at different substrate temperatures ( $T_s$ ) from room temperature to  $250^\circ\text{C}$ . Their thickness is about 100nm. Because these samples have mainly perpendicular c-axis orientation, their time-dependence properties are measured in perpendicular direction. Table 7.2.4 gives some brief descriptions of the investigated samples.

Relaxation curves of the samples were measured at different applied fields and consequently, viscosity as a function of applied field (viscosity curve) was calculated. The behavior of viscosity curves is similar to that of alumite media: they exhibit a short plateau at low field and decrease when the field is further increased. This is undoubtedly due to the demagnetizing effect. This behavior is well known and has been observed by other researchers working on CoCr perpendicular thin films [Webb-88, Lintelo-93, Lintelo-94]. However, in these references, the authors could not explain clearly the nature of this behavior. Examples of the viscosity curves of samples Ta2-200 and Ta5-200 are illustrated in Fig. 7.2.11. In the graphs, the viscosity is normalized on  $M_s$ . These two samples

7. Experimental and fitting results of time-dependence effect in recording media

have been chosen for thorough investigations because they both have the highest perpendicular coercivity compared to other samples of the same group.

Table 7.2.4. Names and general properties of two groups of CoCrTa samples.

Compositions	Names	T <sub>s</sub> (°C)	Perpendicular H <sub>c</sub> (kA/m)	In-plane H <sub>c</sub> (kA/m)
Co <sub>86</sub> Cr <sub>12</sub> Ta <sub>2</sub>	Ta2-RT	RT	17.7	17.1
	Ta2-100	100	15.0	16.4
	Ta2-150	150	40.3	11.1
	Ta2-200	200	104.4	14.5
	Ta2-250	250	63.5	20.7
Co <sub>82</sub> Cr <sub>13</sub> Ta <sub>5</sub>	Ta5-RT	RT	5.0	11.1
	Ta5-100	100	6.2	11.5
	Ta5-150	150	62.2	6.8
	Ta5-200	200	124.7	38.7
	Ta5-250	250	88.5	12.3

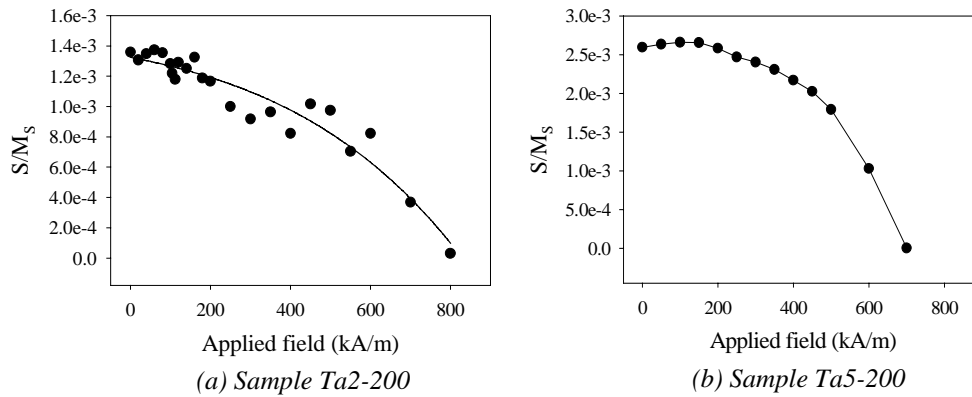


Fig. 7.2.11. Normalized viscosity curves of Ta2-200 and Ta5-200 as a function of applied field.

There is a remarkable difference in the viscosity values of these two curves. In general, viscosity values of sample Ta2-200 are smaller than those of Ta5-200. At low fields,  $S/M_s$  values of Ta2-200 are about 1.5 times lower than  $S/M_s$  values of Ta5-200. This difference could be qualitatively interpreted. From Table 7.2.5 we can see that at zero applied field, the product  $KV_{act}$  of Ta2-200 is about double that of Ta5-200. Sample Ta2-200 is therefore more magnetically stable than Ta5-200, resulting in the observed fact that at low field, viscosity of Ta2-200 is lower than that of Ta5-200.

## 7.2. Time-dependence effect in perpendicular media

Table 7.2.5.  $KV_{act}$  products of samples Ta2-200 and Ta5-200.

	<b>Ta2-200</b>	<b>Ta5-200</b>
$K_1$ (kJ/m <sup>3</sup> )	74.58	65.25
$V_{act}$ at zero applied field (m <sup>3</sup> )	8.0E-24	4.3E-24
$K_1 V_{act}$ (kJ)	596.6E-42	280.6E-24

Moreover, from Fig. 7.2.11 we can notice that the viscosity curve of Ta2-200 has a very short plateau at low field whereas viscosity curve of Ta5-200 exhibits a longer plateau up to about 200 kA/m and decreases faster at high field. We will show later that this feature is correlated to the squareness of the hysteresis loop and SFD.

Since the main difference of the viscosity curves of the samples is the difference in their values, for the rest of the samples, we only measured their average viscosity at the plateau, i.e. at low applied field. This value is denoted as  $S_{plateau}$ . Figure 7.2.12 shows the dependence of  $S_{plateau}/M_s$  on the perpendicular coercivity. Because  $S_{plateau}$  is normalized to  $M_s$ , the ratios  $S_{plateau}/M_s$  of the samples are comparable.

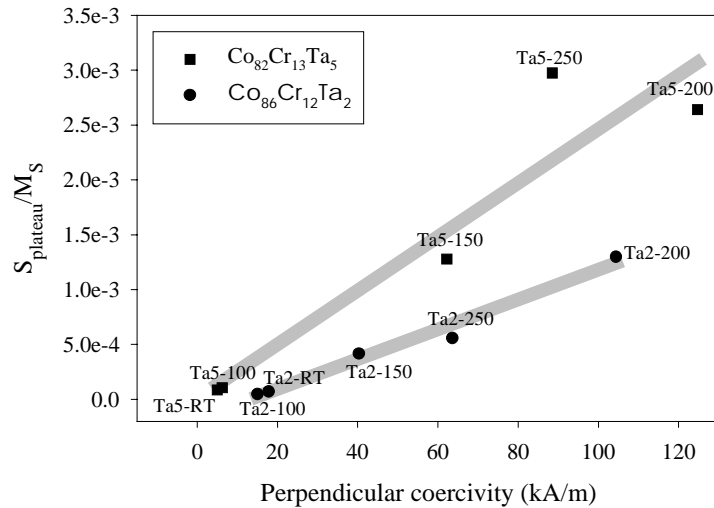


Fig. 7.2.12. Normalized viscosity at the plateau as a function of perpendicular coercivity.

From Fig. 7.2.12, we can easily recognize an interesting feature that  $S_{plateau}/M_s$  increases with increasing  $H_c$ , in the case of group Ta2, the increase is almost linear. Values of  $S_{plateau}/M_s$  of each group of samples (groups Ta2 and Ta5) follow a distinct trend. The mechanism leading to this phenomenon is very complicated and temporarily not understood. The trend of group Ta5 is at higher values than that of group Ta2. Similarly to the explanation in the case of Ta2-200 and Ta5-200

## 7. Experimental and fitting results of time-dependence effect in recording media

above, this could be due to the fact that anisotropy constants  $K_1$  of group Ta2 are generally higher than those of group Ta5 (see Section 5.3.2).

By the same way described in Section 3.4, viscosity curves of samples Ta2-200 and Ta5-200 are corrected for the demagnetizing effect (Fig. 7.2.13). After correction, viscosity peaks appear near the values of  $H_c$ , as in the case of alumite samples (Section 7.2.1). Similarly to the uncorrected viscosity curve, the intrinsic (corrected) viscosity  $S_0$  curve of Ta2-200 decreases faster than that of Ta5-200.  $S_0$  of Ta2-200 almost vanishes at  $H_i$  of 130kA/m whereas  $S_0$  of Ta5-200 gradually vanishes at a field higher than 200kA/m. In other words, the viscosity peak of the first case is “narrower” than that of the second case. In Section 7.1.1, we have pointed out that the width of the viscosity peak (characterized by  $S_{\text{half-width}}$ ) of in-plane media correlates closely with SFD. Now this correlation happens again in this case where the demagnetizing effect has been eliminated by correction.

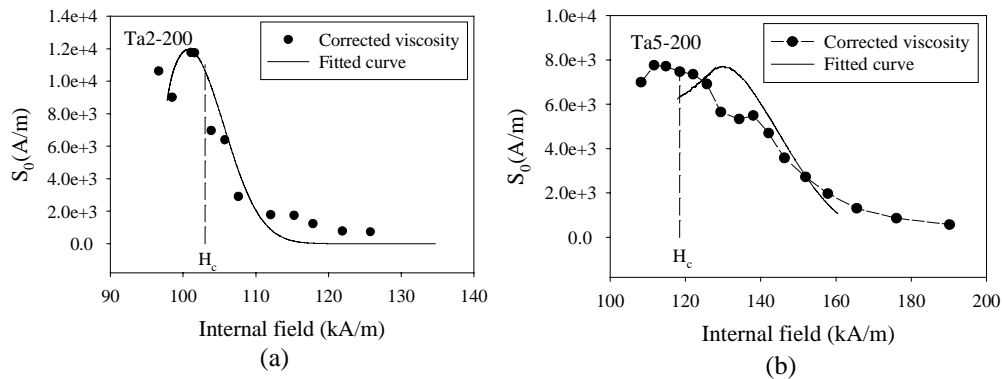


Fig. 7.2.13. Corrected viscosity as a function of internal field and fitted curves for samples Ta2-200 (a) and Ta5-200 (b).

Figure 7.2.14 shows two distinct corrected hysteresis loops and the corresponding total susceptibility curves ( $dM_{\text{hys}}/dH$ ) of these two samples. Apparently, the hysteresis loop of Ta2-200 is squarer than that of Ta5-200 (Fig. 7.2.14.a). Consequently, the total susceptibility curve of Ta2-200 exhibits a higher and narrower peak than Ta5-200 (Fig. 7.2.14.b). Calculations of switching field distribution, SFD of the two samples give that SFD of Ta2-200 is  $84.3 \times 10^{-3}$ , smaller than SFD of Ta5-200 which is  $138.4 \times 10^{-3}$ . In Section 7.1.2, we have proven that a wider SFD means a wider distribution of energy barrier and according to the fit, this results in a wider viscosity peak. This is the reason why the intrinsic viscosity peak of Ta5-200 is wider and its uncorrected viscosity curve (Fig. 7.2.11.b) has a longer plateau.

## 7.2. Time-dependence effect in perpendicular media

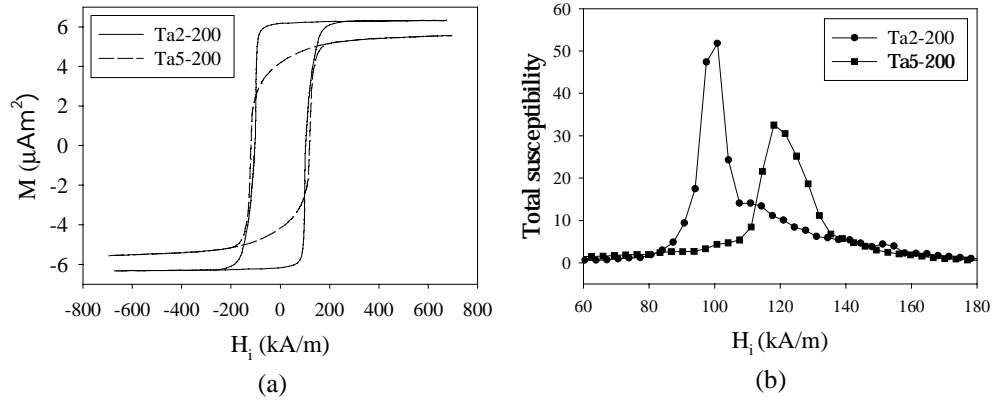


Fig. 7.2.14. Hysteresis loops and total susceptibility curves of samples Ta2-200 and Ta5-200.

### 7.2.2.2. Activation volumes

Figure 7.2.15 plots the activation volumes as a function of internal field. The curves have the same shapes as the corresponding intrinsic viscosity curves. The activation volumes of these two samples have the same order of magnitude of  $10^{-24} \text{ m}^3$ . In Chapter 5, we have shown a TEM plane-view image of an 100nm  $\text{Co}_{82}\text{Cr}_{13}\text{Ta}_5$  layer deposited on  $\text{Si}_3\text{N}_4$  membrane at  $T_s=150^\circ\text{C}$  and estimated that the grain size of this sample is about 23nm. Except the substrate temperature, the sputtering conditions of this sample are the same as those of sample Ta5-200. The difference in  $T_s$  of these two cases is not too large that the grain size could be changed considerably. So we can now consider the grain size of sample Ta5-200 is also about 23nm, which is equivalent to a grain volume of about  $4 \times 10^{-23} \text{ m}^3$ . In Section 5.3.2, we compared AFM images of two  $\text{Co}_{86}\text{Cr}_{12}\text{Ta}_2$  and  $\text{Co}_{82}\text{Cr}_{13}\text{Ta}_5$  samples deposited at  $200^\circ\text{C}$  and concluded that their grain sizes are only slightly different. This fact suggests that the grain volume of sample Ta2-200 is also very close to the value  $4 \times 10^{-23} \text{ m}^3$  of Ta5-200 as estimated above. This value is about several times larger than their activation volumes. The ratios  $V_{\text{act}@H_c}/V_{\text{grain}}^*$  are about 0.22 for Ta2-200 and 0.11 for Ta5-200. Similarly to the arguments in Section 7.1 and 7.2.1, we can conclude here that the reversal mechanism of Ta2-200 and Ta5-200 is incoherent. Their ratios  $V_{\text{act}@H_c}/V_{\text{grain}}$  are considerably smaller than those of alumite and in-plane  $\text{CoCrTa/Cr}$  samples investigated in Section 7.2.1 and 7.1. This indicates that the reversal mechanisms of grains of the alumite and  $\text{CoCrTa/Cr}$  samples are closer to the coherent rotation than that of  $\text{CoCrTa}$  single layer studied in this section.

\*  $V_{\text{act}@H_c}$  is the activation volume at coercivity

7. Experimental and fitting results of time-dependence effect in recording media

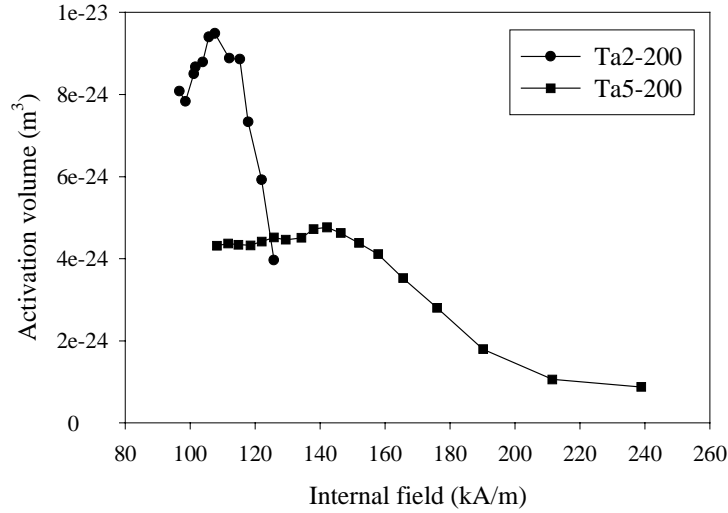


Fig. 7.2.15. Activation volumes of samples Ta2-200 and Ta5-200 as a function of internal field.

Figure 7.2.16 shows a relationship between the activation volume at coercivity and coercivity. We found that this relation is  $V_{act} \propto H_c^{-1.7}$  or  $H_c \propto V_{act}^{-0.59}$ . For many bulk magnetic materials, the relationship has been reported to be  $H_c \propto V_{act}^{-0.73}$  [Wohlfarth-84], which is rather close to our case.

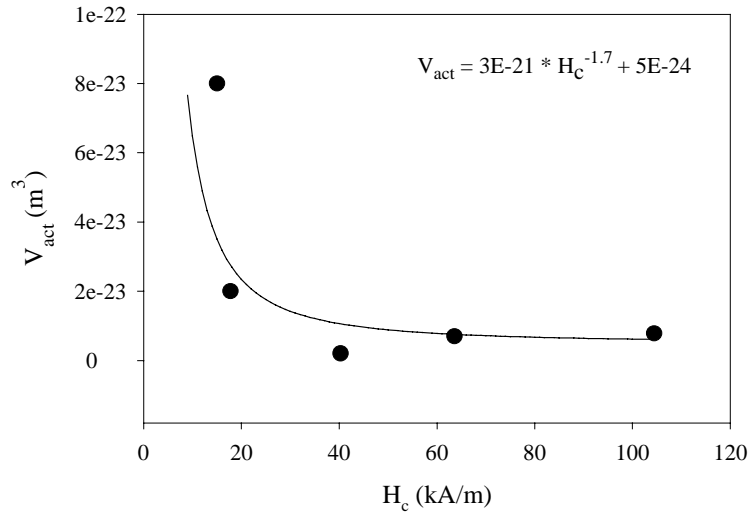


Fig. 7.2.16. Relationship between activation volumes (at  $H_c$ ) and  $H_c$  of series Ta2.

### 7.2.2.3 Fitting results and discussion

In Fig. 7.2.13, fitted curves are plotted together with the intrinsic viscosity curves calculated from measurements. The fit seems to be pretty good for sample Ta2-200 but not for sample Ta5-200. It is impossible to make the fitted peak of Ta5-200 coincide with that of the experimental. However, at least the fit can reflect the shape of the curve. Table 7.2.6 gives some important parameters of the fit.

It is reasonable that the standard deviation  $\sigma$  of Ta5-200 is larger than  $\sigma$  of Ta2-200. The larger the standard deviation, the wider the distribution of the energy barrier and the larger SFD are. Similarly to the in-plane CoCrTa/Cr samples investigated in Section 7.1, the switching volumes are very close to the activation volumes at  $H_c$ , and they are a few times larger than the critical volume. The reversal mechanism of these two samples could be concluded to be incoherent, similar to the arguments drawn from  $V_{act}$ . The misfit of the fitted curve of Sample Ta5-200 with the experimental one could be attributed to the fact that the fit is based on coherent (Stoner-Wohlfarth) rotation while in practice, the reversal mechanism is incoherent rotation.

*Table 7.2.6. Some important input and out put parameters of the fit. Parameters in italic are inputs, the others are outputs. The switching volume is actually an effective switching volume found to fit to the model.*

<b>Parameters of the fit</b>	<b>Ta2-200</b>	<b>Ta5-200</b>
<i>Fitting parameter <math>F</math></i>	<i>0.16</i>	<i>0.77</i>
<i>Standard deviation <math>\sigma</math></i>	<i>0.09</i>	<i>0.60</i>
<i>Switching volume, <math>V_{switching}</math> (<math>m^3</math>)</i>	<i>4.87E-24</i>	<i>6.754E-24</i>
$V_{switching}/V_{grain}$	0.12	0.17
Critical volume ( $m^3$ )	1.53E-24	1.75E-24
Calculated $H_c$ (kA/m)	98.8	105.6

## 7.3. Conclusion

We have presented some studies of the time-dependence effect in three types of recording media, namely, CoCrTa/Cr in-plane media, perpendicular alumite media and CoCrTa single layer media. The studies dealt with the field dependence of magnetic viscosity, activation volume, etc. and the relation between these quantities and other properties of the media. Viscosity curves (curve of viscosity versus field) were fitted to a model, from which, some observed behaviors and the nature of the viscosity curve have been interpreted.

## 7. Experimental and fitting results of time-dependence effect in recording media

---

Although alumite media are not the main objective of this thesis, we still put considerable effort to study these media. The studies of alumite not only give some understanding about the time-dependence effect in perpendicular media in general but also help us to understand the similar effect in perpendicular CoCrTa single layer media.

Experimental results on CoCrTa/Cr in-plane media showed that their magnetic viscosity exhibits a peak near  $H_{cr}$ . There is a close correlation between the width of the peak and SFD. Activation volumes were found to be close to the physical volume of the grains. From the fitting results, the nature of the viscosity curve has been suggested. Based on these results, we were able to understand the factors which affect the shape of the viscosity curves. The switching volumes, which are the fitting parameters of the fit, were found to be close to the measured activation volume and the physical volumes of the grains. This suggested that the switching mechanism of the samples is probably incoherent or partly coherent rotation.

Viscosity curves of perpendicular alumite media, however, were found to have different shapes than the in-plane media. Viscosity values exhibit a plateau at low applied field and then decreases with the field. This behavior is due to the demagnetizing effect. After correcting for this effect, the shape similar to that of in-plane media is recovered. Fitting results of these alumite samples revealed that the model only accepts a switching volume which is much smaller than the activation volume and the physical volume of the sample. The reversal mechanism of the samples is supposed to be curling and it tends toward coherent rotation when the thickness is reduced.

The last part of the chapter showed some results of two groups of CoCrTa single layer media. These samples are considered perpendicular media because their c-axis orientation is mainly perpendicular. The viscosity curves of the samples have similar shape as those of alumite media. We found that the value of viscosity at low field (at the plateau) increases almost linearly with increasing  $H_c$ . The switching volumes found from the fit are close to the activation volumes, however, they are several times smaller than the physical volumes of the grains. This indicates that the reversal mechanism of the samples is incoherent.

## 7.4. References

- [Batlle-97] X. Batlle, M. Garcia del Muro and A. Labarta. "Interaction effects and energy barrier distribution on the magnetic relaxation of nanocrystalline hexagonal ferrites". *Phys. Rev. B*, Vol 55(10) (1997), 6440.
- [Brown-63] W. F. Brown Jr., *Phys. Rev.* 130, (1963) 1677.

#### 7.4. References

---

- [Chantrell-88] R. W. Chantrell, G. N. Coverdale and K. O'Grady. "Time dependence and rate dependence of the coercivity of particulate recording media". J. Phys. D. Appl. Phys. 21 (1988), 1469.
- [Chantrell-91] R. W. Chantrell. "Magnetic viscosity of recording media" J. Magn. Magn. Mat. 95 (1991), 365.
- [Chantrell-94] R. W. Chantrell, A. Lyberatos, M. El-Hilo and K. O'Grady. "Models of slow relaxation in particulate and thin film materials (invited)". J. Appl. Phys. 76(10) (1994), 6407.
- [Chantrell-98] Private communications.
- [Charap-88] S. H. Charap. "Magnetic viscosity in recording media". J. Appl. Phys. 63(6) (1988), 2054.
- [Crew-96] D. C. Crew, S. H. Farrant, P. G. McCormick and R. Street. "Measurement of magnetic viscosity in a Stoner-Wohlfarth material". J. Magn. Magn. Mat. 136 (1996), 299
- [Cullity-72] B. D. Cullity. "Introduction to magnetic materials". Addison-Wesley (1972).
- [Dova-97] P. Dova, K. O'Grady, M. F. Doerner and M. Mirzamaani. "Coupling and crystallographic effects in thin film Cobalt alloy recording media". IEEE Trans. Magn. 33 (1997), 2953.
- [Folks-94] L. Folks and R. Street. "Analysis and interpretation of time dependent magnetic phenomena (invited)". J. Appl. Phys. 76(10)(1994), 6391.
- [Gaunt-76] P. Gaunt. "Magnetic viscosity in ferromagnets - I. Phenomenological theory". Physiological Magazine, 34 (1976), 775.
- [Granqvist-76] C. G. Granqvist and R. A. Buhrman. "Ultrafine metal particles". J. Appl. Phys, Vol. 47(5) (1976), 2200.
- [Huysmans-88] G. T. A. Huysmans and J. C. Lodder. "Magnetization curling in perpendicular iron particle arrays (alumite media)". J. Appl. Phys 64(4) (1988), 2016.
- [Li-97a] F. Li and R. M. Metzger. "Activation volume of  $\alpha$ -Fe particles in alumite films". J. Appl. Phys. 81 (8) (1997), 3806.
- [Li-97b] F. Li, R. M. Metzger, and W. D. Doyle. "Influence of particle size on magnetic viscosity and activation volume of  $\alpha$ -Fe nanowires in alumite films". IEEE Trans. Magn. 33 (1997), 3715.
- [Lintelo-93] H. te Lintelo, W. Streekstra, J. C. Lodder and T. Popma. "The influence of demagnetization on the after-effect of Co-Cr micro structure". IEEE Trans. Magn. 29 (1993), 3748.
- [Lintelo-94] J. G. Th. te Lintelo and J. C. Lodder. "On the relationship between magnetic viscosity and coercivity of perpendicular media". J. Appl. Phys

## 7. Experimental and fitting results of time-dependence effect in recording media

---

- 76(3) (1994), 1741.
- [Lodder-89] J. C. Lodder and L. C. Zhang. "Reversal behaviour in perpendicular iron particle arrays (alumite media). IEEE Trans. Magn. 25 (1989), 4171.
- [Lodder-95] J. C. Lodder. "Co-Cr-(X) thin films for high density recording". Ph.D. thesis – University of Twente, the Netherlands, 1995.
- [Lodder-97] J. C. Lodder and S. de Haan. J. Mag. Soc. Jap. 21 Suppl. S2 (1997), 17.
- [Lodder-98] J. C. Lodder. "Magnetic recording hard disk thin film media". Handbook of magnetic materials. Vol. 11 (1998), edited by K. H. J. Buschow.
- [Lottis-90] D. Lottis, R. White and E. D. Dahlberg. "The magnetic aftereffect in CoCr films: A model". J. Appl. Phys. 67(9) (1990), 5187.
- [Lyberatos-94] A. Lyberatos, R. W. Chantrell and K. O'Grady. "Activation volumes and magnetization reversal in fine particles". Nato ASI Series E: Applied Sciences, 1994. Vol. 260, 653.
- [Lyberatos-91] A. Lyberatos, R. W. Chantrell, E. R. Sterringa and J. C. Lodder. "Magnetic viscosity in perpendicular media". J. Appl. Phys 70(8) (1991), 4431.
- [Lyberatos-97] A. Lyberatos and R. W. Chantrell. "The fluctuation field of ferromagnetic materials". J. Phys: Condens. Matter. 9 (1997), 2623.
- [Mayo-91] P.I. Mayo, K. O'Grady, R.W. Chantrell, J.A. Cambridge, I.L. Sanders, T. Yogi and J.K. Howard. "Magnetic measurement of interaction effects in CoNiCr and CoPtCr thin film media". J. Magn. Magn. Mat. 95(1991), 109
- [Neel-51] L. Néel, J. Phys. Rad. 12 (1951), 339 .
- [Oseroff-87] S. B. Oseroff, D. Franks, V. M. Tobin and S. Schultz. "Magnetization time decay in particulate media". IEEE Trans. Magn. MAG-23 (1987), 2871.
- [Ross-98] C. A. Ross, F. M. Ross, G. Bertero and K. Tang. "Microstructural evolution and thermal stability of thin CoCrTa/Cr films for longitudinal magnetic recording media". IEEE Trans. Magn. 34 (1998), 282.
- [Sharrock-90] M. P. Sharrock. "Time-dependent magnetic phenomena and particle-size effects in recording media". IEEE Trans. Magn. 26 (1990), 193
- [Shiraki-85] M. Shiraki, Y. Wakui, T. Tokushima and N. Tsuya. "Perpendicular magnetic media by anodic oxidation method and their recording characteristics". IEEE Trans. Magn. MAG-21 (1985), 1465.
- [Sterringa-90] E. R. Sterringa. "Magnetic properties of alumite media" M.Sc.Eng. report - Faculty of Electrical Engineering - University of Twente, October 1990

#### 7.4. References

---

- [Stoner-48] Stoner, E. C. and Wohlfarth. "A mechanism of magnetic hysteresis in heterogeneous alloys". E. P., Phil. Trans. Roy. Soc. A-240 (1948), 599.
- [Street-49] R. Street and J. C. Woolley. "A study of magnetic viscosity". Proc. of Phys. Soc. A62 (1949), 562.
- [Street-52] R. Street, J. C. Woolley and P. B. Smith. "Magnetic viscosity under discontinuously and continuously variable field conditions". Proc. of Phys. Soc. B.65 (1952), 679.
- [Suzuki-96] H. Suzuki, P. R. Bissell, R. W. Chantrell and N. Kodama. "In-plane time-dependent magnetisation and magnetic interactions of Co-Cr-Ta thin films". J. Magn. Magn. Mat. 155 (1996), 196.
- [Tsuya-86] N. Tsuya, T. Tokushima, M. Shiraki, Y. Wakui, Y. Saito, H. Nakamura, S. Hayano, A. Furugori and M. Tanaka. "Alumite disc using anodic oxidation (invited)". IEEE Trans. Magn. MAG-22 (1986), 1140.
- [Uwazumi-97] H. Uwazumi, Jinghuan Chen and J. H. Judy. "Time decay of remanent magnetization, remanent coercivity, and readback signal of ultra-thin longitudinal CoCr<sub>12</sub>Ta<sub>2</sub>/Cr thin film media". IEEE Trans. Magn. 33 (1997), 3031.
- [vanDrent-91] W. van Drent, E. Sterringa, J. C. Lodder, G. Bottoni, D. Candolfo, A. Cecchetti and F. Masoli. "Rotational hysteresis measurements on alumite perpendicular media". J. Magn. Soc. Japan 15 (Supp. S2) (1991), 951.
- [Webb-88] B. C. Webb, S. Schultz and S. B. Oseroff. "Magnetization decay in Co-Cr films". J. Appl. Phys 63(8) (1988), 2923.
- [Witte-90] A. M. De Witte, K. O' Grady, G. N. Coverdale and R. W. Chantrell. "Activation volumes of reversal in ultrafine particles and recording media". J. Magn. Magn. Mat. 88 (1990), 183.
- [Witte-93] A. M. de Witte, K. O' Grady and R. W. Chantrell. "The determination of the fluctuation field in particulate media". J. Magn. Magn. Mat. 120 (1993), 187.
- [Wohlfarth-84] E. P. Wohlfarth. "The coefficient of magnetic viscosity". J. Phys. F: Met. Phys. 14(1984), L155
- [Zhu-88] J. G. Zhu and H. N. Bertram. "Micromagnetic studies of thin metallic films (invited)". J. Appl. Phys 63(8) (1988), 3248.

# Chapter 8

---

## Summary, general conclusions and future trends

### 8.1. Summary

This thesis has been devoted to deposition process, structures, magnetic properties and time-dependence effect of CoCrTa magnetic thin films for recording media. The experimental study began from Chapter 5 by investigating properties of single layer CoCrTa thin films, produced under different sputtering conditions. Next, in Chapter 6, structure of Cr single layer has been studied separately, in order to find a key to control the crystallography of this layer. After that, the CoCrTa layer was deposited onto the Cr underlayer, to form a configuration of typical longitudinal recording media. The dependence of various properties of CoCrTa/Cr media samples on thickness of each constituent layer has been investigated. In the second half of the thesis, which was presented in Chapter 7, we concentrated on the time-dependence effect in CoCrTa media samples, as both longitudinal (in-plane) and perpendicular media. The field dependence of viscosity, which belongs to the time-dependence effect, was the main subject of this study. In addition to CoCrTa media, we also studied perpendicular alumite media because this type of media is considered a good model to study various magnetic behaviors of recording media.

**Chapter 5** reported the study of CoCrTa single layer thin films having c-axes perpendicular to the film plane, grown on Si substrate, under various sputtering conditions. An aim of the studies is to prepare knowledge for further studies of CoCrTa/Cr thin films in Chapter 6.

First of all, Ar pressure was varied. We found that in all examined films at different PAr's and at RT, the (0002) texture is dominant. The sample produced at  $2 \times 10^{-2}$  mbar was found to have the strongest (0002) texture. Measurements of film compositions showed that when PAr increases, the Cr content increases, the Ta content decreases and the Co content is almost unchanged. Besides, we found that

## 8.1. Summary

---

Ar atoms are entrapped inside the films and the Ar content decreases with increasing PAr. Concerning the crystallographic spacings, it was observed that both (0002) and (10 $\bar{1}$ 0) spacings contract when PAr increases, which is associated with the decrease in the Ta and Ar contents in the films. Both in-plane and perpendicular coercivities increase slightly with PAr. Saturation magnetization decreases with increasing PAr, which is proven to be caused by the decrease in the film density.

In the second series of samples, we varied Ar pressure while setting substrate temperature  $T_s$  at 150°C. We found that the optimum PAr in this case is about  $3 \times 10^{-2}$  mbar, instead of  $2 \times 10^{-2}$  mbar in the case at room temperature.

The second parameter to be varied was the substrate temperature  $T_s$ . It was found that the optimum  $T_s$  to obtain good (0002) texture is about 150°C. From the depth profiles of the composition, we found that the samples are oxidized from the surface to a depth of about 5-10nm. Co seems to accumulate to the surface to form Co oxide. The interface region between the film and the substrate, where Co, Cr and Ta diffuse into the Si substrate, extends as  $T_s$  increases. Regarding magnetic properties, we found that the perpendicular coercivity increases drastically with  $T_s$  and becomes saturated at  $T_s$  higher than 200°C. The ratio  $H_{c\perp}/H_{c\parallel}$  and the first anisotropy constant, characterizing the perpendicular anisotropy, get maximum at 150°C. From the studies in this section, it could be concluded that 150°C is the optimum substrate temperature.

The second part of the chapter presented some studies of CoCrTa films of various thicknesses. By making several films of different thicknesses and comparing the in-plane hysteresis loops, we estimated that the initial layer in our films has a thickness of about 20nm.

The last part of the chapter dealt with the influences of CoCrTa alloy composition on the properties of CoCrTa films. Magnetic and structural properties of perpendicular media samples made of two different compositions ( $\text{Co}_{86}\text{Cr}_{12}\text{Ta}_2$  and  $\text{Co}_{82}\text{Cr}_{13}\text{Ta}_5$ ) deposited on Si substrates and at different substrate temperatures from room temperature to 250°C have been studied and interpreted. It was found that perpendicular  $H_c$  of the two compositions reaches maximum at  $T_s$  of about 200°C. Generally,  $H_c$  of  $\text{CoCrTa}_5$  is higher than that of  $\text{CoCrTa}_2$ . Contrary to the behavior of  $H_c$ , c-axis orientation of  $\text{CoCrTa}_2$  samples was found to be better than that of  $\text{CoCrTa}_5$  samples. To get an optimum material, suitable for making magnetic recording media, we suggested that Ta content should be in between 2 and 5 at.% to compromise the two contrary trends as mentioned above and  $T_s$  should be about 150 to 200°C.

**Chapter 6** began with the study of single Cr layers on different types of substrates and under different sputtering conditions, in order to find a way to control and to optimize the texture of the Cr layer. A substrate temperature  $T_s$  of about 200-250°C was found to create a Cr film (100nm-thick) with both (110) and (200) textures. High  $T_s$  promotes the (200) texture, whereas at low  $T_s$ , only Cr(110) exists. Varying Cr film thickness, we found that 100nm-thick film has comparably strong (110) and (200) textures. Argon pressure has equal effects on both textures, and it was found to be optimum at  $3 \times 10^{-2}$  mbar.

In the next step, we deposited CoCrTa layer of various thicknesses on a Cr underlayer of fixed thickness. Measurements of in-plane coercivity and other parameters suggested that 20nm is the optimum thickness for CoCrTa layer. Angular dependence of coercivity and hysteresis loss of the samples has been studied. Comparison between the measurements and theories of reversal mechanisms indicates that the magnetization of the samples switches mainly by incoherent rotation mode. There is a tendency to change from incoherent to coherent rotation when CoCrTa thickness is reduced.

Finally, we deposited a CoCrTa layer of fixed thickness onto a Cr underlayer of various thicknesses. Plane-view TEM images show that grain size increases with increasing Cr underlayer thickness. From the cross-sectional images, it was found that the samples have a clear columnar structure. Concerning magnetic properties, we observed that the in-plane coercivity increases abruptly when the Cr underlayer is introduced and tends to be saturated when the Cr layer is about 50nm thick. The squareness  $S$  and the in-plane anisotropy constant were found to peak at about 45-75nm. This suggested that a Cr underlayer of thickness in this range is considered the optimum thickness for longitudinal recording. Moreover, from the initial susceptibility measurements and angular dependence of coercivity and hysteresis loss, we found that the sample without an underlayer switches by domain wall motion mode. When the Cr underlayer is introduced, the reversal mode changes to incoherent and tends to move to coherent mode in samples having thick Cr underlayer.

**Chapter 7** was devoted to the time-dependence effect in three types of recording media, namely, CoCrTa/Cr in-plane media, perpendicular alumite media and CoCrTa single layer media.

Experimental results on CoCrTa/Cr in-plane media showed that their magnetic viscosity exhibits a peak near  $H_{cr}$ . There is a close correlation between the width of the peak and SFD. Activation volumes around  $H_c$  were found to be close to the physical volumes of the grains. From the fitting results, the nature of the viscosity curve has been suggested. Based on these results, we were able to understand the factors which affect the shape of the viscosity curves. The switching volume,

## 8.1. Summary

---

which is a fitting parameter of the fit, was found to be close to the measured activation volume around  $H_c$  and the physical volume of the grains. This suggested that the switching mechanism of the samples is probably incoherent or partly coherent rotation.

Viscosity curves of perpendicular alumite media, however, were found to have different shapes than in-plane media. Viscosity values exhibit a plateau at low applied field and then decreases with the field. After correction for the demagnetizing effect, the shape of the viscosity curves similar to that of in-plane media is recovered. Fitting results for these alumite samples revealed that the model only accepts a switching volume which is much smaller than the activation volume and the physical volume of the sample. The reversal mechanism of the samples is supposed to be curling and it tends toward coherent rotation when the thickness is reduced.

CoCrTa single layer media were studied in the last part of the chapter. The samples are considered perpendicular media because their c-axis orientation is mainly perpendicular. The viscosity curves of the samples have similar shape as those of alumite media. We found that the value of viscosity at low field (at the plateau) increases almost linearly with increasing  $H_c$ . The switching volumes found from the fit are close to the activation volumes, however, they are several times smaller than the physical volumes of the grains. This indicates that the reversal mechanism of the samples is incoherent.

## 8.2. General conclusions

1. Among sputtering parameters,  $T_s$  is the strongest factor influencing properties of CoCrTa media. In general,  $H_c$  increases with increasing  $T_s$ . However,  $T_s$  should not exceed 200°C.
2. PAr is the second important parameter. There exists an optimum PAr for CoCrTa media at a certain condition. The optimum PAr is commonly around  $2 \times 10^{-2}$  -  $3 \times 10^{-2}$  mbar (valid for our sputtering equipment).
3. The initial layer thickness of CoCrTa thin films produced under our conditions is about 20nm.
4. In CoCrTa media, optimum Ta content should be in between 2 and 5 at.%.
5. Concerning the Cr underlayer, high  $T_s$  promotes the Cr(200) texture while at low  $T_s$ , only Cr(110) exists.

6. Without a Cr underlayer, CoCrTa film has very low in-plane  $H_c$ . However, in-plane  $H_c$  increases abruptly when a Cr underlayer is introduced and tends to be saturated when the Cr underlayer is about 50nm thick.
7. Reversal mechanism changes from domain wall motion to incoherent and heading towards coherent mode when the Cr underlayer is thicker.
8. In CoCrTa/Cr media, CoCrTa layer thickness of 20nm is the optimum thickness.
9. There is a tendency to change from incoherent to coherent rotation when CoCrTa layer thickness is reduced.
10. Magnetic viscosity of in-plane media exhibits a peak near  $H_{cr}$ . The shape of the viscosity versus applied field curve (viscosity curve) and the position of the viscosity peak can be fully understood.
11. Due to the demagnetizing field, viscosity curve of perpendicular media generally has a plateau at low field and then decreases to zero with increasing the field. The peak-shaped viscosity curve similar to the in-plane case can be recovered by correcting for the effect of the demagnetizing field.
12. The value of viscosity at low field (i.e. at the plateau) of CoCrTa single layers increases almost linearly with increasing  $H_{c\perp}$ .

### 8.3. Future trends of data storage technologies

The development of human society nowadays and in the next millennium creates an enormously increasing amount of information and the demand for devices to store information is growing every year. This evolution requires more and more huge storage media with smaller sizes, higher capacity and low prices. Currently, magnetic recording is still a leader in digital data storage, especially computer hard disks. At the moment, the highest areal density of magnetic recording, achieved by IBM, is 5.7 Gbits/in<sup>2</sup> in the Travelstar family and 11.6 Gbits/in<sup>2</sup> in the laboratory (see Chapter 1).

In the near future, **hard disk drives based on Co-alloy longitudinal recording media** will still be used with further improvement, chiefly due to their high density and fast access time [Lodder-98]. The improvement includes further scaling of recording parameters, such as head-to-medium spacing (flying height), gap length, media thickness and grain size of the medium, and improvement of GMR head [Speliotis-99]. Today's IBM disk drives have flying heights as low as 20 nm. They announced that a 10 nm flying height will be attained not long after the year 2000 [IBM-99a]. This means that the surface of the media should be extremely smooth.

Unfortunately, further reducing grain size and medium thickness will hit the "brick wall" at about 20-30 Gbits/in<sup>2</sup> due to the superparamagnetic limit, as mentioned in Chapter 3. To cope with this problem, very high crystalline anisotropy media, such as CoSm, CoPt, FePt, barium ferrite will probably replace conventional alloy such as CoCrTa [Speliotis-99].

Another possibility is to switch to **perpendicular recording**, because this recording mode allows to use a thick medium, therefore better stability and higher SNR. If several problems (see [Thompson-97]) can be solved, perpendicular recording will become a winner for media with extremely high areal density of 100 Gbit/in<sup>2</sup>.

Nowadays, the most prominent candidate for extremely high density magnetic recording media, that is **patterned media**, is being developed. In a conventional high density hard disk, a bit with a sufficient signal to noise ratio consists of some hundreds single-domain grains. The size of a grain is typical 10-30 nm. As said above, grain size can not be reduced liberally due to the superparamagnetic limit. A solution to that is to pattern the magnetic layer in a regular matrix of dots [ISTG-99, Haast-98]. Each dot is a single domain and can serve as one bit. By this way, bit size can be drastically reduced. Optimists say that patterned media can propel magnetic recording technology not only to 100Gbit/in<sup>2</sup> but perhaps to 1 Tbit/in<sup>2</sup> and even beyond [Speliotis-99].

For the past ten years, **optical and magnetooptical (MO) recording media** has become a potential rival to the magnetic recording media. The products of these technologies appear as removable media, such as CD-ROM, CD-R, CD-RW, Phase-change WORM, MD, DVD, etc (see List of symbols and abbreviations). Although the current DVD technology offers up to 17 billion bytes of digital data storage per disc, the search for media with greater capacities continues. Hitachi is an example of one vendor researching the use of smaller wavelength lasers to increase data capacity per layer. Using blue lasers, current efforts have shown that up to 14 billion bytes of data can be stored on a single layer [IBM-99a]. In the future, emerging DVD standard can reach seven times the data capacity of a CD-ROM. Dual-layer DVDs can carry even more, up to twelve times the data on a single side ! [Sony-99]. Moreover, a significant breakthrough can be obtained by near-field recording, which can attain sub-wavelength recording resolution through solid immersion lenses and truncated fiber-optic structures [Speliotis-97].

Pioneers in data storage technology are now conceiving many other types of recording media, based on different principles. Among these, holographic recording and Scanning Probe Microscope (SPM) -based recording are often mentioned.

**Holographic recording** uses lasers to store information as "pages" of electronic patterns within the volume of special optical materials. Because a million or more data bits are placed on each page and thousands of pages can be stored in a material no larger than a small coin, holographic systems offer the possibility of compact devices holding many trillions of bytes of information. Since there are no moving parts and all the information in each page is accessed simultaneously in parallel, the technology also has the potential for very rapid access to any of the stored data [IBM-99b]. Downloading a movie from a sugar cube-sized crystal may therefore no longer be the stuff of sci-fi.

**SPM-based recording** works like an AFM, that could provide 100 times or more the density, thereby permitting the continued increase in computer data storage capacity. This AFM technology is related to other probe-based microscopes, such as the scanning tunneling microscopes (STM), which can write and read atomic-scale surface features. Operating under normal temperature and atmospheric conditions, AFM recording could provide the capability of writing and reading information at densities of up to 300 Gbits/in<sup>2</sup>. This would represent a sharp increase over the 20-50 Gbits/in<sup>2</sup> where stability problems are expected to be seen in conventional magnetic media [IBM-99c].

## 8.4. References

- [Haast-98] M. A. M. Haast, J. R. Schuurhuis, L. Abelmann, J. C. Lodder and T. J. Popma. "Reversal mechanism of submicron patterned CoNi/Pt multilayers". IEEE Trans. Magn. 34 (1998), 1006.
- [IBM-99a] IBM website : <http://www.storage.ibm.com/hardsoft/diskdrdl.htm>
- [IBM-99b] IBM website: <http://www.ibm.com/stretch/mindshare/holo.html>
- [IBM-99c] IBM website: <http://www.research.ibm.com/topics/popups/serious/nano/html/ahow.html>
- [ISTG-99] Website of the Information Storage Technology Group (ISTG) - University of Twente: <http://www.el.utwente.nl/tdm/istg/research/research-frame.html>
- [Lodder-98] J. C. Lodder. "Magnetic recording hard disk thin film media". Handbook of magnetic materials. Vol. 11 (1998), edited by K. H. J. Buschow.
- [Sony-99] Website of Sony: <http://www.sel.sony.com/SEL/rmeg/digitalfuture/>
- [Speliotis-97] D. Speliotis. "Magnetic recording: 100 years old and still growing". J. Magn. Soc. of Japan 21 (Supp. No. S2) (1997), 119.

#### 8.4. References

---

- [Speliotis-99] D. E. Speliotis. "Magnetic recording beyond the first 100 years". J. Magn. Magn. Mat. 193 (1999), in press.
- [Thompson-97] D. Thompson. "The role of perpendicular recording in the future of hard disk storage". J. Magn. Soc. of Japan 21 (Supp. No. S2) (1997),9.

# Appendix

---

## Standard crystallographic XRD data

Table A.1. Crystallographic XRD data of **hcp Co** powder standard specimen [JCPDS-97a]. The angle  $\theta$  is the Bragg angle. Values of  $2\theta$  are angles at which the peaks corresponding to the lattice planes (hkil) appear. The data are calculated for Cu-K $\alpha$  radiation,  $\lambda = 1.54056\text{\AA}$ .

$2\theta$	Intensity	h	k	i	l
41.683	20	1	0	-1	0
44.762	60	0	0	0	2
47.568	100	1	0	-1	1
62.726	1	1	0	-1	2
75.939	80	1	1	-2	0
84.195	80	1	0	-1	3
90.619	20	2	0	-2	0
92.537	80	1	1	-2	2
94.733	60	2	0	-2	1
98.734	20	0	0	0	4

Table A.2. Crystallographic XRD data of **bcc Cr** powder standard specimen [JCPDS-97b]. The angle  $\theta$  is the Bragg angle. Values of  $2\theta$  are angles at which the peaks corresponding to the lattice planes (hkl) appear. The data are calculated for Cu-K $\alpha$  radiation,  $\lambda = 1.54056\text{\AA}$ .

$2\theta$	Intensity	h	k	l
44.392	100	1	1	0
64.581	16	2	0	0
81.721	30	2	1	1
98.146	18	2	2	0
115.259	20	3	1	0
135.416	6	2	2	2

## References

- [JCPDS-97a] JCPDS - International Centre for Diffraction Data, Card number: 05-0727. PCPDFWIN version 1.30 (1997).
- [JCPDS-97b] JCPDS - International Centre for Diffraction Data, Card number: 06-0694. PCPDFWIN version 1.30 (1997).

## List of symbols and abbreviations

$\alpha$	[degree]	Angle between the field and the normal direction of the film plane (in torque measurement).
$\chi_{ini}$	[-]	Initial susceptibility.
$\chi_{ini-max}$	[-]	Peak height of the initial susceptibility curve.
$\chi_{irr}$	[-]	Irreversible susceptibility.
$\chi_{irr-i}$	[-]	Intrinsic irreversible susceptibility.
$\chi_{rev}$	[-]	Reversible susceptibility.
$\chi_{tot}$	[-]	Total susceptibility = $\chi_{irr} + \chi_{rev}$ .
$\Delta E$	[J]	Energy barrier (for magnetic reversal).
$\Delta E_c$	[J]	Critical energy barrier.
$\Delta E_m$	[J]	Median energy barrier.
$\Delta\theta_{50}$	[degree]	The width at half height of a rocking curve peak.
$\lambda$	[m]	Mean free path.
$\mu_0$	[JA <sup>-2</sup> m <sup>-1</sup> ]	Magnetic permeability of empty space = $1.2566 \times 10^{-6}$ .
$\theta$	[degree]	Angle between the magnetization vector and the easy-axis (in torque measurements).
$\theta$	[degree]	Bragg angle (in XRD measurements).
$\theta$	[degree]	Angle between the incident X-ray beam and the normal direction of sample plane in rocking curve measurements.
$\sigma$	[-]	Standard deviation of distribution.
$\tau$	[s]	Relaxation time.
a	[nm]	Transition length.
AES		Auger Electron Spectroscopy.
AFM		Atomic Force Microscopy.
bcc		Body-Centered Cubic.
CD-ROM		Compact Disc - Read Only Memory.
CD-R		CD - Recordable.
CD-RW		CD - Read Write.
CP		Chrysanthemum-like Pattern.
CS		Compositional Separation.
DCD		DC-Demagnetization.
$d_{crit}$	[m]	Critical particle diameter between coherent and incoherent modes.

## List of symbols and abbreviations

---

DVD		Digital Video Disc.
DWM		Domain-Wall Motion.
EDS		Energy Dispersion x-ray Spectrometer.
EELS		Electron Energy Loss Spectroscopy.
$f_0$	[Hz]	Frequency of gyromagnetic precession $\approx 10^9$ .
GMR		Giant Magnetoresistive.
$H_a$	[A/m]	Applied field.
$H_{app}$	[A/m]	Ditto.
$H_c$	[A/m]	Coercivity.
$H_{c\perp}$	[A/m]	Perpendicular coercivity.
$H_{c//}$	[A/m]	In-plane coercivity.
hcp		Hexagonal Close-Packed.
$H_{cr}$	[A/m]	Remanence coercivity.
HDD		Hard Disk Drive.
$H_f$	[A/m]	Fluctuation field.
$H_i$	[A/m]	Internal field.
$H_K$	[A/m]	Anisotropy field.
$H_{peak}$	[A/m]	Field at viscosity peak.
$H_{sus-peak}$	[A/m]	Field value at the peak of the initial susceptibility curve.
$I$	[Am <sup>2</sup> ]	Magnetic moment.
IRM		Isothermal Remanence Magnetization.
$I_s$	[Am <sup>2</sup> ]	Saturation magnetic moment.
$k$	[J/K]	Boltzmanns constant = $1.3807 \times 10^{-23}$ .
$K$	[J/m <sup>3</sup> ]	Anisotropy constant.
$K_d$	[J/m <sup>3</sup> ]	Demagnetizing anisotropy constant.
$L$	[J/m <sup>3</sup> ]	Torque.
$M$	[A/m]	Magnetization.
MD		MiniDisc.
$M_{irr}$	[A/m]	Irreversible magnetization.
MR		Magnetoresistive.
$M_r$	[A/m]	Remanence magnetization.
$M_{rev}$	[A/m]	Reversible magnetization.
$M_s$	[A/m]	Saturation magnetization.
$N$	[-]	Demagnetizing factor.
PAr	[mbar]	Ar pressure.
$R_1$	[J/m <sup>3</sup> ]	First Fourier coefficient.

## List of symbols and abbreviations

---

$R_2$	[J/m <sup>3</sup> ]	Second Fourier coefficient.
RT		Room Temperature.
S	[-]	Remanence squareness.
S	[A/m]	Magnetic viscosity.
S*	[-]	Coercive squareness.
S <sub>0</sub>	[A/m]	Intrinsic magnetic viscosity.
SEM		Scanning Electron Microscopy.
SFD		Switching Field Distribution.
S <sub>half-width</sub>	[-]	Half-width of the viscosity peak.
SNR		Signal-to-Noise Ratio.
S <sub>plateau</sub>	[A/m]	Magnetic viscosity at the plateau of the viscosity curve (especially in perpendicular media).
S-W		Stoner-Wohlfarth.
t	[s]	Time.
t	[nm]	Film thickness.
TEM		Transmission Electron Microscopy.
T <sub>s</sub>	[°C]	Substrate temperature.
V	[m <sup>3</sup> ]	Volume.
V <sub>act</sub>	[m <sup>3</sup> ]	Activation volume.
V <sub>act@H<sub>c</sub></sub>	[m <sup>3</sup> ]	Activation volume at H <sub>c</sub> .
V <sub>col</sub>	[m <sup>3</sup> ]	Column volume (of alumite media).
V <sub>critical</sub>	[m <sup>3</sup> ]	Critical volume.
V <sub>eff</sub>	[m <sup>3</sup> ]	Effective volume.
V <sub>grain</sub>	[m <sup>3</sup> ]	Grain volume.
V <sub>particle</sub>	[m <sup>3</sup> ]	Particle volume.
V <sub>rf</sub>	[kV]	RF voltage (of sputtering equipment).
V <sub>sample</sub>	[m <sup>3</sup> ]	Sample volume.
VSM		Vibrating Sample Magnetometer.
V <sub>switching</sub>	[m <sup>3</sup> ]	Switching volume.
WORM		Write Once Read Many
XRD		X-Ray Diffractometer.
XRF		X-Ray Fluorescence Spectroscopy.



## Acknowledgements

Post-graduation is a process of self-study. However, as the old Vietnamese saying goes: "You can never succeed without a teacher", indeed, I could not have completed this thesis without the guidance of many experienced people. The person to whom I am most grateful is *Associate Prof. Dr. Cock Lodder*, for being my mentor from beginning to end and for his kindness to me. He is the person who made me feel so grateful by once saying to me, "I never put my hands off you". He has always cared about my work and my personal life in the Netherlands, even though he doesn't even have time for a relaxed coffee. I would also like to acknowledge *Prof. Dr. Theo Popma* for being my *promotor*. I appreciate the comments on my concept thesis from all members of the promotion committee. Especially, I would like to thank *Prof. Dr. Roy Chantrell* for the useful discussions on time-dependence measurements.

Although a major part of my work was carried out in the Netherlands, I have constantly received support from my home institute, the International Training Institute for Materials Science (ITIMS), Hanoi, Vietnam. First of all, I would like to thank my Vietnamese *promotor*, *Prof. Dr. Than Duc Hien* for his support and correction of my thesis. I am also grateful to *Ass. Prof. Dr. Nguyen Hoang Luong* for his advice during my working period in Vietnam. Moreover, I must always remember *Prof. Dr. Nguyen Phu Thuy* and *Ass. Prof. Dr. Nguyen Duc Chien* - vice directors of ITIMS - with gratitude. They have been willing to give me all the help they can.

It has been a great honor for me to work in the Information Storage Technology Group (ISTG), of the MESA research institute, the University of Twente (UT), where I found a friendly atmosphere created by humorous and helpful colleagues. Among them, first of all, *Thijs Bolhuis* is gratefully acknowledged for his technical help during my study and for making my life in the Netherlands more easy and interesting. No one who ever works in this group can forget him, a nice and skillful technician. More than a technician, he is an expert on VSM and other magnetic measurements. I have learned a lot from him. Another important person I would like to mention is *Poul de Haan*. I am grateful to him for his assistance in sputtering technique and XRD measurements. The cozy dinners at his home and the walks in the woods with his family and his dogs will always be in my mind.

A man who has recently had a lot of influence on my way of thinking is *Dr. Abdellah Lisfi*. I would like to express my sincere thanks to him for his kind help and discussions on magnetism and magnetic measurements. He often asks me "Is

## Acknowledgements

---

*alles goed?*" (Is everything OK?, in Dutch) whenever we meet and if something is *niet goed*, he is willing to help me with his whole heart.

Besides, all other members of ISTG are kindly acknowledged for their cooperation and friendship. Especially, I am grateful to *Martin Bijker* and *Leon Abelmann* for their advice on my research, *Erik Samwel* for useful discussions on VSM measurements and *Johan Knol* for being a nice friend and a "mensa-mate" when I was alone during the early years of my study in the Netherlands. Furthermore, I would like to express my gratitude to *Dr. Takehiro Shimatsu*, an old member of ISTG, now working at the Tohoku University, Sendai, Japan, for his interesting discussions on perpendicular measurements and other things. In addition, two persons I should not forget to thank are the secretaries of ISTG and MK *leerstoel*, *Simone Heideman* and *Judith Beld*. Without them, life would have been more difficult !

I have spent many days working in the MESA clean room of UT, where I immediately found that the whole cleanroom team members are very kind and skillful. Among them, I would like to express my deep thanks to *Johnny Sanderink*, *Stan Krüger* and *Bert Otter*, who kept my equipment alive and who would help me enthusiastically at anytime I needed. They are not only technicians, but also nice friends in between working hours. I also would like to thank *Rico Keim* of CMO analytical laboratory for his TEM observations. It is so pleasant for anyone to work with him, a friendly and careful man. He was trying his best to help me even when loads of work accumulated during the last few days before his holiday trip to Australia.

Differently from other AIO and OIO Ph.D. students of UT, my thesis was mainly sponsored by NUFFIC (The Netherlands Organization for International Cooperation in Higher Education) and partly by the Vietnamese Ministry of Education and Training. Many skillful people were involved in managing my study in the Netherlands. The most important persons that I greatly appreciate are *Peter de Goeje*, *Arend van Leeuwen* and *Frans Bekker* at the University of Amsterdam. In spite of the distance between them and me, they cared about a lot of things with regard to my life in the Netherlands. I will never forget the wonderful party they organized for us on the occasion of the Vietnamese New Year. Furthermore, I would like to thank *Jisk Holleman* at UT, who is the manager of ITIMS' Ph.D. students studying at UT, including me. He is not only a nice friend of mine, but also a friend of the Vietnamese people.

At this point I want to say that the Dutch people are always so nice and helpful, anywhere and in any situation. The Netherlands is a small but great country where I found that all public and administrative systems worked so well and smoothly.

I will remember the period of about a year I worked in the laboratories of ITIMS in Vietnam, among my best friends and colleagues. The most esteemed person I would like to mention and express my thanks to is *Prof. Nguyen Xuan Chanh*. Although he was not officially responsible for my study, I still received a lot of help and advice from him. I am also grateful to *Dr. Nguyen Huu Duc* for his kind support and useful discussions. I felt so happy to work within a team of young and nice colleagues: *Nguyen Anh Tuan, Luong Anh Trong, Pham Duc Thang, Nguyen Thanh Ngoc, Tran Mau Danh, etc.* I am thankful for their cooperation and friendship. Besides, I would like to thank *Nguyen Van Hoang, Vu Ngoc Hung, Dao Duong Hanh, Tran Kim Tu, Nguyen Thi Thuan* and all other members of ITIMS staff for their support during my research at ITIMS.

My life in the Netherlands would be very boring without my Vietnamese friends *Nguyen Hoang Viet, Du Thi Xuan Thao, Nguyen Phuc Duong, Pham Thanh Huy, Nguyen Nhu Toan, Le Minh Phuong* and the others. I appreciate my friendship with all of them.

Last but not least, I would like to thank my dearest beloved ones - my parents and grandparents. They have raised me, formed my character when I was a child and have given themselves over to helping and encouraging me during my study, even over the distance of a six-guilder-per-minute phone call ! Furthermore, I am deeply grateful to my uncle *Dao*, who always tries to take care of me, even though he holds a busy position. Finally, I would like to thank *Van Anh*, who has always been with me, filling me with pleasure and smiles. Her contribution to the preparation of the manuscript of my thesis is also appreciated.

Enschede, February 27<sup>th</sup>, 1999

Phan Le Kim

## Lời cảm ơn

Đào tạo trên đại học là một quá trình tự học. Tuy nhiên, như tục ngữ Việt nam đã có câu: "Không thầy đố mày làm nên", tôi sẽ không thể nào hoàn thành được bản luận văn này nếu không có sự giúp đỡ và hướng dẫn của những người đi trước. Người mà tôi phải chịu ơn nhiều nhất là thầy hướng dẫn của tôi, *PGS. TS. Cock Lodder*. Tôi xin được bày tỏ lòng biết ơn sâu sắc nhất đến ông, người đã kèm cặp và dẫn dắt tôi từ những ngày đầu khi tôi mới bắt tay vào nghiên cứu cho đến những ngày cuối cùng của bản luận văn này. Tôi vô cùng cảm kích về một câu mà ông đã có lần nói với tôi: "Tôi sẽ không bao giờ rời bỏ trách nhiệm của tôi đối với cậu!". Ông lúc nào cũng tử tế và quan tâm đến công việc và đời sống của tôi ở Hà lan, cho dù ông luôn luôn bận rộn tới mức chưa lần nào tôi thấy ông được uống một cốc cà phê trong trạng thái thư giãn. Tôi cũng xin cảm ơn *GS. TS. Theo Popma* là người thay mặt hội đồng bảo vệ của nhà trường cấp bằng cho tôi, *GS. TS. Roy Chantrell* vì những cuộc trao đổi bổ ích về các phép đo hiệu ứng phụ thuộc theo thời gian, và các thành viên khác thuộc hội đồng bảo vệ đã nhận xét cho bản luận văn của tôi.

Mặc dù những phần chính trong bản luận văn này được thực hiện tại Hà lan, nhưng tôi vẫn luôn nhận được sự giúp đỡ vô cùng nhiệt tình từ cơ quan chủ quản, Trung tâm Quốc tế Đào tạo về Khoa học Vật Liệu (ITIMS), Hà nội, Việt nam. Đầu tiên, tôi xin chân thành cảm ơn thầy hướng dẫn phía Việt nam của tôi là *GS. TS. Thân Đức Hiến*, người đã thường xuyên quan tâm và đã chữa bản thảo luận văn cho tôi. Tôi cũng xin cảm ơn *PGS. TS. Nguyễn Hoàng Lương* về những giúp đỡ và góp ý trong thời gian tôi làm việc tại Hà nội. Bên cạnh đó, tôi xin bày tỏ lòng biết ơn đến *GS. TS. Nguyễn Phú Thủy* và *PGS. TS. Nguyễn Đức Chiến*, hai phó giám đốc ITIMS, đã luôn quan tâm đến công việc và đời sống của tôi, giúp đỡ tôi rất nhiệt tình mỗi khi cần thiết.

Tôi đã có một vinh dự lớn khi được làm việc tại Nhóm Kỹ thuật Lưu trữ Thông tin (ISTG) thuộc viện nghiên cứu MESA, trường Đại học Tổng hợp Twente, Hà lan, nơi tôi đã tìm thấy một bầu không khí chan hoà tình thân ái, được tạo nên bởi các thành viên vui tính và tốt bụng. Trong số đó, tôi xin chân thành cảm ơn ông *Thijs Bolhuis* đã giúp đỡ tôi rất nhiều về kỹ thuật trong quá trình nghiên cứu. Hơn thế nữa, ông đã giúp tôi tìm thấy nhiều điều thú vị trong cuộc sống tại Hà lan. Không một ai đã từng làm việc tại đây có thể quên được người kỹ thuật viên lành nghề và tốt bụng này. Không chỉ là một kỹ thuật viên, ông còn là một chuyên gia về VSM và các phép đo từ khác. Trong thời gian làm việc tại đây, tôi đã học hỏi được nhiều ở ông. Một thành viên quan trọng khác trong nhóm mà tôi rất biết ơn đó là ông *Poul de Haan*, người đã nhiệt tình giúp tôi trong kỹ thuật phún xạ và các phép đo nhiễu xạ tia X. Tôi không thể nào quên được những bữa cơm tối ấm cúng tại gia đình và những cuộc dạo chơi trong rừng cùng vợ chồng ông.

Một người mà trong thời gian gần đây đã có nhiều ảnh hưởng đến những suy nghĩ trong nghiên cứu của tôi đó là *TS. Abdellah Lisfi*. Tôi xin được bày tỏ lòng biết ơn tới ông về những cuộc thảo luận rất thú vị giữa chúng tôi về từ học và các phép đo từ. Mỗi khi gặp tôi, ông thường hỏi "*Is alles goed ?*" (Mọi việc đều ổn cả chứ ?, bằng tiếng Hà lan), và nếu có việc gì đó "*niet goed*" (không ổn), thì ông sẵn sàng bỏ thời gian ra giúp đỡ tôi hết sức mình.

Ngoài ra, tôi xin cảm ơn tất cả các thành viên khác của ISTG về những giúp đỡ và hợp tác trong khoa học và về tình cảm mà họ đã dành cho tôi. Trong những người đó, đặc biệt tôi xin gửi lời cảm ơn tới các anh *Martin Bijker* và *Leon Abelmann* về những lời khuyên trong nghiên cứu, anh *Erik Samwel* về những cuộc trao đổi bổ ích xung quanh các phép đo VSM và anh *Johan Knol* về tình bạn bên bàn ăn tối tại *mensa* (nhà ăn ở khu ký túc xá của trường), trong thời gian mà tôi là người Việt duy nhất học tại trường này. Tôi cũng xin cảm ơn *TS. Takehiro Shimatsu*, một thành viên cũ của ISTG, nay công tác tại trường Đại học Tổng hợp Tohoku, Sendai, Nhật bản, về những cuộc trao đổi thú vị liên quan tới các phép đo từ theo phương vuông góc và nhiều vấn đề khác. Ngoài ra, còn hai người mà tôi không thể không cảm ơn, đó là các thư ký của ISTG và nhóm MK, chị *Simone Heideman* và *Judith Beld*. Không có họ, cuộc sống sẽ trở nên khó khăn hơn !

Từ những ngày đầu làm việc tại phòng sạch của Viện nghiên cứu MESA của trường, tôi đã nhận thấy đội ngũ kỹ thuật viên tại đây rất tốt bụng và làm việc có hiệu quả. Trong số họ, tôi xin gửi lời cảm ơn chân thành tới các ông *Johnny Sanderink*, *Stan Krugger* và *Bert Otter*, những người đã duy trì sự sống cho những máy móc mà tôi làm việc, những người đã luôn nhiệt tình giúp đỡ tôi mỗi khi tôi gặp khó khăn trong thực nghiệm. Trong giờ làm việc, họ là các kỹ thuật viên lành nghề nhưng ngoài giờ làm việc, họ trở thành những người bạn vui tính và nồng nhiệt. Bên cạnh đó, tôi xin cảm ơn ông *Rico Keim* ở phòng thí nghiệm phân tích CMO về những phép phân tích TEM mà ông đã giúp tôi thực hiện. Những ai đã từng làm việc với ông đều dễ dàng nhận thấy ở ông một con người chu đáo và luôn quan tâm tới người khác. Thậm chí, trong những ngày cuối cùng của ông trước chuyến đi du lịch tại Úc, cho dù các công việc chất đống trên bàn làm việc, ông vẫn lo lắng giúp tôi hoàn thành nốt những kết quả cuối cùng của bản luận văn này.

Khác với các nghiên cứu sinh dạng AIO và OIO khác của trường, luận văn của tôi đã được tổ chức NUFFIC (Tổ chức Hợp tác Quốc tế về Đào tạo Trên Đại học của Hà lan) tài trợ. Trong thời gian làm việc tại Việt nam, tôi đã được Bộ Giáo dục và Đào tạo tài trợ. Tôi thực sự biết ơn những người đã liên quan tới việc quản lý, tổ chức công việc và cuộc sống của tôi tại Hà lan, đặc biệt là các ông *Peter de Goeje*, *Arend van Leeuwen* và *Frans Bekker* của trường Đại học Tổng hợp Amsterdam. Mặc dù ở xa, các ông đã thường xuyên quan tâm tới đời sống của tôi tại Hà lan. Tôi sẽ không thể quên bữa tiệc vui vẻ nhân dịp Tết cổ truyền của Việt nam mà các ông đã đứng ra tổ chức cho chúng tôi vừa qua. Bên cạnh đó, tôi xin được bày tỏ lòng biết ơn tới *TS. Jisk Holleman*, người chịu trách nhiệm quản lý các nghiên cứu sinh Việt nam chúng tôi tại trường ĐHTH Twente. Ông không chỉ là một người

## Acknowledgements

---

bạn tốt của tôi nói riêng, mà ông còn là một người bạn của nhân dân Việt nam nói chung.

Đến đây, tôi xin có một nhận xét rằng, người Hà lan luôn tốt bụng và sẵn lòng giúp đỡ người khác ở mọi nơi, mọi chỗ. Nước Hà lan là một quốc gia tuy nhỏ bé nhưng thật tuyệt vời, ở nơi đó, mọi guồng máy hành chính và các hệ thống công cộng đều hoạt động trơn tru và có hiệu quả.

Trong thời gian làm luận văn tại các phòng thí nghiệm của ITIMS, Hà nội, bầu không khí thân mật của bè bạn và đồng nghiệp đã để lại trong tôi nhiều kỷ niệm gắn bó và những ấn tượng khó quên. Người đáng kính nhất mà tôi muốn bày tỏ lòng biết ơn, đó là *GS. Nguyễn Xuân Chánh*. Mặc dù không phải là người hướng dẫn nhưng giáo sư đã thực sự giúp đỡ và cho tôi nhiều lời khuyên rất bổ ích. Tôi cũng xin cảm ơn *TS. Nguyễn Hữu Đức* về những giúp đỡ quý báu và những cuộc thảo luận thú vị. Tôi đã cảm thấy vô cùng hạnh phúc khi được làm việc với những đồng nghiệp trẻ và vui tính. Họ là các anh *Nguyễn Anh Tuấn, Lương Anh Trọng, Phạm Đức Thắng, Nguyễn Thanh Ngọc, Trần Mậu Danh, .v.v.* Tôi biết ơn họ về những giúp đỡ và cộng tác trong công việc, cũng như những tình cảm mà họ đã dành cho tôi. Bên cạnh đó, tôi xin chân thành cảm ơn các anh, chị *Nguyễn Văn Hoàng, Vũ Ngọc Hùng, Đào Dương Hạnh, Trần Kim Tú, Nguyễn Thị Thuận* và toàn thể các thành viên khác của ITIMS đã luôn giúp đỡ tôi trong thời gian tôi làm việc tại đây.

Cuộc sống của tôi tại Hà lan sẽ vô cùng trống vắng và buồn tẻ nếu không có các bạn *Nguyễn Hoàng Việt, Dư Thị Xuân Thảo, Nguyễn Phúc Dương, Phạm Thành Huy, Nguyễn Như Toàn, Lê Minh Phương* và những bạn khác. Tôi xin được cảm ơn tình bạn mà họ đã dành cho tôi.

Trong đoạn văn cuối cùng này, tôi muốn dành lời cảm ơn đến những người thân yêu nhất của tôi, đó là ông bà và bố mẹ tôi, những người đã nuôi dạy tôi từ tấm bé và đã luôn dành hết tình cảm của mình để hỗ trợ, khuyến khích tôi trong thời gian tôi học tập và nghiên cứu, cho dù trong thời gian đó, giữa tôi và gia đình là một khoảng cách của nửa vòng trái đất ! Ngoài ra, tôi cũng rất biết ơn bác *Đào* của tôi đã luôn quan tâm và tìm mọi cách chăm sóc, động viên tôi, mặc dù bác vẫn rất bận với công việc của mình. Cuối cùng, tôi xin cảm ơn *Vân Anh*, người luôn ở bên cạnh tôi, chia sẻ với tôi những niềm vui trong cuộc sống hàng ngày, và cũng là người đã đóng góp một phần vào khâu chuẩn bị bản thảo cho quyển luận văn này.

Enschede, ngày 27 tháng 2 năm 1999

Phan Lê Kim

## Biography

Phan Le Kim\* was born on March 2<sup>nd</sup>, 1971 in Hanoi, Vietnam. From 1988 to 1992, he studied at the Faculty of Physics, the University of Hanoi. He received his Bachelor Degree in Solid State Physics in 1992, graduated with the University Honor for the best student of the batch. After graduation, he worked for the Department of Electron Microscopy of the National Center for Natural Sciences for one year, as a technician in Transmission Electron Microscopy. In 1994, he enrolled in the International Training Institute for Materials Science (ITIMS), Hanoi and gained the Ph.D. project on CoCrTa magnetic recording media, which resulted in the contents of this thesis. The project was carried out at the Information Storage Technology Group (ISTG), MESA research institute of the University of Twente, under the supervision of Dr. Cock Lodder. A part of the research was done at the laboratories of ITIMS, Hanoi.

## Publications and presentations

1. Phan Le Kim, Cock Lodder, Than Duc Hien and Nguyen Hoang Luong, *"The Influence of Sputtering Parameters on Magnetic and Structural Properties of Co-Cr-Ta Magnetic Thin Films"* Proc. Second Int. Workshop on Materials Science (IWOMS'95), part II. Hanoi, Vietnam, (1995), 299-302.
2. Luong Anh Trong, Nguyen Xuan Chanh, Nguyen Huu Duc, Phan Le Kim *"Structure and magnetic properties of vacuum deposited Co, Co-Cr thin films"* Proc. Second Int. Workshop on Materials Science (IWOMS'95), part II. Hanoi, Vietnam, (1995), 311-314.
3. Phan Le Kim, Nguyen Hoang Luong, Than Duc Hien. *"Development of field-dependence remanence measurements in perpendicular direction, applied to magnetic thin films"* (in Vietnamese) Proceedings of the Second National Workshop on Condensed Matter Physics, Dason, Vietnam, August 6-8<sup>th</sup> 1997, printed by Science and Technology Publishing house (1998), p. 402-408.
4. Phan Le Kim and Cock Lodder *"Time-Dependence Effects in Recording Media"*. Poster presentation at MESA-day, Enschede, June 23<sup>rd</sup>, 1998.

---

\* Phan is his family name.

5. Phan Le Kim, Cock Lodder, Than Duc Hien and Nguyen Hoang Luong. *"The influence of tantalum content in relation to substrate temperature on magnetic and structural properties of Co-Cr-Ta thin films"*. J. Magn. Magn. Mat. 193(1999) 117-120.
6. Phan Le Kim, Cock Lodder and Theo Popma. *"Field dependence of magnetic viscosity of CoCrTa in-plane media"*. J. Magn. Magn. Mat. 193(1999), 249-252.
7. Phan Le Kim and Cock Lodder. *"Magnetic viscosity of alumite recording media with perpendicular anisotropy"*. Accepted for publication in the special issue on "Information Storage Technologies for the 21st Century" IEICE Transactions on Electronics (1999).
8. Phan Le Kim and Cock Lodder. *"Influence of CoCrTa layer thickness on structural and magnetic properties of CoCrTa/Cr media"*. To be published.
9. Phan Le Kim and Cock Lodder. *"Influence of Cr underlayer thickness on structural and magnetic properties of CoCrTa/Cr media"*. To be published.